https://ntrs.nasa.gov/search.jsp?R=19780022712 2020-03-22T03:18:45+00:00Z

General Disclaimer

One or more of the Following Statements may affect this Document

- This document has been reproduced from the best copy furnished by the organizational source. It is being released in the interest of making available as much information as possible.

- This document may contain data, which exceeds the sheet parameters. It was furnished in this condition by the organizational source and is the best copy available.

- This document may contain tone-on-tone or color graphs, charts and/or pictures, which have been reproduced in black and white.

- This document is paginated as submitted by the original source.

- Portions of this document are not fully legible due to the historical nature of some of the material. However, it is the best reproduction available from the original submission.

Produced by the NASA Center for Aerospace Information (CASI)

(NASA-CR-157547) SILICON RIBBON GROWTH BY A CAPILLARY ACTION SHAPING TECHNIQUE Final Report, 8 May 1975 - 8 Nov. 1977 (International Business Machines Corp.) 352 p HC A16/MF A01 CSCL 10A

N78-30655

Unclas
G3/44 28623

CONTENTS

		Page
TECHNICAL CONTENT STATEMENT		vi
RESEARCH PROGRAM PLAN		vii
HIGHLIGHTS		viii
ACHIEVEMENTS		ix
PUBLICATIONS AND PRESENTATIONS		xv
INVENTION DISCLOSURE ACTIVITY		xxi
COMPUTER SIMULATION MODELS-PROGRAMS		xxiii
I	CRYSTAL GROWTH	1
1.0	Introduction	1
2.0	Growth of 25 mm Silicon Ribbons	4
2.1	Description of Experimental Apparatus	4
2.2	Growth Procedure	9
2.3	Die Material Investigations	10
2.3.1	Materials Investigated	12
2.3.2	Die Fabrication and Evaluation	15
2.3.3	Results	17
2.4	Process Development For 25 mm Ribbons	30
2.4.1	Die Design	32
2.4.2	Ribbon Surface Quality	36
2.4.3	Dopant Distribution in 25 mm Silicon Ribbons	45
2.4.4	Thermal Stress Modification in the 25 mm Growth System	51

78 06 15 053

Page

2.4.5 Maximum Growth Rates for Melt-Grown Ribbon-Shaped Crystals 63
3.0 Growth of 38 mm Silicon Ribbons 69
3.1 Process Development for 38 mm Ribbons 69
3.1.1. Die Design 69
3.1.2 Reuse of Quartz Crucibles 73
3.1.3 Thermal Geometry Control 77
3.2 Physical Characteristics of 38 mm Ribbons 84
4.0 Growth of 50 mm Silicon Ribbons 85
4.1 Description of Experimental Apparatus 85
4.2 Meniscus Effects 87
4.2.1 Meniscus Height Measurements 87
4.2.2 High Melt Meniscus (HMM) Growth 90
4.3 Evaluation of an SiC-Coated Graphite Die 100
4.4 Dopant Distribution in 50 mm Silicon Ribbons 103
4.5 Stress Level in 50 mm Ribbons 105
5.0 Growth of 100 mm Silicon Ribbons 109
5.1 Description of Experimental Apparatus 109
5.2 100 mm Growth Experiments 112
6.0 Large-Grain Directional Solidification of Silicon 119
6.1 Experimental Procedure 119
6.2 Physical Characteristics of Directionally Solidified Silicon (DSS) 120
6.3 Discussion 123
7.0 Acknowledgments 127

Page

8.0 References 128

Appendix I. RIBBON GROWTH EXPERIMENTS PERFORMED DURING THE CURRENT REPORTING PERIOD 130

Appendix II. DIMENSIONAL CHARACTERISTICS OF RIBBONS GROWN IN THE CURRENT REPORTING PERIOD 172

Appendix III. DESIGN DETAILS FOR 25 MM DIES, DIE HOLDERS, AND HEAT SHIELDS 177

II STRUCTURAL AND ELECTRICAL CHARACTERIZATION OF CAST SILICON RIBBONS 182

1.0 Introduction 182

2.0 Silicon Carbide Formation 183

2.1 SiC Crystallites 183

2.2 SiC Carbide Films 184

2.2.1 Analysis of Surface Films 188

2.2.2 Optical Microscopy 188

2.2.3 Transmission Electron Microscopy 189

2.3 Summary 203

3.0 Ribbon Quality 204

3.1 Seeding and Surface Problems 204

3.2 Analysis of Surface Orientation 210

3.2.1 <112> Twinning 210

3.2.2 Non-Parallel Twinning 218

Page

		Page
3.3	Analysis of Twin Lamellae	219
4.0	Electrical Characterization of Silicon Ribbons	225
4.1	Experimental	225
4.2	Fabrication of MOS Capacitors and Solar Cells	226
4.3	Measurements	227
4.3.1	EBIC Measurements	228
4.3.2	Lifetime Measurements	231
4.5	Discussion	236
4.6	Summary	240
5.0	Structural Characterization of Silicon Ribbons	241
5.1	Measurements	241
5.2	Experimental	242
5.3	Results	245
5.3.1	Defects in Class I Ribbons	245
5.3.2	Defects in Class II Ribbons	259
5.3.3	Defects in Class III Ribbons	274
5.3.4	Defects in Class IV Ribbons	288
6.0	Future Quality Improvements	292
7.0	Acknowledgments	293
8.0	References	294
III	SILICON RIBBON TECHNOLOGY ASSESSMENT: 1978-1986	297
1.0	Introduction	297
2.0	PECAN Decision Analysis System Description	298
3.0	Interactive Simulation And The Production Unit Concept	299

Page

4.0 Economic Outlook For $50/m^2$ Silicon Ribbon (Scenario Set 1) 302

4.1 Business Strategy of Hypothetical Firm 302

4.2 Silicon Ribbon Technology Requirements 304

4.3 Discussion of Business Implementation Alternative 307

4.3.1 Approach to Scenario Development 307

4.3.2 Three Technology Implementation Scenarios 310

4.4 Sensitivity Analysis 317

5.0 Economic Outlook for $25/m^2$ Silicon Ribbon (Scenario Set 2) 324

6.0 Conclusions 326

7.0 References 327

TECHNICAL CONTENT STATEMENT

This report contains information prepared by the International Business Machines Corporation under the JPL contract. Its contents are not necessarily endorsed by the Jet Propulsion Laboratory, California Institute of Technology, or by the National Aeronautics and Space Administration.

RESEARCH PROGRAM PLAN

OBJECTIVES

1. Technological assessment of ribbon growth of silicon by a capillary action shaping technique.

2. Economic evaluation of ribbon silicon grown by a capillary action shaping technique as low-cost silicon.

SYNOPSIS OF PROGRAM OF STUDY

1. Crystal growth of silicon ribbons.

2. Characterization of silicon ribbons.

3. Economic evaluations and computer-aided simulation of ribbon growth.

HIGHLIGHTS

- Ribbon silicon produced by CAST yields 11.9% solar cell efficiency.

- CAST ribbons up to 95 mm wide and 0.3 mm thick were produced.

- CAST technology - Single ribbon, 100 mm wide ribbon, 0.3 mm thick, 3.8 m/hr growth rate, solar cell efficiency 13% - has the potential to meet a $50/m^2 target. This is based upon the availability of $10/kg polycrystalline silicon.

ACHIEVEMENTS

Ribbon Growth and Characterization

- 123 meters (41,527 cm^2) of uniform-width silicon ribbon were grown.
- Ribbon width capability was increased from 10 mm to 95 mm.
- SiC surface particle density was decreased from $5/cm^2$ to $< 4 \times 10^{-3}/cm^2$ through CAST high melt meniscus growth and use of SiC-coated graphite dies.
- A Growth technique for silicon tubes of 6 mm diameter x 1 m length was developed.
- Maximum growth rate equations for ribbons were devised.
- A new technique for thermal geometry control utilizing multiple inert gas streams was developed.
- The effect of die channel design on dopant distribution was demonstrated.

- The reuse of quartz crucibles through four melt-down cycles was demonstrated.

- A system for 100 mm wide ribbon growth was designed and implemented.

- Crack-free directional solidification of 5 cm diameter silicon ingots in carbon crucibles was achieved.

- Four classes of ribbon perfection were defined. These perfection categories coordinate with lifetime ranges and efficiency ranges of solar cells.

- Electrical activity measurements of crystallographic defects in ribbons were made through the SEM EBIC techniques using Schottky contacts and p-n junction for EBIC contrast.

- Quantitative "electrical activity" measurements of line defects in ribbons were made through carrier diffusion length measurements. Dislocations were shown to decrease minority-carrier lifetime by one to two orders of magnitude.

- Surface films on ribbon surfaces were analyzed as SiC crystallites. Significant structural differences, depending on deposition location, were found.

- Epitaxial growth of SiC through preferential incorporation of (111) SiC planes parallel to (111) silicon planes was identified as an important mechanism for surface film formation.

- Electrically active defects in CAST ribbons were identified as silicon carbide inclusions, high and low angle grain boundaries high order twins boundaries, multiple stacking faults, dislocation bands and dislocations.

- The electrical activity of grown-in dislocations due to their low density was shown to be moderate. It was also shown that grown-in dislocations are generated by thermal gradients associated with the growth technique. Their density varies from 3×10^3 to 5×10^5 per cm^2.

- Dislocation bands with densities larger than 10^6 dislocations/cm^2 were shown to be strongly active. The bands consist of two groups of dislocations. One group is inclined towards the ribbon surface, while the other

is almost parallel to ribbon surface in the growth direction. Both groups of dislocations have the same type of Burgers vectors, a/2[011] and a/2[101]. Dislocation networks are formed through the interaction of the two dislocations which leads to the formation of 90° dislocations.

- Grain boundaries were also shown to be strongly active. Their formation results mainly from foreign inclusions such as silicon carbide or from the non-accommodation of crystal lattice planes. Such non-accommodation of crystal lattices occurs when two crystals of different preferred orientation, such as [011] and [211] orientations, join. The boundaries contain dislocations and/or ledges which are spaced approximately 0.1 μm apart.

- First order (coherent) twins and stacking faults were shown to be nonactive. Their electrical activity increases as they degenerate into multiple overlapping faults and low-angle boundaries. The low-angle boundaries contain a high density of dislocations. The dislocation spacing ranges from 0.1 to 0.4 μm with an average of 0.2 μm. Degenerated twins act as dislocation sources.

General Economic Outlook:

- Silicon technology has the potential for achieving future low-cost material objectives for photovoltaic applications. For single ribbon growth a 1986 sheet price of $\$50/m^2$ is projected.

  Based upon recent significant achievements (e.g., 10 cm wide ribbon; > 11% efficient cell), $\$50/m^2$ silicon sheet price can be obtained with CAST technology without further scientific breakthrough.

Technology Development Guidelines:

Polycrystalline Silicon

- Low-cost polycrystalline silicon of semiconductor-grade quality, at $10/kg, is a prerequisite to achieving 1986 sheet material targets.

Ribbon Technology

- $\$25/m^2$ silicon ribbon by 1986 requires some technology advances. A set of technology requirements has been

defined, which results in ribbon prices ranging from $\$13/m^2$ to $\$30/m^2$.

- Since our ribbon geometry objectives (10 cm wide, 0.3 mm thick) have been achieved, short-range technology development should focus on improving material quality (long-range objective: 13% cell efficiency) and increasing growth rate (objective: 3.8 m/hr).

- Single-ribbon growth systems offer a good potential for achieving low-cost silicon sheet material within the shortest period of time.

- Ribbon thickness is a relatively insignificant factor in determining energy-capacity cost. A thickness compatible with efficient solar-cell processing in the range of 0.3 to 0.4 mm should be selected.

Publications and Presentations

Under Contract JPL 954144

(Subcontract NASA NAS7-100)

SILICON RIBBONS-A NEW APPROACH TO LOW-COST SINGLE CRYSTAL SILICON SOLAR CELLS, by T. F. Ciszek and G. H. Schwuttke, International Conference on Photovoltaic Power Generation, Hamburg, Germany, September 25-27, (1974).

GROWTH AND CHARACTERIZATION OF SILICON RIBBONS PRODUCED BY A CAPILLARY ACTION SHAPING TECHNIQUE, by T. F. Ciszek and G. H. Schwuttke, phys. stat. sol. (a) 27, 231, (1975).

MELT GROWTH OF CRYSTALLINE SILICON TUBES BY A CAPILLARY ACTION SHAPING TECHNIQUE, by T. F. Ciszek, phys. stat. sol. (a) 32, 521, (1975).

MAXIMUM GROWTH RATES FOR MELT-GROWN RIBBON-SHAPED CRYSTALS, by T. F. Ciszek, J. Appl. Phys. 47, 440, (1976).

PROBLEMS RELATED TO THE EFG PROCESS FOR SILICON RIBBON CRYSTALS, by T. F. Ciszek, G. H. Schwuttke and K. Yang, 18th AIME Electronic Matls. Conf., Salt Lake City, Utah, June 23-25, (1976).

DEFECTS IN SILICON RIBBON CRYSTALS AND THEIR INFLUENCE ON GENERATION LIFETIME, by K. Yang, G. H. Schwuttke and T. F. Ciszek, 5th International Conf. on Crystal Growth (ICCG5), Boston, Mass, July 17-22, (1977).

THERMAL BALANCING FOR RIBBON CRYSTAL GROWTH VIA DISTRIBUTED INERT-GAS STREAMS, by T. F. Ciszek and G. H. Schwuttke, Fifth International Conference on Crystal Growth (ICCG5), Boston, Mass., July 17-22, (1977).

GROWTH OF 50-MM WIDE SILICON RIBBONS BY THE CAPILLARY ACTION SHAPING TECHNIQUE, by T. F. Ciszek, 19th Annual AIME Electronic Materials Conference, Ithaca, N. Y., June 29-July 1, (1977). Invited paper.

GROWTH AND PROPERTIES OF CAPILLARY ACTION SHAPED SILICON RIBBONS, by T. F. Ciszek, G. H. Schwuttke and K. Yang, 1977 Meeting of Deutsche Gesellschaft Fur Kristallwachstum and Kristallzuchtung (DGKK), Stuttgart, West Germany, September 28-30, (1977), Invited paper.

SINGLE CRYSTAL SILICON BY CZOCHRALSKI AND RIBBON TECHNIQUES - A COMPARISON OF CAPABILITIES", by A. Kran, Invited paper presented at the Symposium on the Material Science Aspects of Thin Film Systems for Solar Energy Conversion, Tuscon, Arizona, May, (1974).

HIGH-SPEED SILICON PROCESSING FOR LOW-COST SOLAR CELLS, by A. Kran, paper presented at the International Conference, Photovoltaic Power Generation, Hamburg, Germany, September, (1974).

SILICON CRYSTAL REQUIREMENTS FOR LOW-COST SOLAR CELLS, by A. Kran, paper presented at the Electrochemical Society, May, (1975).

ALTERNATIVE STRATEGIES FOR IMPLEMENTING SILICON TECHNOLOGY FOR PHOTOVOLTAIC APPLICATIONS, by A. Kran, paper presented at the Intersociety Energy Conversion Engineering Conference, State Line, Nevada, September, (1976).

SILICON MATERIALS PROCESSING PROBLEMS, by G. H. Schwuttke, Invited paper at NSF Review Meeting, Pasadena, California, June, (1974).

SILICON FOR LOW-COST SOLAR CELLS, by G. H. Schwuttke, Invited paper, American Physical Soc. Meeting, January 31, Anaheim, California.

CHARACTERIZATION OF SILICON RIBBONS, by G. H. Schwuttke, Opening paper at the German National X-ray Topography Meeting, October, (1975), Aachen, Germany.

LOW-COST SILICON FOR SOLAR ENERGY APPLICATION, Opening address at the NPL Silver Jubilee Meeting - New Delhi, India, Dec., 4, (1975).

SEMINAR: STATUS OF SILICON RIBBON GROWTH, by G. H. Schwuttke, conducted at the National Broadcasting Laboratories, Tokyo, Japan, Dec. 2, (1975).

SEMINAR: GROWTH AND CHARACTERIZATION OF RIBBON CRYSTALS, by G. H. Schwuttke, conducted at the Institute of Physics, New Delhi University, Dec. 2, (1975).

SEMINAR: SILICON FOR SOLAR ENERGY CONVERSION, by G. H. Schwuttke, conducted at the Solid State Physics Lab., Ministry of Defense, New Delhi, India, Dec. 6, (1975).

LONG LIFETIME SILICON REQUIREMENTS, by G. H. Schwuttke, Proceedings Solar Energy Symposium, Tuscon, Arizona, (1975).

TECHNOLOGY'S ENERGY PROMISE, by G. H. Schwuttke, Keynote address, Data Processing Seminar, June 23, (1976), Christchurch, New Zealand.

ENERGY SEMINAR Conducted by G. H. Schwuttke, University of Canterbury, Christchurch, New Zealand, June, 24, (1976).

THE POTENTIAL OF SILICON AS ENERGY CONVERTER, Address delivered by G. H. Schwuttke, New Zealand Parliament to Members of the Parliament, Wellington, New Zealand, June 26, (1976).

LOW-COST SILICON FOR SOLAR CELL APPLICATION, by G. H. Schwuttke, Seminar at University of New South Wales, Sidney, Australia, June 30, (1976).

LOW-COST SILICON CELLS AND TUNGSTEN SELECTIVE SURFACES FOR SOLAR ENERGY APPLICATION, by G. H. Schwuttke, Seminar University Hong Kong, July 16, (1977).

SILICON RIBBONS FOR SOLAR ENERGY CONVERSION, by G. H. Schwuttke, Invited paper, Japanese Cryst. Soc. Meeting, Sendai, Japan, July 11, (1977).

SILICON AND SUNSHINE, Seminar by G. H. Schwuttke, Hitachi Central Research Labs., Tokyo, July 8, (1976).

SOLAR ENERGY CONVERSION THROUGH SILICON AND TUNGSTEN SURFACES, Seminar by G. H. Schwuttke, Singapore Science Center, July 20, (1976).

ANALYSIS BY ELECTRONIC CHANNELING OF SILICON RIBBONS, by G. H. Schwuttke, K. Yang and K. Kappert, Electrochemical Society Meeting, October, (1976), Las Vegas, Nevada.

CHARACTERIZATION OF SILICON RIBBONS, by K. Yang, G. H. Schwuttke and T. F. Ciszek, Electronic Material Conference, June, (1976), Salt Lake City, Utah.

LIFETIME CHARACTERIZATION OF SILICON RIBBONS, by G. H. Schwuttke and K. Yang, 12th IEEE Photovoltaic Spec. Conf., November 15, Baton Rouge, Louisiana.

LOW COST SILICON FOR SOLAR ENERGY APPLICATION, by G. H. Schwuttke, Jap. Journal of Crystallography, Vol. 4, No. 1.2, page 40, (1977).

LOW COST SILICON FOR SOLAR ENERGY APPLICATION, by G. H. Schwuttke, phys. stat. sol. (a) 43, 43, (1977).

CHARACTERIZATION OF CRYSTAL DEFECTS IN SILICON RIBBONS, by K. H. Yang, G. H. Schwuttke, Bull. Amer. Phys. Soc., Nov. 1977.

ELECTRICAL ACTIVITY OF CRYSTAL DEFECTS, G. H. Schwuttke, K. H. Yang, Bull. Amer. Phys. Soc., Nov. 1977.

Invention Disclosure Activity

Contract JPL 954144

(Subcontract NAS7-100)

Method For Producing Crystals From Molten Solutions by T. F. Ciszek and G. H. Schwuttke.

Method For Producing Ultra Thin Silicon Sheets by T. F. Ciszek and G. H. Schwuttke.

110 ($\bar{2}$11) Seed Orientation for Perfect Ribbon Growth by G. H. Schwuttke and T. F. Ciszek.

Device for Capillary Action Ribbon Crystal Growth by T. F. Ciszek.

Wide Ribbon Growth Through Thermal Geometry Control by Gaseous Means by T. F. Ciszek and G. H. Schwuttke.

Automated Width Control for Ribbon Crystals Grown by the Capillary Action Shaping Technique by T. F. Ciszek.

Passive Thermal Modifier for Ribbon Crystal Growth by T. F. Ciszek and G. H. Schwuttke.

Inert Gas Purge System For Silicon Ribbon Growth by T. F. Ciszek.

Silicon Carbide Die For Silicon Ribbon Growth by T. F. Ciszek.

Edge-Stabilized Pulling Technique For Ribbon Crystal Growth From the Melt by T. F. Ciszek and G. H. Schwuttke.

Improved Die Material for Silicon Ribbon Growth by Capillary Techniques by T. F. Ciszek.

Method For Producing Liquid-Phase Heteroepitaxial Silicon Sheets Contiguously Distributed by T. F. Ciszek and G. H. Schwuttke.

Simulation of Silicon Ribbon Production Unit by A. Kran.

Computer Simulation Models-Programs

Contract JPL 954144

(Subcontract NAS7-100)

Interactive Computer Simulation Model of Large-Area Silicon Sheet Growth (about 60,000 bytes of code) by A. Kran.

Computer Model to Facilitate Analysis And Review of Silicon Wafer Manufacturing Costs, (SPAR) (about 20,000 bytes of code) by A. Kran.

Interactive Computer Model of Silicon Ribbon Growth. Model design and coding completed (about 25,000 bytes of code) by A. Kran.

Solar Cell Performance Evaluation. A graphics analysis program, designed for interactive applications (about 15,000 bytes) by A. Kran.

Interactive computer program for manipulation, statistical analysis, and graphical representation of lifetime generation data (about 15,000 bytes). by A. Kran.

Computer program to project future ribbon technology based upon current achievement and estimated probability of meeting technology objectives (about 10,000 bytes) by A. Kran.

Computer program to calculate production throughput of Czochralski crystals, based upon stochastic input variables by A. Kran.

Small discrete event program to simulate material processing in a "production unit" environment by A. Kran.

Solar Cell curve fitting and data analysis (SOL). Determines I_o, A, and I_s for best-fit curve of form

$$I = I_o \left(e^{\frac{qv}{AkT}} - 1 \right) - I_s ,$$

as well as P_{max}, V_{pmax}, I_{pmax}, V_{oc}, I_{sc}, C_{ff}, and efficiency. By T. F. Ciszek.

Application of graphics to compare material area throughput capability between ribbon and Czochralski processing, the latter consisting of crystal pulling, slicing, and etching/polishing by A. Kran.

Design and partial coding of a solar cell processing model by A. Kran.

I CRYSTAL GROWTH

by

T. F. Ciszek

1.0 INTRODUCTION

The crystal-growth method under investigation is a capillary action shaping technique. Meniscus shaping for the desired ribbon geometry occurs at the vertex of a wettable die. As ribbon growth depletes the melt meniscus, capillary action supplies replacement material. The configuration of the technique used in our initial studies is shown in Fig. I-1 and is similar to the edge-defined, film-fed growth (EFG) process described by LaBelle[1]. The crystal-growth method has been applied to silicon ribbons for several years[2,3,4]. As our work on silicon ribbon growth has progressed, we have found that substantial improvements in ribbon surface quality could be achieved with a higher melt meniscus than that attainable with the EFG technique. Thus, in our later work we have abandoned the EFG technique in favor of the improved capillary action shaping technique, which employs the capillary die design shown in Fig. I-1.

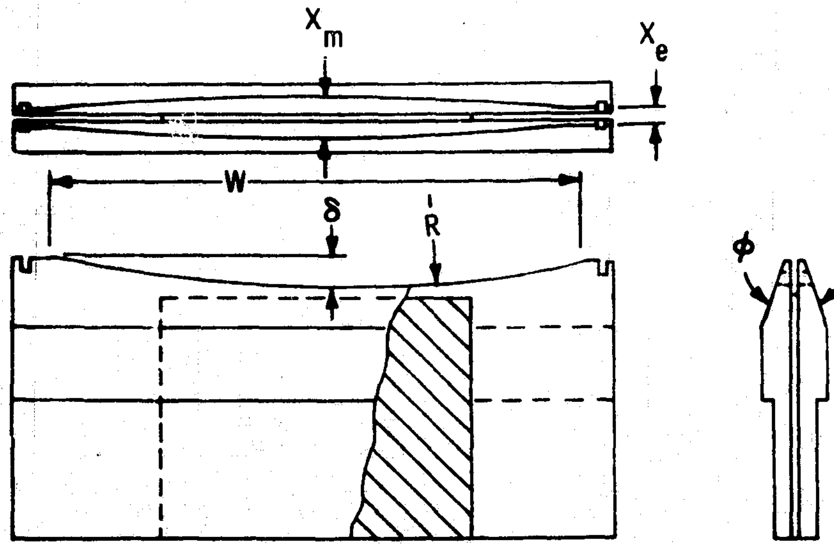

Fig. I-1. Capillary Die Design.

It represents a departure from the die types used for edge-defined, film-fed growth, in that the bounding edges of the die top are not parallel or concentric with the growing ribbon. The new dies allow a higher central melt meniscus (Fig. I-2) with concomitant improvements in surface smoothness and freedom from SiC surface particles, which can degrade perfection.

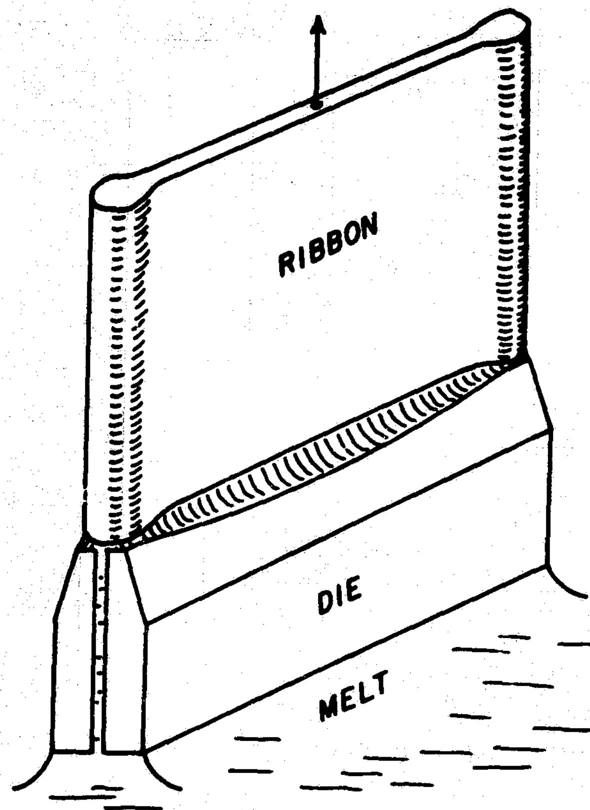

Fig.I-2.CAST High Melt Meniscus Growth

Our objective in this work has been to attain a clear technological assessment of silicon ribbon growth by the capillary action shaping technique and to enhance the applicability of the technique to photovoltaic power device material.

The results of our crystal growth studies will be presented in the following categories:

- Growth of 25 mm wide silicon ribbons
- Growth of 38 mm wide silicon ribbons
- Growth of 50 mm wide silicon ribbons
- Growth of 100 mm wide silicon ribbons

2.0 GROWTH OF 25 MM WIDE SILICON RIBBONS

At the onset of contract work, equipment and expertise existed for growing 12 mm wide silicon ribbons. Initial technician training was conducted at this width on the available equipment. This equipment was modified as required during the course of the contract.

2.1 Description of Experimental Apparatus

Silicon ribbon growth was conducted using a hydraulically actuated pulling mechanism with a 1.37 m maximum stroke. A pressurized air-over-oil reservoir system provided the driving force for actuation of the moving platen upon which the seed holding shaft was attached. X-Y-Z adjustment was provided for the seed shaft. Platen speed adjustment was attained via a needle valve in the oil flow line between the hydraulic cylinder and the oil reservoir tank. The crystal

growth furnace and associated vacuum system were supported on the frame of the hydraulic puller as shown in Fig. I-3. The furnace was powered by a 50-kW, 45-kc-rf generator.

The furnace consisted of a single-walled 94-mm-diameter silica shell with water-cooled stainless-steel end fittings sealed by viton O-rings. The top fitting could be either completely sealed (for vacuum bake-out of dies and furnace components) or provided with an oval cross section pull port through which the growing ribbon passed. The bottom fitting connected the shell to a horizontal base on one arm of a "tee" fitting. A horizontal sliding plate on an X-Y-θ stage was mounted on the opposite arm of the "tee." This plate held the pedestal shaft upon which the crucible assembly rested. The plate also supported an optical temperature sensor which was focused on the bottom of the crucible holder and was part of the closed-loop temperature control system. The third arm of the "tee" was used for evacuation and as a purge gas inlet.

The furnace hot zone is depicted in Fig. I-4. All interior components are graphite except the opaque heat shield and the clear quartz crucible. A 50-mm-OD x 25-mm-high flat-bottomed crucible was used. The EFG die design depicted in Fig. I-5 was used for our initial experiments and

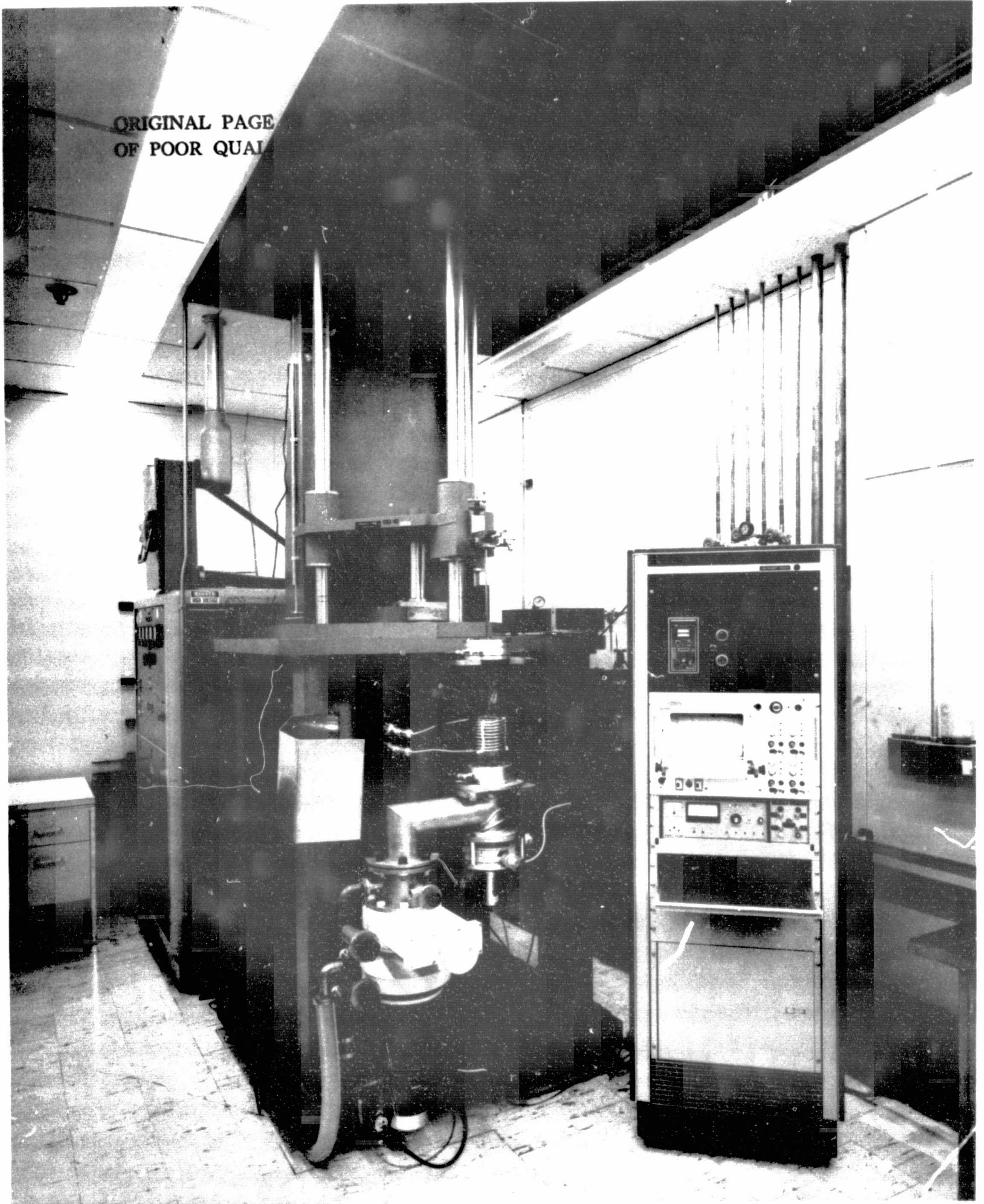

ORIGINAL PAGE
OF POOR QUAL

Fig.I-3. Ribbon growth apparatus

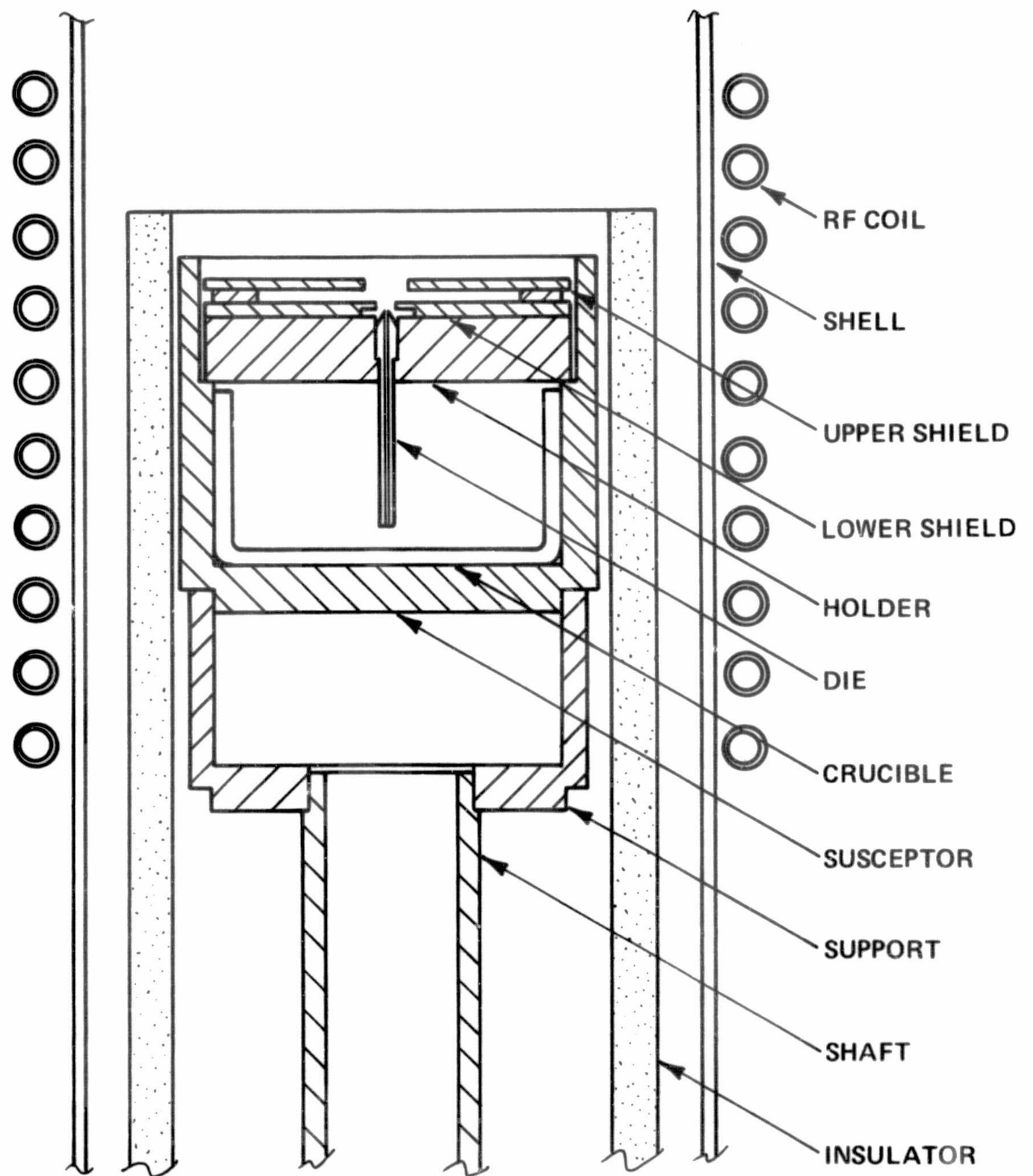

Fig. I-4. Furnace hot-zone components.

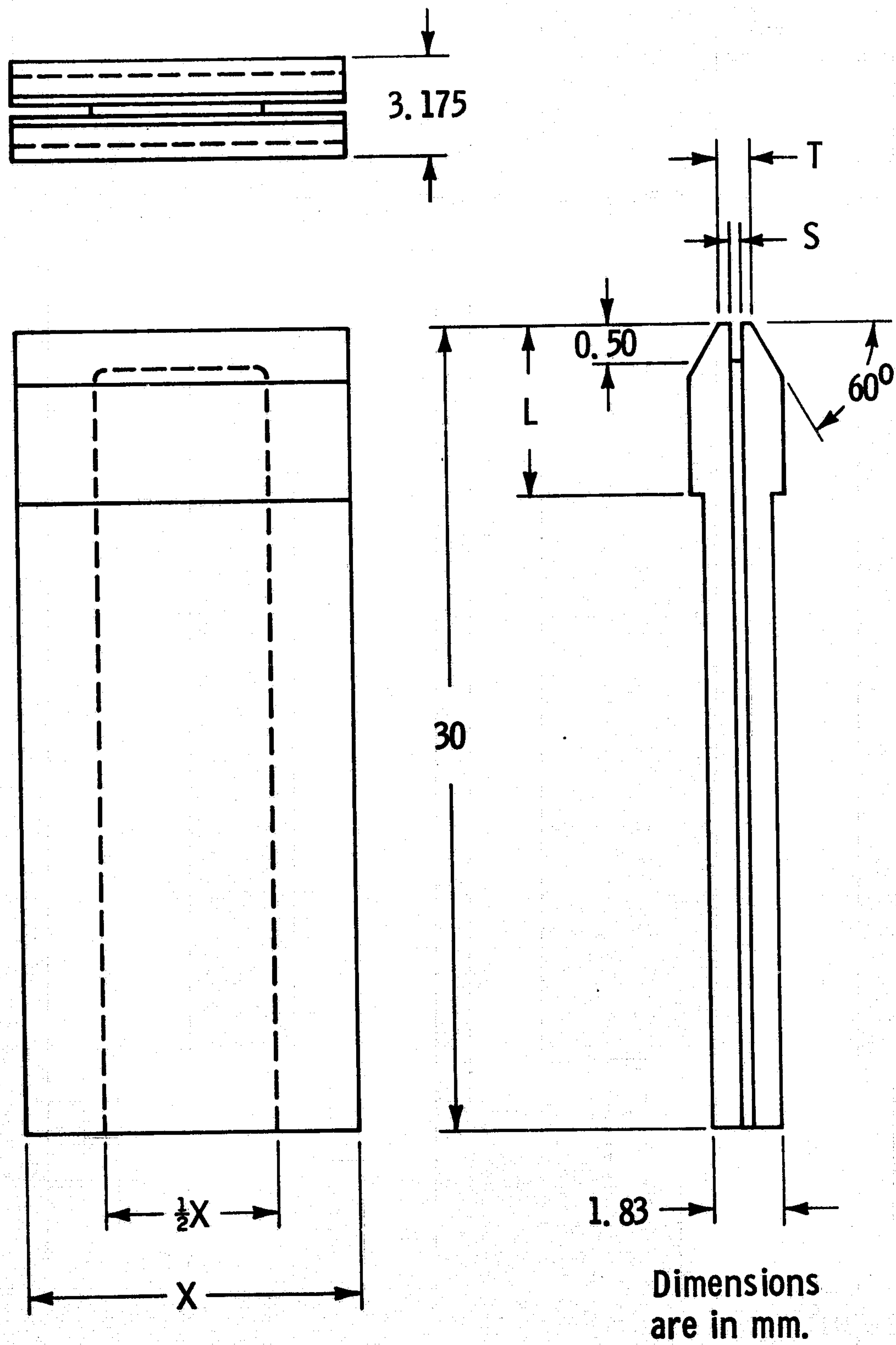

Fig. I-5. Capillary Die.

operator training. The dies were fabricated from Poco DFP-3-2 graphite. For the initial growth attempts, the dies were typically 12.5 mm wide. The capillary slot dimension was 0.26 mm, and the die top thickness was 0.5 mm.

2.2 Growth Procedure

The graphite die and hot-zone components were baked out at 1500°C for one hour in vacuum prior to use. After bake-out, the quartz crucible was loaded with approximately 50 gms of undoped silicon.

P-type doping was achieved using a boron/silicon alloy powder of 1.1 parts per thousand concentration as the source. 2.5×10^{-4} grams of source per gram of silicon was put into the crucible with the silicon charge. The target resistivity was 2 Ω-cm.

Growth was conducted in an argon ambient. After the silicon charge had melted, growth was initiated by touching a 3-mm-wide x 0.4-mm-thick silicon seed to the melt at the die top. A short portion of the seed was melted back, and then the pulling speed was gradually increased and the temperature adjusted to first neck the growth to a width less than that of the seed and then widen the growing ribbon

to full width. A brief description of the growth experiments during the operator training period, and in fact for all growth experiments performed during the course of the contract, may be found in Appendix I.

Early in the contract, a few experiments were conducted with silicon tube growth. Since a tube can be considered to be an "edge-less" ribbon, its growth allows a study of the relationship between growth rate and thickness which is independent of width. The growth procedure for tubes was similar to that for ribbons, and the stages of initiating growth are depicted in Fig. I-6. Details of this work may be found in reference 5.

After the ribbon or tube reached the desired length, growth was terminated by increasing temperature and pulling speed to separate the shaped crystal from the liquid meniscus at the die-top. By reseeding, several pulls could be made from the same charge. At the end of the day, the die was salvaged by freezing a seed crystal to the die top and using it to pull the die assembly (die, holder, shields) free from the liquid in the crucible. Although the frozen silicon within the die frequently cracked upon cooling, the die itself was typically crack-free.

2.3 Die Material Investigations

High-density graphite fulfills the durability and wettabil-

ORIGINAL PAGE IS
OF POOR QUALITY

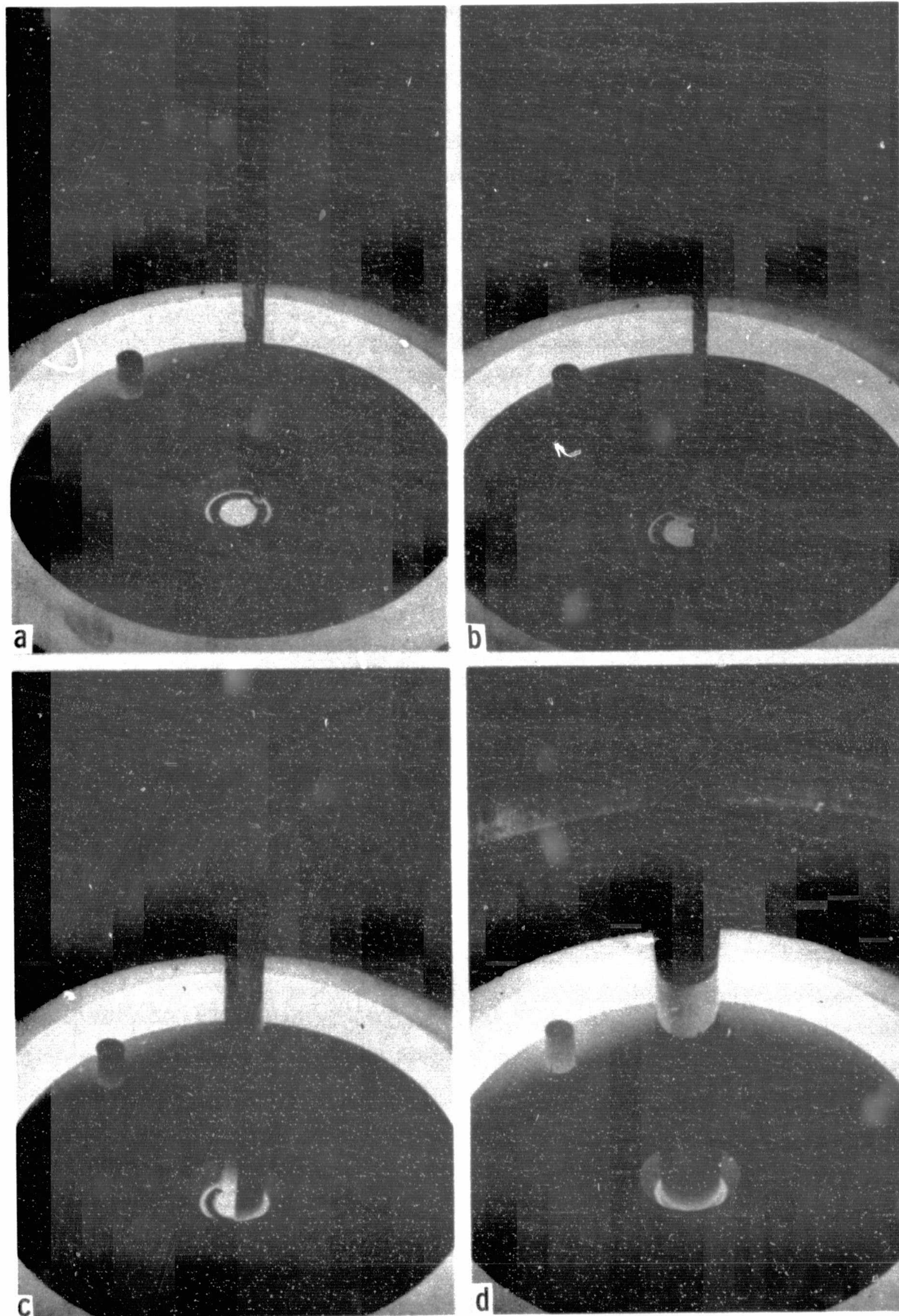

Fig. I-6. Stages in the growth of a silicon tube; (a) Seeding, (b) Circumferential spreading by temperature reduction and pulling rate increase, (c) Further spreading by temperature reduction, (d) Closed, equilibrium growth.

ity requirements of a die[2] and has been used to date for most silicon ribbon growth; it is not, however, completely non-reactive. Good crystallographic perfection has been achieved on small ribbon segments[2,3]; but the structure of large ribbons is marred by planar, line and point defects, as well as surface irregularities. These problems are thought to be at least partially related to the die material; hence a brief study of some non-graphite die materials was conducted.

2.3.1 Materials Investigated

The potential die materials listed in Table I-1 were tested under actual ribbon growth conditions. Hot pressed "high purity" AlB_{12}, TiB_2, ZrB_2, Al_4C_3, B_4C, and Si_3N_4 were obtained from Atomergic Chemetals Co., a division of Gallard-Schleisinger Chemical Mfg. Corp. The materials were obtained in the form of rectangular blocks 3 x 10 x 30 mm in size. No binder was used in hot pressing. Purity levels were 99-99.9%, densities were about 90% of theoretical densities and the starting powder particle size was typically 2-5 μm, according to the manufacturer. Vitreous carbon was also obtained from Atomergic Chemetals Co., in the form of 2 mm thick plates, with properties as shown in Table I-2. Two sources of silicon carbide were used. One

TABLE I-1. Die Material Evaluation

Material	Capillary Rise	Durable In Molten Si	Ribbon Growth
Aluminum Boride[1]	---	---	---
Titanium Boride	Yes	No (dissolves)	Short ribbons
Zirconium Boride	Yes	No (dissolves)	Short ribbons
Aluminum Carbide[2]	---	---	---
Boron Carbide	Yes	Yes	Long ribbons
Silicon Carbide	Yes	Yes	Long ribbons
SiN bonded SiC	No[3]	somewhat	None
Vitreous Carbon	Yes	Yes	Long ribbons
Graphite (dense)	Yes	Yes	Long ribbons
Boron nitride	No	Yes	None
Silicon nitride	No[3]	Yes	None

1. Vapor pressure too high at 1412°C
2. Decomposed and crumbled during storage
3. Evidence of surface wetting, but no rise in capillary slot.

was Crystar silicon carbide from Norton Industrial Ceramics Division, the other was KT silicon carbide from the Carborundum Company. A silicon nitride-bonded silicon carbide was also obtained from Carborundum. The manufacturers data for these three materials is given in

TABLE I-2. Manufacturer's Data for Vitreous Carbon

CHEMICAL CHARACTERISTICS	
Maximum operating temperature	>2,500°C
Apparent density	1.50 to 1.55 g/cm^3
Apparent porosity (no absorption of oil and mercury)	0
Permeability to gas; at normal	better than 10^{-8} cm^2/s
temperature at 2,500°C	approx. 10^{-6} cm^2/s
Ash content	0.005% (50 ppm)
Sulphur content	<50 ppm
Boron content	<2 ppm
Oxidation resistance at 600°C	0.1 mg/cm^2/h
at 800°C	2 mg/cm^2/h
MECHANICAL PROPERTIES	
Transverse breaking strength	600 to 800 mg/cm^2
Compressive strength	1,500-2,000 kg/cm^2
Shore hardness	120-125
Hardness Mohs' scale	6-7
Vickers micro-hardness (30 kgm)	150-175
Young's modulus	2,200 kg/mm^2
THERMAL PROPERTIES	
Coefficient of thermal expansion: at 100°C	3.2 x 10^{-6} per °C
at 650°C	3.5 x 10^{-6} per °C
Thermal Conductivity Resistance to thermal shock	0.06 cal/cm/s/°C
Air quenching acceptable from... to room temperature	2,500°C
ELECTRICAL PROPERTIES	
Electrical Resistivity	4,500 microhm/cm

Table I-3. The Crystar material is nominally 99% pure recrystallized silicon carbide, with Ti, Cr, Co, V, and Al as typical metallic impurities. Purity levels of the carborundum materials are not known at this time. Pyrolytic boron nitride was also investigated.

2.3.2 Die Fabrication and Evaluation

Dies were fabricated from all materials except aluminum carbide, which had crumbled during storage, and boron nitride. The dies were made as shown in Fig. I-5. They were 9.5 mm wide with a 0.76 top thickness and a .56 mm capillary slot thickness. All machining was done with 180 grit diamond wheels. No serious machining problems were encountered, except that vitreous carbon and silicon nitride-bonded silicon carbide chipped easily. Slow machining rates were necessary on silicon carbide and boron carbide to avoid chipping. After machining, the dies were baked out in vacuum at 1500-1600°C for one hour. The AlB_{12} die outgassed severely during bakeout and the temperature could not be raised above 1400°C without causing the pressure to rise above 2×10^{-4} Torr. This die was considerably erroded and broke after bake-out. The Si_3N_4 die was a light tan color - the others were grayish to black.

TABLE I-3. Manufacturer's Data for Various Silicon Carbides

Property	KT Silicon Carbide	REFRAX Silicon nitride-bonded Silicon Carbide	CRYSTAR Silicon Carbide
Apparent specific gravity (g/cm^3)	3.10	2.65	2.6
Working temperature Inert atmosphere Oxidizing atmosphere	 4200°F max. 3000°F max.	 3200°F max. ---	 --- 3200°F max.
Modulus of rupture, psi	22,800 (2200°F)	5000-7000 (2500°F)	10,000-22,000 (2730°F
Modulus of elasticity, psi	56 x 10^6 (70°F) 51 x 10^6 (2200°F)	17 x 10^6 (70°F)	30 x 10^6
Compressive strength, psi	150,000 (70°F)	20,000 (70°F)	100,000
Tensile strength, psi	20,650 (70°F)	3000-3500 (70°F)	---
Thermal conductivity BTU in/hr ft^2 F^o	720 (1140°F mean temp) 465 (1574°F mean temp) 250 (2086°F mean temp) 174 (2292°F mean temp) 94 (2782°F mean temp)	113.5 (2200°F)	180 (1000°F) 165 (1500°F) 145 (2300°F) 135 (2900°F)
Thermal coefficient of expansion in/in/^{o}F x 10^{-6}	1.88 (70°-800°F) 2.60 (70°-1800°F) 2.80 (70°-2500°F)	1.8 (70°-400°F) 2.6 (70°-2500°F)	2.7 (70°-2600°F)
Mean specific heat	.31 (70°-2800°F)	.29 (70°-2500°F)	.35 @ 3000°F
Spectral emissivity at 1600°F	.9	.9	---
Permeability	Impermeable	Negligible	---
Porosity	0%	15%	18%

The growth procedure described in section 2.2 was used in attempting ribbon growth with the new materials. If the die did not fill with liquid silicon, the system temperature was increased considerably above normal levels to attempt to encourage melt rise. If melt rise occurred, crystal growth was attempted. After the growth attempts, the dies were visually checked for durability in molten Si. The appearance of the various die bottoms, where contact with molten Si took place, is shown in Fig. I-7. In the case of boron nitride, the capillary rise check was made by placing silicon in a boron nitride crucible with a slotted wall, and melting the silicon. Brief descriptions of the experiments appear in Appendix I, runs 50805-50826 and 60208-60302.

2.3.3 Results

The results of the evaluation are summarized in Table I-1. For the particular forms of the die materials used here, only boron carbide, KT silicon carbide, Crystar silicon carbide, vitreous carbon, and of course, high density graphite were adequately wettable and durable to allow the growth of long ribbons (> 0.5 m). In addition, TiB_2 and ZrB_2 allowed short ribbon growth, but the dies suffered acute dissolution as can be seen in Fig. I-7(a,b). The ribbons grown from experimental die materials are pictured in Fig. I-8.

7a. TiB_2

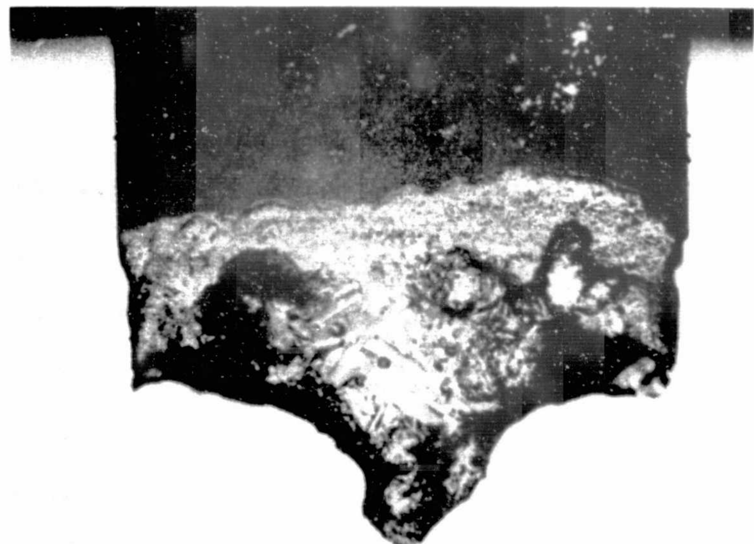

7b. ZrB_2

Fig. I-7. Die bottoms after contact with molten silicon for more than two hours (sheet 1 of 5).

ORIGINAL PAGE IS
OF POOR QUALITY

ORIGINAL PAGE IS
OF POOR QUALITY

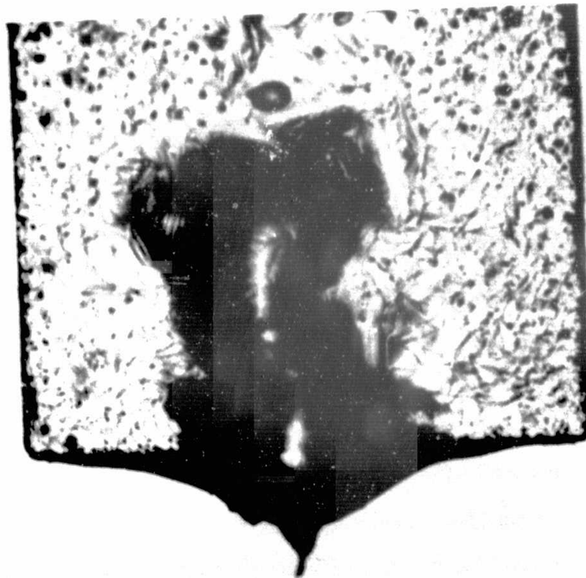

3c. B_4C

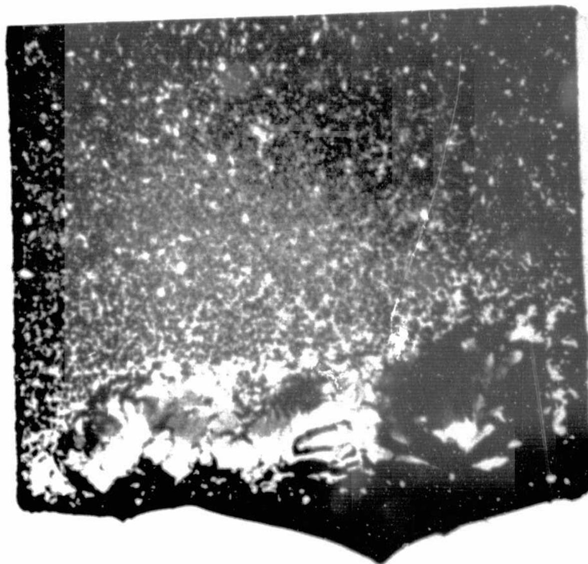

7d. KT SiC

Fig. I-7. Die bottoms after contact with molten silicon for more than two hours (sheet 2 of 5).

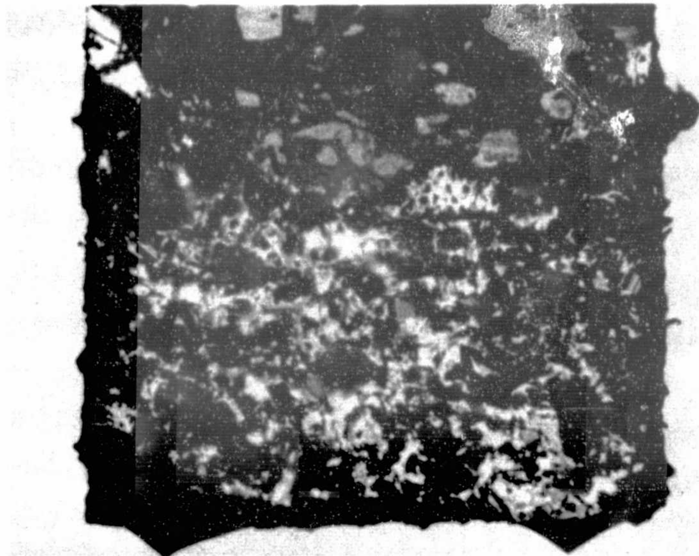

7e. Si_3N_4 - bonded SiC

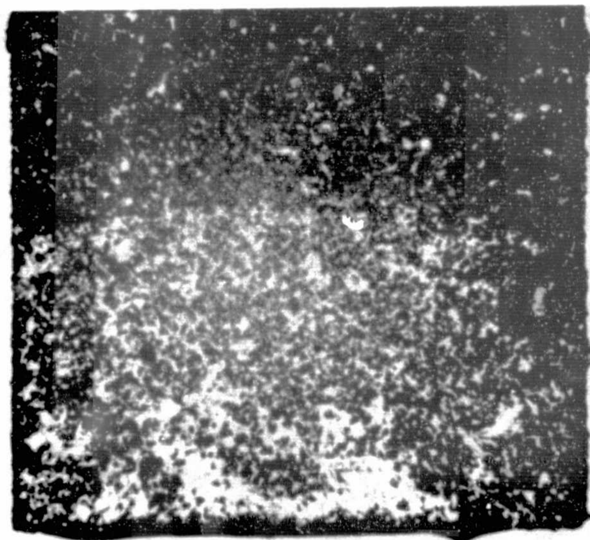

7f. Crystar SiC

Fig. I-7. Die bottoms after contact with molten silicon for more than two hours (sheet 3 of 5).

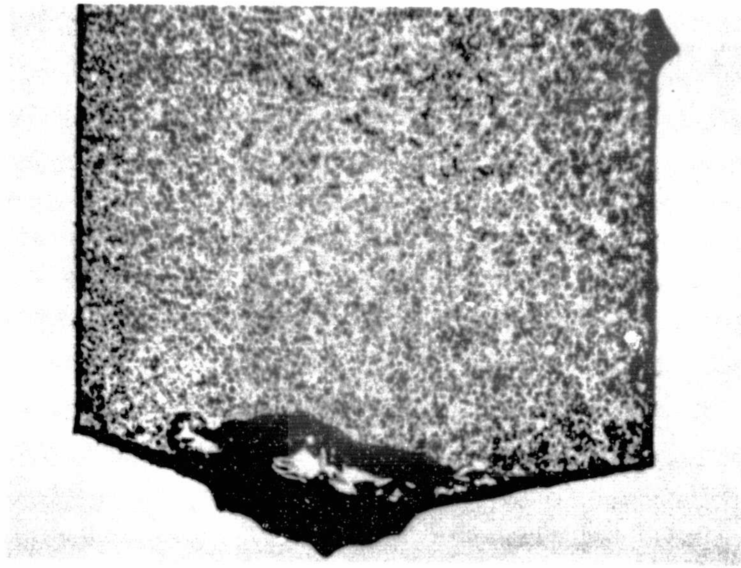

7 g. Vitreous Carbon

ORIGINAL PAGE IS
OF POOR QUALITY

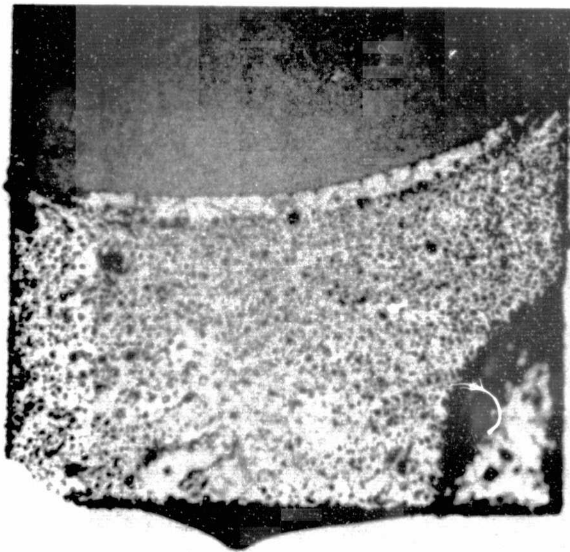

7 h. Si_3N_4

Fig. I-7. Die bottoms after contact with molten silicon for more than two hours (sheet 4 of 5).

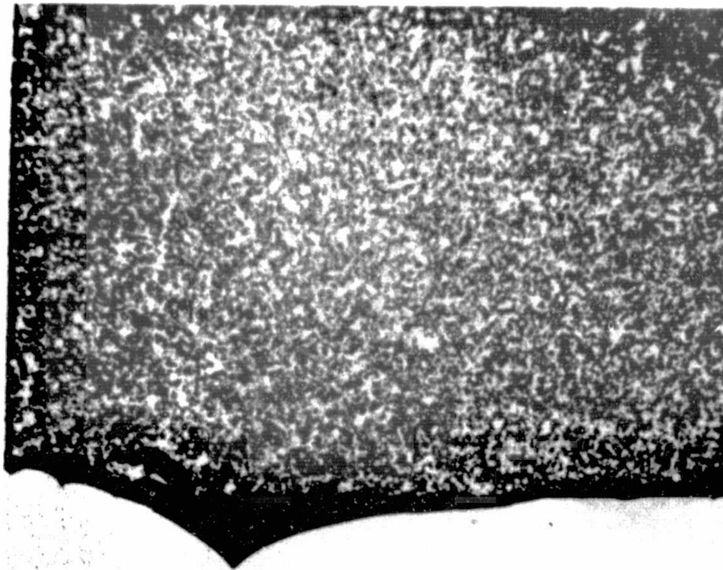

7i. Graphite

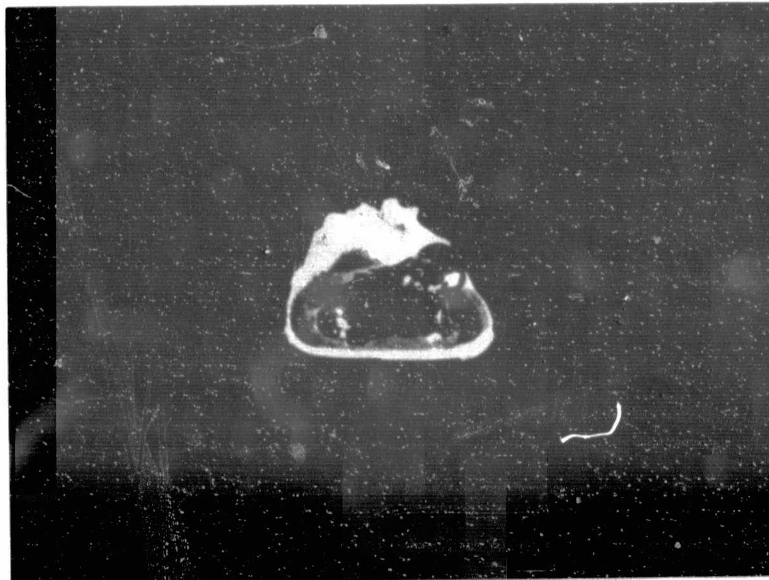

7j. BN

Fig. I-7. Die bottoms after contact with molten silicon for more than two hours (sheet 5 of 5).

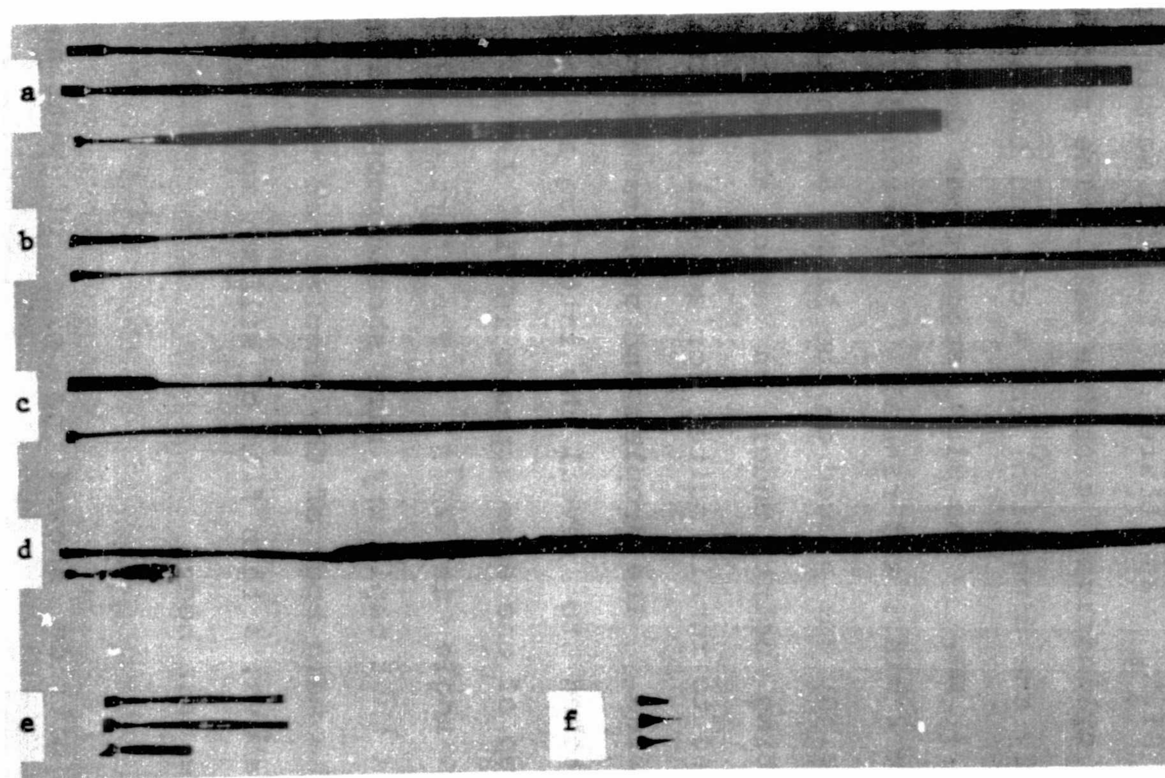

Fig. I-8. Silicon ribbons grown from experimental die materials: (a) KT SiC, (b) Crystar SiC, (c) Vitreous carbon, (d) B_4C, (e) TiB_2, (f) ZrB_2.

ORIGINAL PAGE IS OF POOR QUALITY

Si_3N_4 bonded SiC, and Si_3N_4 were durable, but showed no sign of capillary rise although surface wetting appeared to occur at the die bottom (Fig. I-7(e,h)). Since the results on hot-pressed Si_3N_4 were somewhat encouraging, wetting of silicon on CVD Si_3N_4 was tested. The CVD sample was a segment from a cylindrical crucible wall. The radius of curvature (in only one dimension) was 4 cm, and the segment thickness was 1.1 mm. The Si_3N_4 segment was degreased, etched in HF for 2 min., and rinsed. An etched silicon chip of 0.078 g weight was placed on the Si_3N_4 and heated to the silicon melting point under an argon ambient. The droplet was allowed to remain molten for several minutes and then was solidified. The droplet and substrate were then sectioned and etched to reveal the interface and contact angle; a close-up of one edge appears in Fig. I-9. The observed contact angle is 23°. The partial wetting behavior indicates that capillary rise should occur with CVD Si_3N_4. While the main body of the droplet had the contact angle described above, a thin film of silicon spread on the Si_3N_4 ahead of the main body.

Pyrolitic boron nitride showed no sign of wetting or capillary rise, although it was not appreciably attacked by liquid silicon (Fig. I-7(j)).

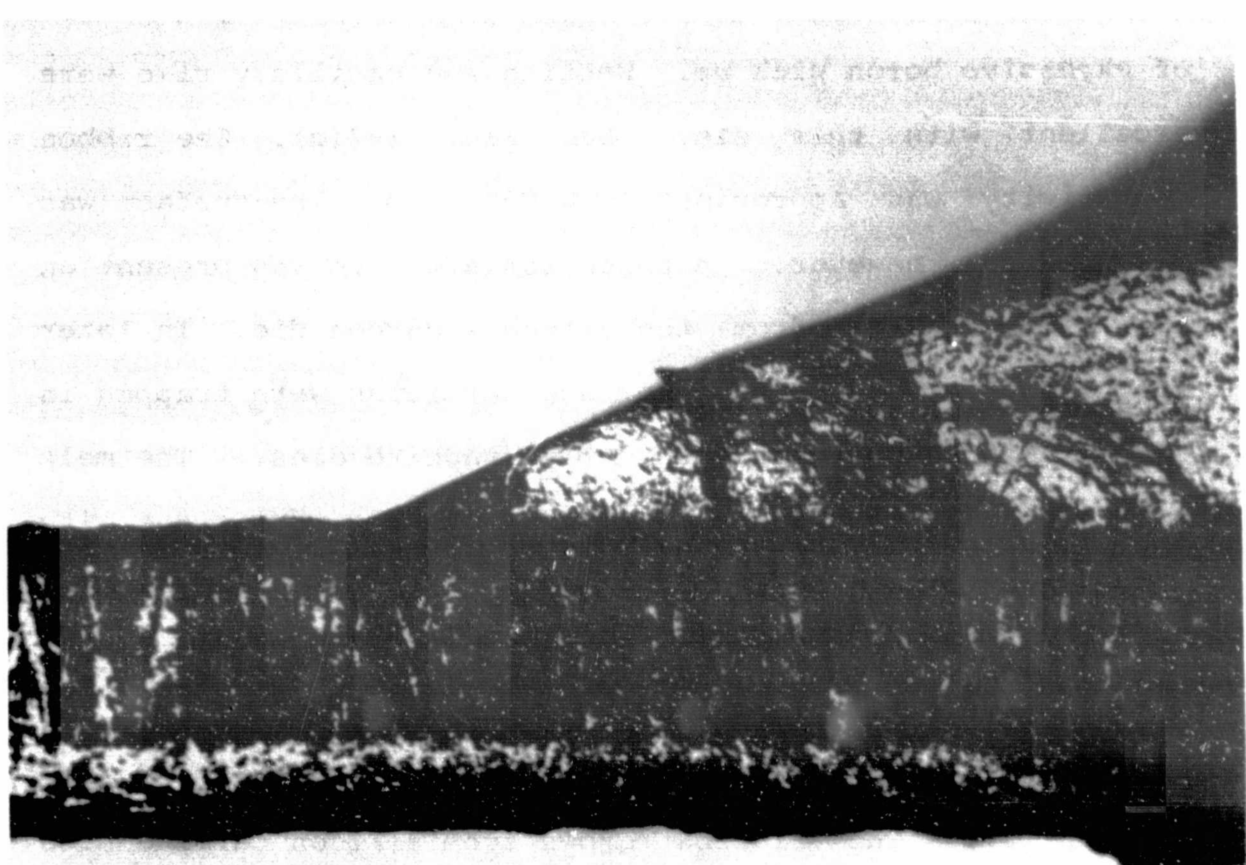

Fig. I-9. Close-up (25X) of one edge of frozen droplet on a CVD Si_3N_4 substrate.

In Fig. I-10, 10X photomicrographs of ribbon surfaces 15 cm from the seed attachment point are shown for the die materials which yielded long ribbons. The strong surface morphology features with the B_4C die are probably a result of excessive boron pick up. Wetting and capillary rise were excellent with this die. See Fig. I-7(c). The ribbon resistivity was approximately 0.004 Ω-cm. The surface was very clean, however. A thick surface film was present on the ribbon grown from the vitreous carbon die. In later stages of growth, numerous surface particles were trapped in the ribbon as occurred with early graphite dies. The melt and wetted region near the die bottom were very clean with vitreous carbon (Fig. I-7(g)), and similar to the appearance of graphite die bottoms (Fig. I-7(i)). Vitreous carbon is also a promising material for use as a crucible both for ribbon growth and for directional solidification (see section 6). The ribbons grown from silicon carbide dies were quite free of surface particles in the early stages of growth as indicated in Figs. I-10(c and d), and some large single crystal regions were seen. Later in growth, these ribbons also incorporated surface particles, but at a low density. For comparison, an old ribbon grown from a graphite die of similar design is shown in Fig. I-11. Because this material showed the most promise of those which were tried, dies for 25-mm-wide ribbon growth were fabricated from Carborundum Company KT silicon carbide.

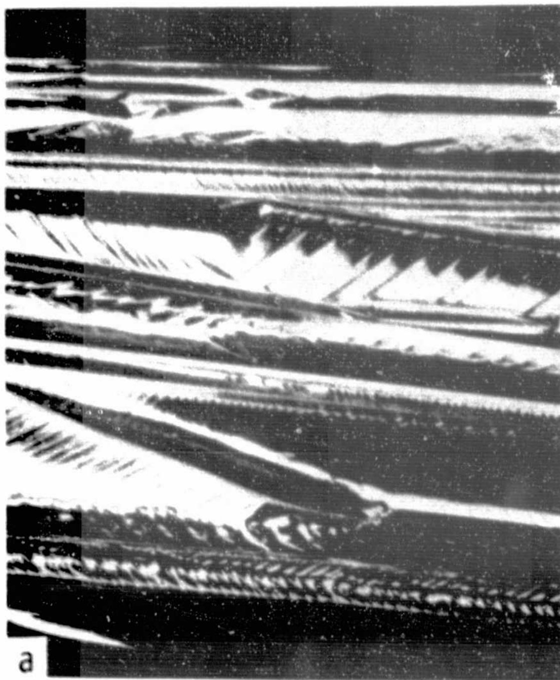

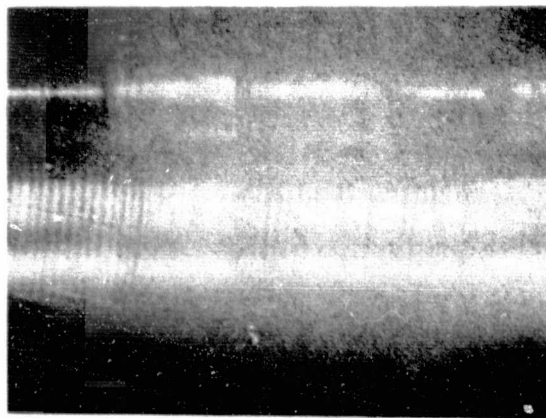

ORIGINAL PAGE IS
OF POOR QUALITY

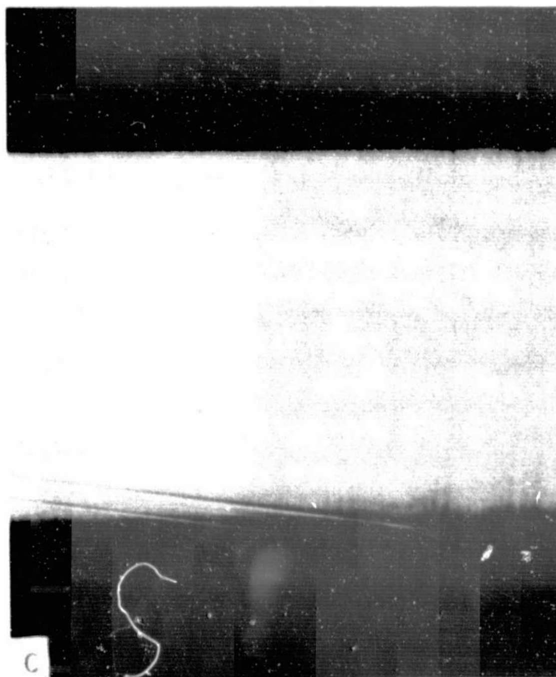

Fig. I-10. 10X photomicrographs of ribbon surfaces 15 cm from seed attachment: (a) B_4C die, ribbon 50811, (b) Vitreous carbon die, ribbon 50825, (c) Crystar SiC die, ribbon 50805, (d) KT SiC die, ribbon 50809.

ORIGINAL PAGE IS
OF POOR QUALITY

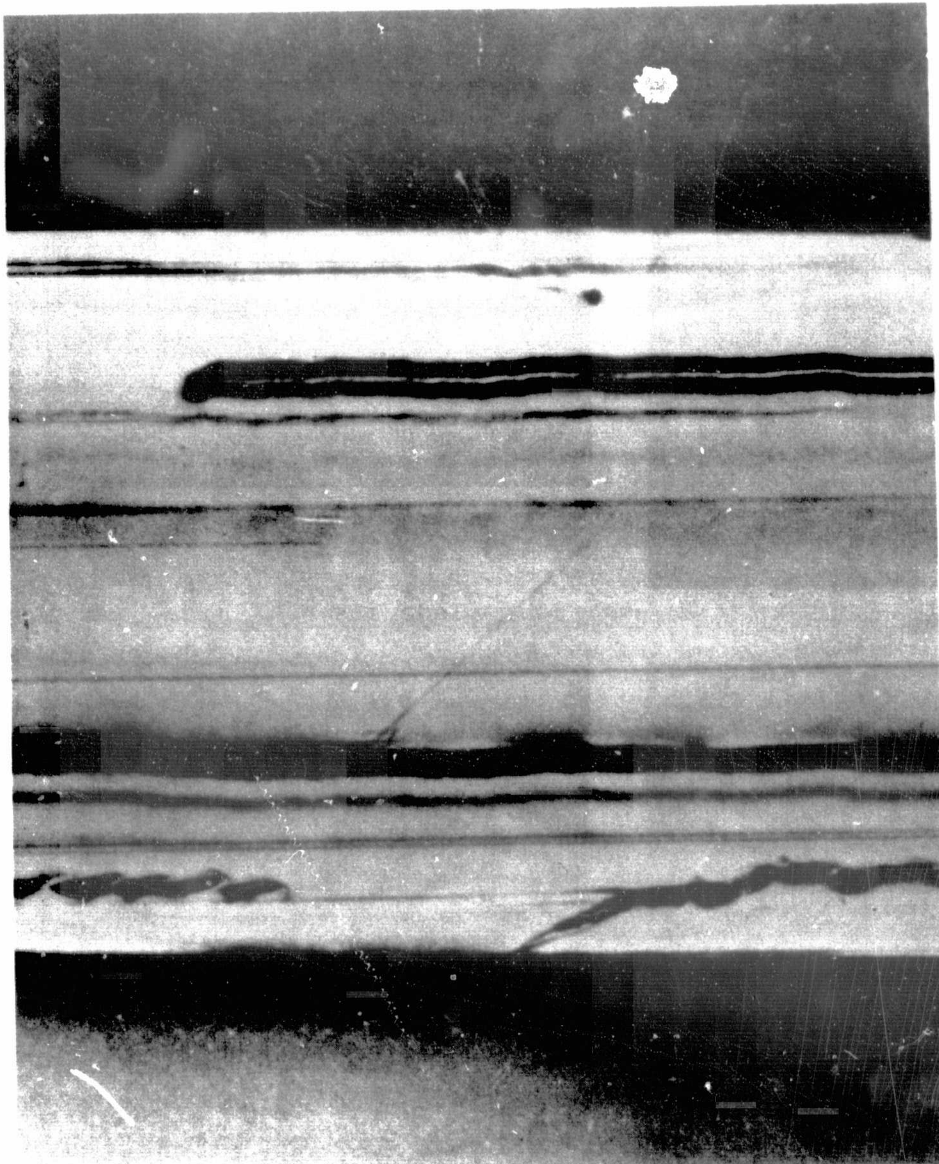

Fig. I-11. 10X photomicrograph of a ribbon surface 15 cm from seed attachment; graphite die, ribbon 50407. Several surface troughs caused by SiC particles are visible.

Several ribbons 0.5 m long x 25 mm wide were successfully grown from this die material. In each growth attempt, it was observed that liquid silicon entered the region between the die and the die holder. While the cause has not been uniquely determined, we speculate that the die material itself is acting as a wick for the silicon melt. The melt in contact with the graphite die holder may tend to contaminate the remaining melt with carbon, obscuring the dissolution behavior of the SiC die.

A distinct difference in the morphology of silicon carbide particle formation at the die top was seen between graphite and silicon carbide dies. In the case of graphite dies, individual yellow β-SiC crystals form at the top and sides. With the KT silicon carbide dies, a dense, continuous film of SiC tends to grow from the carbon-saturated silicon melt near the the die top. When the die is first used, this film does not interfere appreciably with the Si ribbon growth. The initial ribbon perfection (both with KT SiC and with Crystar SiC) can be quite good. As ribbon growth progresses, however, the SiC film also grows and, at some stage, begins to break loose from the die top in clumps, which are then incorporated in the ribbon and disturb its perfection. An example is shown in Fig. I-12. The frequency of this occurrence is similar to that of SiC crystallite incorporation with grahite dies, and the

appearance of the grown ribbons is not too different from that of ribbons grown with graphite dies (Fig. I-13).

Further progress was possible with dies of pure, dense silicon carbide grown by CVD on graphite substrates, and the wetting between the die and the die holder was prevented. (This work was done with 50 mm wide ribbons. See section 4.3.)

In summary, of the materials studied, only SiC, graphite, vitreous carbon, and CVD Si_3N_4 showed promise for capillary action ribbon growth. Si_3N_4 was not tested in an actual die configuration.

2.4 Process Development for 25 mm Ribbons.

Our first 25 mm wide ribbons were grown from graphite dies of the type shown in Figs. 4 and 5. The die width was 25 mm, the capillary slot was 0.26 mm thick, and the die top was 0.51 mm thick. The lower heat shield had a 2.4 mm wide x 28 mm long slot and the upper shield a 4.8 x 30 mm slot. The shields were 1.6 mm thick, and the lower shield had a 0.8 mm deep x 8 mm wide x 33 mm long recess milled in the bottom side. Surface characteristics of these ribbons were similar to those of 12.5 mm wide ribbons. The SiC particle density was approximately $5/cm^2$; the surfaces were generally

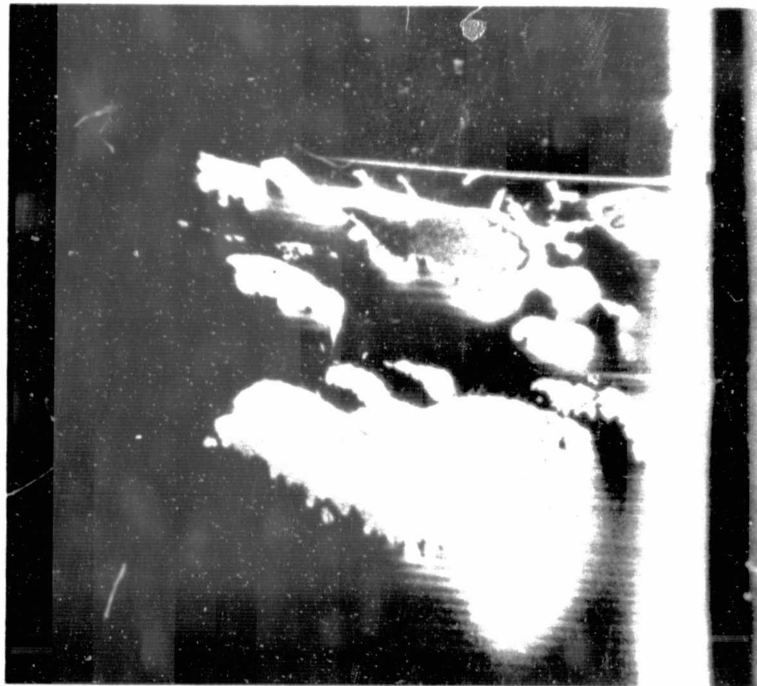

ORIGINAL PAGE IS OF POOR QUALITY

Fig. I-12. Clump-like particles in silicon ribbon when KT SiC die is used (60X).

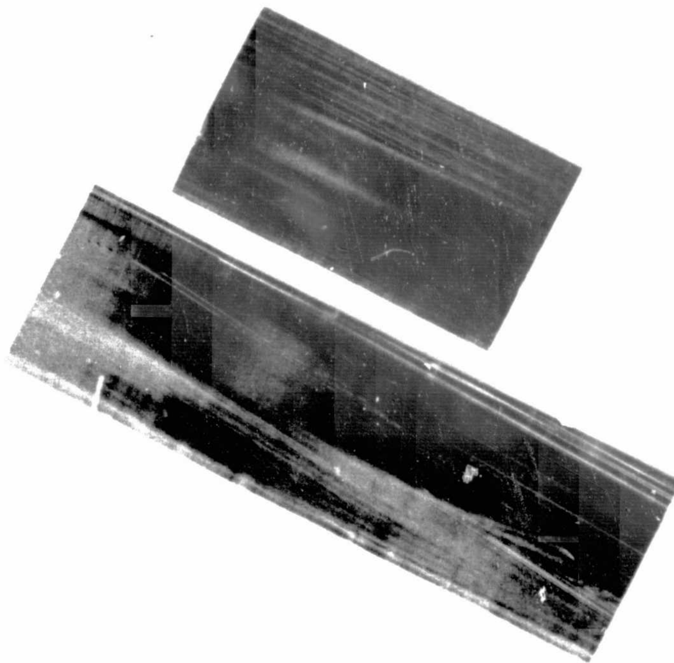

Fig. I-13. Appearance of silicon ribbons, 25 mm in width, grown from KT SiC die (bottom) and POCO graphite die (top).

rough as in Fig. I-14(a) and coated with a thin silicon oxide powder film of yellowish brown color.

An experimental die design (see sec. 2.4.1) was developed which produces a much smoother surface than that possible with the older die. The SiC particle density with the new die is typically less than $0.1/cm^2$. The entire full width surfaces of three consecutively-grown 25 mm wide ribbons were examined for SiC particles. The ribbon lengths were 58, 55, and 27 cm, and the corresponding particle densities were .04, .10, and .03 particles/cm^2. Substantial lengths of the ribbons (> 10 cm) were particle-free. Particles which do form tend to be located within a few mm of the ribbon edge. In Fig. I-14, 21x photomicrographs of the as-grown ribbon surface compare the surface morphology produced with the old and the new dies. While the new dies produce a smoother surface, it is observed that twin planes and grain boundaries are still present, as are surface films.

2.4.1 Die Design

The new capillary die design mentioned above represents a departure from the edge-defined, film-fed technique of crystal growth, in that the cross section of the growing ribbon is not concentric with the top edges of the die. The die top is considerably thicker in the mid-region than at

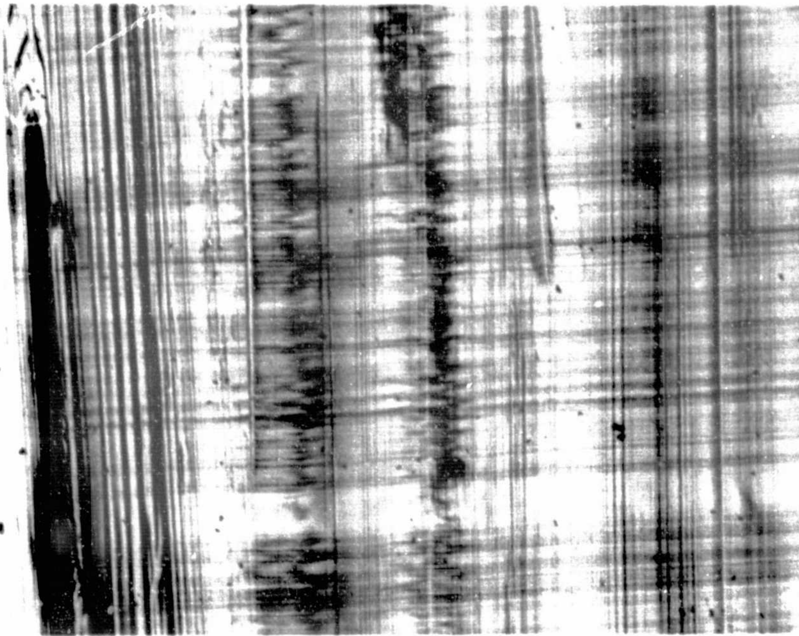

a

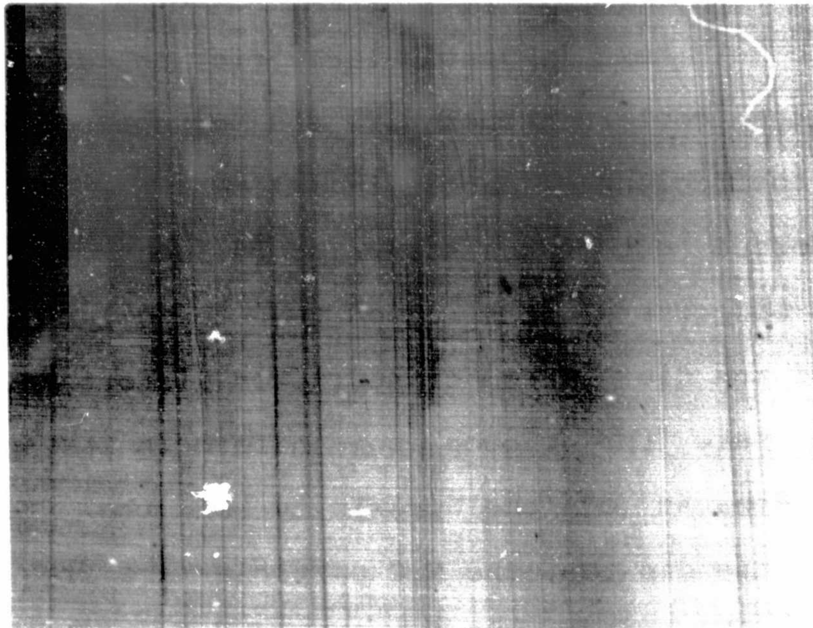

b

ORIGINAL PAGE IS
OF POOR QUALITY

Fig. I-14. 21X micrographs of as-grown ribbon surface; (a) Old die design and (b) new die design.

the edges, yet the resultant ribbon is flat or somewhat thicker at the edges than in the middle. This die design allows a higher meniscus at the central region of the solidification front and thus reduces problems which can occur when using flat-top dies or curved-top dies with parallel top edges as in the EFG technique. Such problems come about primarily from the fact that the graphite die used for silicon growth slowly dissolves in the liquid. Carbon-saturated silicon rises up the capillary slot in the die and comes to the top region where ribbon solidification occurs. This top region is the coolest region in the growth system and the melt here is particularly rich in carbon both because of the cooler temperature and because of the low segregation coefficient of carbon in silicon. Here, excess carbon is forced out of the saturated silicon solution in the form of β-SiC crystallites, which tend to collect at the top surface of the die. These crystallites distort the melt meniscus and make the ribbon non-uniform in its surface smoothness. Because of the proximity of the freezing interface to the die top, the SiC particles are frequently incorporated in the ribbon, where they generate dislocations and other defects (see also section Characterization of this report).

It is advantageous to keep the interface of the freezing ribbon as far as possible from the die top, and this can be

accomplished with the structure shown in Fig. I-1. The die top surface is curved so that it is higher at the edges than in the middle. In this way, if the ribbon's solid-liquid interface is maintained approximately planar, then the interface is further from the die, at least in the central region. The central region is most critical for generation of defects in the ribbon. However, if the thickness of the die top is kept constant while the die top surface is curved, then a higher meniscus in the central region necessarily implies that the top of the meniscus is thinner there. This would cause the ribbon to be very non-uniform in thickness from one edge to the other (i.e., much thinner in the middle than at the ends). Thus, not only should the die top curve downward from the ends toward the central region, but it must also become thicker in the central region than at the ends, as in Fig. I-1. The meniscus, then, has a wider base in the central region. The wider base, combined with the greater meniscus height in the central region, results in a more uniform ribbon thickness at the solid-liquid interface. In summary, there are two things that are important to the die design: one is the curvature of the top surface, and the other is the thickening of the die top in the central region. By proper choice of the curvature of the die top and the taper angle of the sides of the die, an optimum value for this variation of the thickness of the die top with position along the die

can be obtained. R and ϕ (see Fig. I-1) are chosen to optimize the values of $X_m - X_e$ and δ for successful ribbon growth. These parameters are given by

$$\delta = R - \frac{W}{2 \tan (\sin^{-1} \frac{W}{2R})}$$

$$X_m - X_e = 2 \delta \tan \phi/2.$$

For 25 mm ribbon growth, R=10 cm, $\phi=40^{\circ}$, and X_e=0.55-0.80 mm give good ribbon growth conditions. Ribbons grown from such a die typically have an edge thickness of 0.42 mm and a central thickness of 0.21 mm for X_e=0.55 mm. Exact dimensions of course depend upon pulling speed, and the central thickness was as low as 0.1 mm when pulling speeds in excess of 3 cm/min were employed.

The optimum designs which we have developed for the 25 mm die, die holder, and heat shields are detailed in Appendix III. Both a one-piece and a two-piece die design are presented.

2.4.2 Ribbon Surface Quality

Silicon carbide surface particles are the main detractors to ribbon surface quality, both by their physical presence on the surface and because of the longitudinal troughs or tracks they leave on the ribbon when they are present in the

liquid meniscus at the die top. Another major contribution to roughness consists of sporadic, heavy horizontal striations which can arise when the solid-liquid interface is in very close proximity to the die top. As can be seen from Fig. I-14, die design can greatly reduce the severity of these two sources of roughness. A close look at Fig. I-14(b) shows that roughness from grain boundaries and fine horizontal interface striations still remains with the improved die design. Another detractor from surface quality is the formation of surface films on the ribbons due to the presence of quartz and graphite in the growth furnace and their reaction with silicon.

In the growth system of Fig. I-3, the argon inlet was at the bottom of the furnace and the gas flowed upward past the melt region, exiting through an oval tube at the furnace top. The ribbon was also pulled through this tube. In an attempt to eliminate ribbon surface film formation, a closed (gas-tight) system modification was made to the ribbon puller, and the inert argon purge system was altered to direct the purge gas at the ribbon/melt interface. This resulted in a cleaner appearance of the melt at the die top and also a cleaner looking ribbon surface. However, there was still evidence of SiC film formation near the seed interface. The modified purge system is shown in Fig. I-15. As can be seen, the flow direction is reversed and the

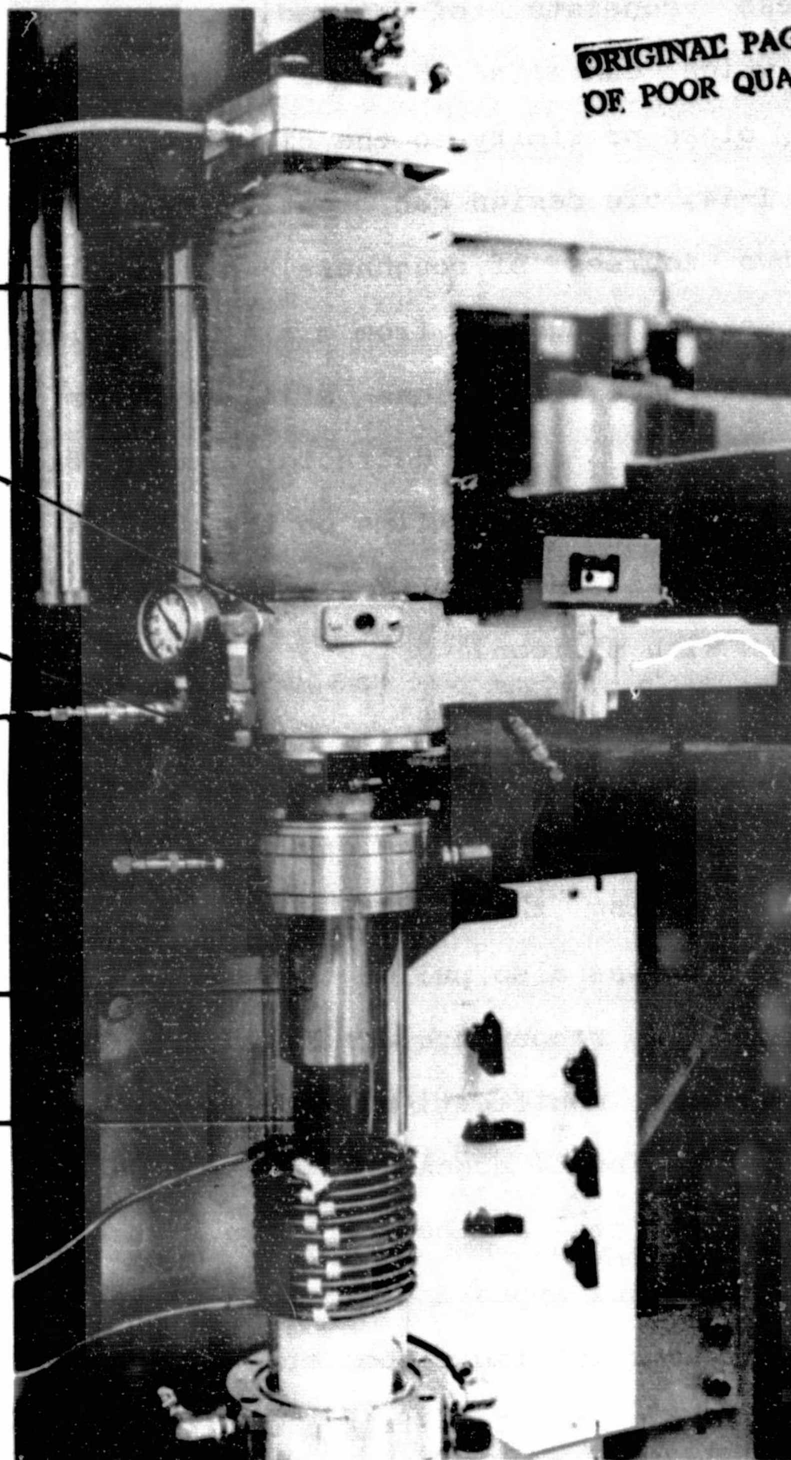

ORIGINAL PAGE IS OF POOR QUALITY

Fig. I-15. Modified Argon Purge System.

ribbon remains in the furnace interior throughout growth.

In use, the gate valve is closed and the region below it is evacuated prior to filling with argon through the inlet below the gate valve. When the lower chamber is filled, an argon outlet to a bubbler at the bottom of the chamber is opened. Simultaneously, the plastic bellows section above the gate valve is argon purged. The seed shaft is initially located in this section. When both sections have been purged an adequate length of time, and the die is at the growth temperature, the argon outlet above the gate is closed and the gate valve is opened. Argon then flows from the inlet at the bellows top and the inlet at the gate valve downward through a water-cooled stainless-steel purge tube which is 55 mm in ID and surrounds the ribbon. From the bottom of this purge tube, a 75 mm long graphite draw tube can be supported. The oval bore of the draw tube causes the purge gas to impinge on the solidification region at the die top. The gas then flows out the bottom of the furnace and through the bubbler. After growth, the ribbon is pulled up into the bellows and the gate valve is closed. The bellows is then opened to remove the ribbon and reseed for subsequent growth attempts.

In the modified system, the routine maximum usable ribbon length at full width is limited to about 0.6 meters as

compared to about 1.2 meters with the old open port system. However, by reseeding, several ribbons can be pulled from one crucible charge. It was found that with the graphite draw tube present, ribbon growth control is best at low purge rates (20-30 CFH). Higher rates tended to promote asymetrical spreading of ribbon growth from seed size to full width. However, little qualitative difference is seen in ribbon surface cleanliness and frozen-in stress whether the graphite draw tube is present or absent. Viewing and growth control are best when the graphite tube is not used. Purge rates up to 80 CFH could then be applied.

The closed bellows system and argon purge from the top (with or without the graphite draw tube) produces a cleaner ribbon surface than that obtained with an open port system. The resultant ribbons have the shiny metallic grey color of polished silicon wafers. Under certain lighting conditions, the ribbons appear to be covered by a multicolored film. However, this has been demonstrated to be a diffraction grating effect caused by the transverse growth striations mentioned earlier, and not a film phenomena. In fact, a spectrum can be projected onto a white surface by using a ribbon as a grating. The striation line density was measured for nine ribbons which were grown at rates from 15 to 31 mm/min (see Table I-4). Line densities ranged from 620-970 lines/cm. The product of the line density and the

TABLE I-4. Growth Rates, Solid/Liquid Interface Striation Line Densities and Line Frequencies for Ten Ribbons

Ribbon Number	Distance from Seed (cm)	Growth Rate (cm/min)	Line Density (lines/cm)	Frequency (lines/sec.)
51007	65	1.5	756	18.9
51012	12	1.9	960	30.4
51012	100	1.9	970	30.7
51014	65	1.7	956	27.1
51017	32	3.1	660	34.1
51019	64	2.9	636	30.7
51022	66	2.0	940	31.3
51023	69	2.2	800	29.3
51027	66	2.5	620	25.8
51107	57	1.5	780	19.5

growth rate yields the striation frequency, which is also given in Table I-4. Line density and frequency do not change appreciably with distance along the ribbon, as can be seen from the data for ribbon 51012. With the exception of the anomalously low frequency values for 15 mm/min growth rates, the average striation frequency on the remaining eight ribbons was 29.9 lines/sec with a standard deviation of 2.6 lines/sec. Several explanations of these striations have been proffered, including a) 60 cycle AC modulation of the rf generator output power, b) room vibration due to

heavy equipment motors (vacuum pumps, air conditioning motors, etc.) running at 1725 RPM (28.8 cycles/sec), and c) oscillations associated with surface tension driven flow in the meniscus[6]. No conclusive cause has been identified. A 93X photomicrograph of the striations on ribbon number 51019 is displayed in Fig. I-16.

To determine whether or not the surface striations correlate with dopant distribution striations, we beveled a ribbon at a 3.5° angle (top, Fig. I-17) so that spreading resistance measurements could be made at 2.5 μm intervals, on the lapped surface, in a direction perpendicular on the striation lines. The striation lines, in this case, were spaced at approximately 10 μm intervals and had a nearly sinusoidal peak-to-valley undulation with an amplitutde of about 0.37 μm (as calculated from the bevel angle and the structure at the bevel/surface intersection in Fig. I-17). Resistance fluctuations of up to about 12% are evident, but do not appear to correlate with the surface striations.

The melt at the die top also appears to remain cleaner with the modified purge system, and the seed/ribbon interface attachment has improved to some extent. However, there is evidence from TEM examinations that a thin SiC film is grown on the seed tip by chemical vapor deposition during the relatively long time (approximately five minutes) the seed

ORIGINAL PAGE IS
OF POOR QUALITY

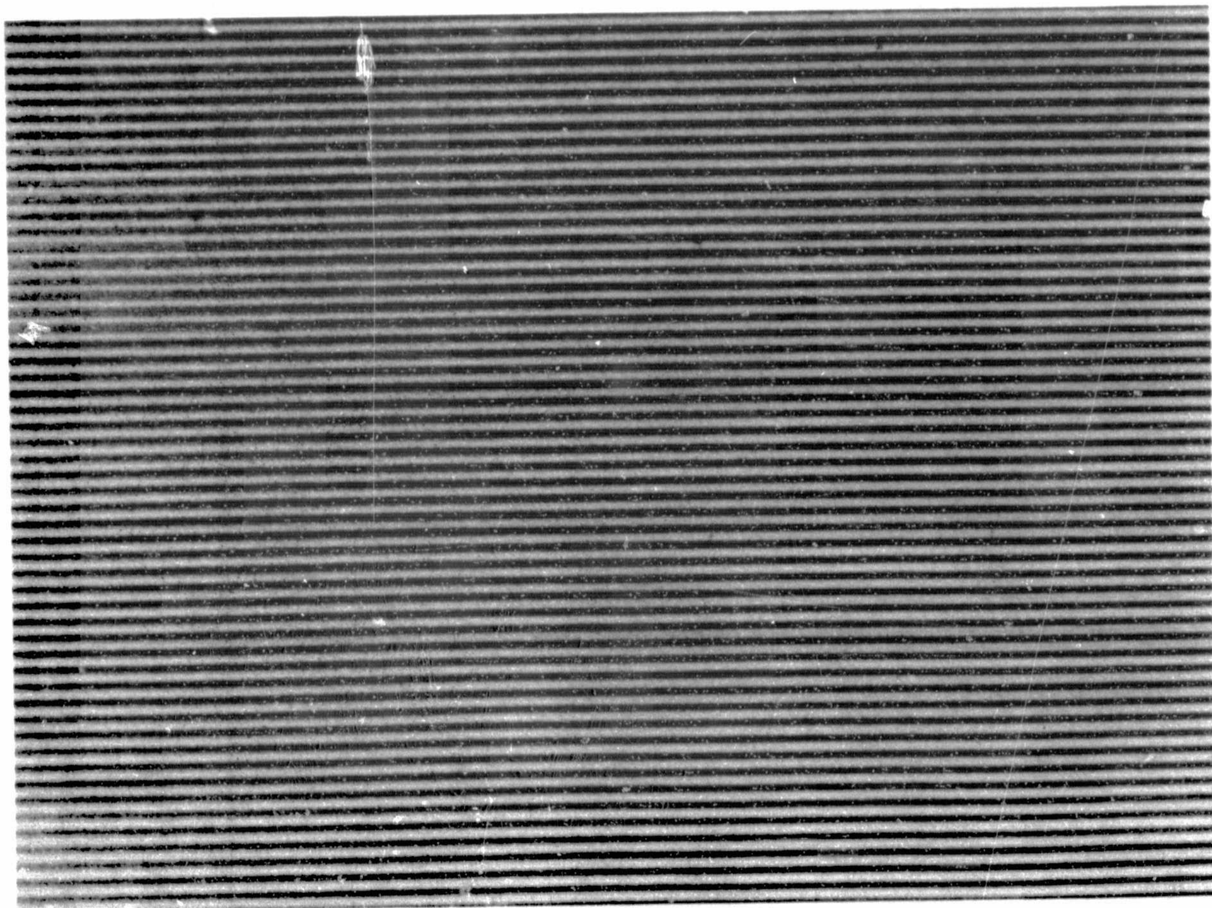

ORIGINAL PAGE IS
OF POOR QUALITY

Fig. I-16. Transverse interface striations on silicon ribbon 51019; magnification 93X.

remains stationary at the die top. A similar film is seen on the ribbon, if growth is halted for several minutes with the ribbon remaining at the die top. During growth at typical speeds, the film is not noticeable, but is probably

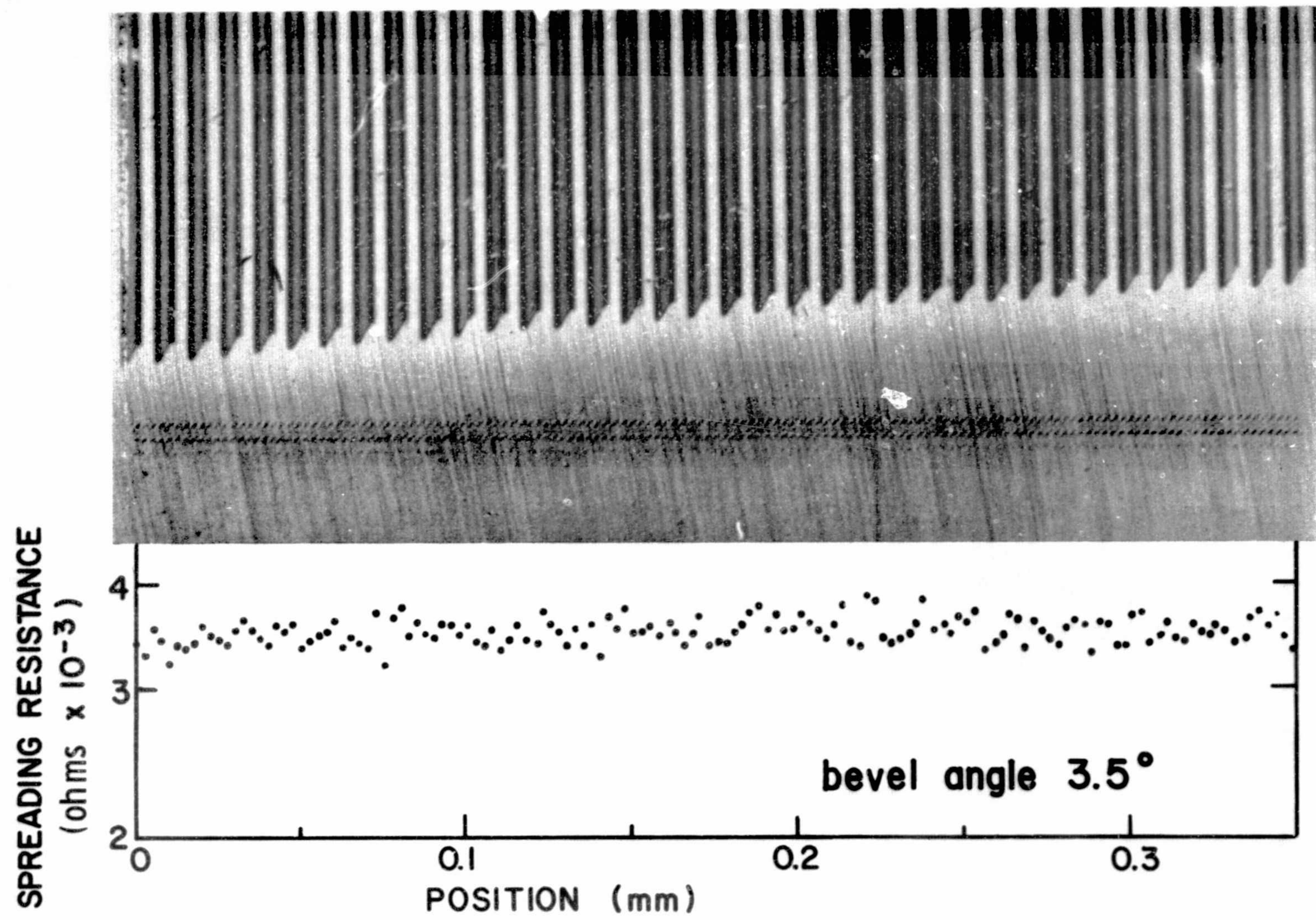

Fig. I-17. Spreading-resistance measurements, on a 3.5° beveled surface, perpendicular to surface striations.

ORIGINAL PAGE IS
OF POOR QUALITY

still diminutively present.

2.4.3 Dopant Distribution in 25 mm Silicon Ribbons

Spreading resistance measurements indicate that the dopant profile in silicon ribbons is influenced by the design of the capillary slots in the shaping die. In our early growth runs, a one-piece, flat-top EFG die of the type shown in Fig. I-5 was used to grow 10 mm wide ribbons. Boron-doped ribbons grown with such a die typically exhibited central resistivity minima similar to that shown in Fig. I-18. The

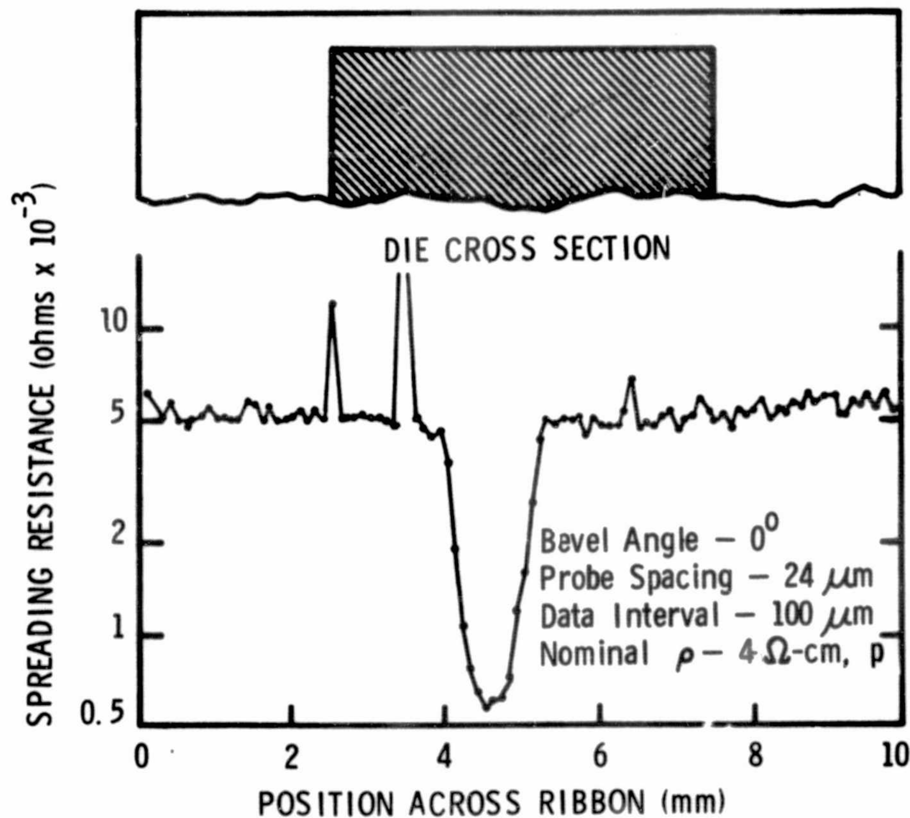

ORIGINAL PAGE IS OF POOR QUALITY

Fig. I-18. Dopant profile with 10-mm-wide, one-piece, flat-top die.

spreading resistance measurements were made transverse to the ribbon axis, on a finely lapped surface. In some measurements to be described subsequently, the transverse measurements were made on a beveled surface. Ribbons grown with a one-piece 25 mm wide, curved top capillary action shaping technique die (Fig. I-1) again exhibited the central resistivity minima as well as narrow dips near the edges of the ribbon (Fig. I-19). The magnitude of the difference between maximum and minimum resistance values was somewhat less with this CAST die than with the 10 mm wide EFG die. In some growth experiments, a die of the type shown in

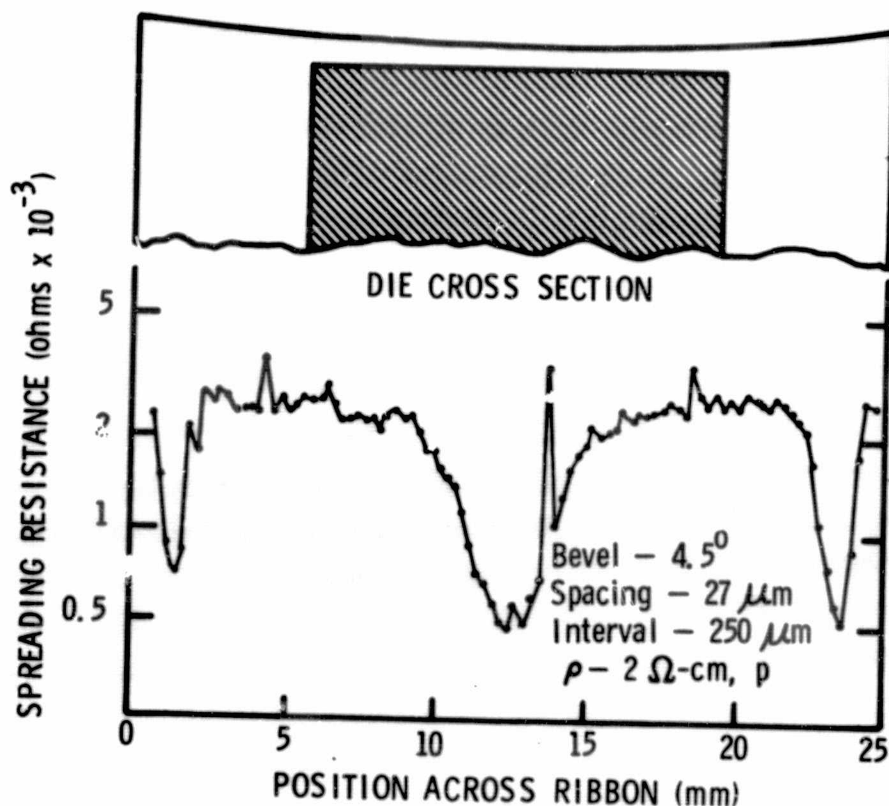

Fig. I-19. Dopant profile with 25-mm-wide, one-piece, curved-top die.

Fig. I-1 was modified by enlarging the top of the transverse channel slot as shown in Fig. I-20. The vee groove was cut with a 92 mm radius saw blade having a symmetrically beveled edge with an included angle of 45°. This was done to determine if the larger channel volume would affect the transverse spreading resistance profile and also to see if the reduction in the graphite surface area of the extreme die top would affect ribbon perfection. No significant change was seen in perfection. The effect on the spreading resistance profile was to cause a slight broadening of the

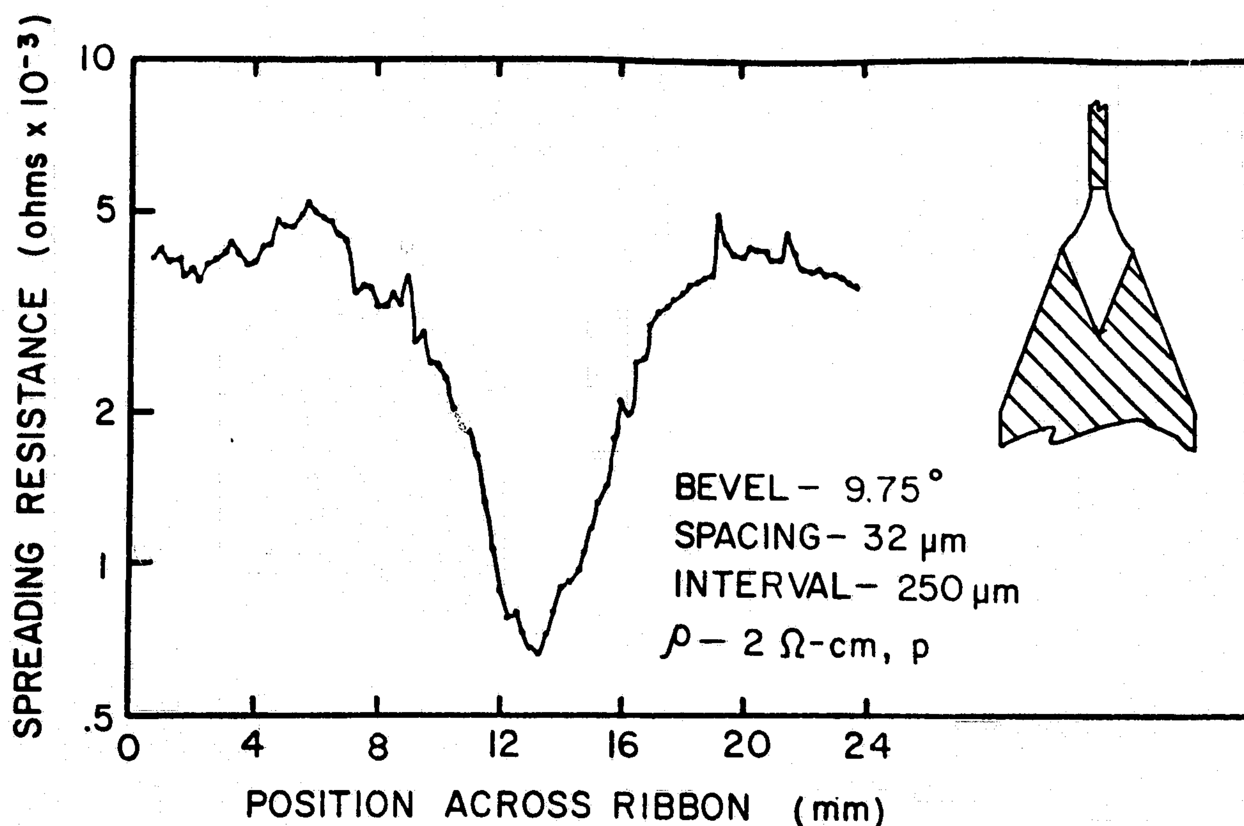

Fig. I-20. Dopant profile of a ribbon grown from a 25-mm-wide die having a V-shaped top cross-section.

central resistivity dip. There was no improvement in transverse resistivity gradient.

The effects of various gross ribbon defects upon dopant distribution were also investigated. Spreading resistance measurements were made on a lapped ribbon surface in a direction perpendicular to a series of twin lines. The surface was then lightly etched to delineate the twins and the probe marks. As shown in Fig. I-21, no appreciable resistance fluctuations were seen in crossing the twin lines.

In another ribbon sample, the resistance was measured across large-angle grain boundaries. The lapped sample was again lightly etched, and in this case, a large increase in spreading resistance (about 200%) was seen upon crossing the grain boundaries, although the resistance in off-boundary regions was reasonably constant. (See Fig. I-22.) Thus, the boundaries either tend to exclude the boron dopant or are contaminated with N-type impurities. It appears that grain boundaries and the transverse dopant distribution anomaly, which was discussed in section 2.4.3 are the known sources of large scale resistivity fluctuations, while twin boundaries and surface striations have a minor, and perhaps negligible, effect upon resistivity.

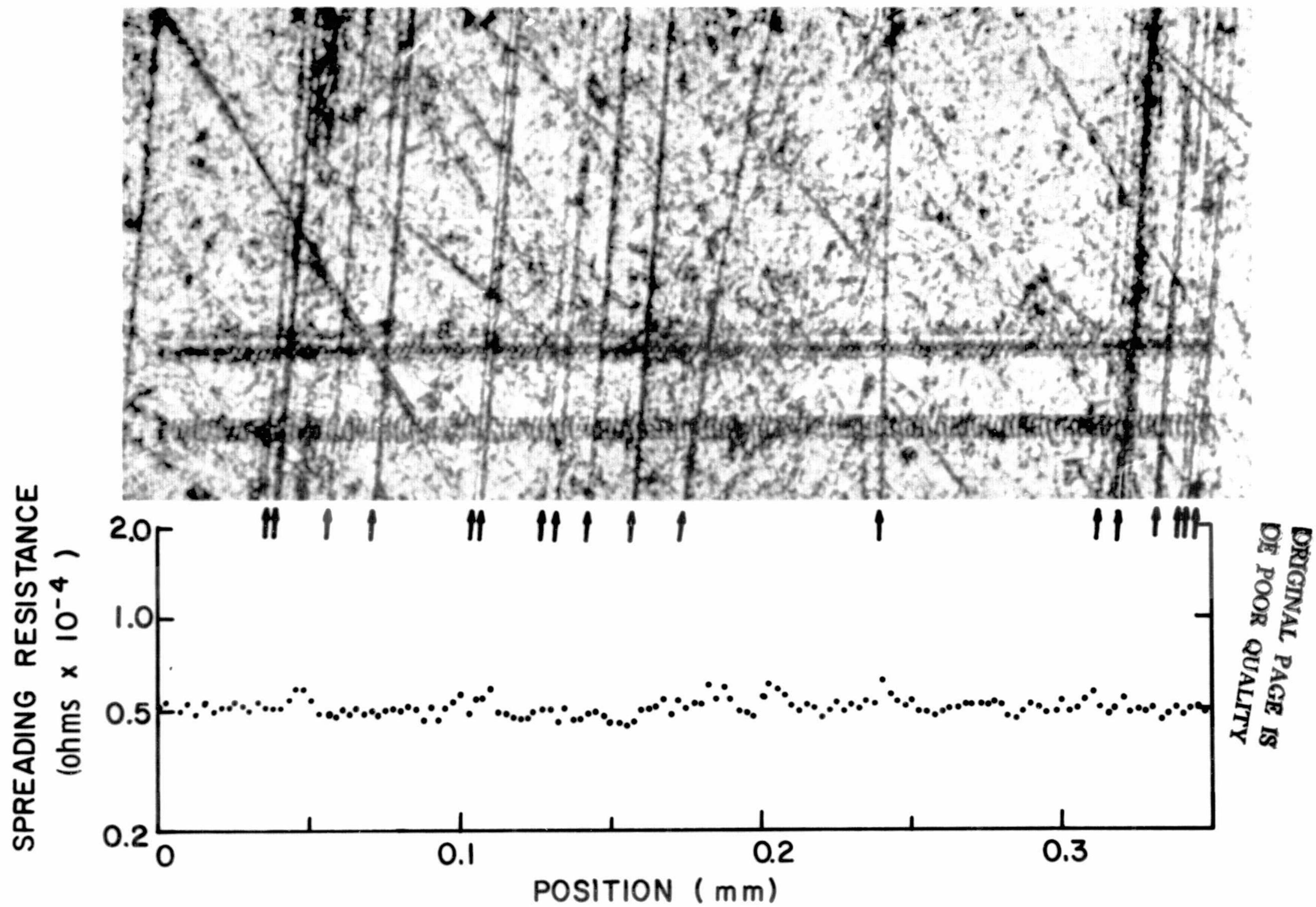

ORIGINAL PAGE IS
OF POOR QUALITY

Fig. I-21. Spreading-resistance measurements across twin boundaries.

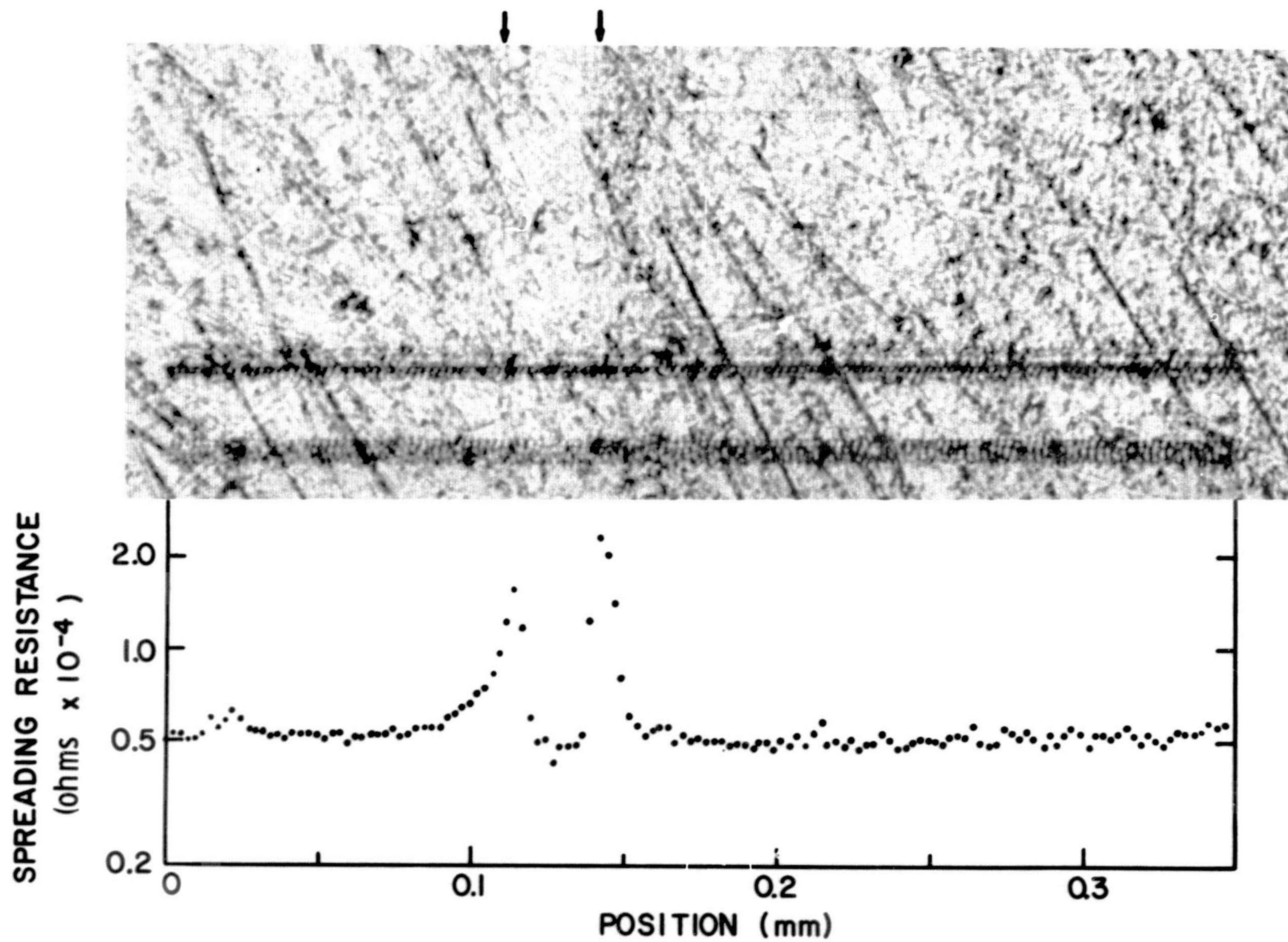

Fig. I-22. Spreading-resistance measurements across grain boundaries.

2.4.4 Thermal Stress Modification in the 25 mm Growth System

Several graphite thermal modifiers have been tested to determine their effect upon two ribbon parameters; transverse thickness uniformity and "frozen-in" stress. The modifiers are passive in that they are not independently variable with respect to the rf susceptor heater. Their design has evolved in an empirical fashion. The basic set-up to which the thermal modifiers were applied is that shown in Fig. I-4.

In the basic setup, the quartz insulator has a 64 mm ID, with a 6 mm wall, and its top is 2 mm lower than the susceptor top. The die top protrudes 1.0 mm above the top plane of the die holder, which is 9.53 mm thick. The susceptor top is recessed 18.3 mm deep to accept the die holder and shields. The upper part of the susceptor wall is 2.67 mm thick, and the lower part of 4.57 mm thick. The susceptor OD is 60.2 mm. The lower shield is 1.57 mm thick. It has a 2.38 mm x 27.78 mm slot, and the bottom is recessed 0.76 mm deep x 7.94 mm wide x 33.34 mm long. A 1.27 mm thick spacer separates the bottom and top shields. The top shield is 1.27 mm thick with a 4.76 mm x 30.16 mm slot. The 10-turn rf coil used with the setup is placed so that two

turns are above the susceptor top and eight turns are below. The coil has a nominal length of 100 mm and a diameter of 100 mm. The susceptor, shields, and die holder are made of graphite.

The first thermal modifier tried was a 50 mm ID graphite tube, 67 mm high with a 5 mm wall thickness. This tube rested on the top rim of the susceptor and had a 12.7 mm diameter viewing port drilled through the wall. Five growth attempts were made with the tube in place. In all attempts, freezing of the liquid film between the die and the ribbon occurred before the ribbon had spread from seed width (4 mm) to full width (25 mm).

The second modifier system consisted of a molybdenum plate 53.6 mm in diameter and 1.59 mm in thickness with a central slot 4.76 mm x 30.16 mm. Vertical parallel plates projected upward along the sides of the slot. These were 12.7 mm high x 22 mm wide x 1.59 mm thick and separated by a distance of 4.76 mm. The modifier rested on the upper heat shield. Five growth attempts indicated that this system was also prone to premature freeze-out. In addition, a short 25 mm wide ribbon grown with this modifier was very non-uniform in thickness, with the edges being thicker than the middle.

The third modifier was a 12.7 mm thick x 53.6 mm diameter

graphite block which rested on the upper shield. The opening through which the ribbon was pulled was tapered from a 7.1 mm width at the bottom surface to an 18.5 mm width at the top surface. Ribbon growth was easier with this setup, and five full width ribbons were grown at speeds ranging from 14 to 23 mm/min. The average ratio of edge thickness to center thickness at the tail end of the ribbons was 1.59 m and did not correlate with growth speed. Actual thickness tended to decrease with increasing growth speed for a given die (e.g., at 14 mm/min, the maximum and minimum thicknesses were 0.51 mm and 0.36 mm; at 20 mm/min, the corresponding values were 0.41 mm and 0.25 mm). The ribbon surface appeared to be duller with this modifier than without it, probably indicating a thicker SiC vapor-grown film on the ribbon. Ribbon 51104, grown at 14 mm/min with the modifier, was deliberately split at the tail end. The split width vs distance curve is shown in Fig. I-23. A rapid increase of split width with distance from the tip implies a large residual stress in the ribbon prior to splitting.

The fourth thermal modifier system was identical with the third except that the opaque quartz insulator was 15 mm taller. In this case, it was observed that the reduction in system temperature required to proceed from seed width to full ribbon width was only 30% of that used without a

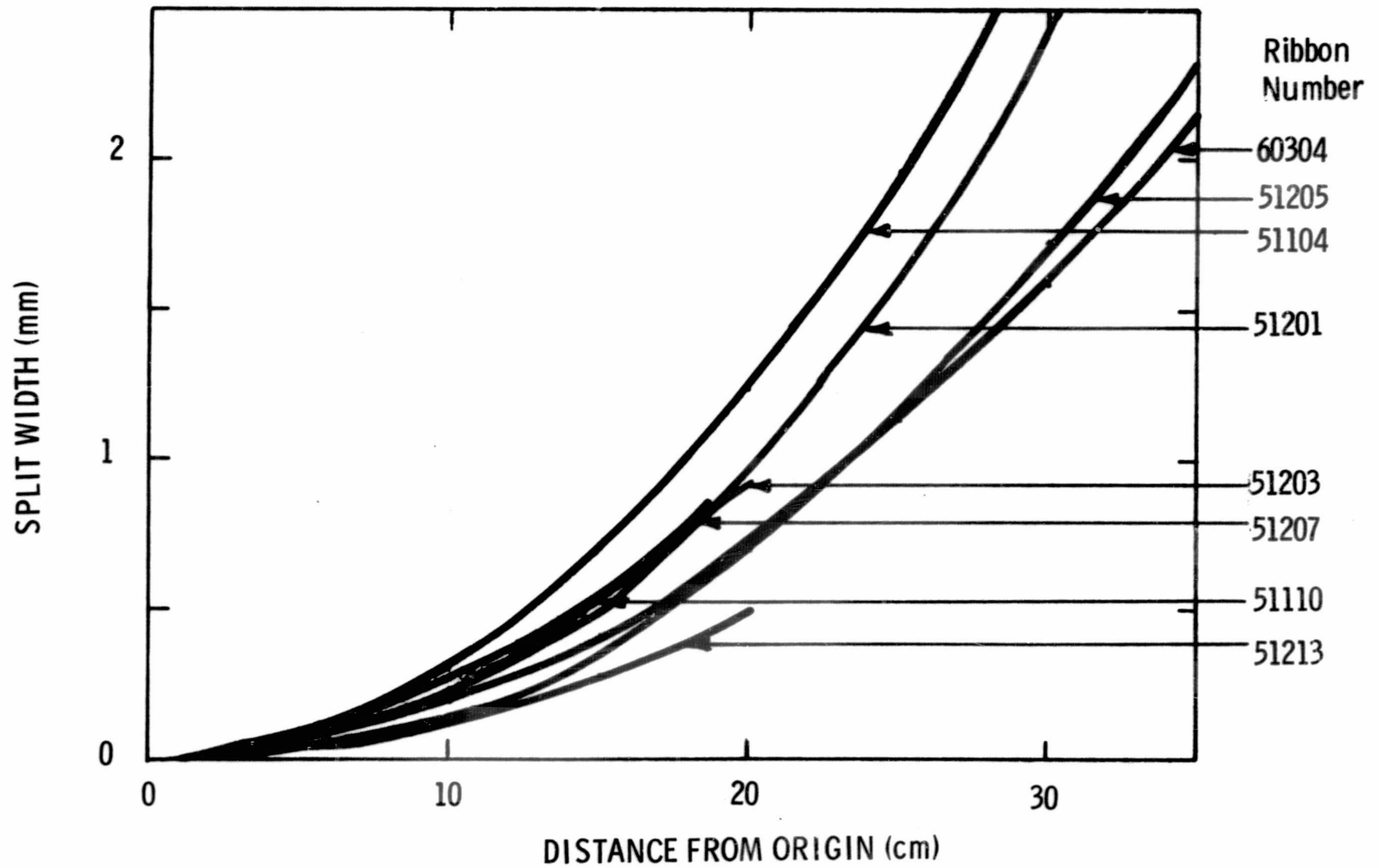

Fig. I-23. Split width vs distance from split origin for delibrately split ribbons.

thermal modifier. The ribbon was susceptible to freezeout unless growth was carried out slowly. The tail end, edge/middle thickness ratio of a ribbon grown at 11 mm/min was only 1.10, and the middle thickness was 0.50 mm. The thickness ratio increased to 1.43 at 18 mm/min, with the middle thickness correspondingly decreased to 0.35 mm. Stress levels of ribbons grown at 11 mm/min (No. 51110), 12 mm/min (No. 51203), and 18 mm/min (No. 51202) with this modifier were lower than that seen with the third modifier system.

The fifth thermal modifier to be tried consisted of two graphite blocks with recessed vertical grooves (Fig. I-24) which were placed at the edges of the ribbon. The blocks rested on the upper heat shield. Three full width ribbons were grown with this modifier. The average edge/middle thickness ratio at the tail ends was 1.19 for growth rates of 17-19 mm/min. Even though the growth rates did not vary appreciably and the same die was used, quite a difference in average thickness was seen among the ribbons. Ribbon 51207 was 0.24 mm thick and had a stress level comparable to that seen with modifier No. 4. Ribbon 41205 was 0.47 mm thick and had a lower stress level. (See Fig. I-23.)

The sixth thermal modifier system was like the fifth, except that the quartz insulator was 15 mm higher than in the basic

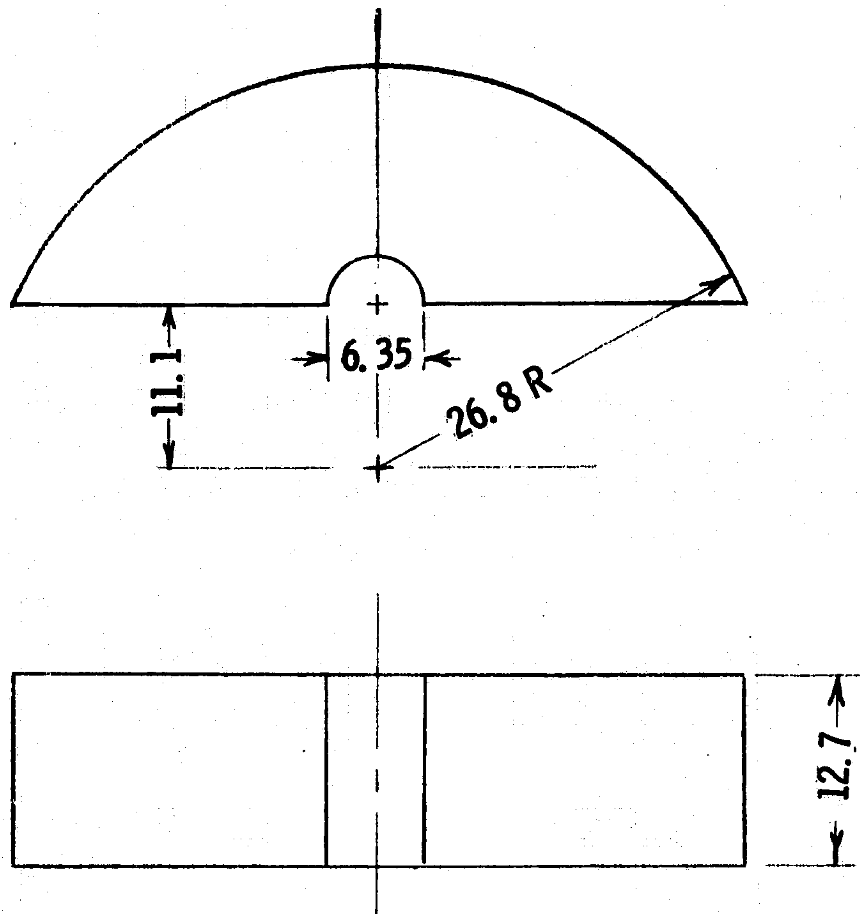

Fig. I-24. Thermal modifier No. 5.

setup. Three ribbons were grown, and it was found that approximately uniform ribbon thicknesses could be produced at selected growth rates. Ribbon 51210 was grown at 14 mm/min and exhibited an inverted thickness profile; the edge-to-middle thickness ratio was 0.77. The edge thickness was 0.50 mm, and the middle thickness was 0.65 mm. Three attempts were made to split this ribbon deliberately; and, in each case, the crack veered to the ribbon edge instead of

propagating up the ribbon. Thus, the frozen-in stress was very low. As the speed was increased to 18 mm/min (ribbon 51213), it was possible to split the ribbon, but the stress level was still relatively low as shown in Fig. I-23. At this speed, and at 17 mm/min (ribbon 51214), the ribbon did not exhibit an edge/middle thickness variation; the ribbon cross section was slightly wedge-shaped, with one edge 0.45 mm thick and the other 0.41 mm thick. This probably reflects non-uniform machining of the die.

In the seventh thermal modifier system, an attempt was made to combine the uniform thickness capability of system number six with a still lower stress level. Towards this end, a modifier was assembled in modular form, as follows. System number six was first assembled. On top of the 12.7-mm blocks, spacer blocks 20 mm high x 37 mm wide x 10 mm thick were placed so that the flat 20 mm x 37 mm surfaces were near and perpendicular to the edges of the ribbon. On top of the spacer blocks was placed a graphite cylinder 53.6 mm in diameter x 12.7 mm high. The latter had a 6 mm x 40 mm milled slot through which the ribbon was withdrawn, as well as a cutout at its edge for viewing purposes. The appearance of this modular assembly (Fig. I-25(a,b and c) was similar in major details to the one-piece thermal modifier which is shown in Fig. I-25(d) and will be described in the next paragraph. It was hoped that the block would reduce the vertical thermal gradient to

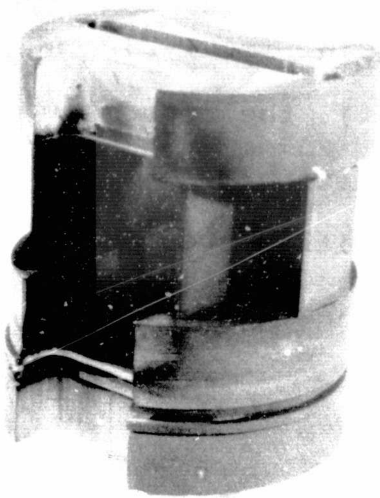

Fig. I-25(a) Thermal Modifier No. 7 Assembly

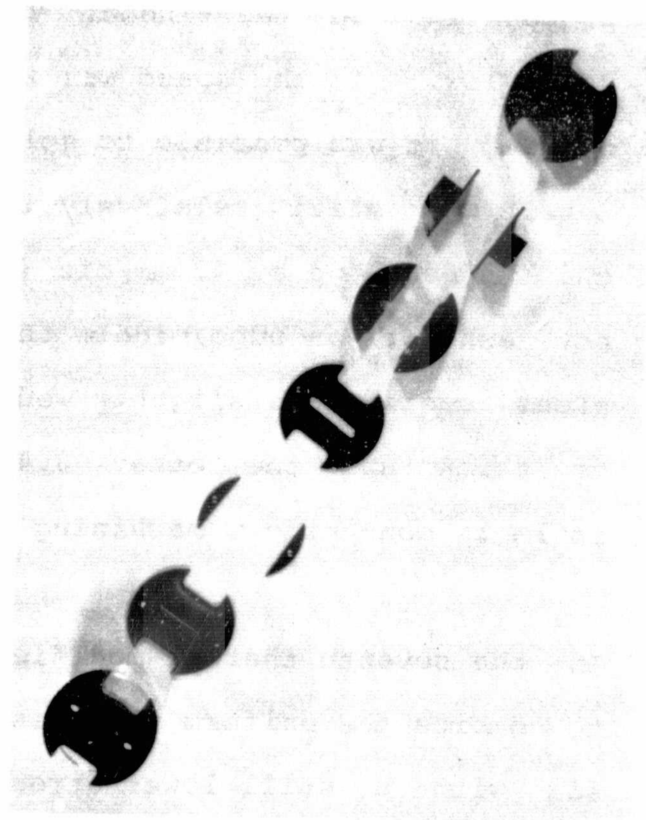

Fig. I-25(b) Thermal Modifier No. 7 Components

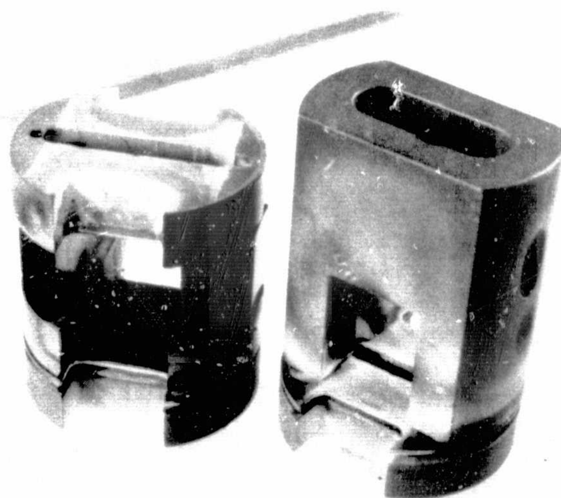

Fig. I-25(c) Thermal Modifiers No. 7 (left) and No. 8 (right)

ORIGINAL PAGE IS OF POOR QUALITY

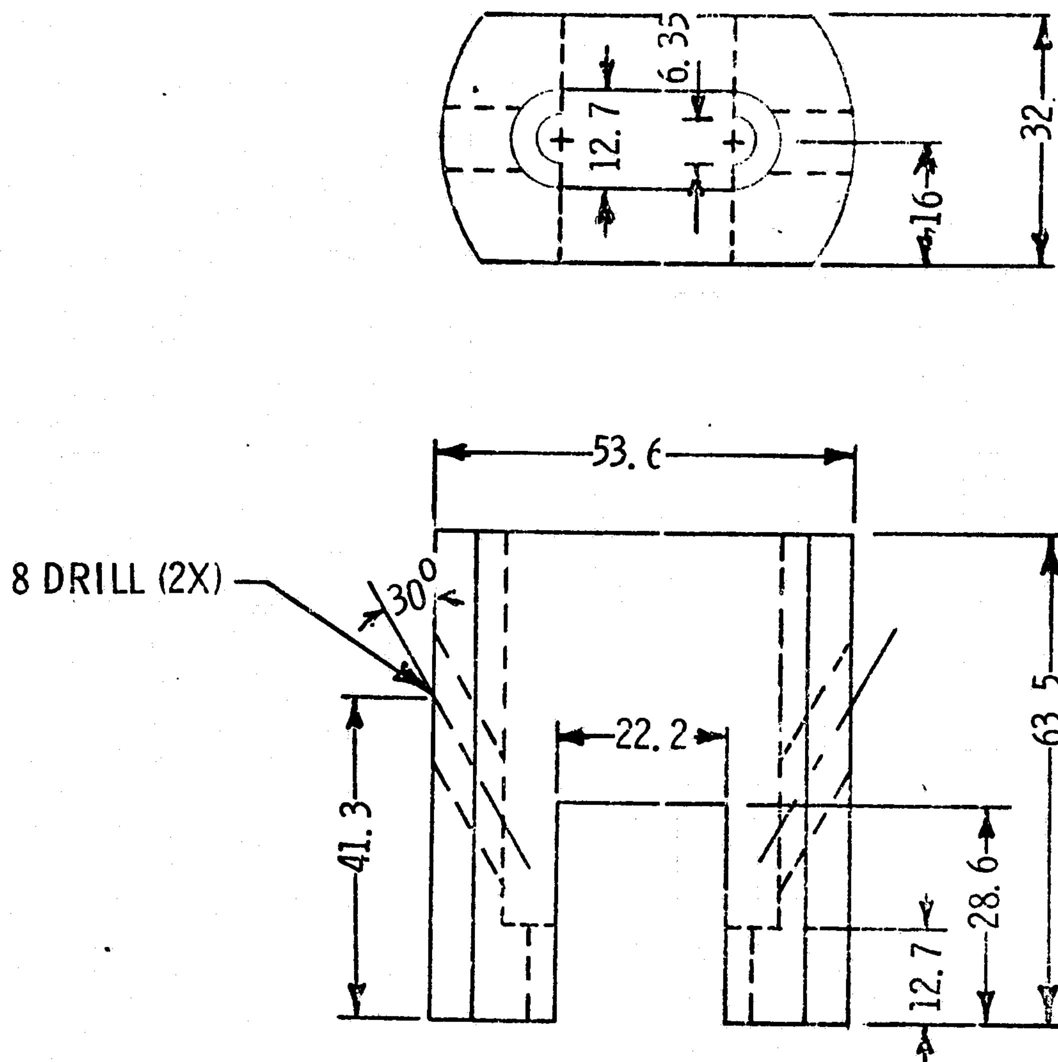

Fig. I-25(d) Thermal Modifier No. 8

some extent and in this way reduce the frozen-in stress. Ribbon 60105 was grown at a speed of 14 mm/min and was found to resist splitting. (See Fig. I-26). The ribbon was essentially uniform in thickness, with a slightly wedge-shaped cross section (0.50 mm thick at one edge and 0.45 mm thick at the other).

In thermal modifier number eight shown in Fig. I-25, an attempt was made to incorporate and enhance the main features of modifier number seven in a one-piece design. Several ribbons were grown with this modifier; and, indeed, good resistance to splitting was seen (see Fig. I-26, ribbon 60203). However, a very high edge/middle thickness ratio was obtained. Ribbon 60202, for example, was grown at 18 mm/min and had an edge/middle thickness ratio of 1.57. The central thickness was 0.30 mm. For comparison purposes, ribbon 60304 was grown at 20 mm/min, using the basic setup with no additional thermal modifiers. The observed splitting (Fig. I-23) was comparable to that seen with ribbon 51205, which was grown using the fifth thermal modifier system. However, the edge-to-middle thickness ratio was 1.91--much higher than was observed with modifier number five. The middle thickness was 0.22 mm.

ORIGINAL PAGE IS
OF POOR QUALITY

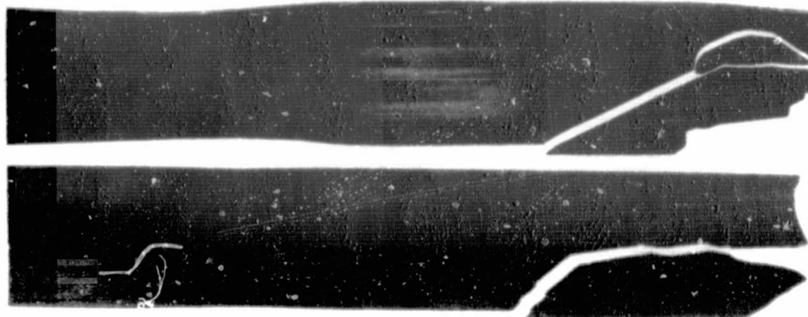

Fig. I-26. Two 25-mm-wide ribbons which resisted attempts at axial splitting. Top, ribbon 60203; bottom, ribbon 60105.

Although the parameters involved are numerous, the observed behavior of passive thermal modifiers can be essentially summarized as follows:

1. Placing relatively massive graphite thermal modifiers, preferentially, near the edges of the ribbon tends to reduce the edge thickness relative to the middle thickness; and, at an optimum growth speed, results in approximately uniform ribbon thickness (e.g., the sixth thermal modifier system, at 17 mm/min growth speed).

2. Decreasing the vertical thermal gradient by extending the height of the thermal insulation or by adding massive, passive graphite thermal modifiers around the ribbon at some distance above the growth interface tends to reduce or eliminate the tendency for splitting to propagate along the ribbon (e.g., the seventh and eighth thermal modifier systems).

As determined from uncorrected optical pyrometer measurements on "interior surfaces" of the graphite components in the basic setup, with thermal modifier number eight in place, the vertical temperature profile of Fig. I-27 is present near each ribbon edge during growth and is sufficient to produce nonsplitting ribbons, such as 60203.

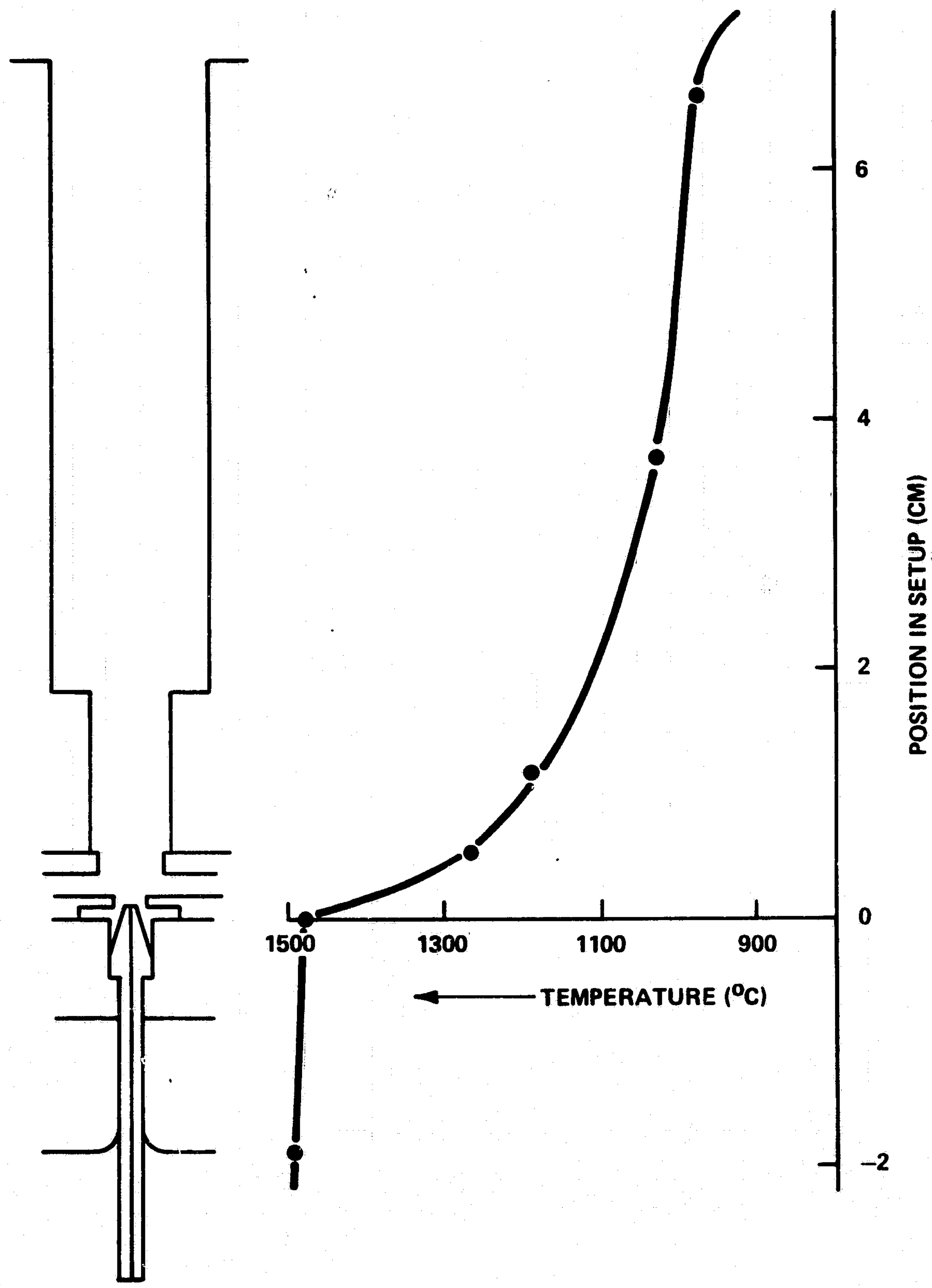

Fig. I-27. Thermal profile near edge of ribbon sufficient for low stress levels.

2.4.5 Maximum Growth Rates for Melt-Grown Ribbon-Shaped Crystals

An analysis of the heat balance at the growing interface for nondendritic crystal growth from the melt has been made by Billig[7]. His calculation indicated that the maximum growth rate or pulling speed V_{max} would occur when the temperature gradient in the melt at the interface approached zero and would be given by

$$V_{max} = \frac{-K_m}{L\rho_m} \left(\frac{dT}{dx}\right)_m , \quad (1)$$

where K_m is the thermal conductivity of the solid crystal at the melting temperature, L is the latent heat of fusion, ρ_m is the density of the crystal at the melting temperature, T is the crystal temperature, x is the distance along the crystal from the growing interface, and $(dT/dx)_m$ is the temperature gradient in the crystal at the growing interface.

A calculation of maximum ribbon growth rates[8] has been carried out under the following assumptions: (i) heat loss from the crystal is only by radiation to a cold environment, (ii) the solid liquid interface is planar, (iii) the thermal

conductivity of the crystal varies inversely with temperature, and (iv) the surface emissivity ε of the crystal is temperature independent.

Heat from the solidification front is dissipated by conduction along the ribbon and radiation from the ribbon surface. Heat conduction along the ribbon is given by

$$Q = AK \frac{dT}{dx} = WtK \frac{dT}{dx} , \tag{2}$$

where A is the ribbon cross-sectional area, K is the thermal conductivity of the ribbon, W is the ribbon width, and t is the ribbon thickness. Heat loss from an element dS of the ribbon surface dx long via radiation to a cold environment is

$$dQ = \sigma\varepsilon T^4 dS = 2 (W+t)\sigma\varepsilon T^4 dx . \tag{3}$$

For many materials of interest, particularly semiconductors such as silicon, the solid conductivity K can be approximately expressed as $K = K_m T_m/T$ [assumption (iii) above]. Making this substitution in Eq. (2), and combining Eqs. (2) and (3), we get the differential equation

$$\frac{d}{dx} \left(T^{-1} \frac{dT}{dx} \right) = \frac{2(W+t)\sigma\varepsilon T^4}{WtK_m T_m} . \tag{4}$$

The solution of Eq. (4) for boundary conditions

$$T = 0, \frac{dT}{dx} = 0 \quad \text{at } x = \infty$$

and

$$T = T_m \text{ at } x = 0$$

is

$$T = \left[2 \left(\frac{(W+t)\sigma\varepsilon}{WtK_m T_m} \right)^{1/2} x + T_m^{-2} \right]^{1/2} . \qquad (5)$$

The derivative of Eq. (5) evaluated at x = 0 is

$$\left(\frac{dT}{dx}\right)_{x=0} = \left(\frac{dT}{dx}\right)_m = -\left(\frac{\sigma\varepsilon(W+t)T_m^5}{WtK_m}\right)^{1/2} . \qquad (6)$$

Combining Eqs. (1) and (6) results in the maximum growth rate under the stated assumptions:

$$V_{max} = \frac{1}{L\rho_m} \left(\frac{\sigma\varepsilon(W + t)K_m T_m^5}{Wt} \right)^{1/2} . \qquad (7)$$

If the width-to-thickness ratio of the growing ribbon is

large (W/t >> 1), Eq. (7) may be simplified to

$$V_{max} = (1/L\rho_m)(\sigma\varepsilon K_m T_m^5/t)^{1/2} \quad . \tag{8}$$

Even for W/t = 10, the maximum growth rate is within 5% of the rate for any greater W/t ratios.
Thus, the maximum growth rate is essentially independent of width for wide ribbons and varies as $t^{-1/2}$.

The curve for maximum growth rate vs ribbon thickness from Eq. (8) is shown in Fig. I-28 for the case of silicon.

Maximum Czochralski growth rates[8] are given by

$$V_{max} = (1/L\rho_m)(\sigma\varepsilon K_m T_m^5/r)^{1/2} \quad , \tag{9}$$

where r is the cylindrical crystal radius.

Although the maximum ribbon growth rates are considerably higher than maximum Czochralski growth rates, the amount of material produced per unit time is, of course, much smaller in the case of ribbons. One way of viewing this is to consider the rate of surface area produced during crystal growth, as is done in Fig. I-29.

Actual growth rates for Czochralski crystals are about 0.2 - 0.3 V_{max} and for ribbons they are 0.3 - 0.4 V_{max}.

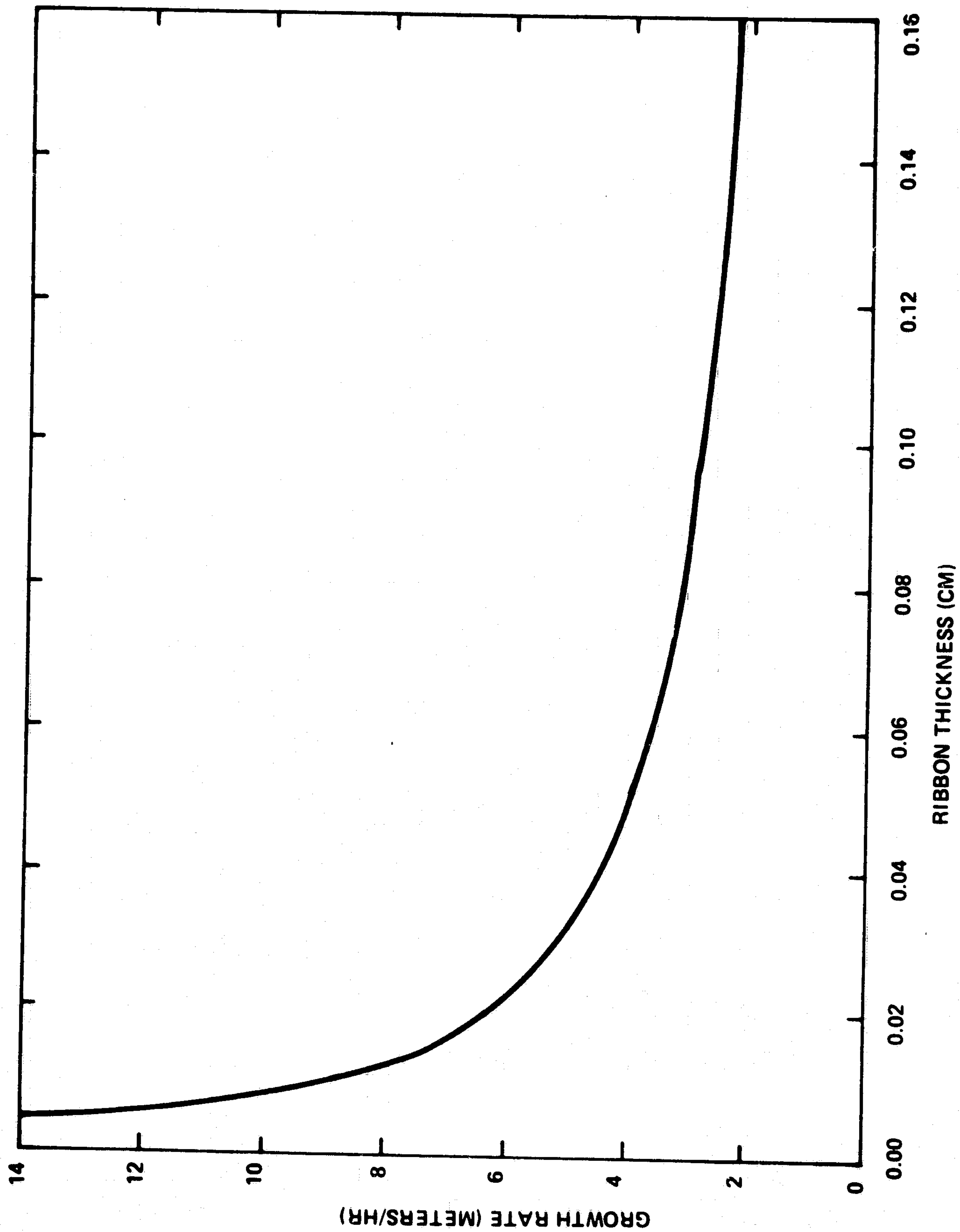

Fig. I-28. Maximum growth rate vs thickness for silicon ribbon.

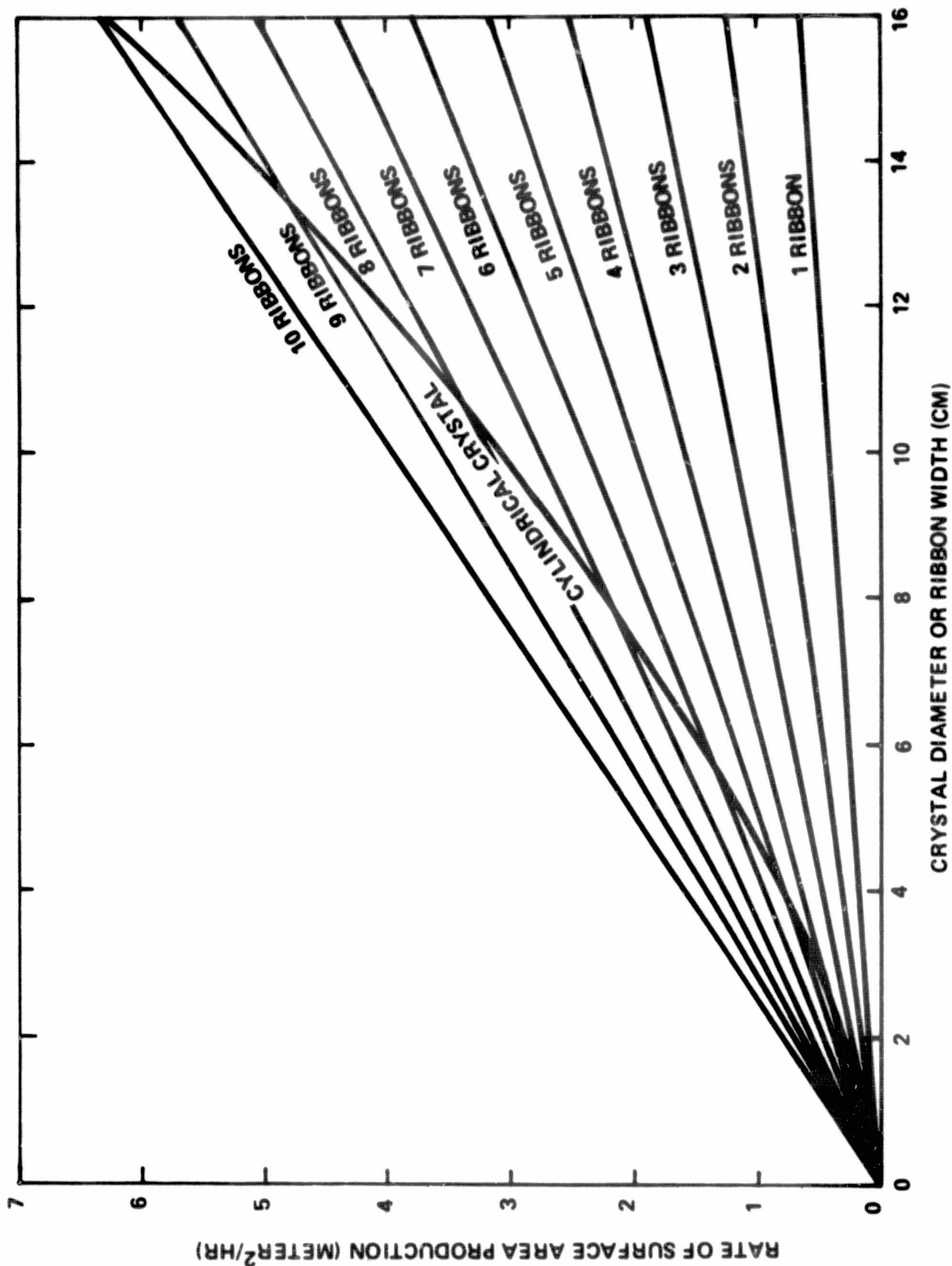

Fig. I-29. Rate of surface-area production during growth vs Czochralski crystal dia. or ribbon width. A 0.05-cm ribbon thickness and postgrowth slicing of the Czochralski crystal into 0.05-mm-thick wafers with 50% material loss is assumed. Maximum silicon growth rates are used. The effect of simultaneous multiple ribbon growth (up to 10 ribbons) is included.

3.0 GROWTH OF 38 MM SILICON RIBBONS

3.1 Process Development for 38 mm Ribbons

The same apparatus and hot-zone design were used for 38 mm growth as for 25 mm growth. The slots in the die holder and heat shields were elongated to accommodate the new die width.

3.1.1 Die Design

The concepts discussed relative to 25-mm-wide capillary action shaping technique dies were extended to the design of a die for 38-mm (1-1/2-inch)-wide ribbons. In this die, δ = 1.0 mm, $\phi = 50^{o}$, X_e = 0.44 mm, and X_m = 1.16 mm. Initial ribbons were grown at speeds of 16-18 mm/min. Typically, the edge thickness was 0.42 mm and the middle thickness was 0.54 mm. A thinner portion (0.37 mm) was present, however, between the edge and the middle. Thus the total deviation from flatness was about 0.09 mm. More difficulty was noticed with freeze-out during the process of spreading from seed-width (3-mm) to full-width growth than had been observed during 25-mm-wide ribbon growth.

For initial 38-mm-wide ribbon growth experiments, five 0.8 mm diameter cylindrical capillary feed holes were drilled in the central region of the die, spaced 3.2 mm apart. These were in addition to the side and top slots which had been used in the smaller dies. Ribbons grown with such a die exhibited resistivity minima near the edges which were similar to those observed using the 25-mm-wide die. However, the central resistivity dip was moderated by the presence of the cylindrical holes as shown in Fig. I-30 and, in fact, was changed to a series of smaller-amplitude minima

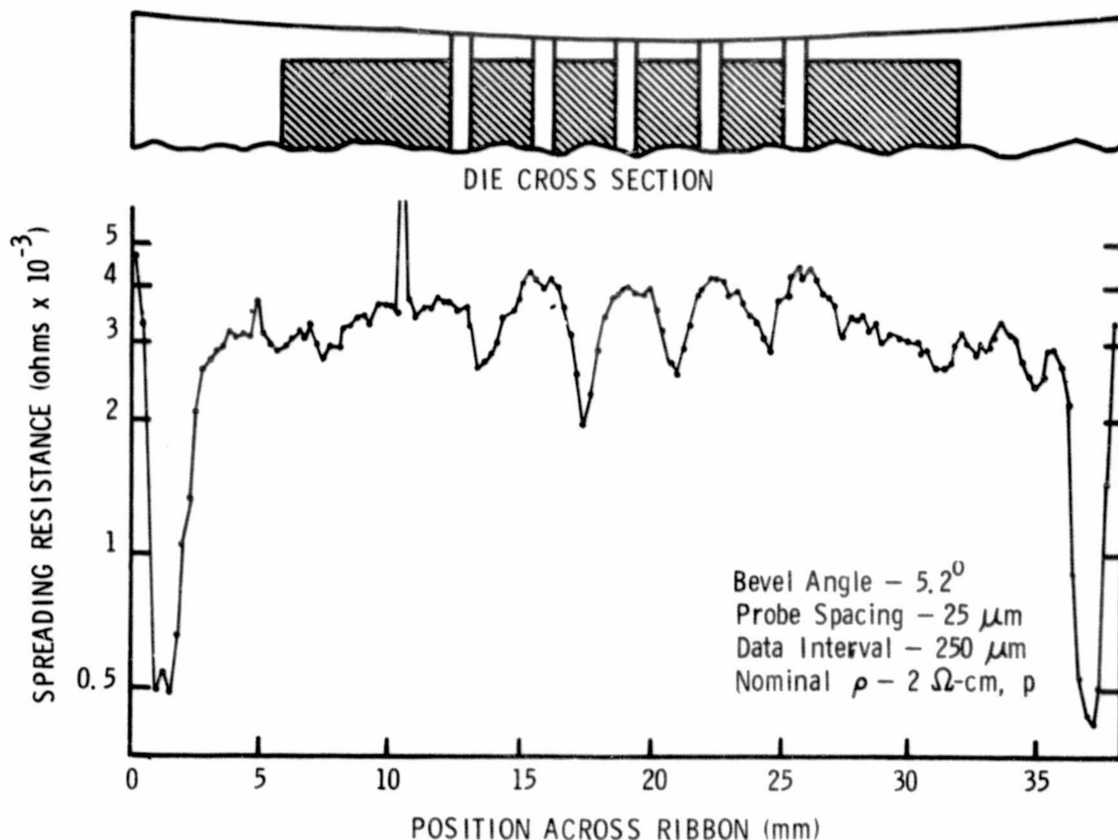

Fig. I-30. Dopant profile with 38-mm-wide, one-piece die having five central, cylindrical capillary feed holes.

occurring approximately at the positions between cylindrical feed holes.

These observations indicate that dies should be fabricated with minimal capillary slot obstruction (i.e., as close as possible to a configuration consisting of parallel, non-contacting plates). Apparently, there is a build-up and stagnation of dopant between vertical capillary rise channels.

To achieve a relatively unobstructed channel, a two-piece die was designed and a number of ribbons have been grown with such dies. The dopant distribution of Fig. I-31 indicates that a flatter profile was obtained with this die than with the one-piece type. However, a smaller amplitude central resistivity dip was still present. Thus, an open channel die improves, but does not completely eliminiate, the transverse dopant gradient problem.

On the other hand, dopant gradients in the thickness dimension have been very low--even near the ribbon surface, as shown by spreading-resistance measurements made on a sample adjacent to the 38-mm-wide sample for which the dopant profile shown in Fig. I-30 was measured. In this case, the sample was beveled at a 9.83^{o} angle so that measurements could be made from the surface down into the

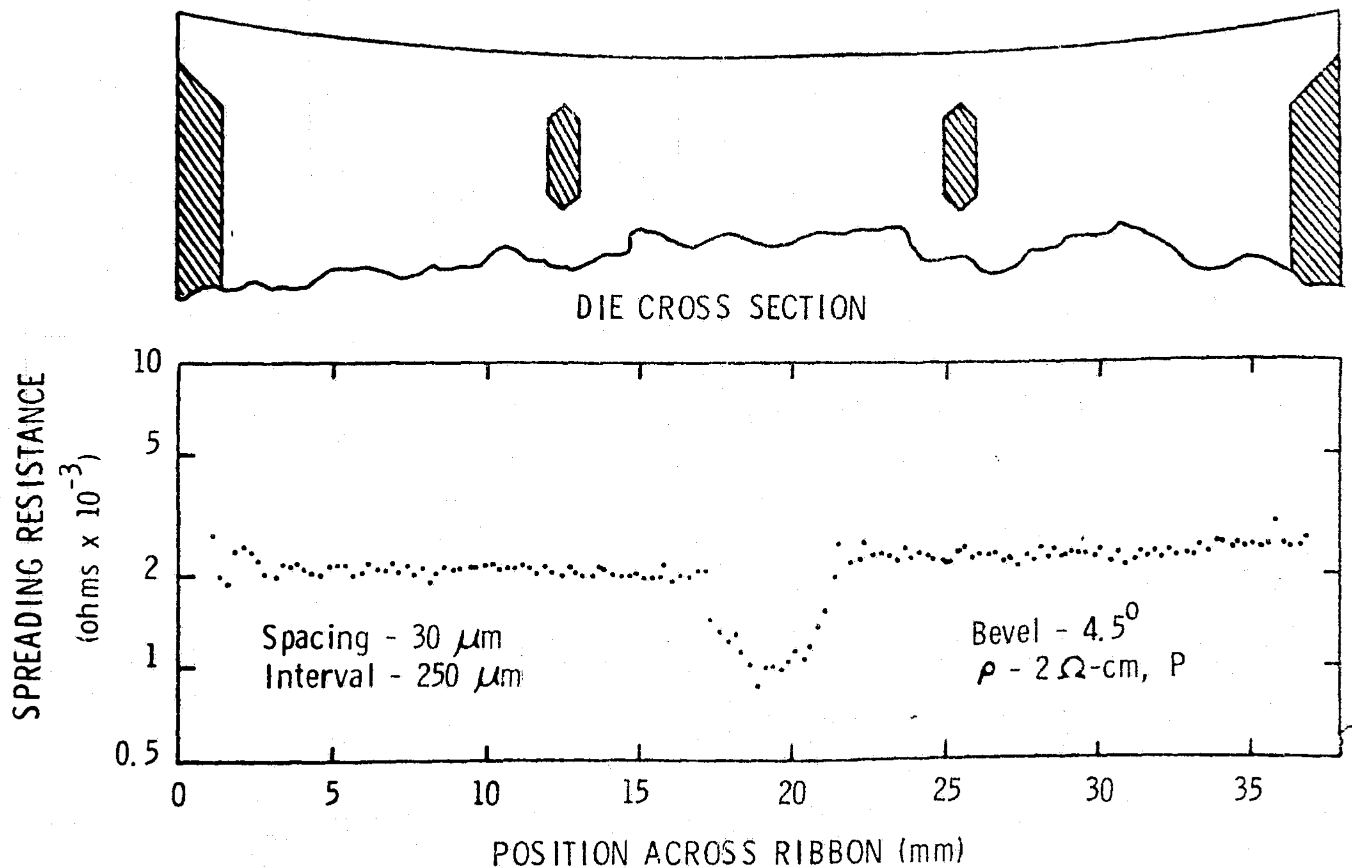

Fig. I-31. Dopant profile of a ribbon grown from a two-piece die.

depth of the ribbon. Such measurements were made at a relative minimum and at a relative maximum of Fig. I-30. The results indicate that there is no resistivity change even as close as 4 μm from the surface as can be seen in Fig. I-32. Similar results were found when using the two-piece die.

As more experience was gained with the 38 mm growth system, it was found that capillary action shaping technique dies with a 152-mm-radius top curvature, a 0.8-mm edge thickness,

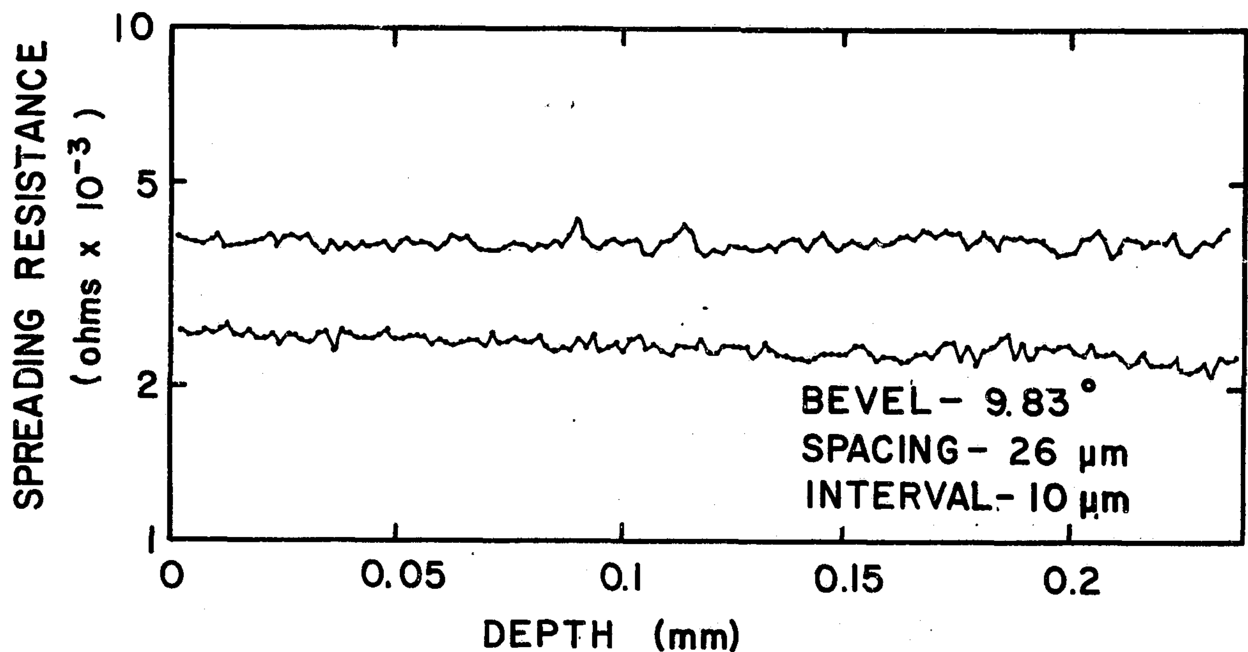

Fig. I-32. Spreading resistance vs depth into ribbon at positions corresponding to a relative maximum and a relative minimum of the surface spreading resistance.

and a 1.52-mm central thickness produced better results than the thinner dies used earlier. It was possible to grow 0.3 mm thick ribbons at 30 mm/min with such dies.

3.1.2 Reuse of Quartz Crucibles

Experiments were performed to demonstrate the feasibility of reusing quartz crucibles. Crucibles with 51-mm outside diameter, 25-mm-height, and 2-mm wall thickness were used. These are the standard crucibles used in the growth of 12.5,

25, and 38-mm-wide ribbons. They are flat-bottomed, and were typically loaded with 50-60 gram silicon charges. The experiments were conducted in conjunction with 38-mm-wide ribbon growth.

In earlier ribbon growth runs (60917, 60918, 61001, and 61008), it was noticed that all silicon except a small droplet 4 to 10 mm in diameter could be removed from the crucible by continuing ribbon growth until capillary flow starvation occurred. The small droplets did not appear to crack the crucible upon cool-down, and so we decided to attempt reuse of such crucibles. In run 70201, the crucible from run 61001 was reused. In Fig. I-33(a), the crucible is shown as it appeared after run 61001, in which a 67 x 3.8-cm ribbon was grown. A 5-mm-diameter droplet of silicon was left in the crucible. The crucible was etched in an acid solution of the following composition (by volume):

HNO_3	(70%)	3 parts
CH_3COOH	(Glacial)	2 parts
HF	(49%)	1 part.

Etching was carried out for 24 hours, and the silicon droplet was completely consumed. The etchant also attacked

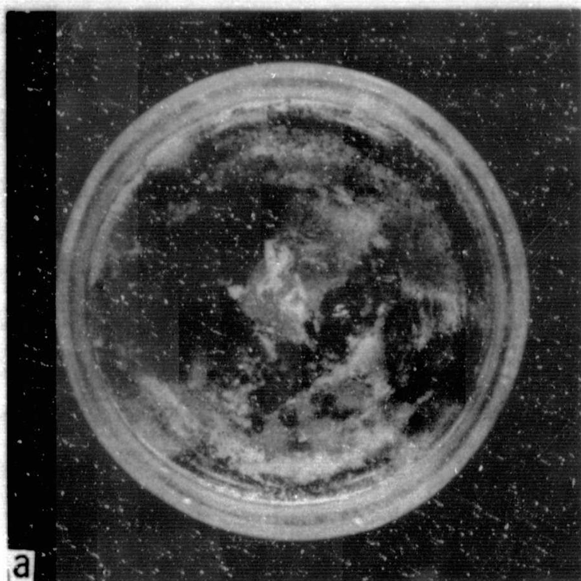

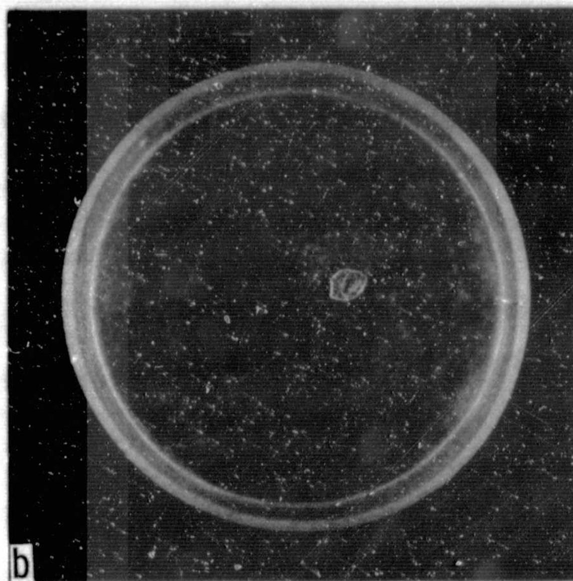

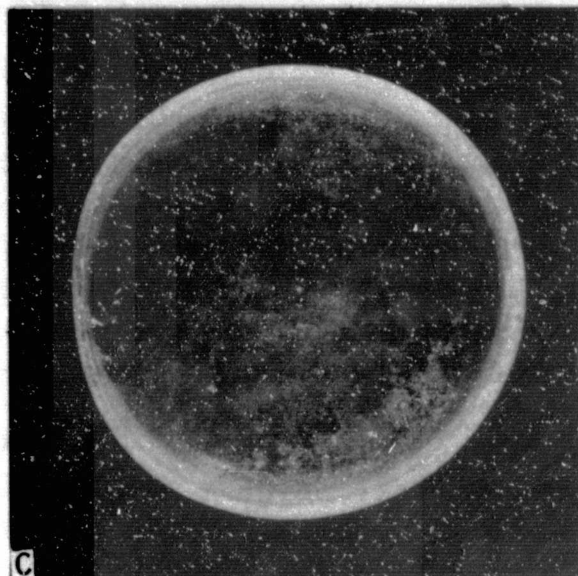

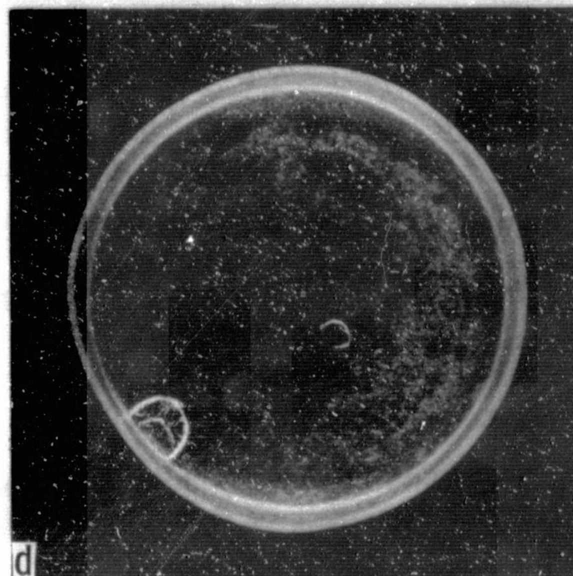

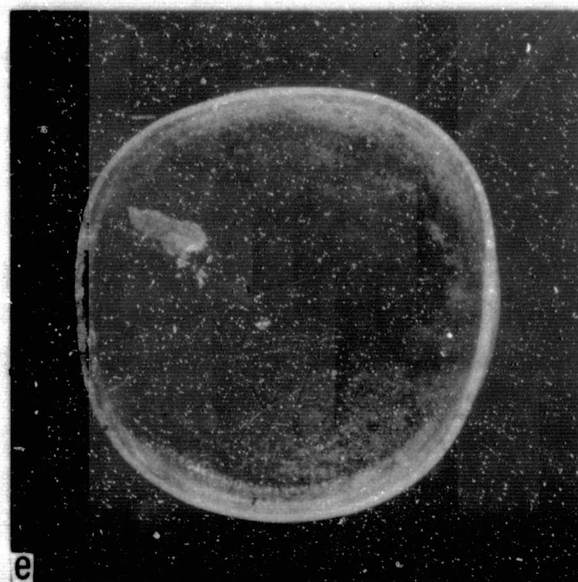

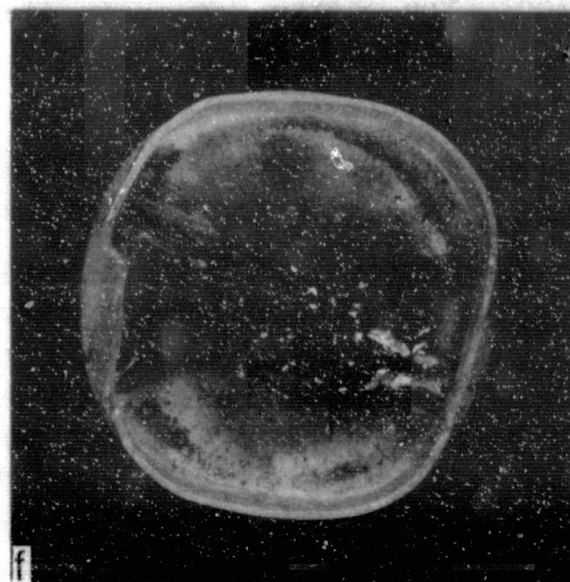

Fig. I-33. Stages in the repeated use and etching of a 51-mm-diameter quartz crucible. See text for details.

ORIGINAL PAGE IS OF POOR QUALITY

the crucible, decreasing its wall thickness from 1.8 to 1.4 mm. Figure I-33(b) shows the crucible after etching and prior to run 70201. The inner surface of the crucible is seen to be slightly crazed where it had been in contact with the frozen droplet. After etching, the crucible was loaded with 56 grams of silicon and a 76 x 3.8 cm ribbon was grown in run 70201. Again the entire melt was consumed except for a 7.2-mm-diameter droplet near the crucible wall (Fig. I-33(c)).

The crucible was again etched to remove the silicon. The larger droplet left a larger crazed area on the crucible (Fig. I-33(d)). The etching further reduced the wall thickness to 1.1 mm.

For the third run with this crucible, another 56-gram charge was loaded and ribbon 70202 was grown 88 cm long x 3.8 cm wide. The charge was again consumed except for a droplet 13 x 6 mm in size. See Fig. I-33(e). As can be seen, crucible deformation which began to be noticeable in Fig. I-33(c) is quite pronounced after the third run. This is probably because of the thinning effect of the etch.

For the fourth run with this crucible, only a light etch (five minutes) was used prior to loading another 55-gram charge. This etch did not remove the silicon droplet. A

short ribbon (20 cm) was grown in run 70203. It froze to the die. Then, after reseeding, ribbon 70204 was grown from the same melt. It was a 44-cm-long x 3.8-cm-wide ribbon, and again all the silicon was consumed except for the small droplets shown in Fig. I-33(f). After run 70204, the crucible was badly deformed, but was still intact and conceivably could have been used again. However, a portion of the upper rim was broken during handling.

In summary, the crucible was used in four melt-down cycles and performed satisfactorily. A small amount of crazing occurred in the immediate vicinity of the residual frozen silicon droplets left in the crucible at the onset of capillary starvation, but the crazing was not substantial enough to interfere with the growth process. The crucible deformed with increasing use. This may have been enhanced by the heavy etching which reduced the crucible wall thickness. On the fourth run made with the crucible, it was demonstrated that heavy etching is not necessary.

3.1.3 Thermal Geometry Control

As mentioned in section 3.1.1, more difficulty with freeze-out during the spreading operation from seed size to full width was encountered with 38 mm wide ribbons than with smaller ribbons. Thermal asymetries in the hot-zone also became more critical. Thus it became apparent that

"on-line" thermal balancing and thermal profile control at the die top would be required.

Processes requiring dynamic thermal control over an extended region have incorporated various means of achieving desired thermal profiles. In the case of ribbon crystal growth, for example, radiation shields or ports[9], multiple minature heaters[9], and shaped "weights" for heat focusing[10] have been employed. Most of these techniques have the disadvantage of not being continuously variable during the process. Minature heaters are continuously variable, but have several drawbacks; e.g., (a) the available materials of construction for the heater and associated insulators may be contaminants at high temperature in some processes and (b) such heaters add additional heat to a process already limited by heat and hence do not provide a way of selectively extracting heat.

A system providing a means for growing wide silicon ribbons through thermal profile control which is continuously variable, inert, and capable of heat extraction has been implemented. The device employs multiple inert-gas jets directed at various parts of the hot zone, each with an individually controlled flow adjustment. In Fig. I-34 a system of four purge jets and flow-meters in a ribbon growth apparatus is shown. The two end jets impinge on the ribbon

ORIGINAL PAGE IS
OF POOR QUALITY

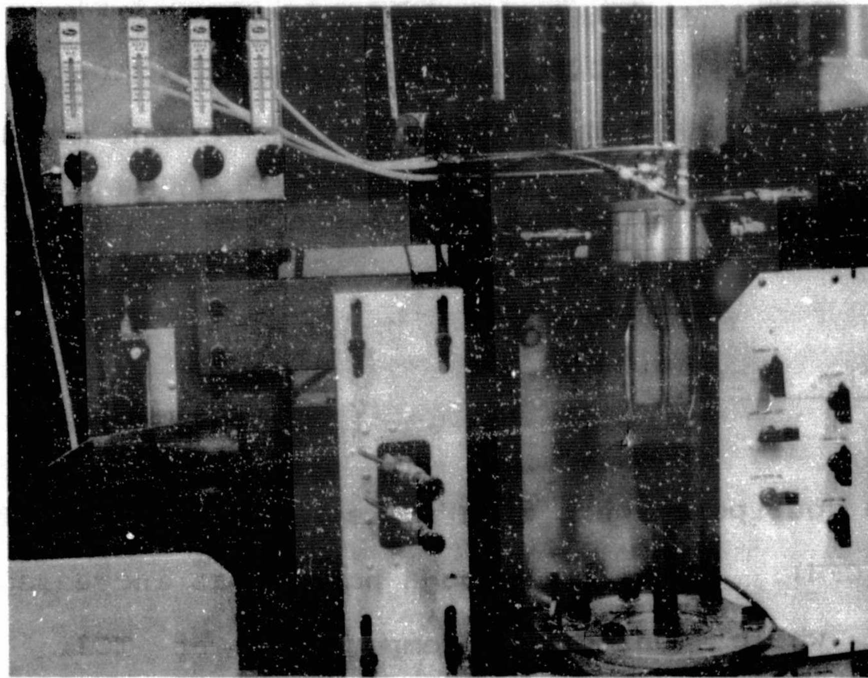

Fig. I-34. Inert-gas purge system for thermal geometry control; flow monitors are at upper left; purge tubes are at middle right.

growth region at points 38 mm apart (corresponding to the edge positions of a 38-mm-wide ribbon). The two middle jets are directed so to be at either side of a ribbon being grown and pulled upward through the large central draw tube (which also serves as the exit tube for the inert gas--argon in this case). To use the system, more argon is directed to those parts of the system where the temperature is locally higher than desired.

Several examples of use of the system are presented here. Three thermocouples (TCs) were placed in a blank graphite die-holder block as shown in Fig. I-35 (bottom). The spacing was 19 mm. The TC junctions were approximately at the growth region of a 38-mm-wide ribbon (edges and middle). The system was heated to approximately 1200°C by an external RF coil.

Example 1 (Fig. I-35)

Flows to the four ports were each adjusted to 8.5 cubic feet per hour (CFH). The flow through port 1 was increased in increments, while monitoring temperature at TC1. The temperature decreased approximately linearly with flow at a rate of -3.2°C/CFH argon (Fig. I-35). The time constant for the response of temperature to a flow change was approximately 11 sec. Progressively smaller cooling effects were seen at positions 2 and 3.

Example 2 (Fig. I-36)

With equal flows of 8.5-CFH argon at all ports, an asymmetrical thermal profile was present (top). Adjusting the left and right port flows to 16.2 and 29.8 CFH, respectively, provided a flat profile (middle). Thus, the 65°C temperature gradient over a 3.8-cm distance has been

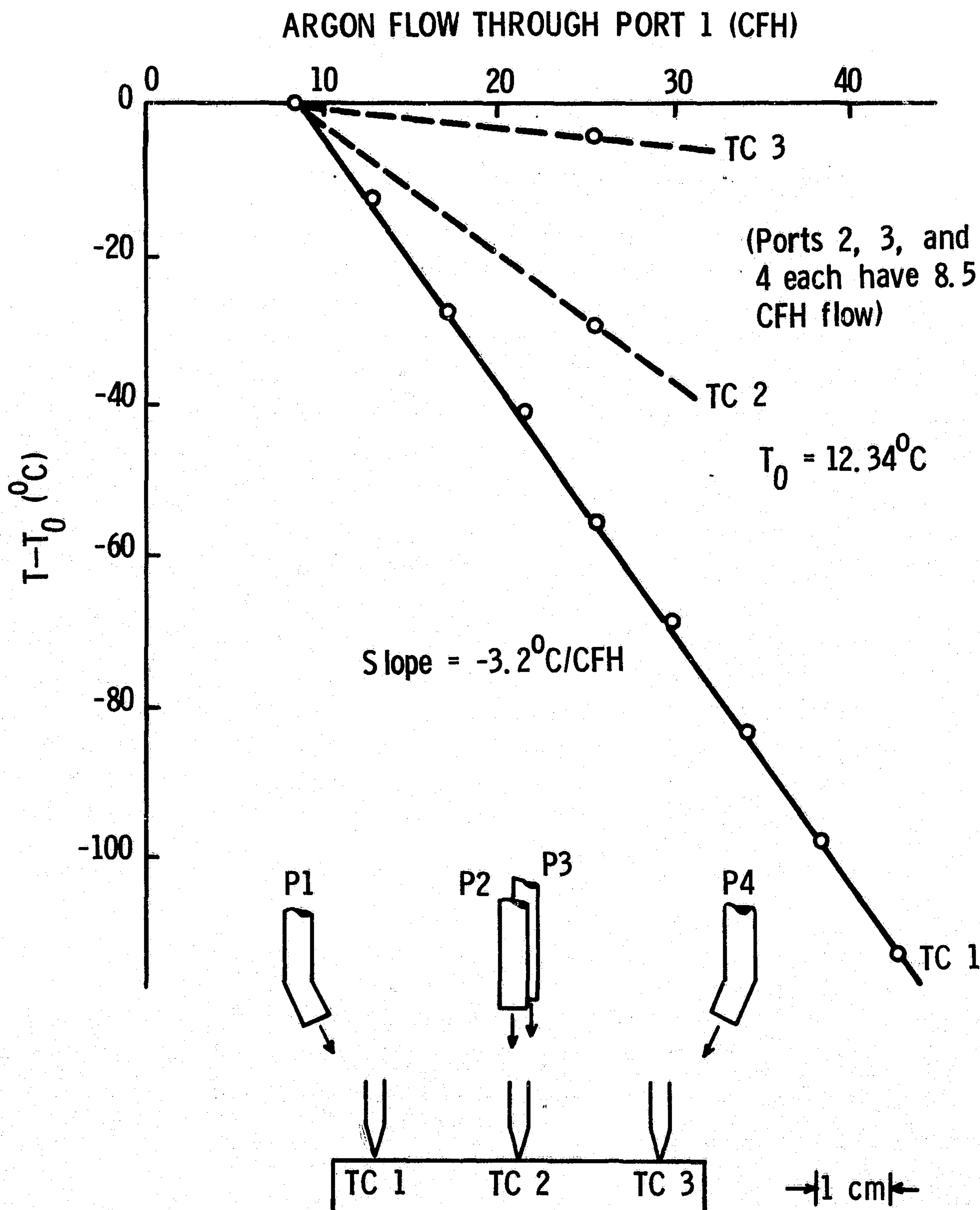

Fig. I-35. Temperature response of a ribbon furnace hot zone to argon flow changes.

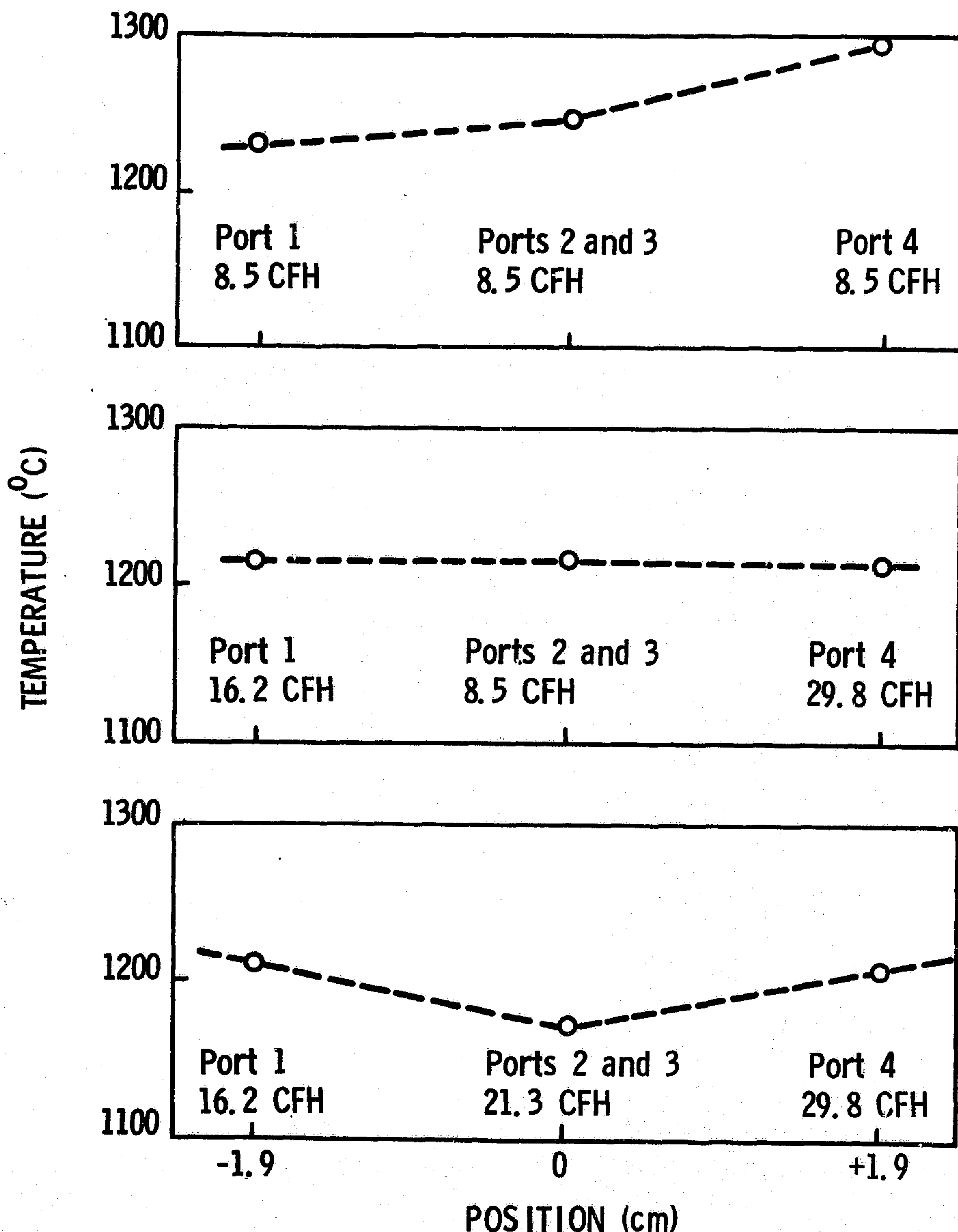

Fig. I-36. An asymmetrical temperature profile (top) can be flattened (middle) or symmetrically tailored (bottom) with the inert-gas system.

flattened to within less than ± 1°C. A symmetrical radially increasing profile could be obtained at flows: P1 = 16.2, P2 = 21.3 = P3, P4 = 29.8 CFH (bottom). Similarly, radially decreasing temperature profiles could be produced.

The system has provided the thermal control necessary for stable 38-mm-wide and 50-mm-wide ribbon growth, and has allowed full-width seeding of the ribbons. The geometrical response of a growing, 38-mm-wide ribbon to step changes in argon flow directed at one of its edges has been checked. The growth conditions were first stabilized by adjusting the argon flows, as necessary, to attain full-width growth with no tendency for the ribbon to drift toward either edge of the capillary action shaping technique die. Then a step decrease in argon flow (directed at one edge of the ribbon) of 0.85 CFH was applied and caused the ribbon width to decrease (at that edge) at a rate of 4.1 mm/min/CFH, nearly linearly. A subsequent increase in flow by 0.85 CFH, back to the original level, returned the ribbon to full width at a slower, non-linear average rate of 1.3 mm/min/CFH. The ribbon pulling speed was 14 mm/min.

Since the gas jets are directed at the growth region, it has been possible to use an open pulling port system and still retain clean ribbon surfaces of the type previously obtained

only with the closed bellows, top-to-bottom purged furnace system of Fig. I-15.

3.2 Physical Characteristics of 38 mm Ribbons

Implementation of the inert-gas thermal modifier and concomitant improved control over the thermal profile near the growth zone have allowed major improvements in 38-mm-wide ribbon growth. About 25 ribbons of average length 0.7 meter were grown with the system. The longest ribbon grown was 1.3 meters in length. Some ribbons have had SiC surface particle densities as low as $0.04/cm^2$ (counted over the entire ribbon) and good surface smoothness. These ribbons were dog-boned in cross-sectional shape, with edge thicknesses of about 0.5 mm (60% of the die top thickness at the edge) and central thicknesses of about 0.3 mm (20% of the central die top thickness). A transverse section of ribbon, No. 61016 was grown at 30 mm/min, was beveled at a 4.6° angle to illustrate the type of thicknesss variations present in the thinner ribbons (see Fig. I-37).

Stress levels in the 38-mm-wide ribbons do not appear to be any worse than in narrow ribbons. A stress of 4,000 psi was measured in one ribbon delivered to JPL[13]. Using a similar methodology (measurement of the split width as a

ORIGINAL PAGE IS
OF POOR

Fig. I-37. Deviations from flatness in ribbon 61016 (4.6^{o} bevel).

function of distance on a split ribbon as detailed in section 4.0), we measured a stress level of 3.5×10^{8} dynes/cm^{2} (3,900 psi) on a different ribbon. The results are in good agreement. Several ribbons have broken transversely during handling without longitudinal splitting.

Several 38-mm ribbons are pictured in Fig. I-38. As shown in the figure, straight ribbon growth can be maintained after making initial thermal adjustments with the inert-gas purge-jet system.

4.0 GROWTH OF 50 MM SILICON RIBBONS

4.1 Description of Experimental Apparatus

Since initial results in using a 2-piece die for 38-mm-wide growth were successful, the same design (Fig. I-31) was used in scaling up to a 50-mm growth system. A 0.8-1.2 mm die edge thickness and 1.8-2.0 mm central thickness with a

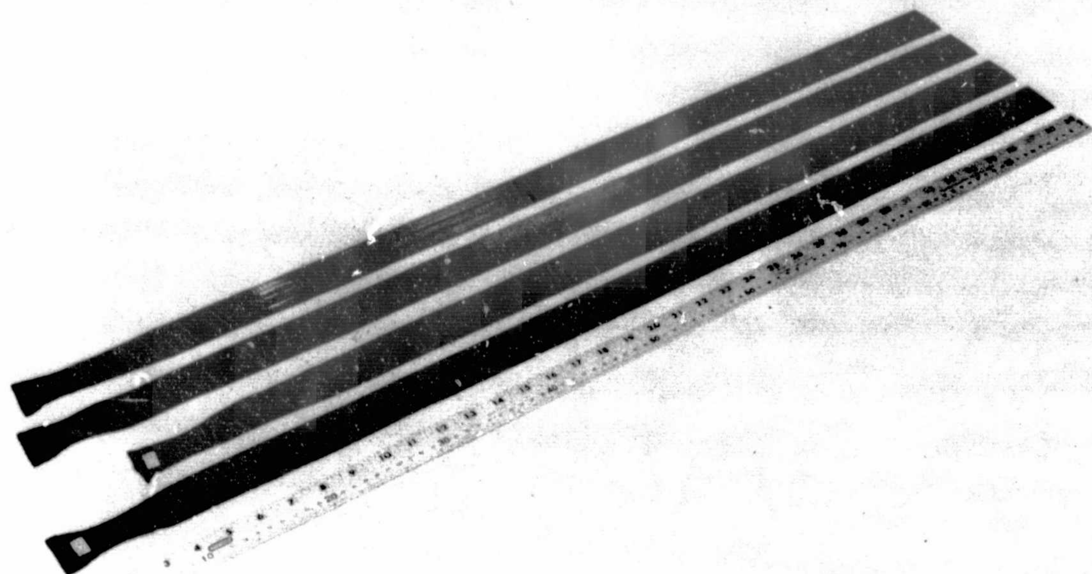

Fig. I-38. Four 38-mm-wide ribbons grown with inert-gas thermal trimming.

1.6-2.0 mm deviation from flatness (δ in Fig. I-1) were found to work well. A capillary channel thickness of 0.4-0.5 mm and a capillary rise height of $\leq$ 45 mm was used in all growth experiments

A 55-mm-ID x 38-mm-high flat-bottomed crucible was used; it accommodates a 150-gram silicon charge. The same die holder, shield, and susceptor designs which were used in the 38-mm system were also kept and scaled up in size for the 50-mm system. The furnace shell size was the same as for

12-38 mm ribbon growth. The inert-gas thermal control system shown in Fig. I-34 was used.

4.2 Meniscus Effects

ORIGINAL PAGE IS
OF POOR QUALITY

4.2.1 Meniscus Height Measurements

A technique was established for meniscus height measurement during 50 mm wide ribbon growth. The meniscus is photographed at a known viewing angle, θ, relative to the horizontal plane. For example, the meniscus of Fig. I-39 was photographed at an angle of 52-1/2°. The distance from

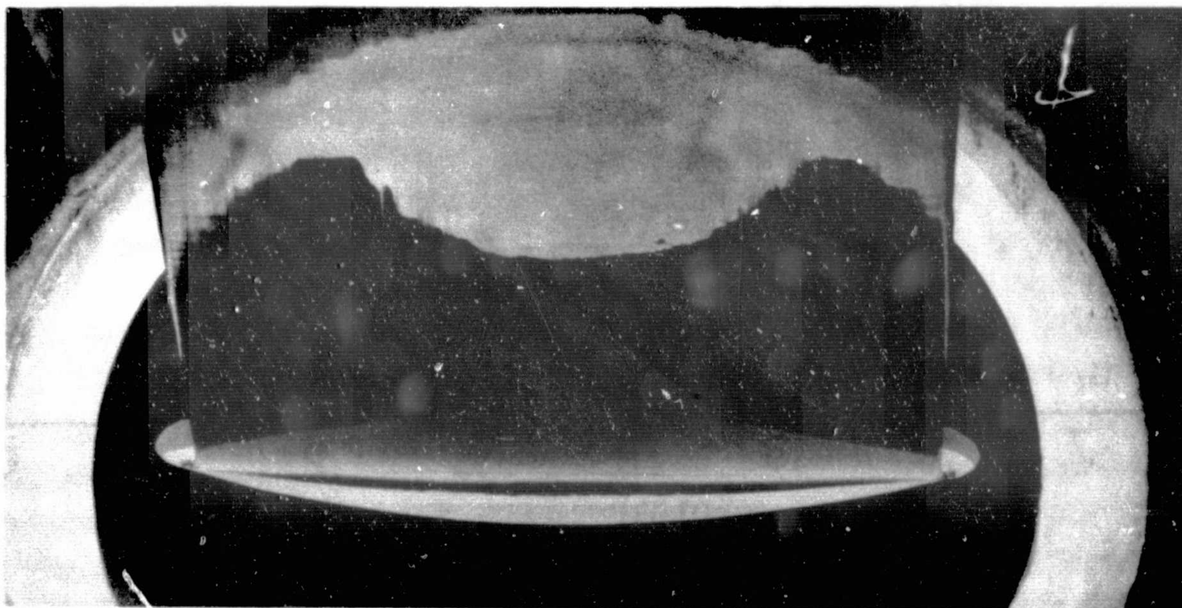

Fig. I-39. Meniscus photograph of ribbon 70410; width, 50 mm; speed, 19 mm/min.

the seed to the solid-liquid interface at the time of the photograph is noted. Then, after growth, the ribbon thickness, t_r, at the location photographed is measured. The die-top thickness, t_d, is measured prior to the growth run. The apparent meniscus height, m, is obtained from a densitometer scan of the photographic negative (Fig. I-40) using a Joyce, Loebl and Co. Ltd., double-beam recording microdensitometer model MK III CS. Once m, θ, t_r, and t_d are known, the meniscus height, h_m, can be obtained

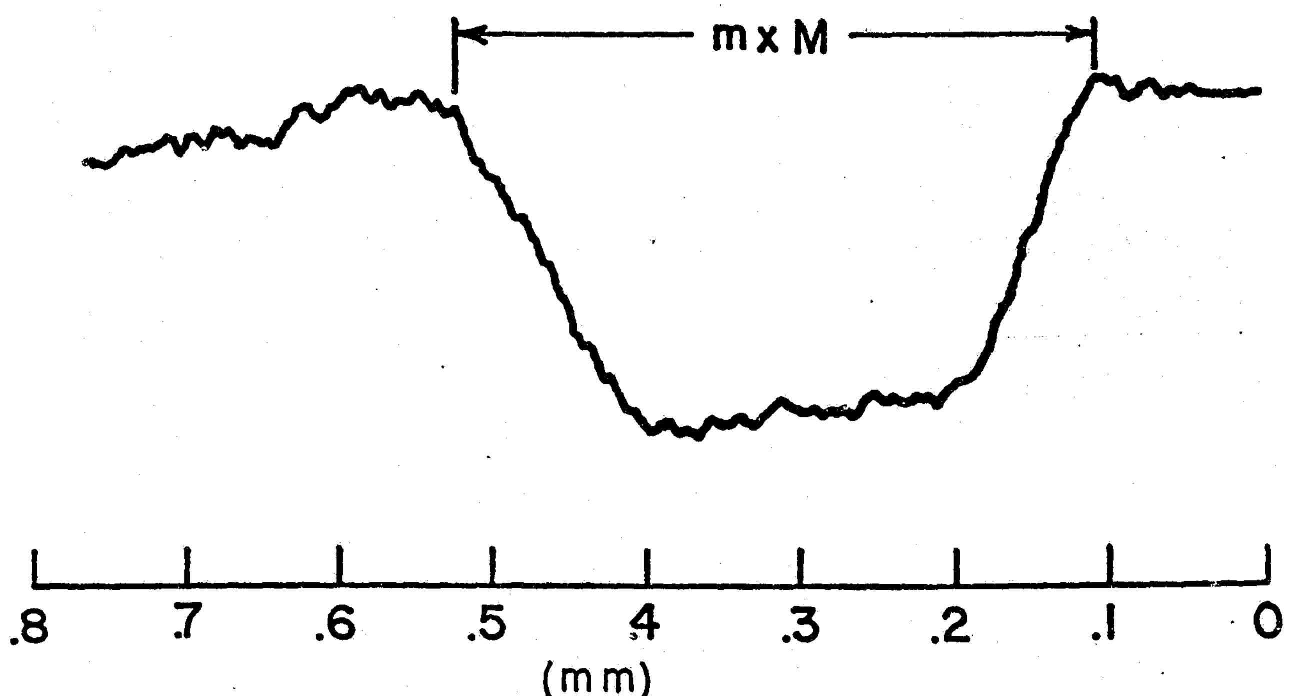

Fig. I-40. Densitometer scan of meniscus region on photographic negative. The apparent meniscus height m is obtained after dividing the scan distance across the meniscus by the magnification of the negative M (usually about 0.4).

graphically as shown in Fig. I-41. In this analysis, it is assumed that the ribbon grows at the geometrical center of the die-top as shown in Fig. I-41.

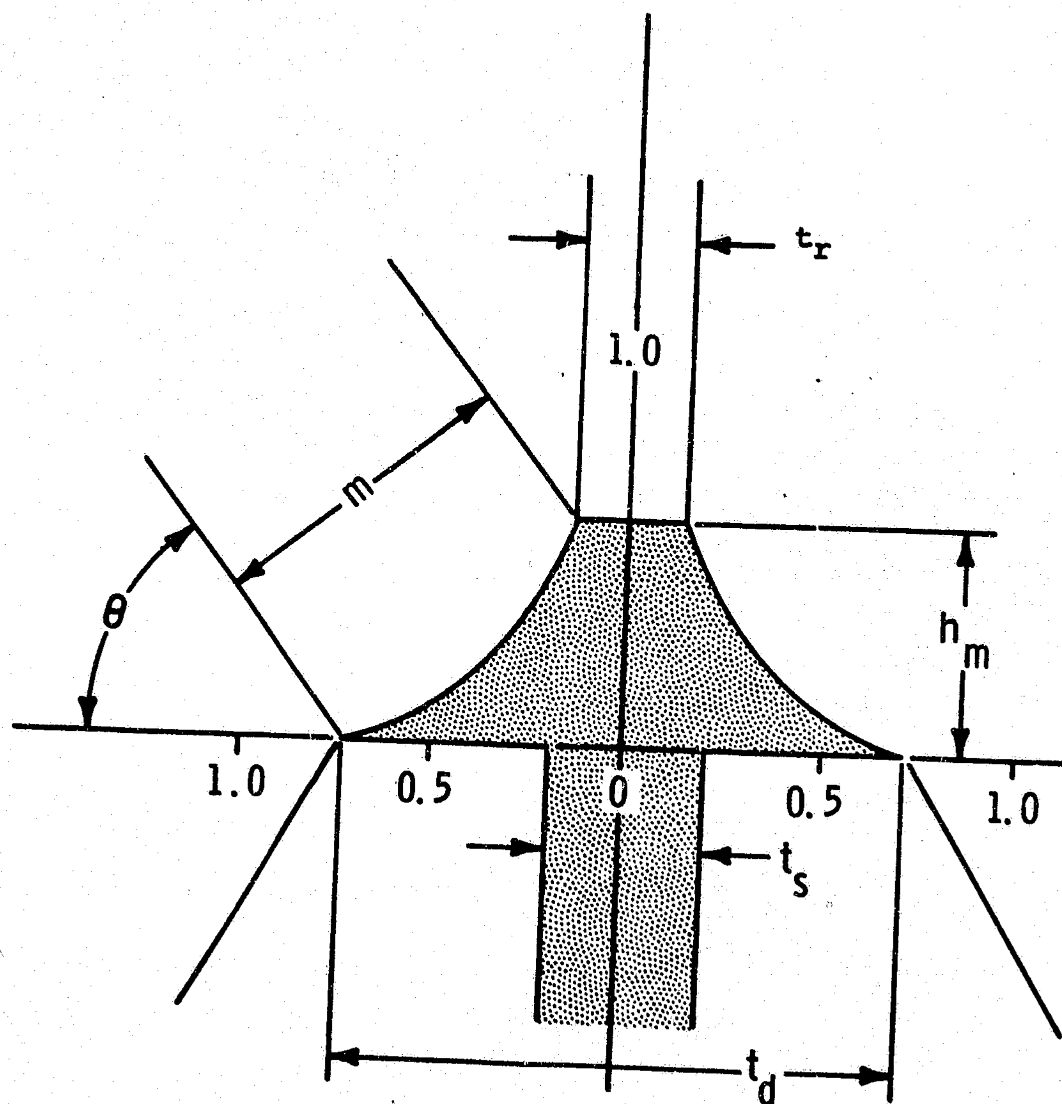

Fig. I-41. Meniscus configuration in CAST ribbons.

One series of measurements was made with a 50-mm-wide die having a 2.01 mm central thickness t_d, a 0.41 mm slot dimension t_s, a 0.84 mm edge thickness, and a 1.73 mm deviation from flatness of the die top (δ in Fig. I-41). The meniscus height h_m was found to increase from .53 mm to 0.75 mm as the central ribbon thickness decreased from .42 to .23 mm. The meniscus cross-sections for the two values of h_m are shown in Fig. I-42. At h_m = 0.75 mm, the ribbon is considered to be growing in the high melt meniscus mode of the capillary action shaping technique. For comparison, in the EFG growth technique the meniscus height is 9.06 mils (0.23 mm) for a 9.5 mil (0.24 mm) thick ribbon[11]. The factor of 3 increase in meniscus heights is a key advantage in obtaining smooth, low SiC particle density ribbons by the CAST method.

4.2.2 High Melt Meniscus (HMM) Growth

Growth run number 70103 is an example of high melt meniscus growth. In this run, a die with 1.2-mm edge thickness, 1.9-mm central thickness, and a 0.46-mm capillary slot was used. The radius of curvature at the die top was 267 mm. During growth at 19 mm/min, a high melt meniscus was maintained and the resultant ribbon had a number of desirable characteristics: it was thin (less than 0.27 mm

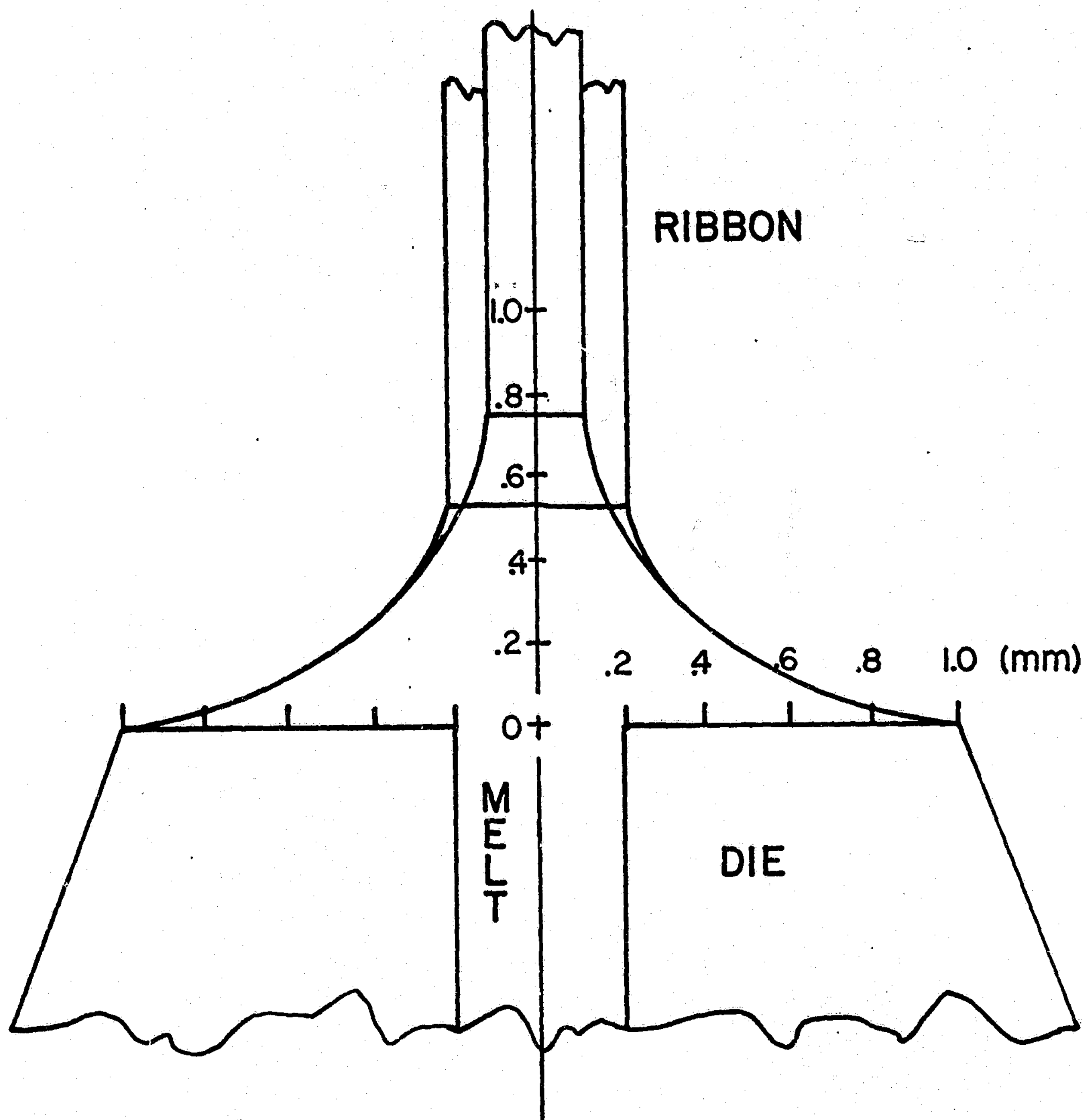

Fig. I-42. Meniscus cross-section for two valves of ribbon thickness, using a 2 mm central die, top thickness. At 0.75 mm meniscus height, the ribbon is considered to be growing in the high meniscus mode.

except for extreme edges), it had a "zero" SiC particle density over its entire length, it was shiny and highly reflective, and it possessed a larger grain morphology than previous ribbons had exhibited. Post-growth examination of the interface striations combined with a knowledge of the curvature of the die top indicates that the meniscus was at least 0.3 mm higher in the central region than at the edges of the growth front. We estimate that the meniscus height was on the order of 0.7 mm in the central region.

In Fig. I-43, die-top thickness, capillary slot thickness,

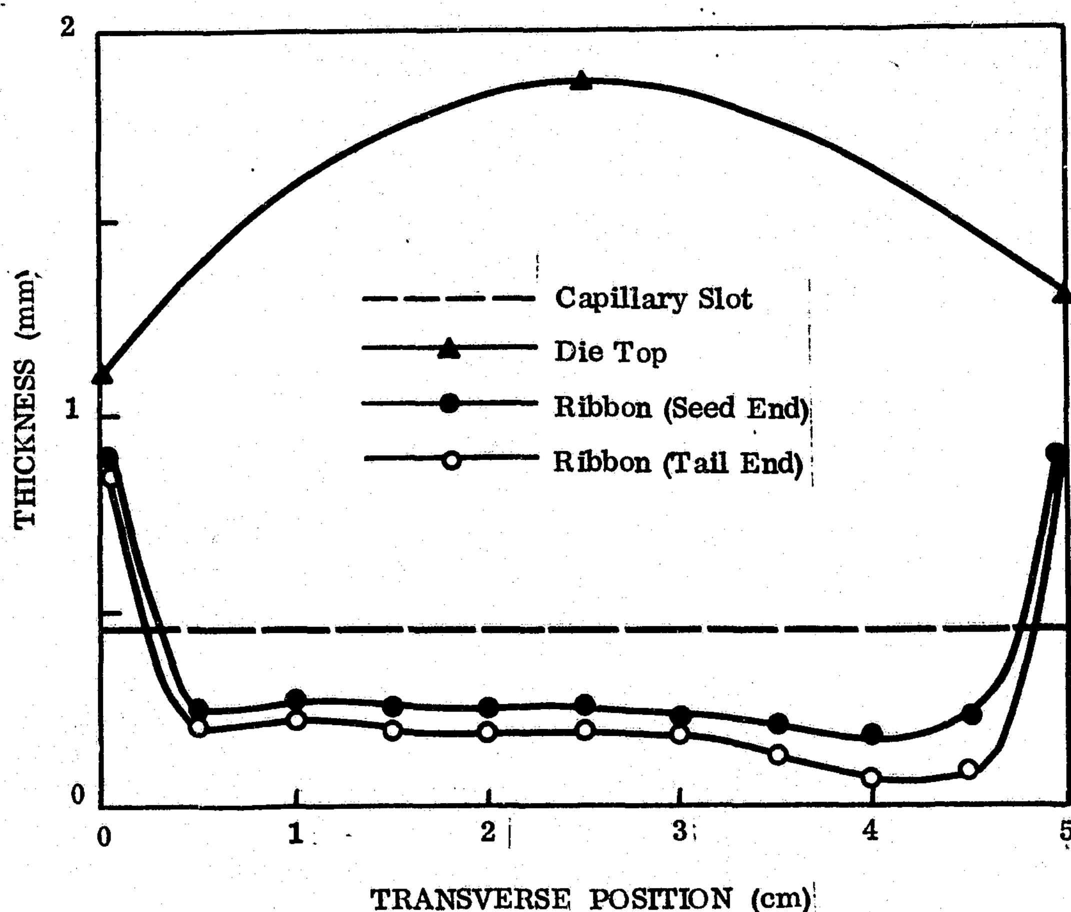

Fig. I-43. Thickness of die top, capillary slot, and ribbon as a function of transverse position for run 70103.

and ribbon thickness are plotted versus transverse position. The ribbon is relatively flat, except for several mm near each edge, and has a thickness of 0.15 x die thickness in the central region. It is thinner than the capillary slot dimension by 50%. These relative dimensions are shown schematically in Fig. I-44. In cross section the extreme edges of ribbon 70103 appear rounded with a radius of 0.38 mm as shown in Fig. I-45. At the cross-sectional position shown in the figure, a maximum thickness of 0.79 mm is reached at a distance of 0.67 mm from the ribbon edge.

The thickness gradually decreases to a uniform value of 0.16 mm at a distance of 4 mm from the edge.

Because of the very low SiC surface particle density, the ribbon surface is relatively free of longitudinal troughs often associated with such particles. Portions of the ribbon exhibited parallel twinning as shown in the central ribbon region of Fig. I-46. However, much of the surface exhibited large single grains of the order of 8 mm in width. Frequently these grains were separated by twins with a raised surface morphology at the twin-ribbon surface intersection. Examples can be seen near the edge of the ribbon in Fig. I-46. Magnified views of some large crystal grains are shown in Fig. I-47. In Fig. I-47(a), a grain is

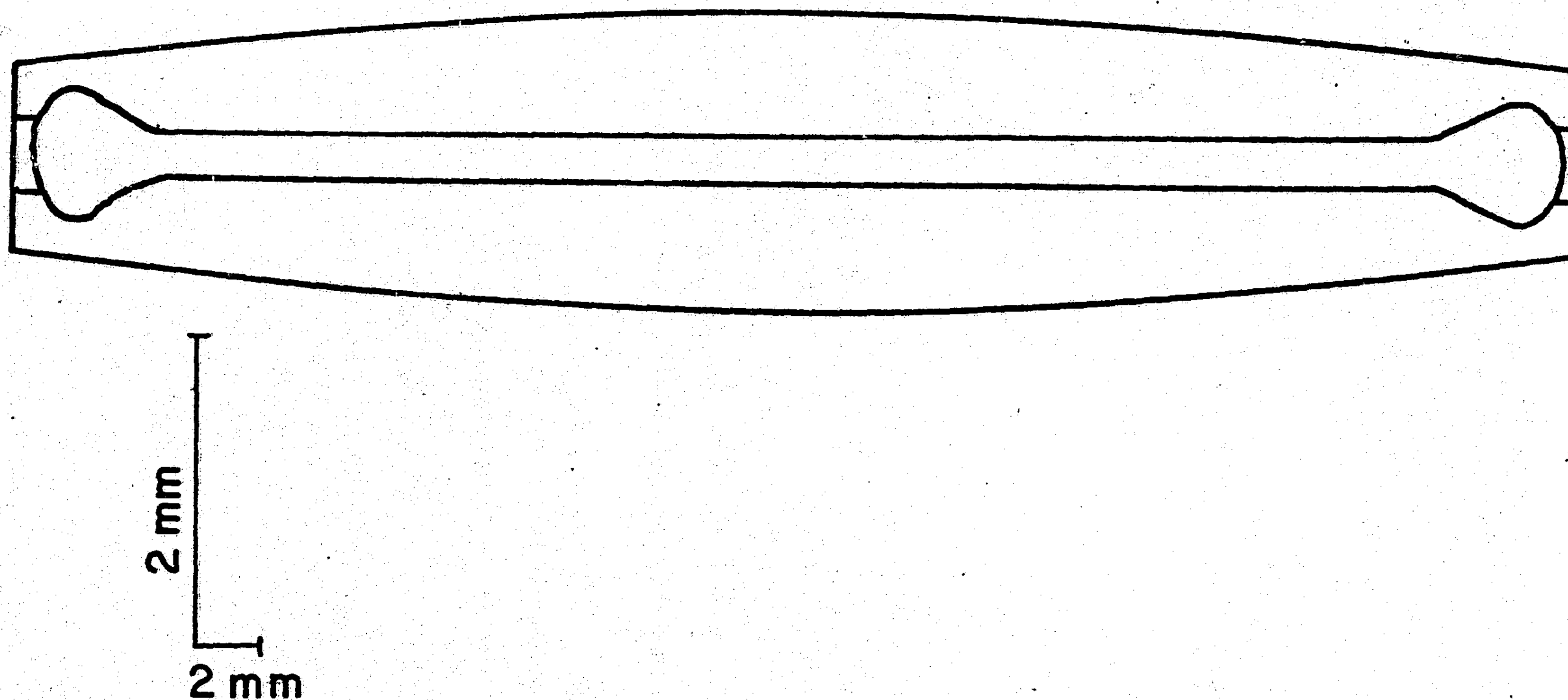

Fig. I-44. Top sectional view, drawn to scale, of the die top and the silicon ribbon during capillary action shaping technique growth in the high melt meniscus mode.

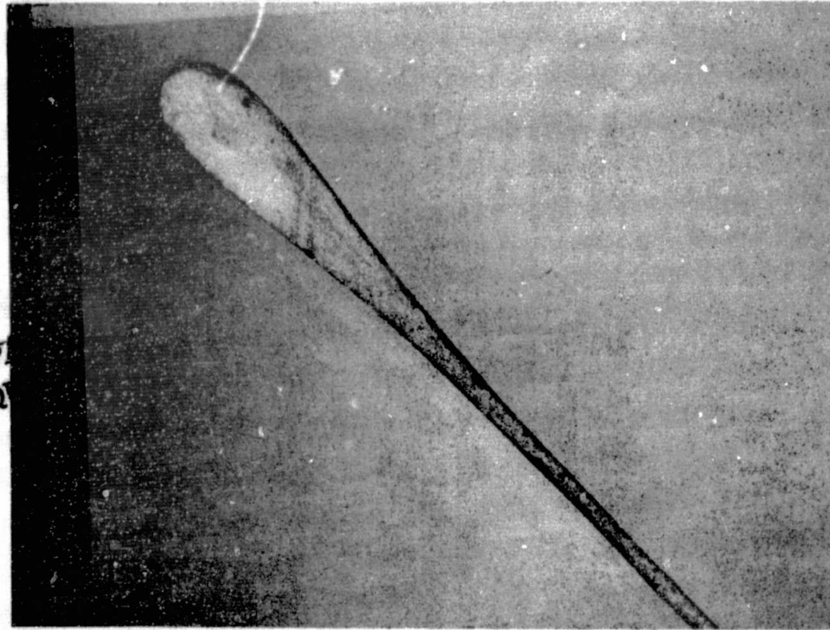

ORIGINAL PA
OF POOR Q

Fig. I-45. Cross section of ribbon 70103-42 near an edge. The maximum thickness is 0.79 mm, and the minimum is 0.16 mm.

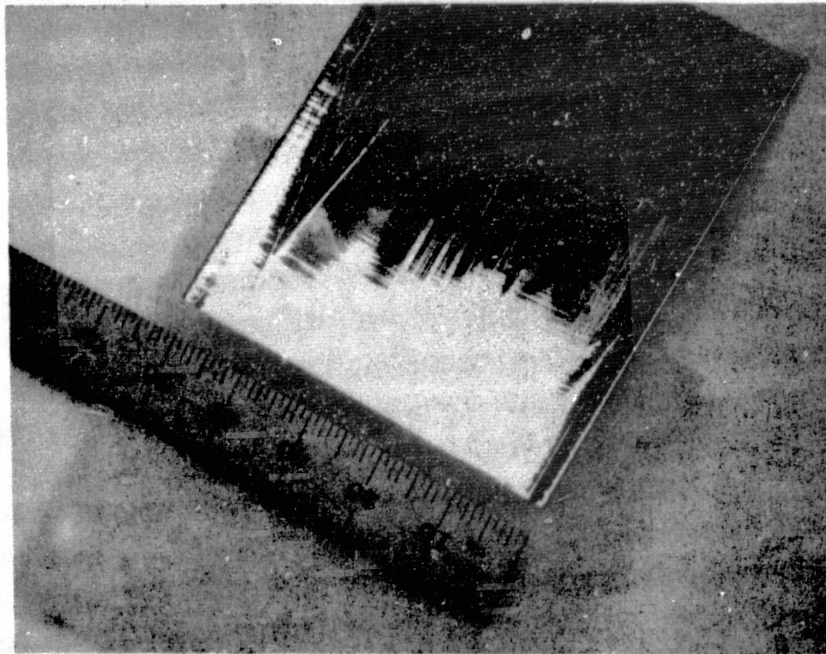

Fig. I-46. High melt meniscus ribbon section 70103-42.

shown which has a nearly flat twin boundary on one edge (left) and a partially raised, partially flat boundary on another edge (upper right).

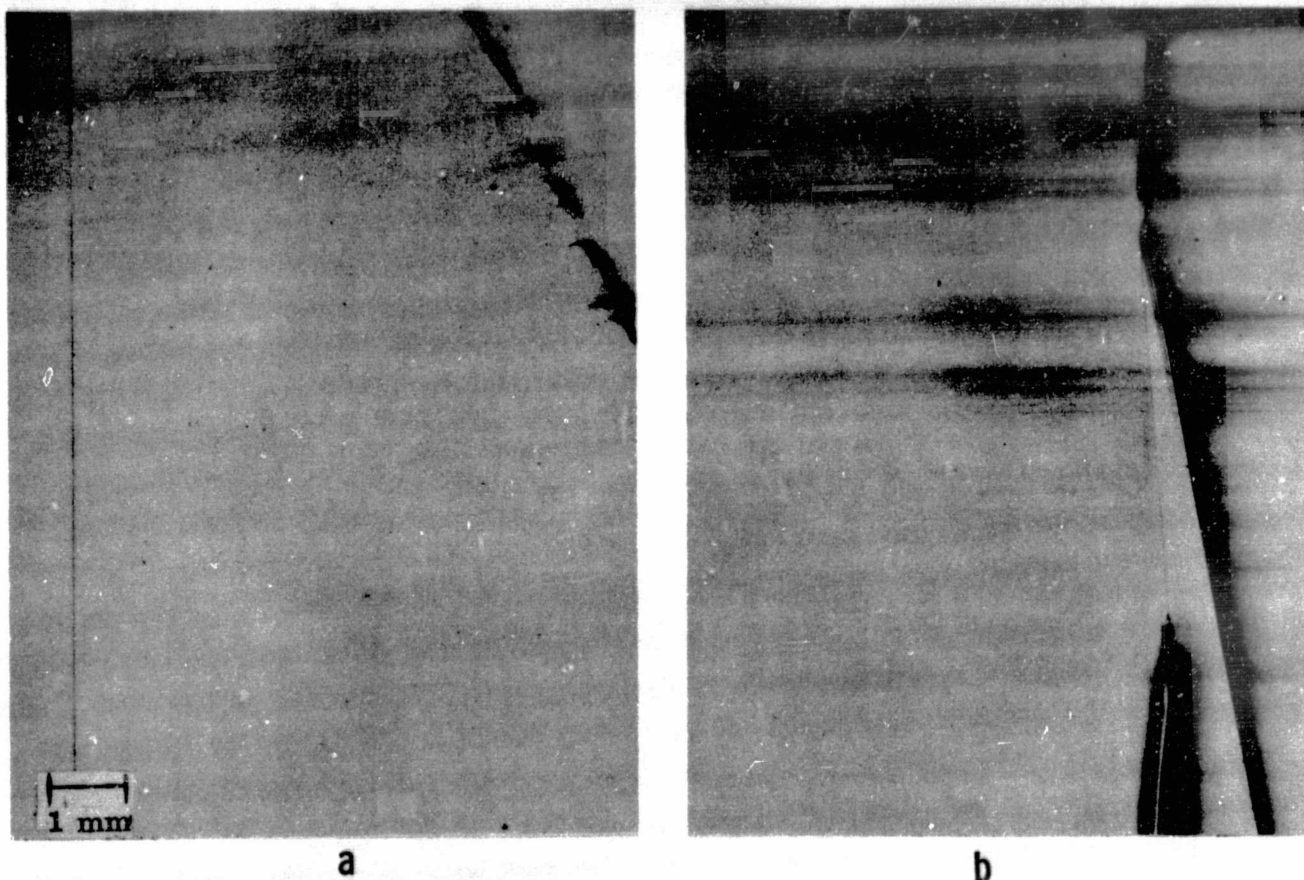

Fig. I-47. Large single-crystal grains in HMM ribbon 70103-42.

In Fig. I-47(b), some twin boundaries are shown which have a prominent, raised-surface morphology. A transverse surface profile scan was recorded (left to right) over the region of the two prominent boundaries at the lower right of Fig. I-47(b). The most prominent (leftmost) boundary had a peak

height of 28 μm, as shown in Fig. I-48, and its influence extended a distance of 1.1 mm from the peak. The rightmost boundary had a peak height of 9 μm and influenced the surface height within 0.7 mm of the peak.

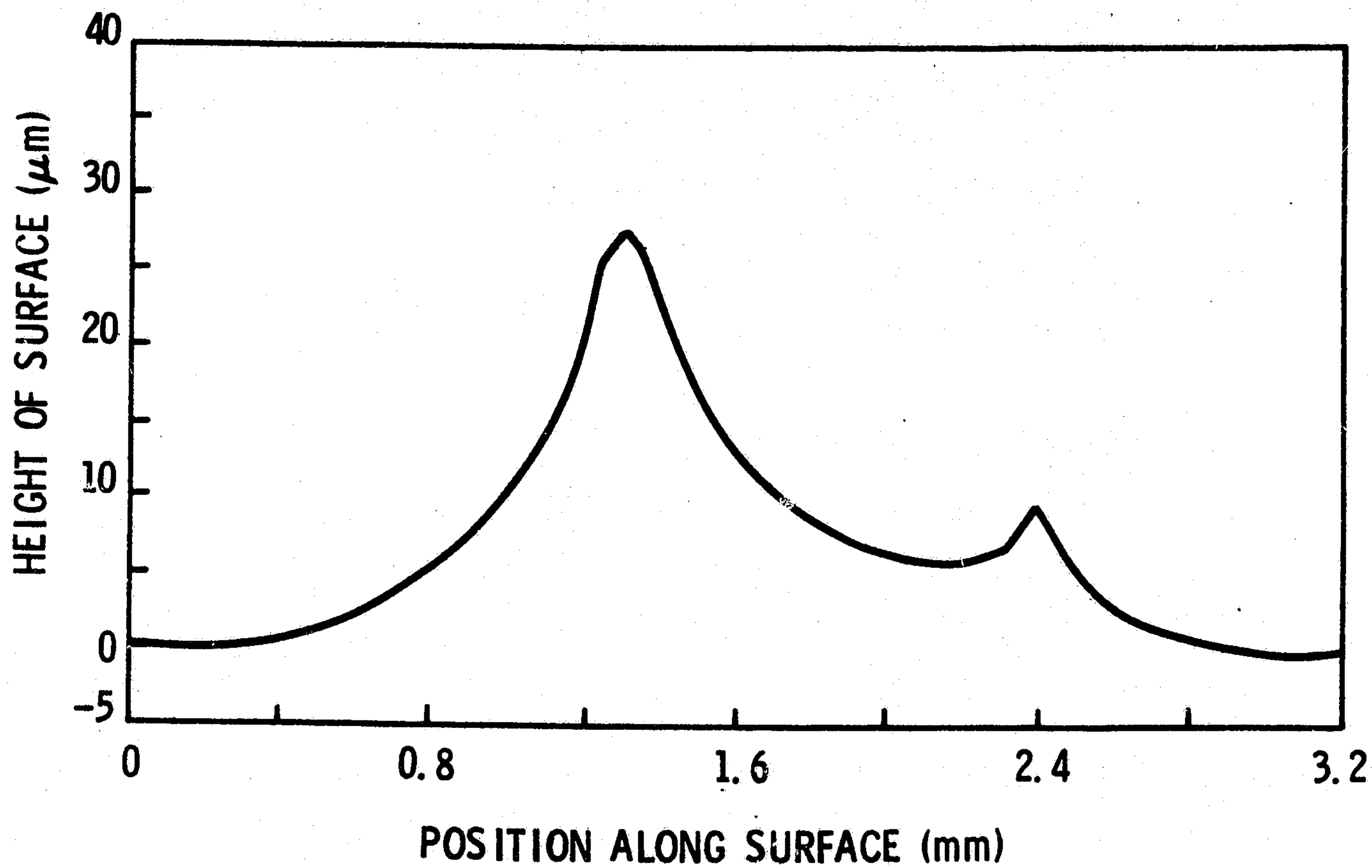

Fig. I-48. Surface profile scan over the two raised-morphology twin boundaries at the lower right of Fig. I-8b.

The single-crystal nature of one particular grain, 8 mm x 27 mm in size, from ribbon 70103 was verified by x-ray topography; the topograph is shown in Fig. I-49. This grain is encompassed by a largely nonlinear boundary.

Fig. I-49. X-ray topography of 8 mm x 27 mm single-crystal grain in ribbon 70103-42.

About 45 ribbons of 50 mm width were grown. An example is shown in Fig. I-50. Minimum thicknesses ranged from 0.09 to 0.82 mm, and maximum thicknesses ranged from 0.17 to 1.10 mm. The fastest growth rate attained to date was for ribbon 70411. The thickness was 0.15 mm at a 4-cm/min growth rate.

Two additional materials were used for 50 mm CAST growth. One is Ultracarbon UT-44 graphite (runs 70407-70412). The

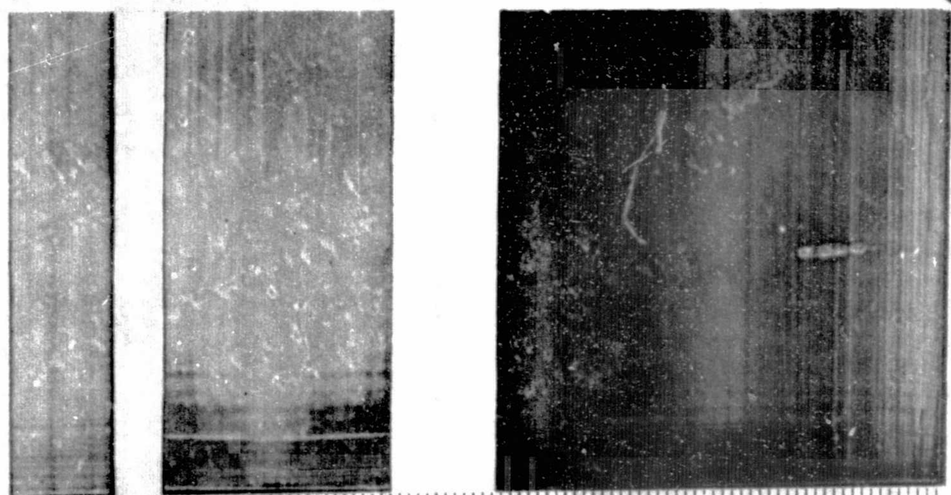

Fig. I-50. A 50-mm-wide by 109-cm-long silicon ribbon grown by the capillary action technique. The insert shows progression in sizes from 12- to 25- to 50-mm-wide ribbons.

ORIGINAL PAGE IS OF POOR QUALITY

other is an impervious SiC-coated die using Ultracarbon UT-86 graphite as a substrate.

4.3 Evaluation of an SiC-coated Graphite Die

The primary objective of growth runs 70413 through 70604 was to monitor the performance of a single SiC-coated graphite die. The graphite grade was Ultracarbon UT-86, and the impervious SiC coating was applied by the manufacturer. The die has been used for 24 growth attempts in 14 melt-down cycles and has produced 17 ribbons of total length 13.1 meters. The SiC particle density for individual consecutive ribbons and also the accumulative density (total SiC particles/total area grown) are summarized in Fig. I-51. The accumulative SiC particle density was $1.3 \times 10^{-3}/cm^2$ after $2 \times 10^3/cm^2$ of ribbon had been pulled and rose to $9 \times 10^{-3}/cm^2$ after $4.5 \times 10^3/cm^2$ of ribbon had been grown from the die. After $6.5 \times 10^3/cm^2$ of growth, the accumulative particle density was $1.6 \times 10^{-2}/cm^2$. The rise in accumulative particle density is largely due to two ribbons which had abnormally high densities of $7.1 \times 10^{-2}/cm^2$ and $1.3 \times 10^{-1}/cm^2$. One of these occurred during run 70601 in which the graphite heat shields were replaced.

Discounting the two high density ribbons, the accumulative SiC particle density was $3.7 \times 10^{-3}/cm^2$. Another way of

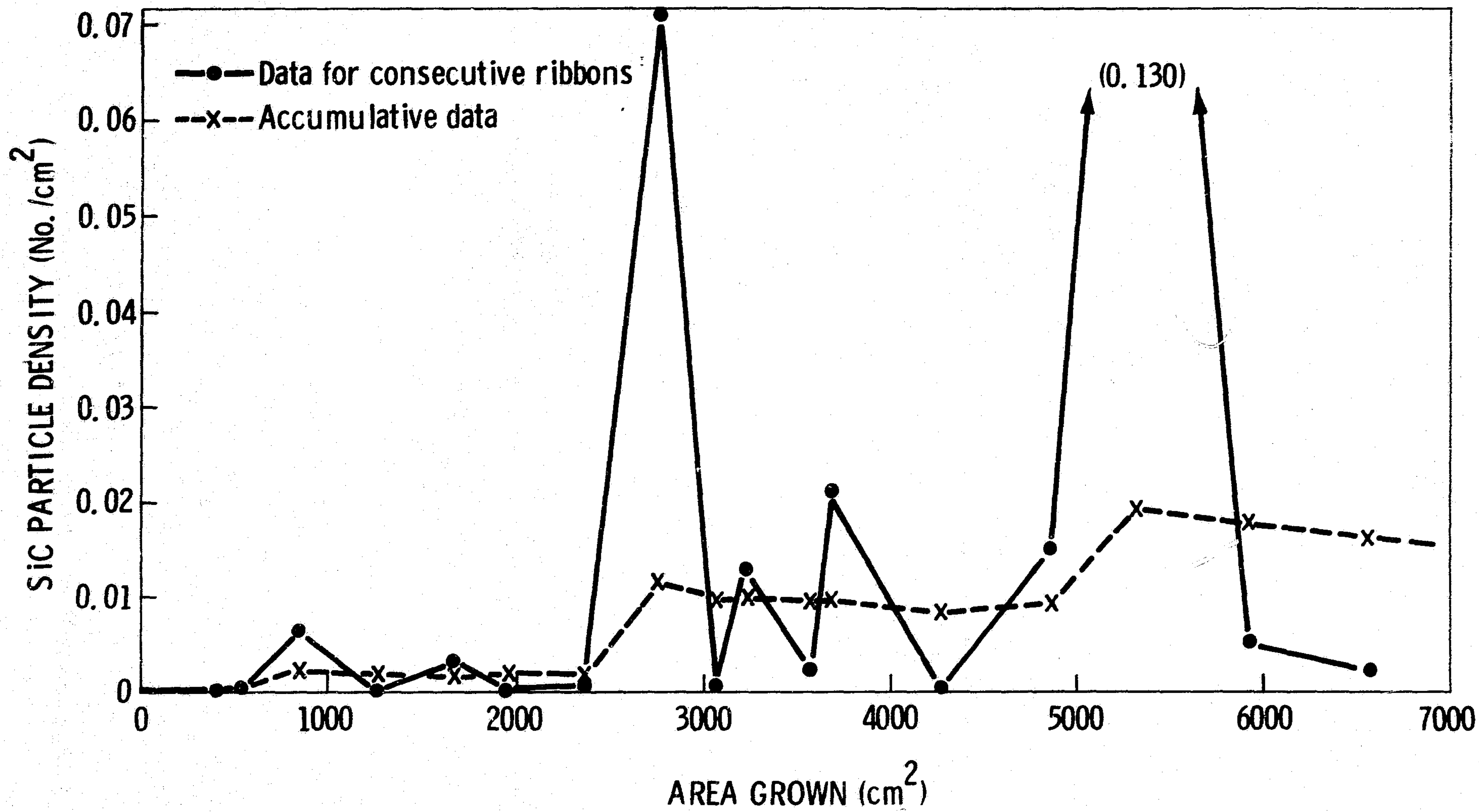

Fig. I-51. Silicon carbide particle densities for 17 ribbons grown from a single SiC-coated graphite die.

expressing this result is that, on the average, one particle occurred after each 0.54 meter of growth.

A statistical break-down of the die's performance is given in Table I-5.

TABLE I-5. Statistical Break-down of SiC Particle Pick-up with SiC-coated Die

Range of total SiC particle Count	No. of ribbons with particles in the range	Area of ribbons with particles in the range	Percentage of Total area grown
0-60	17	6575	100
0-30	16	6120	93
0-10	15	5740	87
0- 2	13	4535	69
0	7	2570	39

SiC particle densities of $< 3 \times 10^{-2}/cm^2$ are not unusual in the CAST growth configuration with graphite dies, and upon occasion a ribbon is grown with no particles - particularly when a very high melt meniscus is maintained. However, the large number of ribbons with zero or ≤ 2 particles seen with the SiC-coated die has not been encountered before with graphite dies. The difference in particle pick-up between graphite and SiC-coated graphite dies is not thought to be related to a difference in solubility. The dissolution[12] and solid contamination[2] characteristics of SiC and C in

silicon have been shown to be similar. The difference may be due to the nature of the nucleation sites for crystallization of excess SiC from the carbon-saturated liquid silicon at the SiC die top. If the SiC die material promotes better epitaxial adherence of SiC grown from solution than does graphite, then less free particulate SiC would be available in the meniscus region for incorporation in the growing ribbon. This concept has neither been verified nor disproved, as yet.

4.4 Dopant Distribution in 50 mm Ribbons

In sections 2.4.3 and 3.1.1, studies of spreading resistance on narrow silicon ribbons grown from various die configurations were reported. It was shown that open-channel dies (2-piece design) produce the most uniform transverse ribbon dopant distribution in 38 mm wide ribbons although a central band of higher dopant concentration still tended to be present as shown in Fig. I-31. We have done similar measurements on a 50 mm ribbon grown from a 2-piece die and still find an enhanced dopant region in the near-central area of the ribbon. See Fig. I-52. The transverse measurements were made on a lapped, 4.67^{o} bevel surface extending across the width of the ribbon. The variation of spreading resistance with depth into the ribbon

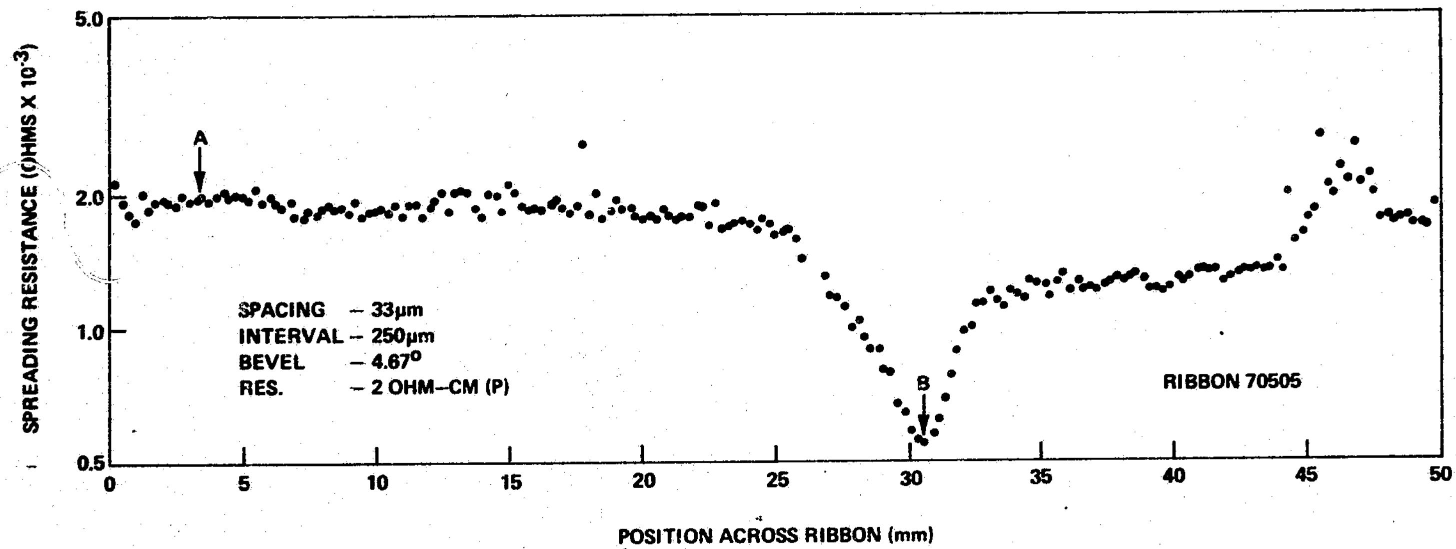

Fig. I-52. Spreading resistance measurements on a 50-mm-wide ribbon grown from a two-piece die.

was checked by making measurements down the bevel both near a high resistivity region (point A of Fig. I-53) and a low resistivity region (point B). In both cases, excellent uniformity was observed in the thickness dimension as can be seen in Figs. 53 and 54.

4.5 Stress Levels in 50 mm Ribbons

Since breakage of 50 mm ribbons during sawing has been a problem, runs 70506-70510 a few runs were made with thermal modifiers near the ribbon edges to see if residual stress levels could be lowered. Stress levels were determined by splitting the ribbons at the tail-ends and measuring the split width, s, as a function of distance, L, from the tip of the wedge-shaped crack or split opening. This was also done for several thin older ribbons not grown with thermal modifiers. Stresses were calculated in two ways. One method, suggested by M. Leipold[13], is to use the expression

$$\sigma = \frac{W\,Y\,s}{4L^2} \qquad (1)$$

where σ is the stress in dynes/cm^2, W is the ribbon width, and Y is Young's modulus [1.9×10^{12} dynes/cm^2 for (111) silicon]. Generally, maximal values of L were used. The

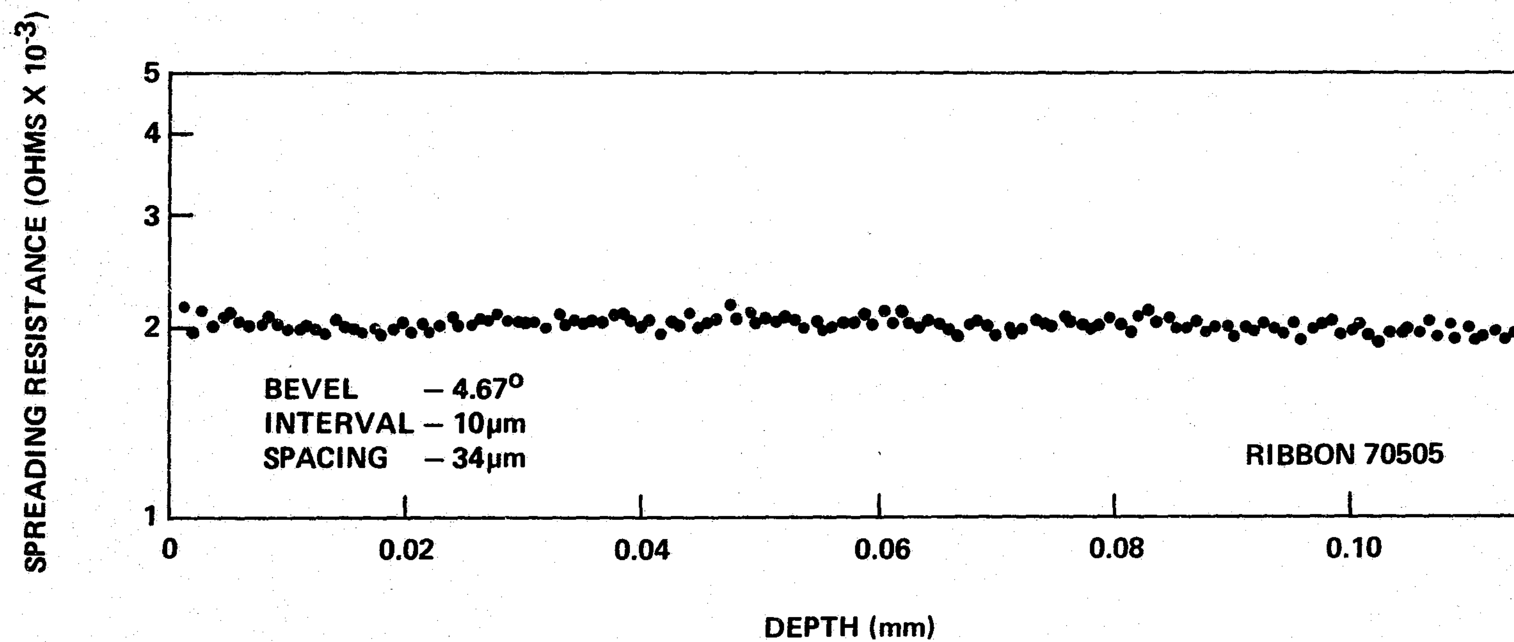

Fig. I-53. Spreading resistance as a function of depth into ribbon, measured, on bevel. Location of measurements corresponds to Point A on Fig. I-52.

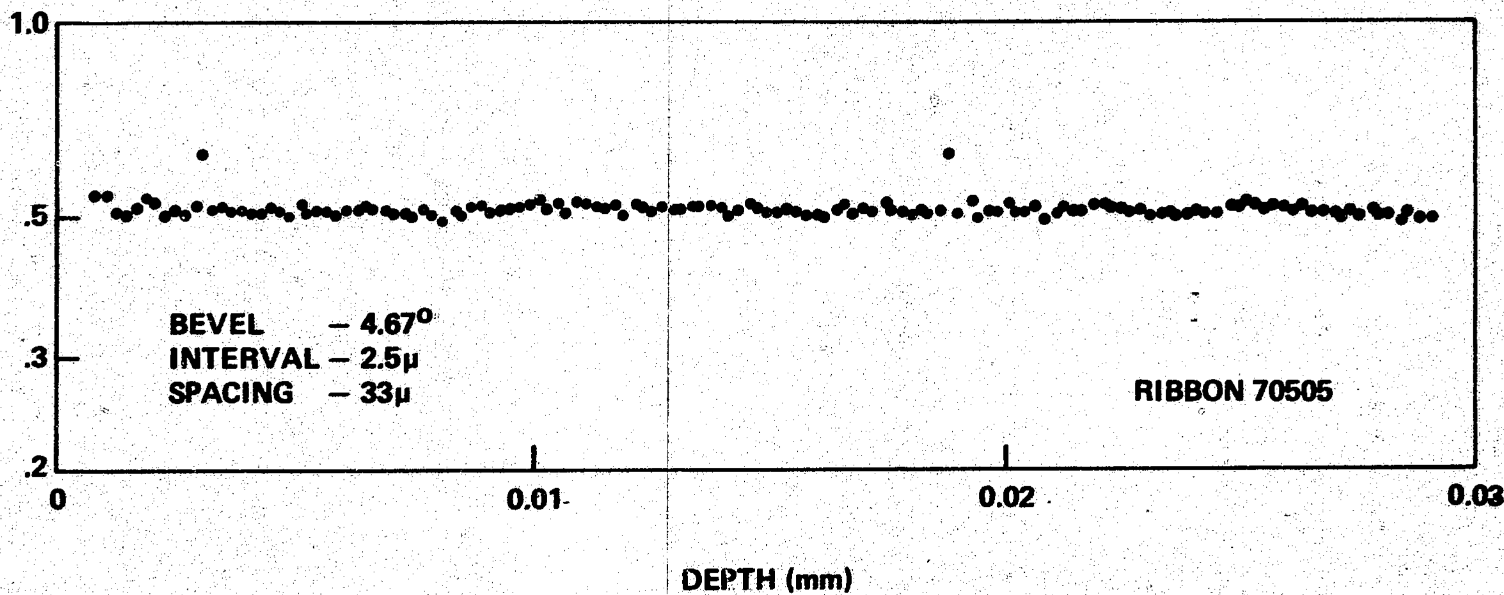

Fig. I-54. Spreading resistance as a function of depth into ribbon, measured on bevel. Location of measurements corresponds to Point B on Fig. I-52.

second method was to find the seven coefficients for a sixth-order polynomial least-squares fit for s vs L. The first and second derivatives ds/dL and d^2s/dL^2 were then evaluated, and the stress was calculated, as an average, over all values of L of the expression

$$\sigma = \frac{WY \quad d^2s/dL^2}{4\ [1 + (ds/dL)^2]^{3/2}} \qquad (2)$$

as proposed by Hurley and Pollock[14]. The second method is very sensitive to the accuracy of the s-vs-L measurements and to the shape of the least-square-fit curve and gives generally larger and less consistent values. The results obtained are given in Table I-6.

TABLE I-6. Stress Values in Silicon Ribbons

Ribbon No.	$\frac{W\ Y\ s}{4L^2}$ (dynes/cm²)	$\frac{WY\ d^2s/dL^2}{4\ [1 + (ds/dL)^2]^{3/2}}$ (dynes/cm²)	W (cm)	Minimum Thickness (mm)	Growth Speed (mm/min)
70308	2.7×10^8	5×10^8	4.95	.14	23
70417	3.7×10^8	6×10^8	4.95	.09	20
70508	4.8×10^8	---	4.4	.95	16
70509	3.5×10^8	7×10^8	4.7	.50	16

Ribbons 70508 and 70509 grown with the thermal modifier could not be brought to full width (hence they are thicker because of the CAST growth geometry). Their stress levels were no lower than those of the normally grown ribbons. All stress levels measured were moderate and of comparable magnitude to those seen in 25- and 38-mm growth.

Even though measured stress levels in 50-mm-wide ribbons are only moderate, considerable breakage occurs when they are sawed into sections. A technique developed by F. Newman has reduced the saw breakage. The ribbon is intimately waxed to a lava substrate which has previously been waxed (with a higher-temperature wax) to an aluminum support bar. The bar can be mounted in a vise on a Micro-Mech. diamond sawing machine. A 7.6-cm-diameter x 0.19-mm-thick blade is used at 450 RPM and at a lateral travel rate of 3 cm/min. The key to reducing breakage appears to lie in not cutting through the entire ribbon thickness in a single pass. Rather, the cut is made in several passes with a 0.25-mm increase in depth per pass.

5.0 GROWTH OF 100 MM SILICON RIBBONS

5.1 Description of Experimental Apparatus

It was necessary to construct a new furnace chamber for 100

mm ribbon growth. The chamber was designed to fit the hydraulic puller which had been used for 50-mm growth and it utilizes the same vacuum system. The design consists of a clear uncooled quartz chamber fitted with cooled metal endplates. RF heating with an exterior coil is used although provisions are made for an interior smaller coil if necessary. The hot-zone and pulling port will accommodate a 100-mm maximum width. Numerous inert-gas, electrical, and sensor feed-throughs are provided for versatility.

The sizing of the hot-zone components is as follows:

ITEM	Max OD (mm)	Min ID (mm)
Crucible	113	108
Susceptor	138	115
Insulation	170	145
Furnace Shell	193	181

Because susceptor cracking during cool down had been an occasional problem in the 50 mm system, two steps were taken to prevent cracking in the 100 mm system. The crucible, which had been a flat-bottom type in the 50 mm system, was given a 305 mm (12 inch) radius bottom. The design is shown in Fig. I-55. The crucible capacity is 500 grams. Another crack-prevention feature is the 2-piece susceptor (items 33

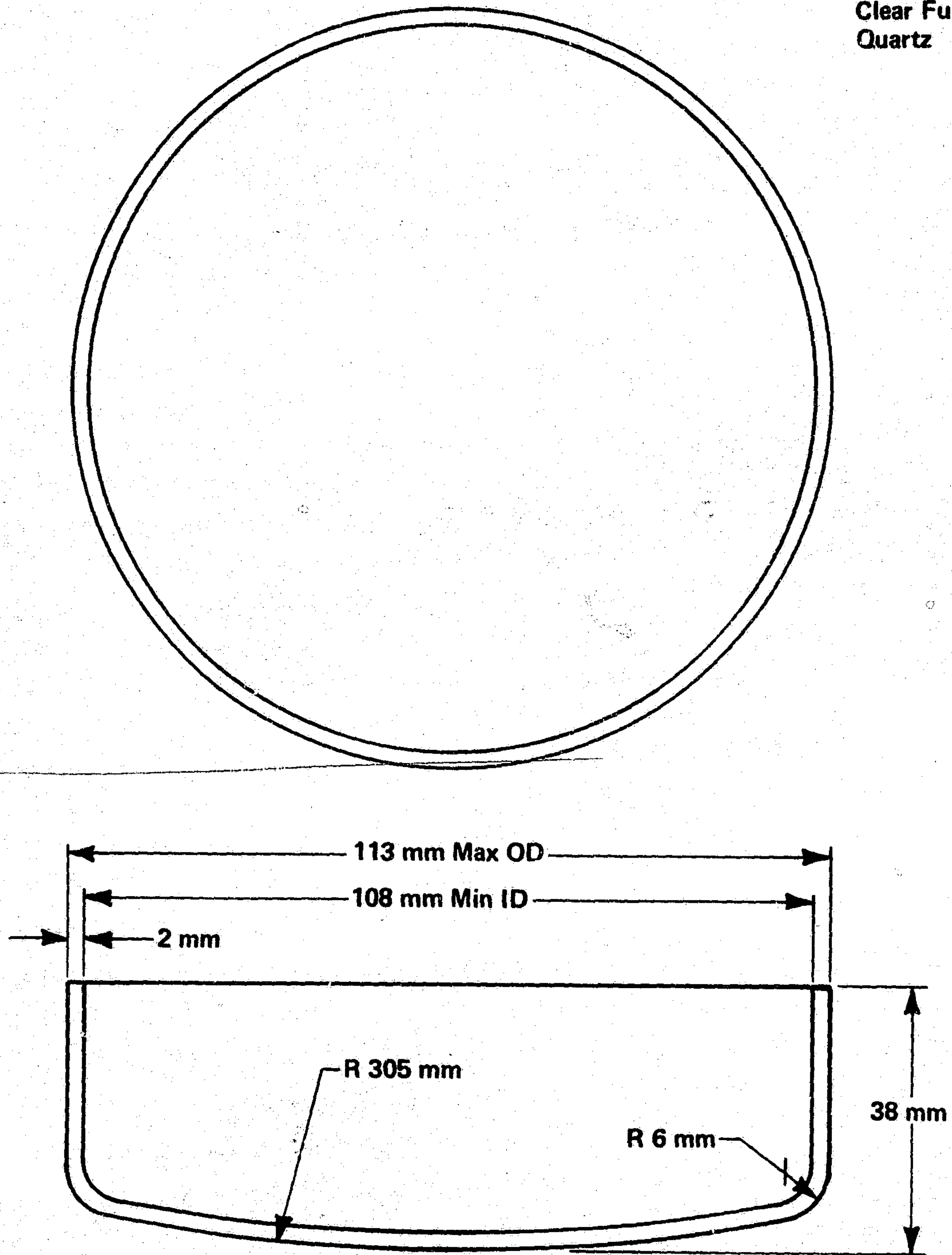

Fig. I-55. Crucible for 100-mm ribbon furnace.

and 34 in Figure 56). The cylindrical wall can separate from the susceptor base during cool-down in lieu of cracking. The graphite hot-zone components have been durable, with the exception of the pedestal support (item 31, Fig. I-56) which tends to crack at the bottom, where it is threaded into the furnace base plate (item 3).

The assembled furnace with the quartz bell jar for vacuum bake out (item 2) in place, but without the exhaust port (item 9) is depicted in Fig. I-57. For size comparison, the furnace shell which had been used for 12-50 mm ribbon growth is also included in the figure.

5.2 100 mm Growth Experiments

In first tests of the 100 mm system, a 210 mm ID x 228 mm long, twelve-turn RF coil was used to outgas the graphite hot-zone components in vacuum. An RF generator power level of 34 kW (3.5 amps at 9.8 kV) was required to heat the system to 1510°C. In comparison, 9 kW was the power level required for the 50 mm system. When ribbon growth was attempted, in an argon ambient, ionization occurred before the growth temperature could be reached. The ionization occurred in the annular space between the quartz furnace shell and the thick-walled quartz insulator. An attempt to

Fig. I-56. Assembly drawing of 100-mm CAST ribbon growth system.

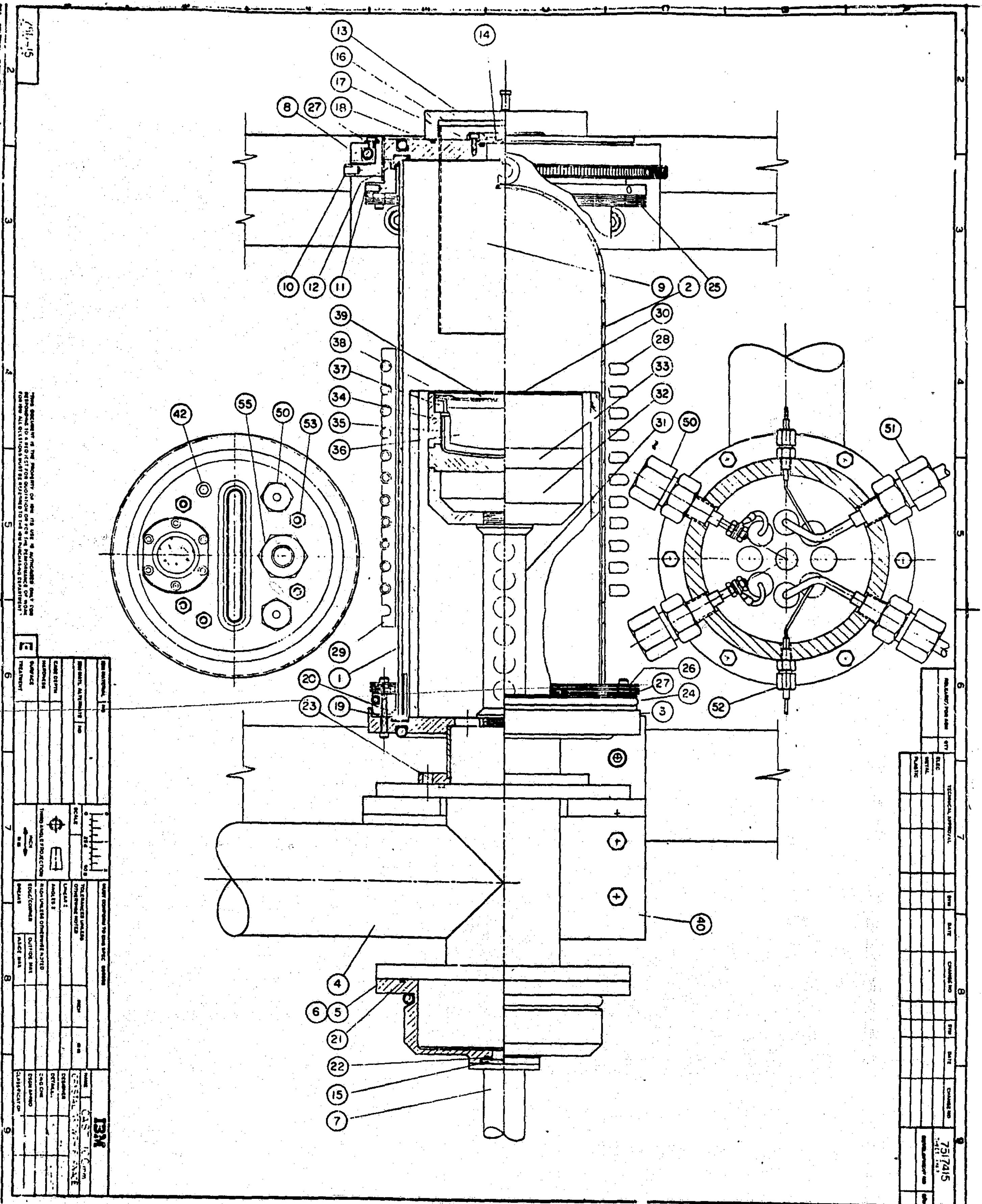

Fig. I-56. Assembly drawing of 100-mm CAST ribbon growth system.

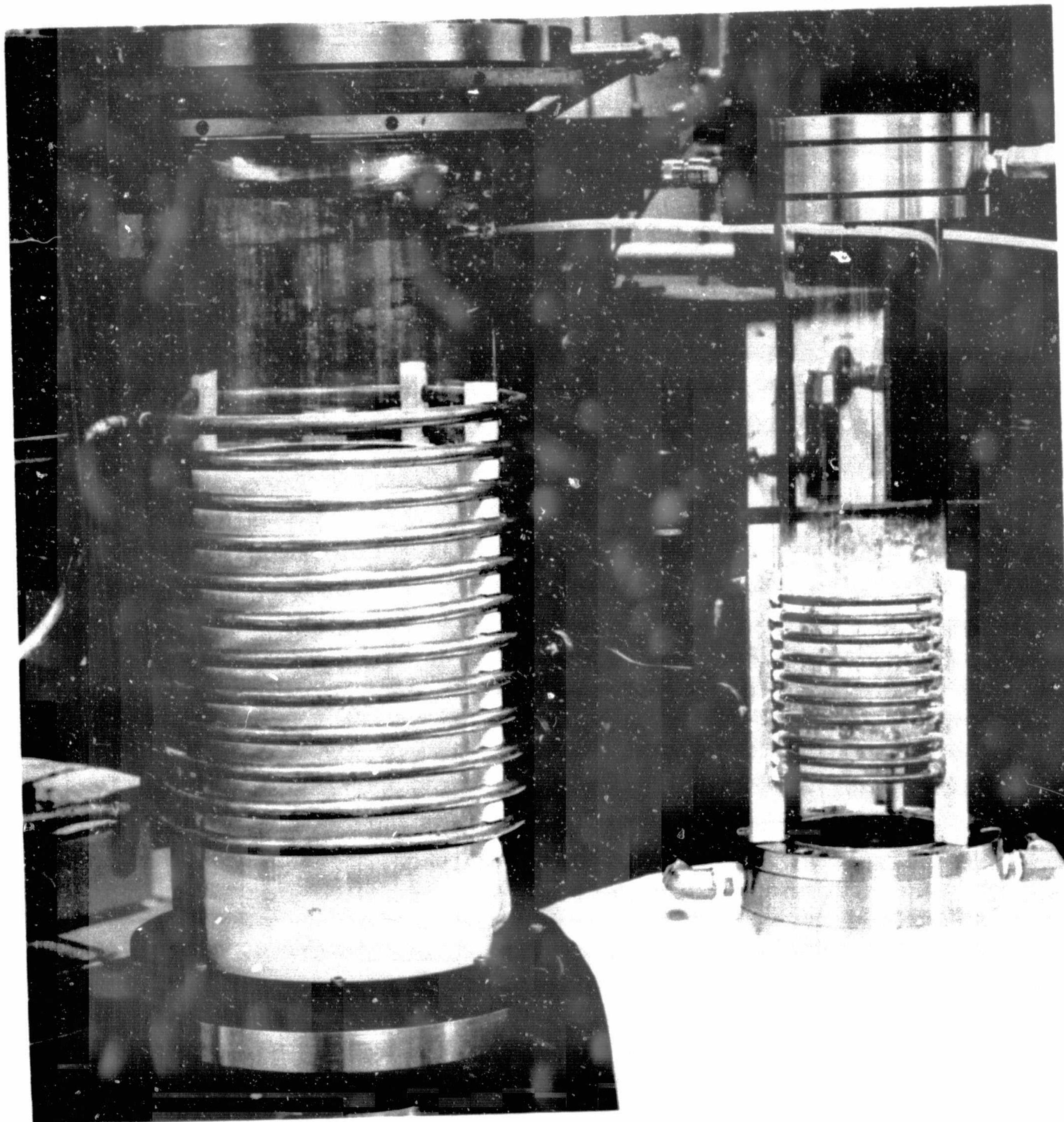

Fig. I-57. 100-mm Furnace (left) and 50-mm Furnace (right).

ORIGINAL PAGE IS
OF POOR QUALITY

eliminate the ionization by placing a third quartz tube between the shell and insulator was only partially successful. Next, an attempt was made to lower the RF coil voltage and the generator output power. The coil inductance was decreased from 17 μH to 10.8 μH (calculated values) by reducing the number of turns from 12 to 9, decreasing the diameter from 210 to 200 mm, and decreasing the length from 228 to 175 mm. The required power was decreased by using two layers of 6.4 mm thick graphite felt insulation to completely fill the space between the furnace shell and the quartz insulator (items 1 and 30, Fig. I-56) and by adding two layers of the same insulation to the top shield of the hot zone. These steps eliminate the ionization problem and reduced the power required for ribbon growth to about 16 kW. However, rapid devitrification of the quartz insulator tends to occur in this configuration.

A 2-piece die with top geometry similar to Fig. I-1 was used for 100 mm growth experiments. The edge thickness (X_e) was 1.52 mm, the middle thickness, (X_m) was 2.49 mm, and the deviation-from-flatness (δ) was 1.8 mm. The 100 mm die and holder with its 50 mm, 38 mm, 25 mm, and 12.5 mm predecessors is shown in Fig. I-58.

100 mm seeding was achieved on run 71003 (see Appendix I), but the ribbon was very non-uniform in thickness. It was

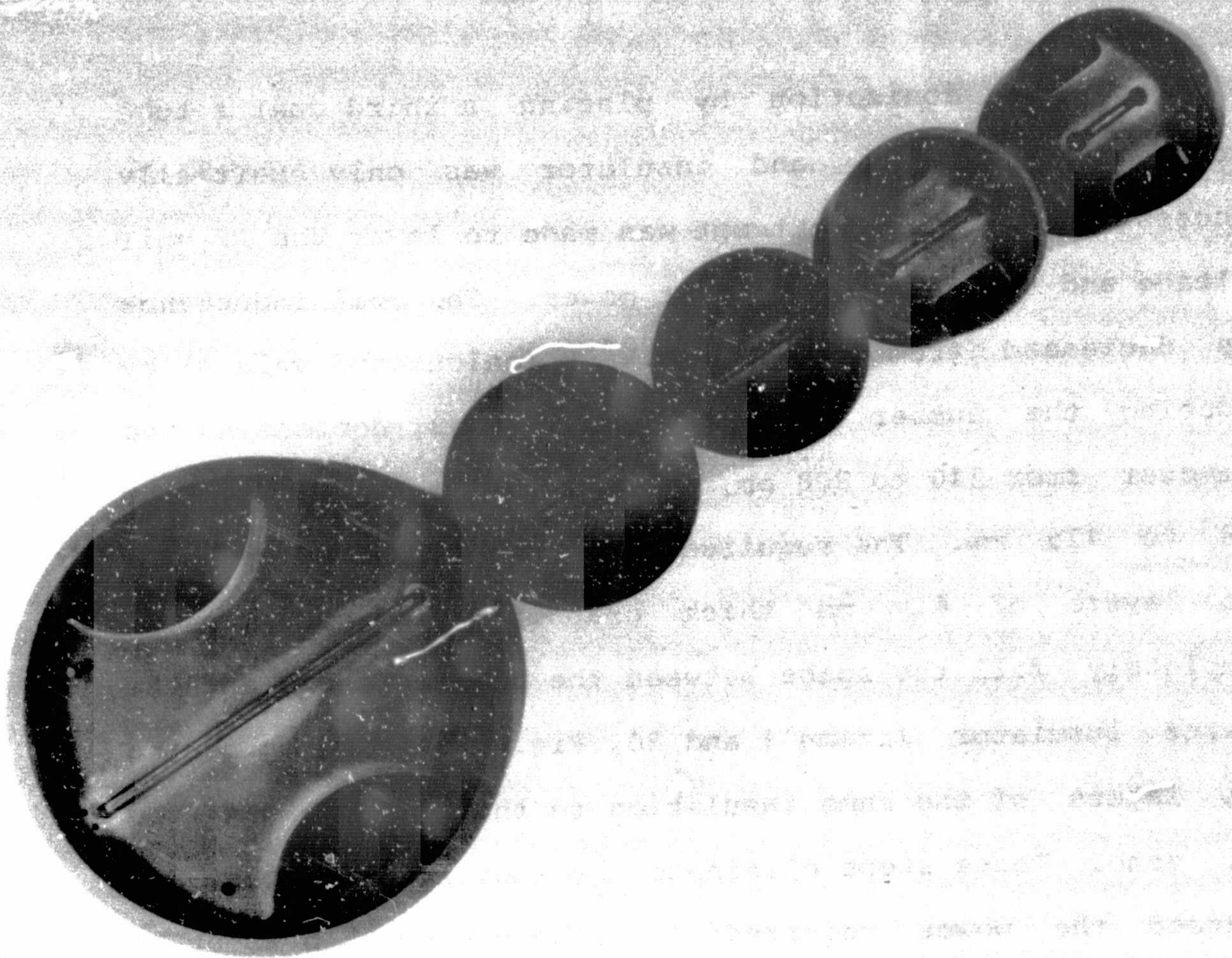

Fig. I-58. Used Dies and Die Holders for 12.5, 25, 38, 50, and 100-mm wide Ribbon Growth.

thick at the edges and the midregion but very thin at 6 to 25 mm from each edge. As growth proceeded, these regions became progressively thinner and ultimately pulled free of the meniscus. A partial ribbon cross section is shown in Fig. I-59.

ORIGINAL PAGE IS
OF POOR QUALITY

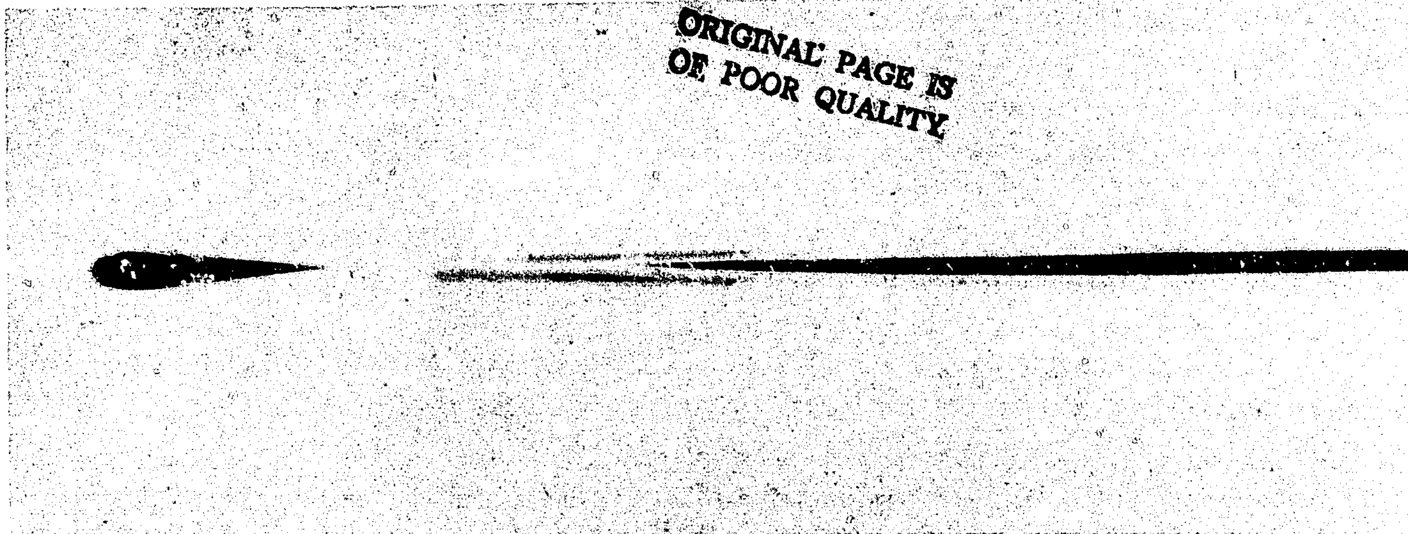
ORIGINAL PAGE IS
OF POOR QUALITY

Fig. I-59. Cross-section of half of 100-mm ribbon showing thinning effect.

To avoid the thinning effect, seeding was tried at 80 mm width in order to lower the melt meniscus. Ribbon width was gradually increased during the run. The thin regions were still present and got thinner as the width increased. The ribbon again pulled off at a width of 95 mm after 170 mm of growth. The ribbon shattered after falling out of the seed holder, but the pieces are shown in Fig. I-60. Details of growth are given in Appendix I.

The heat shields were modified to reduce the observed thinning effect but have not yet been tested because the die cracked, and a second die was apparently made of unsuitable graphite. Die fabrication, from the correct type of graphite, had not been completed by the contract termination date.

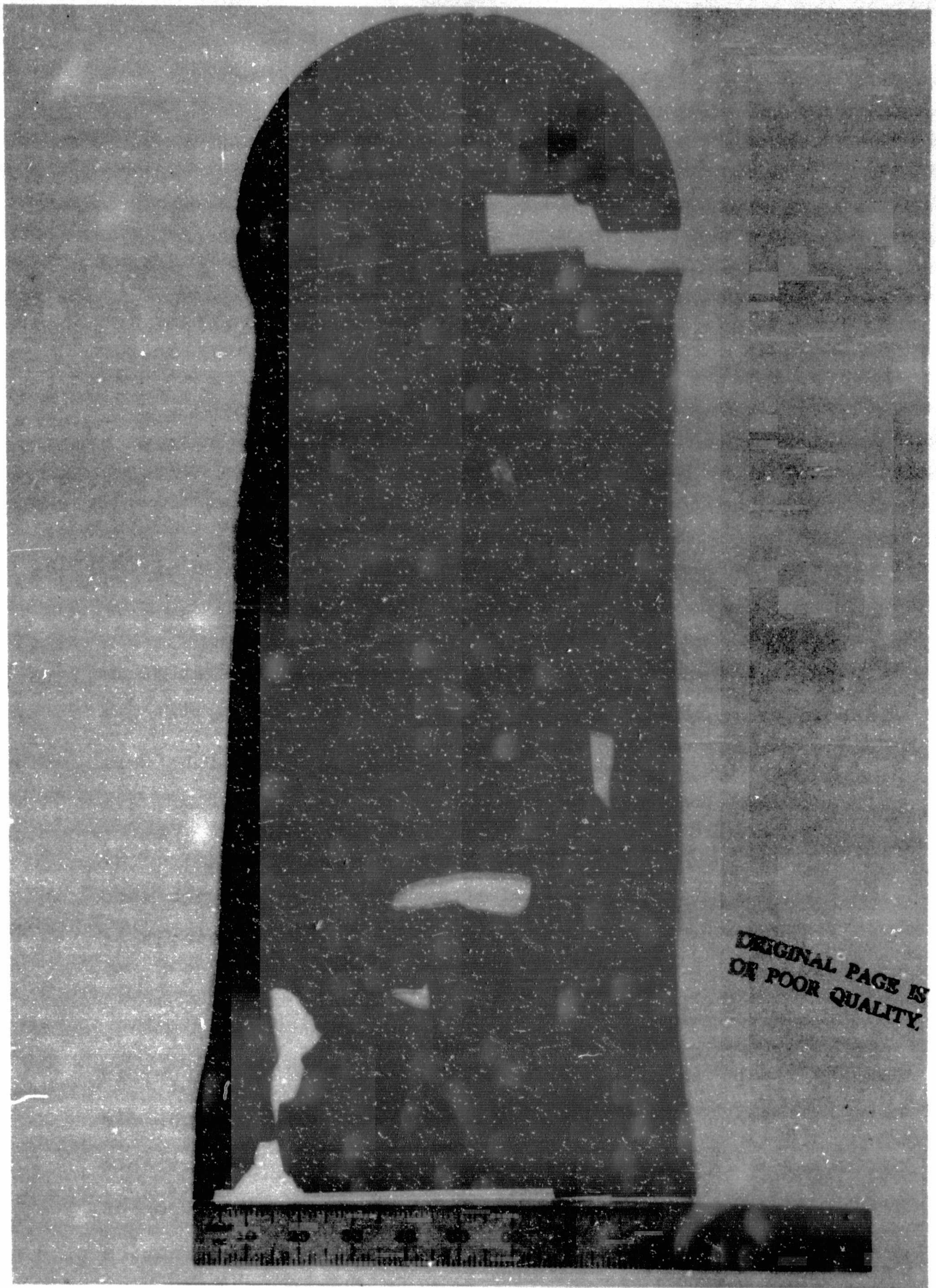
ORIGINAL PAGE IS
OF POOR QUALITY

Fig. I-60. A 170-mm long silicon ribbon grown from a 100-mm die.

6.0 LARGE-GRAIN DIRECTIONAL SOLIDIFICATION OF SILICON

During investigations of the usefulness of vitreous carbon as a die and crucible material, the feasibility of crack-free directional solidification of silicon was demonstrated.

6.1 Experimental Procedure

A 139 gram polycrystalline charge of silicon was placed in a 50 mm diameter x 50 mm high vitreous carbon crucible along with sufficient boron to produce a 2 Ω-cm average resistivity. Graphite rf susceptors and heat shields were arranged to establish a vertically increasing temperature gradient of about 35°C/cm, the top of the crucible being the hottest region. The system was heated to melt the silicon and then additionally heated to a temperature of 1680°C at the top melt surface. Since the melt was about 3 cm deep, the temperature at the bottom of the crucible was approximately 1575°C. The molten silicon was held at this temperature for 15 minutes. The system temperature was then decreased at a rate of 2.5°C/min while maintaining the vertical gradient until the entire charge had solidified (about 2 hours). The cooling rate was then increased to 20°C/min until the silicon temperature was 1000°C, at which time the power was turned off. The growth system was very

clean during this experiment (no silicon oxide fluff deposits as are typically present when using a quartz crucible).

6.2 Physical Characteristics of Directionally Solidified Silicon (DSS)

Upon removal from the furnace, the solifidied silicon was found to be intact and free of cracks as can be seen in Fig. I-61. Several thin slices were sawed from the bottom and top of the cylindrical ingot. Small silicon carbide particles were found at the carbon/silicon interface on the crucible bottom.

At a distance of 0.7 mm from the crucible bottom, the silicon grain distribution was as shown in Fig. I-62. Grain size ranged from 0.05 mm to 2 mm, with 0.5 mm being a typical size. The silicon here was P-type, and resistivities ranged from 1.4-5.0 Ω-cm.

At a distance of 2.5 cm from the crucible bottom, the grains were substantially larger (Fig. I-63). They ranged up to 4 mm in size, with 1 mm being a typical size. Figure I-64 is a photo of the opposite side of the slice region shown in Fig. I-63. The slice was 1.2 mm thick. As can be seen,

ORIGINAL PAGE IS
OF POOR QUALITY

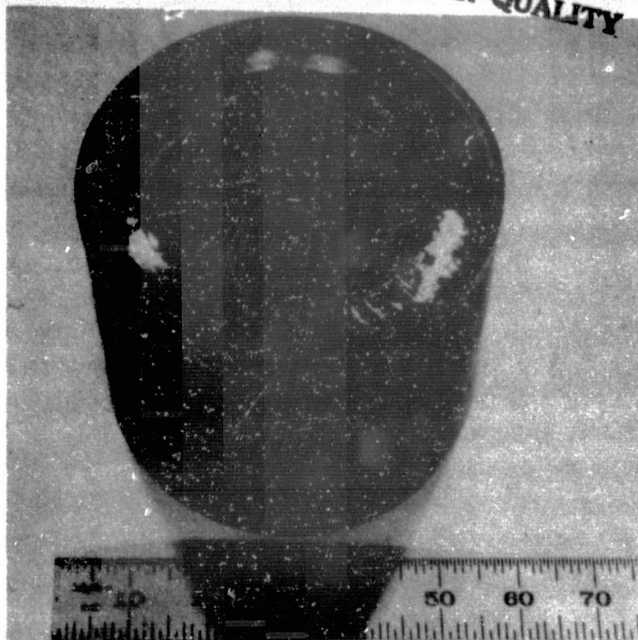

Fig. I-61. Silicon directionally solidified (bottom to top) in a vitreous carbon crucible.

Fig. I-62. Grain characteristics at 0.7-mm from crucible bottom (10X).

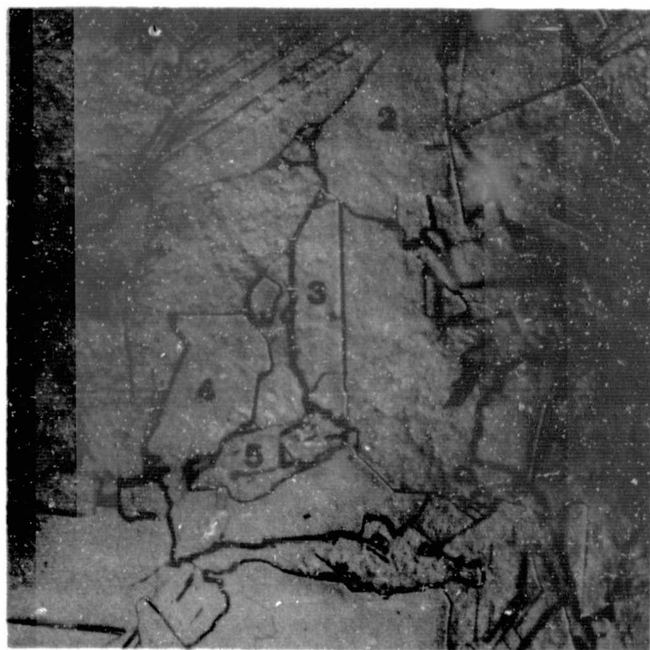

Fig. I-63. Grain characteristics 2.5-cm from crucible bottom (10X).

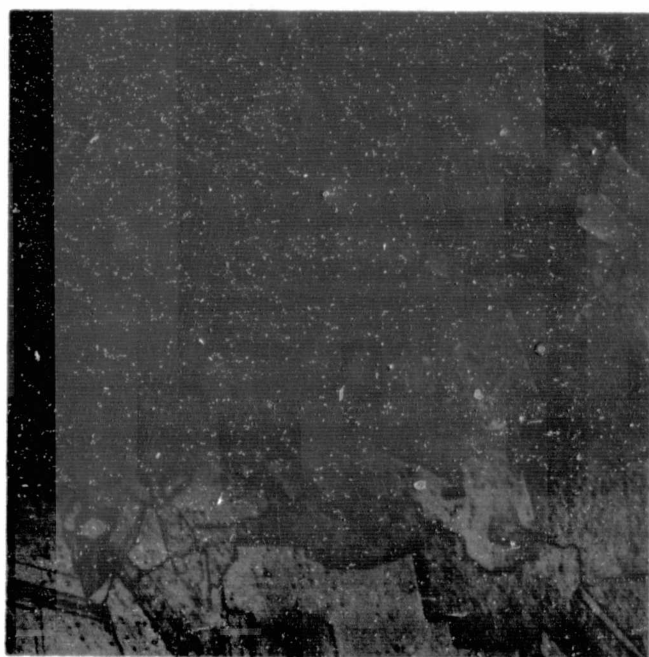

Fig. I-64. Opposite side of 1.2-mm thick wafer shown in Fig. I-3. Some grains visible on both sides are numbered.

there is a substantial amount of vertical boundary behavior. Some of the grains visible from both sides of the slice are identified with corresponding numbers. The resistivity here ranged from 0.5-2.1 Ω-cm, P-type.

Several wafers from the mid-region of the ingot are shown in Fig. I-65.

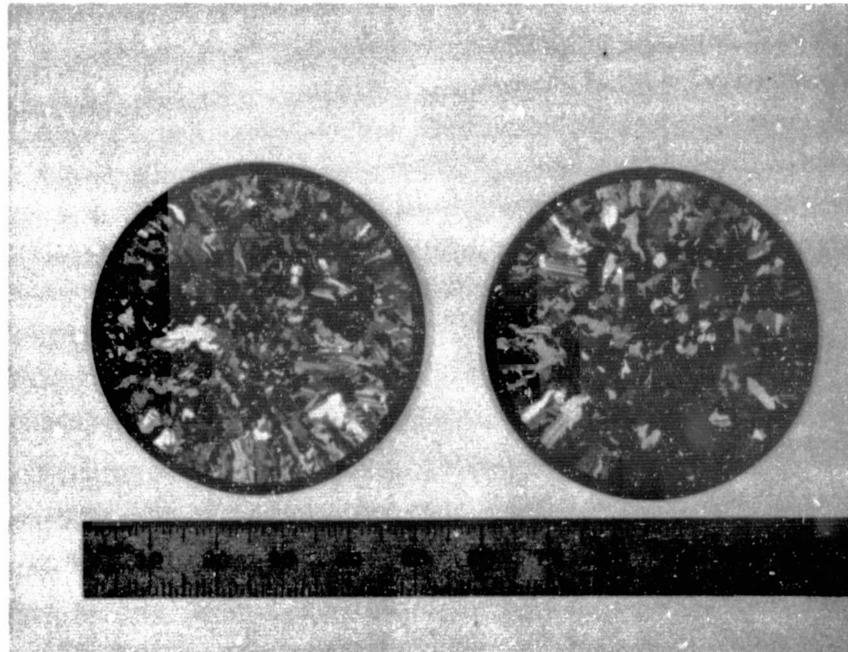

Fig. I-65. Two wafers from a 5-cm diameter directionally solidified silicon ingot.

Since the grains are large and at least some of the boundaries are vertical, these wafers were processed into 2 x 4 cm solar cells to determine their photovoltaic suitability.

Under 100 mW/cm^2 illumination from a Tungsten ELH lamp, the cells exhibited the following characteristics:

V_{oc} - .49-.50 volts
I_{sc} - 14.9-15.6 ma/cm^2
C_{ff} - 0.51-0.56
E - 4.0-4.2%

The cells appeared to suffer from high contact resistance as well as leakage - the latter probably being due to grain boundary effects.

It should be noted that the grain structure of this material is very similar to that reported by Fischer and Pschunder (15) for the Wacker-Chemitronic non-single crystalline silicon upon which solar cells of up to 12.5% AMO efficiency were fabricated.

6.3 Discussion

Directional solidification or Bridgeman/Stockbarger crystal growth is an effective simple technique used for many metals

and alkali halides[16]. The container should be inert and the material to be grown should contract upon freezing or at least not stick to the crucible walls. Silicon with fused quartz crucibles, does neither and has not been successfully grown by this simple process. Recently[17], additional attempts have been made using the traditional fused quartz containers, and cracking of the ingot is a serious problem. Some progress, however, has been made in eliminating the cracking by altering the quartz structure of the inner crucible wall[18].

Silicon is capable of plastic deformation from the melting point (1415°C) down to about 650°C. Below that temperature, silicon responds to an increasing applied stress by deforming elastically until the fracture stress (cracking) is reached. In the temperature range 650° to 20°C, the thermal expansion coefficient monotonically decreases from $5 \times 10^{-6}/^{\circ}C$ to $2.4 \times 10^{-6}/^{\circ}C$ almost linearly. Thus, when silicon is solidified and then cooled below 650°C in a quartz crucible, the silicon shrinks at a much higher rate than the crucible (the thermal expansion coefficient of fused quartz is $0.55 \times 10^{-6}/^{\circ}C$ in the temperature range 15-1000°C). Since the silicon sticks to the quartz, cracking results as the silicon fracture stress is exceeded.

In 1972, it was shown that graphite is a durable substrate in contact with liquid silicon provided that the density is greater than about 1.75 gm/cm^3 and the grain size is less than about 50 μm[12]. The degree of carbon contamination of the silicon (about 20 ppm) is similar to the level of oxygen contamination when silicon is grown from conventional SiO_2 crucibles; however, unlike oxygen, carbon is not electrically active in silicon.

Graphites are available with a wide range of thermal expansion coefficients (1.1 to 8.3 x $10^{-6}/^{o}C$), some being isotropic and some anisotropic. To avoid cracking of the silicon charge and/or the crucible, the graphite or carbon crucible should have a thermal expansion coefficient in the range 650°C to about 20°C which either matches that of silicon or else, on the average, produces the same dimensional change.

The thermal expansion coefficient of vitreous carbon ranges from 3.5 x $10^{-6}/^{o}C$ at 650°C to 3.2 x $10^{-6}/^{o}C$ at 100°C (see Table I-2) and has about the same average dimensional change as silicon in this range (at 650°C, the silicon shrinks more than the carbon with decreasing temperature, while near room temperature, the silicon shrinks less than the carbon with decreasing temperature).

Of course, any cross-sectional ingot shape can be produced by using an appropriate container shape. In Fig. I-66, a 5 cm x 5 cm DSS wafer with rounded corners is shown. A much faster cooling rate of 15°C/min was used in this case, and the solidification rate was about 16 grams/min. In this experiment, the thermal environment was such that the sides and surface of the molten silicon solidified once the system temperature had dropped appreciably. The later freezing of the molten core led to a fine grain structure in the center of the ingot; this is visible in Fig. I-66. The volume

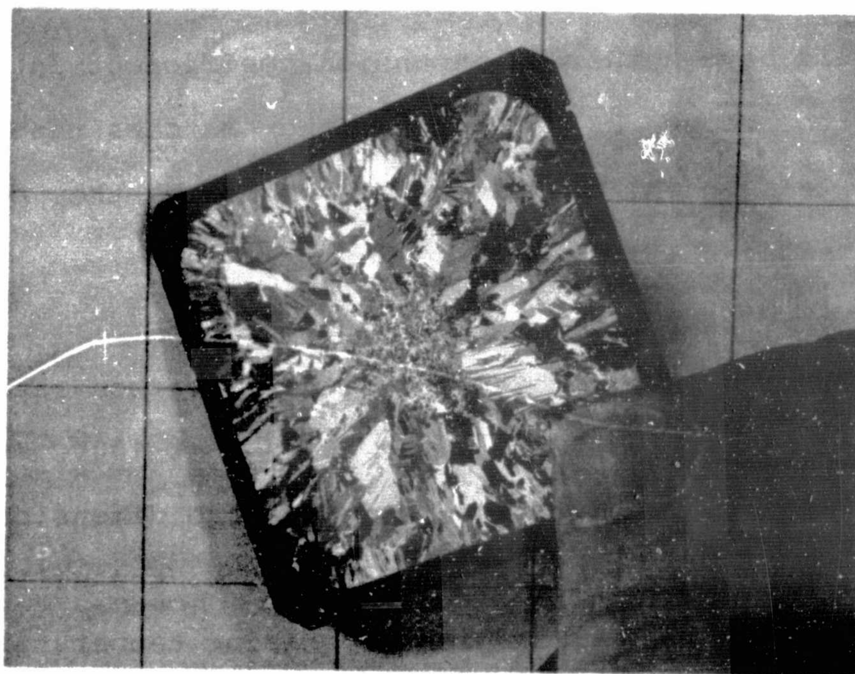

ORIGINAL PAGE IS
OF POOR QUALITY

Fig. I-66. A 5-cm x 5-cm wafer, with rounded corners, from a directionally solidified silicon ingot.

increase upon freezing of the trapped liquid core led to cracking at the top of the ingot, although the lower portion was intact. Thus, it is necessary to prevent a thermal inversion during cool down.

7.0 ACKNOWLEDGMENTS

Frank Newman provided technical support for all phases of the crystal growth experimentation. Some of the experimental die materials were machined by Daniel Weston. Some of the large dies and components were machined by David Shinn. E. F. Gorey provided all spreading resistance data reported in this section.

8.0 REFERENCES

1. H. E. LaBelle, Jr., Mater. Res. Bull. 6, 581 (1971).

2. T. F. Ciszek, Mater. Res. Bull. 7, 731 (1972).

3. T. F. Ciszek and G. H. Schwuttke, phys. stat. sol. (a) 27, 231 (1975).

4. J. C. Swartz, T. Surek, and B. Chalmers, J. Electron. Mater. 4, 255 (1975).

5. T. F. Ciszek, phys. stat. sol. (a) 32, 521 (1975).

6. D. Schwabe, A. Scharmann, F. Preisser, and R. Oeder, J. Crystal Growth, to be published (1978).

7. E. Billig, Proc. R. Soc. 229, 346 (1955).

8. T. F. Ciszek, J. Appl. Phys. 47, 440 (1976).

9. D. L. Barrett, et al., J. Electrochem. Soc. 118, 952 (1971).

10. D. E. Swets, Electrochem. Technology 5, 385 (1967).

11. A. D. Morrison, K. V. Ravi, C. V. Hari Rao, T. Surek, D. F. Bliss, L. C. Garone, and R. W. Hogencamp, "Large Area Silicon Sheet by EFG", Annual Progress Report, ERDA/JPL 954355, Sept. 15, 1976.

12. R. I. Scace and G. A. Slack, "The Si-C and Ge-C Phase Diagrams. Proceedings of the Conference on Silicon Carbide", Boston, April 1959. Pergamon Press, New York (1960).

13. M. Leipold, private communication.

14. G. F. Hurley and J. T. A. Pollock, Metallurgical Transactions 3, 397 (1972).

15. H. Fischer and W. Pschunder, IEEE 12th Photovoltaic Specialists Conference Record, 86 (1976).

16. S. L. Zerfoss, et al., "Crystal Growth at High Temperatures", Trans. Faraday Soc., 1949.

17. JPL LSSA Project Quarterly Report #2, pp. 4-76 - 4-77, Sept. 1976.

18. JPL LSSA Project Quarterly Report #4, pp. 4-24 - 4-25, (1977).

APPENDIX I

SUMMARY OF RIBBON GROWTH EXPERIMENTS

May 1975 to November 1977

Run No.	Die Width mm	Die Material	Experimental Variables	Results
50516	12.5	Graphite DFP-3-2	New die #05. Flat top thickness. 0.25 mm capillary slot. Die holder, lower, upper shield #13. Pull speed 15 mm/min.	43 cm ribbon
50517	12.5	DFP-3-2	Repeat - operator training.	26 cm ribbon @ 25 mm/min
50518	12.5	DFP-3-2	Repeat	No results.
50519	12.5	DFP-3-2	Repeat	71 cm @ 23 mm min
50520	12.5	DFP-3-2	Repeat	94 cm @ 22 mm/min
50521	12.5	DFP-3-2	Remachined susceptor shaft to level susceptor.	No results - die flooded
50522	12.5	DFP-3-2	Repeat	No results
50523	10	DFP-3-2	New die #05A	No results
50524	10	DFP-3-2	Repeat	No results
50525	6.3	DFP-3-2	Cylindrical capillary die for silicon tube growth	65 cm long tube @ 11 mm/min
50526	6.3	DFP-3-2	Repeat. Pull speed constant. Temp. increased in increments	109 cm long tube @ 11 mm/min. Wall thickness decreases with increase in temp.

Run No.	Die Width (mm)	Die Material	Experimental Variables	Results
50601	6.3	DFP-3-2	Drilled six 1 cm dia. holes in die holder and shields on 39 mm dia. circle	Froze
50602	6.3	DFP-3-2	Repeat. Vary pull speed from 13-21 mm/min. Temp. constant	117 cm tube. Wall thickness decreases as speed increases
50603	6.3	DFP-3-2	Repeat	124 cm tube
50604	6.3	DFP-3-2	Repeat. Pull speed - 8 mm/min	Froze
50605	6.3	DFP-3-2	Repeat	Froze
50606	12	Crystar* SiC	Evaluate die made of SiC	Irregular short ribbon grown
50607	12	Crystar* SiC	Repeat	Same. Sensitive to temp. changes
50608	12.5	DFP-3-2	Die type 05. Top protrudes 1 mm above holder	20 cm ribbon bad vibration
50609	12.5	DFP-3-2	Repeat	No results
50610	12.5	DFP-3-2	Repeat	24 cm @ 24mm/min
50611	12.5	DFP-3-2	Repeat	52 cm @ 21 mm/min
50612	12.5	DFP-3-2	Repeat	27 cm then froze
50701	25.4	DFP-3-2	Die, holder, shields, spacers #13 (Capillary action shaping technique die with radiused, beveled top and variable top thickness. Center is thicker than edges.)	No results

Run No.	Die Width (mm)	Die Material	Experimental Variables	Results
50702	25.4	DFP-3-2	Repeat	No results, growth drifts to one edge of die.
50703	25.4	DFP-3-2	Repeat, thicker seed.	No results, froze at 20 mm width.
50704	25.4	DFP-3-2	Repeat	No results, froze
50705	25.4	DFP-3-2	Repeat	Could not control drift, froze towards front.
50706	25.4	DFP-3-2	Repeat. Rotated die 150°	Drifting problem not caused by die. Froze towards front, short ribbon.
50707	25.4	DFP-3-2	Repeat	98 cm @ 21 mm/min, 25 mm wide
50708	25.4	DFP-3-2	Repeat	No results
50709	25.4	DFP-3-2	Repeat	Froze @ full width
50710	25.4	DFP-3-2	Repeat	75 cm @ 21 mm/min. Split during scribing. Split width 1.1 cm after a distance of 57 cm.
50711	25.4	DFP-3-2	Thermal modifiers added. Same shape as die holder 12.5 mm high. 6 mm wide, slot 38 mm long.	No results. Cannot see to seed.
50712	25.4	DFP-3-2	Same as run #50710	Froze
50713	25.4	DFP-3-2	Repeat	Froze
50714	25.4	Graphite HPD-3-2	New die #13	No results
50715	25.4	HPD-3-2	Repeat	No results. Froze @ full width

Run No.	Die Width (mm)	Die Material	Experimental Variables	Results
50716	25.4	HPD-3-2	Repeat	No results. Froze
50717	25.4	HPD-3-2	Repeat	Froze
50718	25.4	DFP-3-2	Die 05, new quartz tube. Flat top EFG die.	No results
50719	25.4	DFP-3-2	Same 50714 plus thermal modifier from run 50711	No results
50720	25.4	DFP-3-2	Repeat	No results. Froze @ 4 mm width
50721	25.4	DFP-3-2	Repeat.	No results. Froze @ 21 mm width
50722	25.4	DFP-3-2	Repeat. Varied coil position	No results
50723	25.4	DFP-3-2	Same as 50714. No thermal modifier	Susceptor broke. No results
50724	25.4	DFP-3-2	New die #13. Adjusted coil	77 cm @ 17 mm/min
50725	25.4	DFP-3-2	Repeat	22 cm @ 22 mm/min
50726	25.4	DFP-3-2	Repeat	No results
50727	25.4	DFP-3-2	Repeat	No results
50728	25.4	DFP-3-2	Repeat	No results
50729	25.4	DFP-3-2	Repeat	No results
50730	25.4	DFP-3-2	Repeat. Doped 2 ohm-cm	86 cm @ 16 mm/min. Edge thickness .67 mm, center thickness .44 mm
50801	25.4	DFP-3-2	Repeat	Froze

Run No.	Die Width (mm)	Die Material	Experimental Variables	Results
50802	25.4	DFP-3-2	Repeat	25 cm @ 17 mm/min
50803	25.4	DFP-3-2	Repeat	78 cm @ 18 mm/min
50804	25.4	DFP-3-2	Repeat. Rotated die 180°	20 cm @ 21 mm/min
50805	9.5	Crystar* SiC	Evaluation of silicon carbide material	50 cm @ 16 mm/min. Surface seems smooth
50806	9.5	Crystar* SiC	Repeat	81 cm @ 17 mm/min
50807	9.5	KT** SiC	Evaluation of silicon carbide die material	28 cm @ 15 mm/min
50808	9.5	KT** SiC	Repeat	34 cm @ 15 mm/min
50809	9.5	KT** SiC	Repeat	113 cm @ 16 mm/min. Surface smooth but has SiC particles
50810	9.5	Si_3N_4/SiC	Evaluation of Refrax** silicon nitride bonded silicon carbide die	Melt will not rise in die capillary slot
50811	9.5	B_4C	Evaluation of boron carbide die	35 cm ribbon, wets extremely well. Clean surface. Strong morphological features. .004 ohm-cm, p-type
50812	9.5	B_4C	Repeat	No results
50813	9.5	B_4C	Repeat, faster speed	Pulled away from melt
50814	9.5	Si_3N_4	Evaluation of silicon nitride die	Melt wets surface, but will not rise in slot

*Trade Mark of Norton Industrial Ceramics Division
**Trade Mark of Carborundum Company

Run No.	Die Width (mm)	Die Material	Experimental Variables	Results
50815	9.5	ZrB_2	Evaluation of zirconium boride die	Short ribbon. Good melt rise, but die dissolves
50816	9.5	TiB_2	Evaluation of titanium boron die	Short ribbon. Good melt rise, but die dissolves
50817	9.5	TiB_2	Repeat	Froze
50818	9.5	TiB_2	Repeat	Froze
50819	9.5	TiB_2	Repeat	Froze
50820	9.5	TiB_2	Repeat	Same as 50816
50821	9.5	TiB_2	Repeat. Narrower slot in lower shield	Same as 50816
50822	9.5	TiB_2	Repeat	Same as 50816
50823	9.5	TiB_2	Repeat	Same as 50816
50824	9.5	TiB_2	Repeat	Same as 50816
50825	9.5	Vitreous carbon	Evaluation of vitreous carbon die	44 cm long, narrow ribbon, with dark coating on surface. Parallel twinning
50826	9.5	Vitreous carbon	Repeat. Die is 1.5 mm lower in holder	30 cm ribbon, same properties as above. SiC particles on surface
50901	25.4	HPD-3-2	Same hot zone as runs 50701-50725. Argon purge system modified by enclosing pull shaft in plastic bellows to completely contain ribbon in Argon during growth. System purged from top to bottom.	Ribbon froze @ 14 mm width

Run No.	Die Width (mm)	Die Material	Experimental Variables	Results
50902	25.4	HPD-3-2	Repeat. Argon flow increased from 50 to 58 CFH	Froze
50903	25.4	HPD-3-2	Repeat	Froze @ 23 mm width
50904	25.4	HPD-3-2	Repeat	Froze
50905	25.4	HPD-3-2	Repeat	Froze at full width
50906	25.4	HPD-3-2	Repeat	Short full width ribbon then froze
50907	25.4	HPD-3-2	Repeat	Same as above
50908	25.4	HPD-3-2	Repeat	8 cm. Ribbon then froze. Ribbon drifts to front.
50909	25.4	HPD-3-2	Repeat. Increased pull speed	50 cm @ 20 mm/min. Ribbon surface clean and melt clean
50910	25.4	DFP-3-2	New die. Installed bubbler on argon outlet to create slight back pressure.	Ribbon froze at full width
50911	25.4	DFP-3-2	Repeat	30 cm @ 19 mm/min
50912	25.4	DFP-3-2	Repeat. Argon flow dropped to 50 CFH	Ribbon and melt still clean
50913	25.4	DFP-3-2	Repeat	Froze
50914	25.4	DFP-3-2	Repeat	Froze
50915	25.4	DFP-3-2	Repeat	Froze
50916	25.4	DFP-3-2	Repeat. Reduced argon flow to 17 CFH	52 cm @ 18 mm/min. Ribbon still clean

Run No.	Die Width (mm)	Die Material	Experimental Variables	Results
50917	25.4	DFP-3-2	Repeat	Froze
50918	25.4	DFP-3-2	Repeat	Froze
50919	25.4	DFP-3-2	Repeat	93 cm @ 18 mm/min. Ribbon and melt residue clean but powder build-up on heat shields
50920	25.4	DFP-3-2	Repeat	Froze
50921	25.4	DFP-3-2	Repeat	Froze
50922	25.4	DFP-3-2	Repeat	Froze
50924	25.4	DFP-3-2	Repeat	Froze
50925	25.4	DFP-3-2	Repeat	Froze
50926	25.4	DFP-3-2	Repeat	35 cm @ 13 mm/min
50927	25.4	DFP-3-2	Repeat @ faster pull speed	40 cm @ 25 mm/min. Fractured during handl-ing.
50928	25.4	DFP-3-2	Repeat @ faster pull speed	46 cm @ 28-30 mm/min
51001	25.4	DFP-3-2	Grew CZ crystal to check dopant	--
51002	25.4	DFP-3-2	Removed graphite drawtube. 60 CFH argon purge, from top	Clean ribbon surface, growth easy to control
51003	25.4	DFP-3-2	Repeat	Same
51004	25.4	DFP-3-2	Argon purge in-creased to 75 CFH	Froze at 15 mm width
51005	25.4	DFP-3-2	Repeat	Clean surface, 50 cm long ribbon

Run No.	Die Width (mm)	Die Material	Experimental Variables	Results
51006	25.4	DFP-3-2	Repeat	Froze
51007	25.4	HPD-3-2	Repeat, growth speed 15 mm/min New die.	51 cm ribbon, 0.45 mm thick middle, 0.73 mm thick at edges
51008	25.4	HPD-3-2	Growth speed increased t0 22 mm/min	Ribbon 0.43 mm thick in middle, 0.66 mm thick at edges
51009	25.4	HPD-3-2	Continuation	Froze
51010	25.4	HPD-3-2	Continuation	Froze
51011	25.4	HPD-3-2	Continuation	Froze - melt level too low
51012	25.4	HPD-3-2	Argon purge 75 CFH from bottom of furnace. Exhaust is draw tube and purge tube around ribbon.	91 cm long ribbon. Easy to grow. Colored film on surface.
51013	25.4	HPD-3-2	Continuation	20 cm ribbon as above
51014	25.4	HPD-3-2	New draw tube - 02. Argon flow is 30 CFH from top.	54 cm long ribbon. Clean surface.
51015	25.4	HPD-3-2	Argon flow 20 CFH	85 cm long ribbon. Clean surface.
51016	25.4	HPD-3-2	New die. Removed draw tube - 02. Argon flow 20 CFH from top. 28 mm/min pull speed	Ribbon surface much rougher. 52 cm long ribbon. 0.39 mm thick in middle, 0.60 mm thick at edges
51017	25.4	HPD-3-2	Repeat, but 81.5 mm/min pull speed	Ribbon 0.26 mm thick in middle, 0.44 mm thick at edges. Rough

Run No.	Die Width (mm)	Die Material	Experimental Variables	Results
51018	25.4	HPD-3-2	Repeat, but 25 mm/min pull speed 65 CFH argon purge	Ribbon smoother, .41 mm thick at middle and .67 mm at edges
51019	25.4	HPD-3-2	Same as above, but 29 mm/min pull speed	Ribbon 0.35 mm thick at middle. 0.55 mm thick at edges
51020	25.4	HPD-3-2	Repeat	Froze. Widened too fast.
51021	25.4	HPD-3-2	New die. 19 mm/min pull speed	0.38 mm thick at middle, 0.66 at edges
51022	25.4	HPD-3-2	Repeat	0.28 mm thick at middle, 0.59 at edges
51023	25.4	DFP-3-2	Repeat, but 24 mm/min. pull speed	0.39 mm thick at middle, 0.59 at edges
51024	25.4	DFP-3-2	Repeat, but 14 mm/min pull speed	0.26 mm thick at middle, 0.64 at edges
51025	25.4	DFP-3-2	Repeat, but 18 mm/min pull speed	0.22 mm thick at middle, 0.56 at edges
51026	25.4	DFP-3-2	Repeat of 50916 run conditions	0.37 mm thick at middle, 0.62 at edges
51027	25.4	DFP-3-2	As above, but 25 mm/min speed	0.26 mm thick at middle, 0.52 at edges
51028	25.4	DFP-3-2	Continuation of above	Froze
51029	25.4	DFP-3-2	Continuation - attempt 30 mm/min pull	Froze. Could not grow at 30 mm/min
51030	25.4	DFP-3-2	60 CFH argon purge from top. No draw tube. After heater - 01.	Difficult to grow. Could not reach full width

Run No.	Die Width (mm)	Die Material	Experimental Variables	Results
51031	25.4	DFP-3-2	Repeat	Same problem
51032	25.4	DFP-3-2	Repeat	Froze
51033	25.4	DFP-3-2	Repeat	Grew 59 cm long ribbon, irregular width
51034	25.4	DFP-3-2	Repeat	Grew 59 cm long ribbon, irregular width. Froze upon reaching 25 mm width
51101	25.4	DFP-3-2	Basic set-up, but with vertical, "parallel plates", after heater (22 mm wide x 12 mm high, spaced 4.7 mm)	Ribbon froze to edge of die
51102	25.4	DFP-3-2	Repeat, new seed	Grew 24 mm wide ribbon, but control is very unstable
51103	25.4	DFP-3-2	Repeat	Ribbon froze to die
51104	25.4	DFP-3-2	Basic set-up, but with 12.6 mm high block graphite after heater. Central opening tapers from 7 mm wide at bottom to 18.5 mm at top. 14 mm/min speed.	Easy to grow, surface is duller. More SiC particles. Ribbon was deliberately split. Spread was 4 mm over a distance of 380 mm
51105	25.4	DFP-3-2	Repeat, at 20 mm/min. Argon flow 80 CFH	Same general appearance. Split width was 1.1 mm over a distance of 170 mm
51106	25.4	DFP-3-2	Repeat, 40 CFH argon flow	Froze

Run No.	Die Width (mm)	Die Material	Experimental Variables	Results
51107	25.4	DFP-3-2	Repeat, 15 mm/min	49 cm ribbon, fewer SiC particles. Ribbon .50 mm thick at edges .28 at center
51108	25.4	DFP-3-2	Height of Quartz insulator increased to 25.5 cm (was 23). After heater from 51104	Cooling water failure. Lost die and holder
51109	25.4	DFP-3-2	New die, repeat of 51108	Froze
51110	25.4	DFP-3-2	Repeat, 10 mm/min	Grew 12 cm long ribbon, then froze. Split width was 0.5 mm over a distance of 130 mm. Thickness .55 to .50 mm
51111	25.4	DFP-3-2	Repeat	Difficulty in spreading to full width
51112	25.4	DFP-3-2	Repeat	Short ribbon. Much smaller temp. adjustment required to spread ribbon with this set-up
51113	25.4	DFP-3-2	Return to basic set-up (23 cm quartz insulator, no after heater, 60 CFH argon flow to make ribbons for solar cell characterization	Froze out
51114	25.4	DFP-3-2	Repeat, 23 mm/min	48 cm ribbon; thickness .50 to .34 mm
51115	25.4	DFP-3-2	Repeat, 20 mm/min	87 cm ribbon; thickness .57 to .30
51116	25.4	DFP-3-2	Repeat	Froze upon reaching full width

Run No.	Die Width (mm)	Die Material	Experimental Variables	Results
51117	25.4	DFP-3-2	Repeat, changed to 25.5 cm quartz insulator	Same as above
51118	25.4	DFP-3-2	Repeat, 21 mm/min	57 cm ribbon; .46 to .29 mm thick
51119	25.4	DFP-3-2	Repeat, 22 mm/min	54 cm ribbon; .46 to .28 mm thick
51120	25.4	DFP-3-2	Repeat, 23 mm/min	21 cm ribbon, then froze
51201	25.4	DFP-3-2	Return to 51108 run conditions, but with 60 CFH flow 20 mm/min	16 cm ribbon; .50 to .35 mm thick
51202	25.4	DFP-3-2	Repeat, 12 mm/min	60 cm ribbon; .52 to .42 mm thick
51203	25.4	DFP-3-2	Repeat	19 cm ribbon; .76 to .38 mm thick
51204	25.4	DFP-3-2	Basic set-up, with 12.5 mm high after heaters at ribbon edges (vertical, 3 mm radius recesses milled out to surround ribbon edge	Froze during spreading
51205	25.4	DFP-3-2	Repeat 18 mm/min	36 cm ribbon; thickness .50 ± .05 mm
51206	25.4	DFP-3-2	Repeat	Froze
51207	25.4	DFP-3-2	Repeat	20 cm ribbon, then froze
51208	25.4	DFP-3-2	Repeat. 19 mm/min	46 cm ribbon, .43 ± .07 mm thick
51209	25.4	DFP-3-2	Repeat. Argon flow reduced to 40 CFH	53 cm ribbon, split width 1.1 mm over a 200 mm distance

Run No.	Die Width (mm)	Die Material	Experimental Variables	Results
51210	25.4	DFP-3-2	Repeat. 25.5 cm high quartz shield 60 CFH argon flow. 14 mm/min speed	46 cm ribbon. Thicker in center (0.65 mm) than at edge (0.5). Three attempts made to split ribbon. In each case, the split veered to the edge and would not propagate axially
51211	25.4	DFP-3-2	Repeat, but higher growth rate (23 mm/min)	Froze at 23 mm width. Difficult to control
51212	25.4	DFP-3-2	Repeat	Froze again. Temp. control seems more critical with high quartz insulator
51213	25.4	DFP-3-2	Repeat. Approx. 18 mm/min	32 cm ribbon. Difficult to control. Cross section thick at one edge, but then uniform
51214	25.4	DFP-3-2	Repeat. 16-17 mm/min	55 cm ribbon. One edge slightly thicker (.45-41 mm at tail end).
51215	25.4	DFP-3-2	Die, holder, shields baked out 4 hrs. at 1250 C in wet argon. Followed by normal vacuum bakeout. Basic set-up, but 25.5 cm high quartz shield	Froze out
51216	25.4	DFP-3-2	Repeat, 17 mm/min	39 cm ribbon, effect on efficiency to be determined
51217	25.4	DFP-3-2	Repeat	57 cm ribbon, .75 to .47 mm thick
51218	25.4	DFP-3-2	Repeat. 18 mm/min	45 cm ribbon. .60 to .50 mm thick.

Run No.	Die Width (mm)	Die Material	Experimental Variables	Results
51219	25.4	DFP-3-2	Repeat	Froze, seed broke
60101	25.4	DFP-3-2	Die bake-out 4 hrs at 1250°C in wet argon plus anhydrous HCl	Die/holder flooded with Si
60102	25.4	DFP-3-2	Die bake-out 4 hrs at 1250°C in dry argon plus anhydrous HCl	58 cm ribbon; effect on efficiency to be determined
60103	25.4	DFP-3-2	Repeat growth, same die	57 cm ribbon
60104	25.4	DFP-3-2	Repeat growth, varied seed orientation	60 cm ribbon
60105	25.4	DFP-3-2	Same set-up, added mock-up of proposed afterheater for uniform thickness (14 mm/min growth speed)	55 cm ribbon, thickness uniform between 0.45 and 0.50 mm
60106	25.4	DFP-3-2	Repeat, but at 23 mm/min	Froze out after 4 cm of growth
60107	25.4	DFP-3-2	Repeat	Small contaminant particle lodged on die preventing growth
60108	25.4	DFP-3-2	New die and holder, repeat of bakeout conditions in 60101	White powder coating on die and Si furnace tube after bakeout (probably SiO). Scraped off. No ribbon
60109	25.4	DFP-3-2	Repeat - Same set-up	No ribbon--froze out
60110	25.4	DFP-3-2	Repeat	32 cm ribbon; effect on efficiency to be determined
60111	25.4	DFP-3-2	Set-up from run 60102 grow full length ribbon	94 cm ribbon
60112	25.4	DFP	Repeat	90 cm ribbon

Run No.	Die Width (mm)	Die Material	Experimental Variables	Results
60113	25.4	DFP-3-2	Repeat	Froze out
60114	25.4	DFP-3-2	Repeat	33 cm ribbon - then froze out
60115	25.4	DFP-3-2	Repeat	36 cm ribbon - then froze out
60116	25.4	DFP-3-2	Repeat	31 cm ribbon - then froze out
60117	25.4	DFP-3-2	Repeat, rotated die 180°	Still freezing out/ uneven spreading
60118	25.4	DFP-3-2	Repeat	Froze out, no ribbon
60119	25.4	DFP-3-2	Repeat	28 cm ribbon--then froze out
60120	25.4	DFP-3-2	Repeat	95 cm ribbon
60121	25.4	DFP-3-2	Repeat, same set-up	Froze out, too little Si
60201	25.4	DFP-3-2	Repeat, same 60121	No results
60202	25.4	DFP-3-2	Thermal modifier No. 8. Coil spread to cover afterheater and die. 18 mm/min.	Smooth shiny surface. Thin in center. 96 cm ribbon
60203	25.4	DFP-3-2	Repeat, 14 mm/min	25 cm ribbon, then froze. Very low stress. Ribbon would not split
60204	25.4	DFP-3-2	Repeat	Froze reaching full width
60205	25.4	HPD-3-2	Hand lapped die to .39 mm edge thickness	Unable to make ribbon spread. Die edge touching L shield
60206	25.4	HPD-3-2	Repeat	9 cm ribbon, froze

Run No.	Die Width (mm)	Die Material	Experimental Variables	Results
60207	25.4	HPD-3-2	Die not centered in holder, touching edge	No results
60208	25.4	KT*SiC	KT*SiC die. Top radi-used to 3.75 inches. No thermal modifier	No results. Melt be-tween die and holder
60209	25.4	KT*SiC	Repeat. Grew ribbon from flooded die	45 cm ribbon. Ribbon curved due to rubbing on lower shield
60210	25.4	KT*SiC	Repeat	Froze
60211	25.4	KT*SiC	Repeat	Froze
60212	25.4	DFP-3-2	Standard procedure	55 cm ribbon @ 17 mm/min
60213	25.4	DFP-3-2	Standard procedure	77 cm ribbon @ 20 mm/min
60214	25.4	DFP-3-2	Thermal modifier No. 8. Measured thermal vertical gradient	Machine problem. No results
60215	25.4	KT*SiC	Cleaned die in HF 24 hr. (die from run 60208)	No results
60216	25.4	KT*SiC	Repeat	40 cm ribbon @ 19 mm/min
60217	25.4	KT*SiC	Repeat	18 cm ribbon @ 20 mm/min
60218	25.4	KT*SiC	SiC die with thermal modifier 08	No results. Edge of die too cold
60219	25.4	KT*SiC	Repeat	No results
60220	25.4	KT*SiC	Repeat	No results. Froze @ 7 mm width
60301	25.4	KT*SiC	Repeat	No results
60302	25.4	KT*SiC	Repeat	No results

*Trade Mark of Carborundum Company

Run No.	Die Width (mm)	Die Material	Experimental Variables	Results
60303	25.4	DFP-3-2	Standard procedure	55 cm @ 17 mm/min
60304	25.4	DFP-3-2	Repeat. Ribbon was split for stress measurements	55 cm @ 20 mm/min. Stress results similar to those with thermal modifier #5
60305	25.4	DFP-3-2	Standard procedure with thermal modifier #8 and 3 mm seed. Neck-in sharply after seeding	Single crystal short distance at seeding
60306	25.4	DFP-3-2	Repeat	No results
60307	25.4	DFP-3-2	Thermal modifier #8	No results. Ribbon drifts to right
60308	25.4	DFP-3-2	Repeat after adjusting rf coil	No results
60309	25.4	DFP-3-2	Std. procedure (Thermal modifier #5)	53 cm @ 16 mm/min. Uniform thickness within 6%, at .45 mm
60310	25.4	DFP-3-2	Repeat, faster pull speed	23 cm @ 20 mm/min, again uniform thickness (.39 mm)
60311	25.4	DFP-3-2	Repeat	No results, froze
60312	25.4	DFP-3-2	Repeat	41 cm @ 21 mm/min, thickness is again uniform (.35 mm)
60313	25.4	DFP-3-2	Argon flow increase from 50 CFH to 67 CFH. Thermal modifier #5	No results, froze. Argon affects direction of spreading
60314	25.4	DFP-3-2	Repeat @ 50 CFH argon flow	No results, froze, right side
60315	25.4	DFP-3-2	Repeat @ 17 CFH argon flow	No results, froze

Run No.	Die Width (mm)	Die Material	Experimental Variables	Results
60316	25.4	DFP-3-2	New die and graphite components. Die top is .52 mm thick at edges, .99 mm at middle	No results, froze right side
60317	25.4	DFP-3-2	Repeat, ribbon drifting to right. Argon flow 50 CFH	Not able to keep centered. Used up all travel and froze
60318	25.4	DFP-3-2	Repeat, rotated die 90°	44 cm @ 18 mm/min
60319	25.4	DFP-3-2	Repeat	No results, froze upon reaching full width
60320	25.4	DFP-3-2	Repeat	55 cm @ 22 mm/min
60321	25.4	DFP-3-2	Repeat, <111> (112) seed	No results, froze
60322	25.4	DFP-3-2	Repeat, adjusted RF coil	57 cm @ 23 mm/min. Edge thickness .41, middle .25 mm
60323	25.4	DFP-3-2	Repeat, faster pull speed	29 cm @ 29 mm/min. Edge thickness .32, center .22 mm
60324	25.4	DFP-3-2	Repeat	54 cm @ 26 mm/min. Edge thickness .32, center .24 mm
60325	25.4	DFP-3-2	Repeat <110> (100) seed	18 cm @ 20 mm/min. Edge thickness .50, center .40 mm
60326	25.4	DFP-3-2	Repeat	38 cm @ 18 mm/min
60327	25.4	DFP-3-2	Repeat	No results, froze
60328	25.4	DFP-3-2	Std. procedure	35 cm @ 23 mm/min
60329	25.4	DFP-3-2	Repeat	65 cm @ 23 mm/min
60330	25.4	DFP-3-2	Repeat	43 cm @ 27 mm/min

Run No.	Die Width (mm)	Die Material	Experimental Variables	Results
60331	25.4	DFP-3-2	Thermal modifier #5	No results, froze
60332	25.4	DFP-3-2	Repeat	No results, froze
60333	25.4	DFP-3-2	Repeat	No results, froze
60334	25.4	DFP-3-2	Std procedure, removed thermal modifier	No results, froze
60335	25.4	DFP-3-2	Repeat adjusted RF coil	No results, froze
60336	25.4	DFP-3-2	Repeat	No results, froze
60337	25.4	DFP-3-2	Repeat	52 cm @ 20 mm/min. .5 mm @ edge, .22 mm @ center
60338	25.4	DFP-3-2	Repeat	No results, froze reaching full width
60339	25.4	DFP-3-2	Std procedure. Adjusted RF coil because of uneven spreading	No results
60340	25.4	DFP-3-2	Repeat	No results, froze @ full width
60341	25.4	DFP-3-2	Repeat	55 cm @ 23 mm/min
60342	25.4	DFP-3-2	Repeat, increased pull speed to 28 mm/min	No results, froze @ full width
60343	25.4	DFP-3-2	Repeat, reduced pull speed to 20 mm/min	No results, froze @ full width
60401	25.4	DFP-3-2	Std procedure	56 cm @ 19 mm/min
60402	25.4	DFP-3-2	Repeat	57 cm @ 24 mm/min
60403	25.4	DFP-3-2	Repeat at faster pull speed	No results, froze @ seeding
60404	25.4	DFP-3-2	Repeat	76 cm @ 27 mm/min

Run No.	Die Width (mm)	Die Material	Experimental Variables	Results
60405	25.4	DFP-3-2	Std procedure	No results, froze
60406	25.4	DFP-3-2	Repeat	56 cm @ 21 mm/min
60407	25.4	DFP-3-2	Repeat increased speed while lowering temp. after full width	56 cm @ from 26-29 mm/min
60408	25.4	DFP-3-2	Repeat at faster speed	65 cm @ 32 mm/min. .3 mm thick @ edge, .15 @ center
60409	25.4	DFP-3-2	Repeat at faster pull speed	48 cm @ 33-36 mm/min. .35 mm thick @ edge, .10 mm center. Note: 9.4 meter of ribbon grown with this die
60410	25.4	DFP-3-2	25 cm quartz insulator, thermal modifier #5, new die	No results, froze
60411	25.4	DFP-3-2	Repeat	No results, froze
60412	25.4	DFP-3-2	Repeat	No results, froze
60413	25.4	DFP-3-2	Repeat	No results, froze
60414	25.4	DFP-3-2	Std procedure, 23 cm quartz insulator. No thermal modifier	56 cm @ 27 mm/min
60415	25.4	DFP-3-2	Repeat	No results, froze
60416	25.4	DFP-3-2	Repeat	58 cm @ 29 mm/min
60417	25.4	DFP-3-2	Repeat	No results, froze @ full width
60418	25.4	DFP-3-2	Repeat, seed <121> (111)	54 cm @ 26 mm/min
60419	25.4	DFP-3-2	Repeat	56 cm @ 30 mm/min. .32 mm thick @ edge, .1 mm @ center

Run No.	Die Width (mm)	Die Material	Experimental Variables	Results
60420	25.4	DFP-3-2	Repeat	32 cm @ 30 mm/min. .35 mm thick @ edge. .1 mm center
60421	25.4	DFP-3-2	New die baked out @ 1225°C in argon/HCl	50 cm @ 20 mm/min
60422	25.4	DFP-3-2	Repeat same die	52 cm @ 25 mm/min
60423	25.4	DFP-3-2	Repeat	No results, froze
60424	25.4	DFP-3-2	Repeat	No results, froze
60425	25.4	DFP-3-2	Repeat	No results, ribbon drifts to right
60426	25.4	DFP-3-2	Repeat	No results, froze
60427	25.4	DFP-3-2	Repeat	No results, froze
60428	25.4	DFP-3-2	Repeat, rotated die 90°	No results, froze
60429	25.4	DFP-3-2	Std procedure adjusted RF coil spacing	No results, froze
60430	25.4	DFP-3-2	Repeat	No results, ribbon drifts to right and froze
60431	25.4	DFP-3-2	Repeat	No results, same as above
60432	25.4	DFP-3-2	Std. procedure, rotated die 180°	55 cm @ 23 mm/min, less drifting less drifting
60433	25.4	DFP-3-2	Repeat	No results, froze
60434	25.4	DFP-3-2	Repeat	No results, froze. Drifting to right

Run No.	Die Width (mm)	Die Material	Experimental Variables	Results
60435	25.4	DFP-3-2	Repeat	No results, froze
60436	25.4	DFP-3-2	New die. Std procedure	53 cm @ 28 mm/min
60437	25.4	DFP-3-2	Repeat	53 cm @ 23 mm/min
60438	25.4	DFP-3-2	Repeat	43 cm @ 32-36 mm/min .28 mm thick @ edge .18 @ center
60439	25.4	DFP-3-2	Std procedure	54 cm @ 25 mm/min
60440	25.4	DFP-3-2	Repeat	56 cm @ 25 mm/min
60441	25.4	DFP-3-2	Repeat	No results, froze
60442	25.4	DFP-3-2	Std procedure	16 cm @ 23 mm/min
60443	25.4	DFP-3-2	Repeat	38 cm @ 24 mm/min
60444	25.4	DFP-3-2	Repeat	39 cm @ 25 mm/min
60445	25.4	DFP-3-2	Repeat	No results
60446	25.4	DFP-3-2	Std procedure	56 cm @ 22 mm/min
60447	25.4	DFP-3-2	Repeat	58 cm @ 21 mm/min
60448	25.4	DFP-3-2	Repeat	53 cm @ 23 mm/min
60449	25.4	DFP-3-2	Std procedure	No results, ribbon drifting
60450	25.4	DFP-3-2	Repeat, adjusted coil	Seed broke, ruined die
60451	25.4	DFP-3-2	Repeat, using die from run 60435	No results, froze
60452	25.4	DFP-3-2	Repeat	No results, froze

Run No.	Die Width (mm)	Die Material	Experimental Variables	Results
60453	25.4	DFP-3-2	Repeat, rotated die 180°	No results, froze
60501	38	DFP-3-2	New die 38 mm wide (# 15) with five 0.80 mm dia. capillary holes	No results, froze @ 26 mm width
60502	38	DFP-3-2	Repeat	No results, froze @ 25 mm width
60503	38	DFP-3-2	Repeat	No results, froze @ 24 mm width
60504	38	DFP-3-2	Repeat	No results, froze
60505	38	DFP-3-2	Repeat	10 cm @ 16 mm/min
60506	38	DFP-3-2	Std for 38 mm die	44 cm @ 17 mm/min. .5 mm thick @ edge, .65 mm @ center
60507	38	DFP-3-2	Repeat	No results, froze
60508	38	DFP-3-2	Repeat, raised coil	No results, froze
60509	38	DFP-3-2	Std for 38 mm die	No results, froze
60510	38	DFP-3-2	New die. Std for 38 mm	No results
60511	38	DFP-3-2	Repeat	36 cm @ 18 mm/min. Resistivity decreases in regions between capillary holes
60512	38	DFP-3-2	Std for 38 mm die	No results
60513	38	DFP-3-2	Repeat	No results
60514	38	DFP-3-2	38 mm die cleaned in 3:2:1 etch over weekend	No results

Run No.	Die Width (mm)	Die Material	Experimental Variables	Results
60515	25.4	DFP-3-2	Std procedure 25.4 mm die	No results
60516	25.4	DFP-3-2	Repeat	No results
60517	25.4	DFP-3-2	Repeat	20 cm @ 22 mm/min
60518	25.4	DFP-3-2	Std procedure	No results
60519	25.4	DFP-3-2	Repeat	No results
60520	25.4	DFP-3-2	Std procedure, new die 25.4 mm	58 cm @ 18 mm/min
60521	25.4	DFP-3-2	Repeat	91 cm @ 21 mm/min
60422	25.4	DFP-3-2	Repeat	90 cm @ 20 mm/min
60523	25.4	DFP-3-2	Repeat	60 cm @ 23 mm/min
60524	25.4	DFP-3-2	Std procedure 25.4 mm die <121> (101) seed	No results, froze @ full width
60525	25.4	DFP-3-2	Repeat	55 cm @ 21 mm/min. .45 mm thick @ edge. .40 @ center
60526	25.4	DFP-3-2	Repeat <110> (112) seed	58 cm @ 24 mm/min
60527	25.4	DFP-3-2	Repeat	81 cm @ 23 mm/min
60601	38	DFP-3-2	Std procedure 38 mm die	No results, froze
60602	38	DFP-3-2	New die	Froze @ full width
60603	38	DFP-3-2	Repeat	38 cm @ 17 mm/min
60604	38	DFP-3-2	Repeat	Froze
60605	38	DFP-3-2	Repeat	No results, froze

Run No.	Die Width (mm)	Die Material	Experimental Variables	Results
60606	25.4	DFP-3-2	Top of capillary slot modified to vee grove using a 184 mm dia. grinding wheel with a 45° included angle	6.3 cm @ 18 mm/min
60607	25.4	DFP-3-2	Repeat	Froze
60608	25.4	DFP-3-2	Repeat	Froze
60609	25.4	DFP-3-2	Repeat	Froze
60610	25.4	DFP-3-2	Repeat	Froze
60611	25.4	DFP-3-2	Repeat. Raised rf coil	50 cm @ 20 mm/min. Broad central dip in transverse resistivity profile
60612	25.4	DFP-3-2	Repeat	65 cm @ 23 mm/min
60613	25.4	DFP-3-2	Repeat	Froze
60614	25.4	DFP-3-2	Repeat	48 cm @ 20 mm/min
60615	25.4	DFP-3-2	Repeat	91 cm @ 20-26 mm/min
60616	25.4	DFP-3-2	Repeat	No results
60701	25.4	DFP-3-2	New die. Duplication of 60606. Baked out in argon/HCl	No results
60702	25.4	DFP-3-2	Repeat	85 cm @ 18 mm/min. .50 mm thick at edge, .51 mm center
60703	25.4	DFP-3-2	Repeat	Froze at full width
60704	25.4	DFP-3-2	Repeat	Froze
60705	25.4	DFP-3-2	Repeat. New RF coil	57 cm @ 22 mm/min

Run No.	Die Width (mm)	Die Material	Experimental Variables	Results
60706	25.4	DFP-3-2	Repeat	94 cm @ 24 mm/min
60707	25.4	DFP-3-2	Repeat	Froze
60708	38	DFP-3-2	Std procedure	Froze during seeding
60801	38	DFP-3-2	New die, 13B with 152 mm top curvature, .68 mm edge thickness and 0.4 mm capillary slot	53 cm @ 14 mm/min. .64 mm thick at edge .68 mm center
60802	38	DFP-3-2	Repeat	6 cm @ 13 mm/min
60803	38	DFP-3-2	Repeat	22 cm @ 17-19 mm/min
60804	38	DFP-3-2	Repeat	29 cm @ 16 mm/min
60805	38	DFP-3-2	Repeat	No results
60806	38	DFP-3-2	Repeat	Froze @ full width
60807	38	DFP-3-2	Repeat. Rotated die 180°	16 cm @ 21 mm/min
60808	38	DFP-3-2	New die #13B. Std procedure	Edge of die touched lower shield. Could not run
60809	38	DFP-3-2	Repeat. Filed away lower shield where die touched	59 cm @ 16 mm/min. Ribbon shattered during handling
60810	38	DFP-3-2	New die #15A	10 cm @ 13 mm/min. Rough ribbon surface
60811	38	DFP-3-2	Repeat. Seed <121>	26 cm @ 16 mm/min
60812	38	DFP-3-2	Repeat	Ribbon drifting. Froze @ full width

Run No.	Die Width (mm)	Die Material	Experimental Variables	Results
60901	38	DFP-3-2	Four port argon thermal modifier system used. Open pull port. Bellows removed	No results. Froze
60902	38	DFP-3-2	New die #13B plus argon thermal modifier	Demonstrated that drifting could be reversed by changing argon flow
60903	38	DFP-3-2	Repeat, evaluate argon thermal modifier	No ribbon
60904	38	DFP-3-2	Repeat	No results. Center of die too hot compared to edges
60905	25.4	DFP-3-2	Argon thermal modifier used with flat die	No results. Froze
60906	25.4	DFP-3-2	Repeat	Froze
60907	25.4	DFP-3-2	Repeat using full width seed. <110> (100)	Froze
60908	25.4	DFP-3-2	Repeat @ faster pull speed (17mm/min)	Edge colder than center Ribbon pulled out in center
60909	25.4	DFP-3-2	Repeat. Spreading responds to argon flow changes	Ribbon froze after short distance
60910	25.4	DFP-3-2	Repeat. Slow pull speed and higher argon flow at ends of ribbon	Froze after short distance
60911	25.4	DFP-3-2	Repeat @ 11 mm/min	Meniscus hotter in center, ribbon pulled out
60912	25.4	DFP-3-2	Repeat @ 5 mm/min	Same as above

Run No.	Die Width (mm)	Die Material	Experimental Variables	Results
60913	25.4	DFP-3-2	Repeat @ 9 mm/min	Same as above. Center region too hot
60914	25.4	DFP-3-2	Repeat, rotated die 180°. Speed 15 mm/min	Meniscus still too hot in center
60915	25.4	DFP-3-2	Repeat, upper and lower shield openings modified to navette shape. Argon flow about 3 CFH directed @ ends of die	112 cm ribbon @ 14 mm/min. Very smooth surface, few SiC particles
60916	25.4	DFP-3-2	Repeat	90 cm @ 14 mm/min
60917	25.4	DFP-3-2	Repeat with diffuse argon flow of 25 CFH from bottom of furnace in addition to flow @ die ends	83 cm @ 14 mm/min
60918	25.4	DFP-3-2	Repeat of conditions in 60915. Study width response to argon flow changes	Good response of ribbon width changes to argon flow
60919	38	DFP-3-2	New die #15A.	Power failure of rf system
60920	38	DFP-3-2	Repeat	Die chipped, could not reach full width
60921	38	DFP-3-2	New die #13B. Finer resolution argon flow meters installed. Argon flow @ die ends 3 CFH	47 cm @ 14 mm/min
60922	38	DFP-3-2	Repeat	No results
60923	38	DFP-3-2	Repeat	Froze
60924	38	DFP-3-2	Repeat with argon flow of 1.5 CFH @ die ends	42 cm @ 13 mm/min

Run No.	Die Width (mm)	Die Material	Experimental Variables	Results
60925	38	DFP-3-2	Repeat with argon flow of 3.5 CFH @ die ends	Froze
60926	38	DFP-3-2	Repeat. Rotated die 90°.	45 cm @ 14 mm/min
60927	38	DFP-3-2	Repeat, same die as used in run #60918	20 cm @ 17 mm/min
60928	38	DFP-3-2	Repeat	Ribbon froze at speed of 19 mm/min
60929	38	DFP-3-2	Repeat, attempting higher pull speed	Seed broke and ruined die
61001	38	DFP-3-2	New die #15A.	67 @ 15 mm/min
61002	38	DFP-3-2	Repeat at 16 to 18 mm/min	No results
61003	38	DFP-3-2	Repeat	75 cm @ 17 to 27 mm/min. At 27 mm/min edge thickness is .55 mm. Center thickness is .38 mm
61004	38	DFP-3-2	Repeat at 25-30 mm/min	No results, froze
61005	38	DFP-3-2	Repeat	Froze
61006	38	DFP-3-2	Repeat	35 cm @ 25 mm/min. .45 mm thick at edge, .40 at center
61007	38	DFP-3-2	Repeat	No results, froze
61008	38	DFP-3-2	Repeat @ 20 mm/min	37 cm @ 20 mm/min. Smooth surface
61009	38	DFP-3-2	New 2 piece die 17-38A	No results, froze
61010	38	DFP-3-2	Repeat	122 cm @ 18-20 mm/min

Run No.	Die Width (mm)	Die Material	Experimental Variables	Results
61011	38	DFP-3-2	Repeat	100 cm @ 22-25 mm/min .45 mm thick at edge, .35 mm center. Less variation in transverse dopant profile than with one piece die
61012	38	DFP-3-2	Repeat @ 30 mm/min	No results
61013	38	DFP-3-2	Repeat	No results
61014	38	DFP-3-2	Repeat. Argon flow die ends 6 CFH	80 cm @ 25-30.5 mm/min .45 mm thick at edge, .25 mm center
61015	38	DFP-3-2	Repeat	No results, froze
61016	38	DFP-3-2	Repeat @ 25 mm/min	50 cm. Controlled width with argon flow rather than temp.
61017	38	DFP-3-2	Repeat	131 cm @ 25 mm/min
61018	44	DFP-3-2	New setup for 50 mm growth	Froze @ 40 mm width
61019	44	DFP-3-2	Repeat	25 mm @ 15 mm/min. Width 43-44 mm. Smooth surface
61020	50	DFP-3-2	New 2 piece die #2P501	Froze reaching 44 mm width
61021	50	DFP-3-2	Repeat	Same as above
61022	50	DFP-3-2	Repeat	No results
61101	50	DFP-3-2	New die 2P502. Shield slots opened to form a navette shape	109 cm ribbon. 50 cm wide @ 14 mm/min

Run No.	Die Width (mm)	Die Material	Experimental Variables	Results
61102	50	DFP-3-2	Repeat of 61101 conditions	Ribbon separated from die after 1.5 cm of growth
61103	50	DFP-3-2	All components carefully aligned. Die rotated 90° from run 61102	Could not grow without freezing to die. Die damaged
61201	38	DFP-3-2	Gain experience with 38 mm die while waiting for 50 mm dies	91 cm x 38 mm ribbon grown at 19 mm/min
61202	38	DFP-3-2	Die has 0.75 mm diameter capillary holes and 101 mm radius top (die for fun 61201 had 0.38 mm capillary slot and 152 mm radius top	80 cm x 38 mm ribbon grown at 18 mm/min
61203	38	DFP-3-2	Repeat at faster speed	Froze at 23 mm/min speed and 24 mm width
61204	38	DFP-3-2	Repeat	Identical results
61205	38	DFP-3-2	Die with 1.05 mm edge thickness, 1.93 mm central thickness, and 254 mm top radius	Heavy residue from vacuum bake-out. Grew 90 cm x 49.4 mm ribbon, 0.72 mm thick. Ribbon has very heavy SiC particle density ($7.5/cm^2$). Ribbon split while being measured
61206	50	DFP-3-2	New die. Baked out under argon flow instead of vacuum	95 cm long ribbon, similar to 61205 (high SiC density). Growth speed 16 mm/min
61207	50	DFP-3-2	Same die. Checking to if rerunning die and slower growth speed (9 mm/min) affect SiC density	SiC density was reduced

Run No.	Die Width (mm)	Die Material	Experimental Variables	Results
61208	50	DFP-3-2	Same die. Checking to see if rerunning die and faster growth speed affect SiC density (speed = 24 mm/min	SiC density lower yet. Ribbon is 86 cm long, 0.8 mm thick at the edge and 0.5 mm thick over large central region
61209	50	DFP-3-2	New die, 2P502. Baked out in argon	Froze during seeding
61210	50	DFP-3-2	Same conditions. 15-18 mm/min growth speed	120 cm long ribbon, 49.6 mm wide. High SiC density (0.76/cm^2)
61211	50	DFP-3-2	Same die, repeat	44 cm long ribbon, very smooth (0.03 SiC particles/cm^2)
70101	50	DFP-3-2	Fourth run with die, to see if SiC particle density changes. Speed = 18 mm/min	Very smooth (0.014 particles/cm^2) ribbon 1.2 m long x 4.9 cm wide x 0.2-0.8 mm thick
70102	50	DFP-3-2	Repeat	Die ruined by Si flow into die holder
70103	50	DFP-3-2	New die, 1.2 mm thick at edges and 1.9 mm thick at midpoint. 0.46 mm capillary slot. 19 mm/min growth speed	"Zero" SiC particle density on 0.56 m x 4.9 cm x 0.07-0.9 mm thick ribbon. Reflective surface, large grains. Thinnest ribbon grown to date (less than 0.27 mm except for extreme edges)
70104	50	DFP-3-2	Repeat	Froze before reaching full width
70106	50	DFP-3-2	Repeat	Same. Having problems with alignment of furnace components

Run No.	Die Width (mm)	Die Material	Experimental Variables	Results
70107	50	DFP-3-2	Repeat. Die had shifted and froze un-even in holder. Lower heat shield was shimmed to make it even with die top	1.08 m long by 4.93 cm wide ribbon, 0.23 to 0.90 mm thick. Surface looks good
70108	50	DFP-3-2	Repeat	Ribbon shattered while growing. Apparently seed holder caught on pull port
70109	50	DFP-3-2	Repeat, improved alignment	0.96 m x 4.9 cm x .35-.90 mm thick ribbon, at 18 mm/min speed
70110	50	DFP-3-2	Repeat with higher pulling speed (27 mm/min)	.57 m x 4.9 cm x .32-.88 mm thick ribbon. Ran out of melt. Die holder and susceptor cracked
70111	50	DFP-3-2	6 mm taller susceptor support used. New die	Ribbon froze at 0.66 mm length. Much higher operating temperature required. Ribbon 4.9 cm wide x .30-.88 mm thick
70201	38	DFP-3-2	Crucible from run 61001 etched to re-move residual Si, and reused	Crucible worked OK. Grew 76 cm ribbon, again nearly emptied crucible
70202	38	DFP-3-2	Crucible from last run etched again and re-used	Crucible again worked OK. Grew 88 cm ribbon, nearly emptying crucible
70203	38	DFP-3-2	Crucible etched only lightly (not enough to remove Si) and reused	Froze after 16 cm of growth

Run No.	Die Width (mm)	Die Material	Experimental Variables	Results
70204	38	DFP-3-2	Repeat (same melt)	44 cm ribbon. Crucible worked OK, but deformed during run
70205	50	DFP-3-2	New die, 2PA501, with thicker walls and reinforced edges. Growth speed 19 mm/min	Grew 121 cm long ribbon, but melt flooded into space between die and holder because of re-entrant corners on die. Ribbon thickness 0.5-0.6 mm in central region
70206	50	DFP-3-2	Repeat at 30 mm/min speed	29 cm long ribbon, 0.25-0.3 mm thick in central region. Die split after run
70301	50	DFP-3-2	New die. Reentrant corners filed away in critical areas to avoid flooding	No flooding of melt. Grew 64 cm x 50 mm ribbon, 0.4 to 0.55 mm thick in central region
70302	50	DFP-3-2	Repeat 70301 conditions	None
70303	50	DFP-2	Installed new quartz insulator tube. Adjusted right argon flow balancing tube.	Froze, unable to maintain full-width growth
70304	50	DFP-2	Repeat	Silicon splashed on die and ruined it.
70305	38	DFP-3-2	Standard growth conditions, to produce ribbons for cutting experiments	114-cm ribbon
70306	50	DFP-3-2	Photographic recording of meniscus heights, at speeds of 1.5-3.2 cm/min. New die	Good ribbon. Meniscus heights under evaluation. Susceptor broke on cool-down. Photos not sharp

Run No.	Die Width (mm)	Die Material	Experimental Variables	Results
70307	50	DFP-3-2	As above, except constant pull speed of 1.9 cm/min, while varying temperature and argon flows	92-cm-long ribbon. Meniscus heights under evaluation. Photos not sharp
70308	50	DFP-3-2	Meniscus heights photographed at constant temperature, but varying argon flows and pull speed. Also to measure ribbon stress.	Five photos made. Ribbon is 120 cm long, 0.14-0.19 mm thick in central region. Stress calculated to be 3 x 10^8 dynes/cm^2 by measuring split widths. Photos not sharp.
70309	38	DFP-3-2	Standard conditions, to grow ribbon for cutting experiments. Also increased argon flow from furnace bottom to avoid fogging of quartz furnace tube.	90 cm x .55 mm thick ribbon grown. No change in fogging
70310	38	DFP-3-2	Standard conditions, to grow ribbons for cutting experiments	114 cm x .4 mm x 38 mm wide ribbon
70311	50	DFP-3-2	New die 2PA-502.	None. Die not seated in holder. Flooded
70312	50	DFP-3-2	2P501 die (new). Photograph of meniscus directly (no water filter).	Photos of meniscus much sharper without water filter. Good looking ribbon
70313	50	Ultracarbon UT-44	New die. New graphite material. Design 2PA501.	Two short pieces of ribbon grown, but froze out. Die ruined

Run No.	Die Width (mm)	Die Material	Experimental Variables	Results
70314	38	DFP-3-2	Standard process to grow ribbon for cutting experiments	78-cm-long ribbon grown
70401	50	DFP-3-2	Evaluate thicker die top (1.3-mm edges, 2-mm center). 20-mm/min growth speed	27-cm ribbon. Very rough. 0.95 mm thick at edges/.66 mm thick in center
70402	50	DFP-3-2	Repeat.	110-cm-long ribbon grown, 0.39 mm thick in center
70403	50	DFP-3-2	Repeat.	All growth attempts with this die have been easy to start
70404	50	DFP-3-2	Repeat. Die was splayed from previous run. Argon flow directed at front of furnace tube to avoid oxide buildup	Easy to start. 111-cm-long ribbon grown. Quartz tube stayed clear through run
70405	50	DFP-3-2	Repeat. Splayed die closed again at growth temperature. Will pull crucible nearly empty for reuse	Crucible OK for reuse
70406	50	DFP-3-2	Reused crucible from previous run. Photograph meniscus with this 1.3-mm to 2-mm-thick die	Five photos made. Will be analyzed. 64-cm-long ribbon grown
70407	50	UT-44	Evaluate new die material and design. Die is 0.82 mm thick at edges and 1.99 mm thick in middle. Top has 1.7-mm deviation from flatness.	Meniscus photographed. Nice looking ribbon 35 cm long x 50.1 mm wide x .55 mm thick at edges (.28 mm in middle).

Run No.	Die Width (mm)	Die Material	Experimental Variables	Results
70408	50	UT-44	Repeat.	Temperature lowered too far. Ribbon froze
70409	50	UT-44	Repeat, photograph meniscus at 20-mm/min growth speed	80 cm x 50 mm x .50 mm thick ribbon. Three photos made
70410	50	UT-44	Repeat, more meniscus photographs	Five photos made. 110 cm x 50 mm x .4 mm thick ribbon
70411	50	UT-44	Repeat, to explore faster pull speeds.	Attained speed of 40 mm/min for a distance of 11 cm. Then froze. Dendritic surface morphology developed at fast speeds. Overall length is 104 cm. Thickness ranged from .30 to .15 mm (the latter at 40 mm/min).
70412	50	UT-44	Repeat, but at slow speed (18 mm/min) to see if dendritic surface morphology recurred.	No dendritic features. Ribbon is thicker (.48 mm) at slow speed.
70413	50	SiC/ Graphite	Evaluate SiC-coated graphite die. 20/mm min growth speed.	Very smooth reflective ribbon. Zero SiC partiticle density. 82 cm x 50 mm ribbon. .85 mm thick at edges/.35 mm thick in center.
70414	50	SiC/ Graphite	Repeat at 26 mm/min.	Thinner ribbon (.65 edge/.27 center) 23 cm long. Again zero SiC density but ribbon has some morphological features in a thin central strip.
70415	50	SiC/ Graphite	Repeat.	Temperature lowered too far. Ribbon froze.

Run No.	Die Width (mm)	Die Material	Experimental Variables	Results
70416	50	SiC/ Graphite	Repeat, 20-mm/min speed.	62-cm-long, ribbon. Thicker (.6-.70 in center). Two SiC particles on surface (density .006/cm^2). Same rough features present as in run 70414.
70417	50	SiC/ Graphite	Repeat, 20-mm/min speed. Photograph meniscus.	Very smooth, thin (.09-.15 mm in central region) ribbon. Zero SiC particle density. Similar appearance to run 70413.
70418	50	SiC/ Graphite	Repeat of above.	79-cm-long, smooth thin ribbon (.11-.18 mm in central region). One particle (.003/cm^2) on entire surface.
70501	50	SiC/ Graphite	Die material performance test. 18 mm/min growth speed.	60 cm x 5 cm x .32-.70 mm ribbon. Zero SiC density.
70502	50	SiC/ Graphite	Repeat.	Ribbon pulled out upon reaching full width. Seed broke.
70503	50	SiC/ Graphite	Repeat. New thick susceptor.	None. Could not seed.
70504	50	SiC/ Graphite	Repeat. Added argon flow directed at backside of ribbon. 20-25 mm/min growth speed.	82 cm x 5 cm x 0.30 to 0.68 mm ribbon. Zero SiC particles. Backside of ribbon clean, but now front side has oxide power coating. Seed was loose and ribbon shifted laterally several times.

Run No.	Die Width (mm)	Die Material	Experimental Variables	Results
70505	50	SiC/ Graphite	Repeat. But no argon flow to ribbon back-side. 16 mm/min growth speed.	76 cm x 5 cm x 0.37 to 1.00 mm thick ribbon. 0.071 SiC particles per cm^2. Susceptor broke during unloading.
70506	50	SiC/ Graphite	Repeat. Heat shields placed at edges of ribbon. New susceptor.	Froze upon reaching full width.
70507	50	SiC/ Graphite	Repeat. 19 mm/min growth speed. Meniscus photos made. 1.2 cm x 2 cm heat shields placed on susceptor rim near ribbon edges.	61 cm x 5 cm x .25 to .55 mm ribbon. Zero SiC density.
70508	50	SiC/ Graphite	Repeat. 16 mm/min speed.	31 cm x 4.4 cm x .95 to 1.20 mm ribbon. 0.013 SiC particles/ cm^2. Stress level 4.8×10^8 dynes/cm^2.
70509	50	SiC/ Graphite	Repeat.	72 cm x 4.7 cm x .50 to 1.04 mm ribbon. Difficult to reach full width with shields. SiC density 0.002/cm^2.
70510	50	SiC/ Graphite	Repeat.	Froze at 19 cm length. .021 SiC particles/ cm^2. Width = 4.3 cm.
70511	50	SiC/ Graphite	Repeat. Heat shields at edges re-moved, 25 mm/min speed.	120 cm x 5 cm x .16 to .62 mm ribbon. Zero SiC density.
70512	50	SiC/ Graphite	Repeat.	Froze during seeding.

Run No.	Die Width (mm)	Die Material	Experimental Variables	Results
70513	50	SiC/ Graphite	Repeat. 18 mm/min speed.	120 cm x .30 to .88 mm ribbon. 0.15 SiC particles/cm^2. Right side pulled out during seeding.
70514	50	SiC/ Graphite	Repeat.	Could not achieve proper seeding conditions.
70601	50	SiC/ Graphite	Replaced upper and lower shields. They had warped. Growth speed 16 mm/min	91 cm x 5 cm x .40 to .68 mm ribbon. 0.13 SiC particles/ cm^2. Rough surface.
70602	50	SiC/ Graphite	Repeat (continuing long-term evaluation of die first used in run 70413). 20 to 30 mm/min growth speed.	121 cm x 5 cm x 0.18 to 0.63 mm ribbon. 0.005 SiC particles/ cm^2.
70603	50	SiC/ Graphite	Repeat @ 17 mm/min growth speed. Took meniscus photos.	130 cm x 5 cm x 0.15 to 0.79 mm thick ribbon. 0.002 SiC particles/ cm^2.
70604	50	SiC/ Graphite	Repeat (continuation)	Could not seed.
71001	100	DFP-3-2	Initial start-up of 100 mm system	Argon ionization in growth chamber before growth temperature was reached.
71002	100	DFP-3-2	Added third quartz tube between furnace shell and quartz insulator.	Ionization still occurs, but at slightly higher temperature

C-3

Run No.	Die Width (mm)	Die Material	Experimental Variables	Results
71003	100	DFP-3-2	Lowered coil inductance from 17 to 10.8 μH and insulated hotzone with 2 layers of 6.4 mm thick graphite felt.	Eliminated ionization, reduced growth power to 16 kW. Seeded at 96 mm width with a 100 mm seed. Ribbon was thin at ~ 20 mm from each edge and one side pulled off after 13 mm of growth
71004	100	DFP-3-2	Repeat, but using 80 mm wide seed, and keeping ribbon narrower so that meniscus is lower.	Seeded full width, gradually increased width. Ribbon was thin about 15 mm from each edge, and finally pulled off at a width of 95 mm, after 170 mm of growth. Ribbon fell out of seed holder and shattered during withdrawal from furnace.
71005	100	DFP-3-2	25 mm diameter holes cut in upper and lower heat shields, 20 mm from each edge. Purpose is to allow more heat loss and hence make ribbon thicker in spots where it is now thin and pulling off	Started several growth attempts with 80 mm wide seeds. Thickness seems more uniform, but could not spread growth without freezing. Die found to be cracked after this run.
71006	100	DFP-3-2 (uncertain)	New die and holder. Will use 100 mm seeds to attain higher central meniscus.	Die swelled, distorted, and cracked in 8 places. Obviously there is a material mix-up.

Appendix II. Dimensional Characteristics of Silicon Ribbons Grown During Contract

August 1975 to November 1977

Ribbon Run No.	Seed Orientation Axis	Seed Orientation Surf.	Usable Length (cm)	Width (mm) Max	Width (mm) Min	Thickness (mm) Seed Max	Thickness (mm) Seed Min	Thickness (mm) Tail Max	Thickness (mm) Tail Min
50805	0	0	38	8.6	6.7	1.01	.00	1.03	.00
50806	0	0	65	8.1	6.2	1.00	.00	1.05	.00
50807	0	0	25	8.7	7.6	1.10	.00	1.15	.00
50808	0	0	34	8.4	8.1	1.06	.00	1.21	.00
50809	0	0	114	7.3	6.7	1.01	.00	1.05	.00
50811	0	0	28	8.0	7.1	1.35	.00	1.35	.00
50825	0	0	32	4.7	4.2	1.58	.00	1.60	.00
50826	0	0	32	5.5	3.8	1.25	.00	1.43	.00
50909	0	0	23	26.2	25.8	.70	.35	.67	.39
50911	110	111	24	25.7	24.4	.65	.35	.62	.41
50916	110	100	46	26.0	.0	.73	.54	.62	.33
50919	110	100	90	26.0	.0	.55	.23	.65	.36
50926	110	100	18	26.0	.0	.65	.57	.65	.56
50927	110	100	40	26.0	.0	.53	.40	.54	.34
50928	110	100	45	26.0	.0	.49	.32	.50	.31
51003	110	112	49	25.6	23.6	.67	.51	.63	.46
51005	110	112	50	26.1	24.7	.63	.44	.66	.45
51007	110	112	51	26.4	23.0	.75	.53	.73	.45
51008	110	112	44	25.6	23.7	.63	.40	.66	.43
51012	100	110	91	25.9	24.3	.69	.49	.68	.47
51013	100	110	20	26.0	25.0	.64	.42	.68	.51
51014	100	110	54	25.7	21.2	.69	.62	.62	.34
51015	110	100	84	25.1	23.4	.61	.35	.64	.34
51016	110	100	52	24.8	17.0	.73	.48	.60	.39
51017	110	100	22	24.7	23.8	.64	.45	.44	.26
51018	110	100	23	25.1	25.0	.72	.43	.67	.41
51019	110	100	56	25.0	23.6	.67	.44	.55	.35
51021	110	100	54	26.2	24.4	.65	.49	.66	.38
51022	110	100	63	25.6	23.8	.63	.38	.59	.28
51023	110	100	63	25.5	24.1	.62	.35	.59	.39
51024	110	100	24	26.2	12.5	.63	.35	.64	.26
51025	110	100	58	25.7	23.3	.54	.31	.56	.22
51026	110	100	62	25.4	24.6	.62	.42	.62	.37
51027	110	100	59	24.9	24.5	.51	.29	.52	.26
51102	110	112	12	.0	.0	.00	.00	.00	.00
51104	110	100	59	25.3	23.5	.54	.40	.51	.36
51107	110	112	49	25.5	24.1	.45	.29	.50	.28
51110	110	100	10	25.7	23.3	.55	.50	.55	.50
51114	110	100	48	25.4	24.4	.50	.36	.50	.34
51115	110	100	87	25.6	25.2	.46	.30	.57	.35

Ribbon Run No.	Seed Orientation Axis	Surf.	Usable Length (cm)	Width (mm) Max	Min	Thickness (mm) Seed Max	Min	Tail Max	Min
51118	110	100	57	25.2	24.8	.46	.31	.45	.29
51119	110	100	54	24.7	24.5	.43	.28	.46	.29
51120	110	100	21	24.9	23.8	.45	.32	.47	.25
51201	110	100	16	24.6	17.4	.47	.50	.50	.35
51202	110	100	60	25.0	24.1	.52	.42	.50	.45
51203	110	100	19	25.5	24.1	.76	.50	.45	.36
51205	110	100	36	25.0	24.9	.55	.45	.50	.45
51207	110	100	20	24.5	22.2	.61	.40	.26	.22
51208	110	100	46	24.6	24.3	.50	.40	.46	.36
51209	110	112	53	.0	.0	.45	.35	.00	.00
51210	110	112	46	24.9	20.6	.67	.50	.65	.50
51213	110	112	32	23.5	14.0	.38	.32	.53	.40
51214	110	100	55	24.8	23.2	.48	.40	.45	.41
51216	110	100	39	25.3	22.7	.71	.52	.73	.45
51217	110	100	57	24.7	23.4	.74	.48	.75	.47
51218	110	100	45	22.9	22.4	.55	.50	.60	.50
60102	110	100	56	25.5	24.9	.53	.39	.50	.33
60103	110	100	51	25.2	24.2	.48	.31	.45	.27
60104	110	112	60	25.4	24.3	.49	.29	.52	.33
60105	110	100	58	24.9	18.8	.50	.45	.50	.45
60110	110	100	46	24.8	23.6	.53	.42	.50	.37
60111	110	100	94	25.4	23.8	.00	.00	.00	.00
60112	110	100	90	24.9	23.4	.45	.35	.50	.27
60114	110	100	33	25.4	22.7	.50	.45	.53	.36
60115	110	100	36	25.2	20.1	.50	.40	.40	.30
60116	110	100	31	25.2	22.4	.53	.42	.37	.28
60119	110	100	28	25.4	25.1	.55	.50	.54	.38
60120	110	100	95	.0	.0	.00	.00	.00	.00
60202	110	100	96	24.6	23.7	.50	.32	.47	.30
60203	110	100	25	25.5	22.2	.57	.38	.55	.25
60206	110	100	9	23.1	18.1	.62	.70	.60	.64
60209	110	100	45	25.9	24.2	.80	.90	.64	.90
60212	110	111	55	25.7	25.1	.60	.50	.60	.40
60213	110	111	77	25.6	25.4	.60	.85	.00	.00
60216	110	100	40	24.6	24.2	.70	.80	.55	.65
60217	110	100	18	24.4	24.2	.60	.85	.42	.52
60303	110	111	55	24.9	22.5	.47	.43	.45	.35
60304	100	110	55	25.5	22.6	.45	.42	.42	.22
60309	100	110	53	25.6	23.4	.47	.50	.42	.45
60310	100	110	23	25.2	23.9	.35	.35	.38	.40
60312	111	110	41	24.7	21.7	.32	.32	.35	.37
60318	100	110	44	25.6	23.7	.44	.40	.45	.37
60320	100	110	55	25.3	24.3	.42	.38	.36	.30
60322	111	112	57	24.7	24.0	.40	.34	.41	.25
60323	111	112	29	24.6	22.0	.30	.27	.32	.22
60324	111	112	54	24.4	22.2	.35	.28	.32	.24
60325	110	100	18	23.9	18.6	.65	.70	.50	.40
60326	110	100	38	25.5	21.9	.45	.38	.54	.46
60328	110	100	35	25.3	25.0	.45	.42	.40	.28
60329	110	112	56	24.8	22.7	.30	.25	.40	.28

Ribbon Run No.	Seed Orientation Axis	Seed Orientation Surf.	Usable Length (cm)	Width (mm) Max	Width (mm) Min	Thickness (mm) Seed Max	Thickness (mm) Seed Min	Thickness (mm) Tail Max	Thickness (mm) Tail Min
60330	110	112	43	25.4	24.7	.30	.26	.38	.30
60337	100	110	52	25.2	18.0	.40	.27	.50	.22
60341	100	110	55	25.1	23.7	.40	.35	.48	.32
60401	100	110	56	26.2	25.8	.50	.35	.50	.37
60402	100	110	57	25.7	25.2	.45	.32	.45	.30
60404	110	100	76	26.4	24.6	.40	.21	.50	.32
60406	100	110	56	25.8	25.0	.52	.36	.52	.24
60407	100	110	56	.0	.0	.00	.00	.00	.00
60408	100	110	56	25.0	24.2	.30	.16	.30	.15
60409	100	110	48	24.8	23.7	.30	.15	.35	.10
60414	110	100	56	25.6	25.0	.45	.25	.35	.20
60416	100	110	58	25.4	23.6	.45	.22	.38	.18
60418	121	111	54	25.4	20.5	.45	.22	.35	.10
60419	121	111	56	25.2	24.5	.40	.22	.32	.10
60420	121	111	32	25.2	25.0	.32	.19	.35	.15
60421	121	101	50	25.2	22.4	.48	.37	.48	.32
60422	121	101	52	25.0	23.1	.45	.25	.43	.25
60432	100	110	55	24.9	24.7	.40	.30	.00	.00
60436	100	110	52	24.8	24.1	.48	.41	.00	.00
60437	121	111	55	25.2	24.1	.40	.28	.45	.32
60438	121	111	43	25.0	22.9	.35	.23	.28	.18
60439	121	111	54	25.5	24.1	.45	.29	.42	.30
60440	121	111	56	24.5	24.3	.40	.25	.39	.24
60442	121	111	16	24.4	23.1	.42	.27	.42	.25
60443	121	111	38	24.3	20.5	.40	.32	.36	.16
60444	121	111	39	24.4	24.3	.42	.19	.45	.20
60446	100	110	56	24.4	17.2	.38	.25	.38	.22
60447	121	111	58	24.6	19.7	.35	.19	.45	.21
60448	121	101	53	24.4	24.1	.45	.20	.40	.15
60506	100	110	46	38.2	37.8	.55	.65	.50	.65
60511	110	112	36	39.2	37.4	.43	.55	.44	.53
60520	110	112	58	25.2	25.0	.52	.45	.51	.45
60521	121	101	91	24.7	22.7	.40	.38	.40	.28
60522	110	112	90	25.2	24.8	.40	.35	.45	.28
60523	110	112	63	24.7	24.5	.42	.30	.39	.30
60525	121	101	55	24.7	24.6	.45	.40	.45	.40
60526	110	112	58	24.6	23.3	.40	.20	.40	.25
60527	110	112	81	25.0	24.3	.40	.20	.50	.25
60612	110	112	65	24.4	23.7	.47	.42	.40	.32
60702	110	112	85	24.8	23.2	.45	.50	.50	.51
60801	110	112	53	38.1	37.9	.81	.67	.68	.64
60803	110	112	22	38.0	.0	.65	.57	.63	.59
60915	110	100	112	37.7	37.5	.75	.50	.60	.49
60916	110	100	90	37.6	37.4	.92	.74	.71	.60
60917	110	100	83	37.5	37.4	.80	.58	.80	.63
60918	110	100	90	38.0	.0	.77	.64	.83	.68
60920	110	100	54	34.0	.0	.89	.73	.80	.53
60924	110	100	42	38.0	.0	1.04	.75	1.10	.75
60926	110	100	45	38.0	.0	.95	.85	.77	.56
60927	110	100	20	38.0	.0	1.45	1.15	1.00	.80

Ribbon Run No.	Seed Orientation Axis	Seed Orientation Surf.	Usable Length (cm)	Width (mm) Max	Width (mm) Min	Thickness (mm) Seed Max	Seed Min	Tail Max	Tail Min
60928	110	100	23	38.0	.0	1.05	.82	1.00	.84
61001	110	100	67	38.0	.0	1.10	.80	1.18	.80
61003	110	100	75	38.0	.0	.75	.55	.55	.38
61006	110	100	35	38.0	.0	.65	.58	.45	.40
61008	110	100	37	38.0	.0	.48	.47	.50	.48
61010	110	100	122	38.0	.0	.68	.50	.63	.40
61011	110	100	100	38.0	.0	.48	.42	.44	.32
61014	110	100	80	38.0	.0	.56	.50	.43	.28
61016	110	100	50	38.0	.0	.40	.28	.60	.27
61017	110	100	131	38.0	.0	.60	.41	.55	.35
61019	110	100	21	43.6	41.4	.70	.43	.78	.68
61020	110	100	17	43.7	42.9	1.40	.82	1.50	1.10
61101	110	100	109	49.5	49.1	1.20	.60	1.20	.50
61201	110	100	91	38.1	37.2	.80	.72	.61	.51
61202	110	100	80	38.0	37.4	.80	.70	.70	.60
61205	110	100	90	49.4	48.6	.98	.72	.90	.72
61206	110	100	95	48.4	47.6	.95	.85	.90	.75
61208	110	100	86	50.0	.0	.70	.50	.80	.53
61210	110	100	120	49.6	48.6	1.02	.57	.96	.39
61211	110	100	44	.0	.0	.00	.00	.00	.00
70101	110	100	120	49.0	47.0	.80	.40	.80	.20
70103	110	100	56	49.6	48.2	.90	.18	.92	.07
70107	110	100	108	49.3	49.1	.90	.33	.90	.23
70109	110	100	96	48.6	48.2	.82	.48	.90	.35
70110	110	100	57	48.6	48.1	.85	.44	.88	.32
70111	110	100	66	48.7	48.2	.87	.42	.88	.30
70201	110	100	76	37.9	36.2	.65	.70	.82	.85
70202	110	100	88	37.5	36.8	.80	.70	.60	.50
70204	110	100	44	37.8	37.2	.80	.70	.70	.60
70205	110	100	121	50.0	49.2	.82	.60	.45	.52
70206	110	100	29	49.7	46.2	.38	.25	.40	.30
70301	110	100	64	50.0	49.7	.70	.55	.55	.40
70305	110	100	114	37.4	37.1	.70	.36	.60	.28
70306	110	100	108	49.7	49.4	.73	.38	.64	.20
70307	110	100	92	49.5	49.2	.55	.36	.60	.35
70308	110	100	120	49.5	49.2	.50	.19	.48	.14
70309	110	100	90	37.6	37.1	.75	.55	.60	.52
70310	110	100	114	38.1	37.9	.62	.42	.92	.33
70312	110	100	85	49.2	48.8	.78	.25	1.08	.40
70314	110	100	78	37.6	36.5	.82	.60	.56	.45
70401	110	100	27	49.1	48.2	.85	.75	1.02	.58
70402	110	100	110	50.2	49.1	.65	.45	1.00	.33
70403	110	100	18	48.7	47.2	.90	.82	.95	.72
70404	110	100	111	49.7	48.6	.60	.70	.64	.38
70405	110	100	51	49.0	48.5	.95	.82	.90	.70
70406	110	100	64	49.3	48.7	.92	.73	.42	.32
70407	110	100	35	50.5	50.1	.50	.28	.60	.28
70409	110	100	80	50.4	47.4	.52	.40	.70	.50
70410	110	100	110	50.5	49.7	.61	.40	.52	.42
70411	110	100	104	50.5	49.7	.21	.15	.17	.15

Ribbon Run No.	Seed Orientation Axis	Surf.	Usable Length (cm)	Width (mm) Max	Min	Thickness (mm) Seed Max	Min	Tail Max	Min
70412	110	100	50	49.8	49.6	.65	.45	.52	.48
70413	110	100	82	50.1	48.6	.80	.37	.92	.32
70414	110	100	23	49.3	47.6	.65	.35	.64	.27
70416	110	100	62	49.4	46.9	.92	.75	.92	.57
70417	110	100	86	49.5	49.4	.36	.15	.60	.09
70418	110	100	79	49.4	47.0	.56	.11	.42	.18
70501	110	100	60	49.6	49.2	.52	.35	.70	.32
70504	110	100	82	49.4	45.4	.68	.31	.65	.30
70505	110	100	76	49.9	46.7	.84	.43	1.00	.37
70507	110	100	61	49.5	47.4	.55	.42	.37	.25
70508	110	100	31	44.6	43.9	1.10	.95	1.20	.95
70509	110	100	72	47.7	47.0	.96	.72	1.04	.50
70510	110	100	19	42.8	42.1	.70	.50	.95	.72
70511	110	100	120	49.9	49.4	.60	.25	.62	.16
70513	110	100	120	49.8	49.2	.88	.42	.84	.30
70601	110	100	91	50.5	50.3	.60	.40	.68	.42
70602	110	100	121	50.1	49.8	.63	.40	.60	.18
70603	110	100	130	50.1	49.6	.60	.22	.79	.15
71004	110	100	17	95.0	80.0	1.74	.78	1.52	.21

A 0.0 ENTRY INDICATES NO MEASUREMENT WAS MADE.

APPENDIX III. Design Details for 25 mm Dies, Die Holders, and Heat Shields

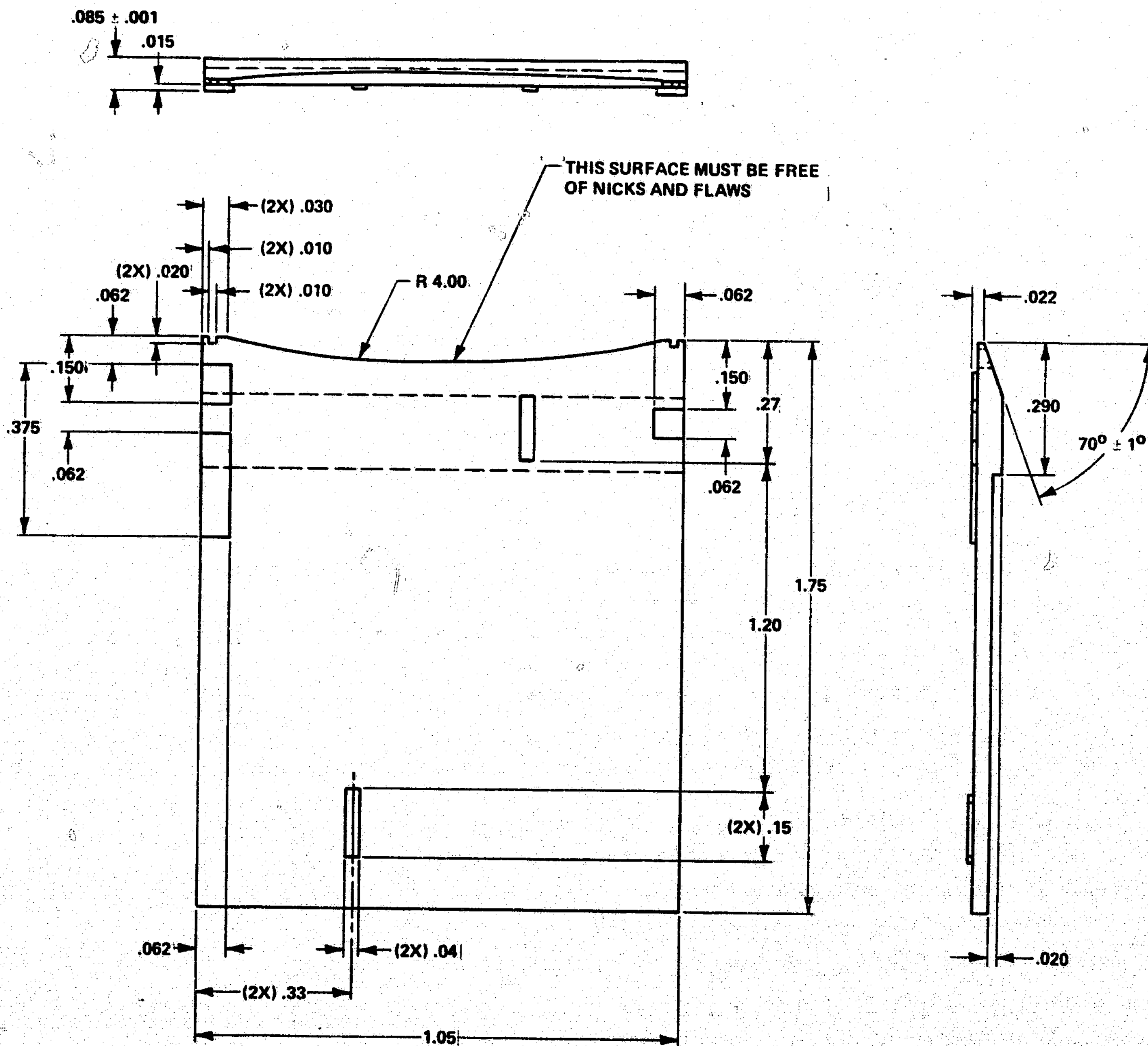

Fig. 1. Die plate, 2P-25L.

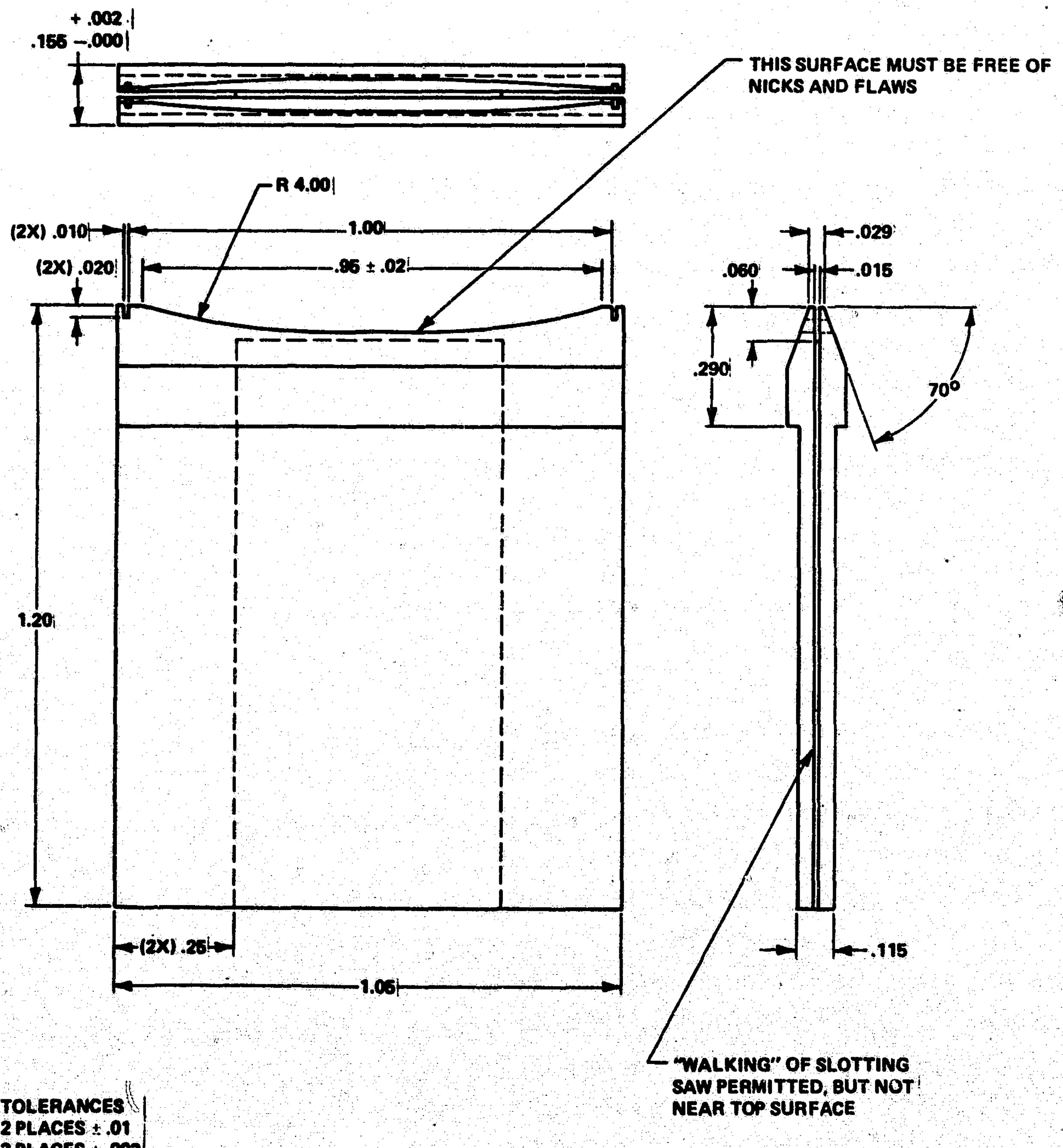

Fig. 2. Die plate, 13L.

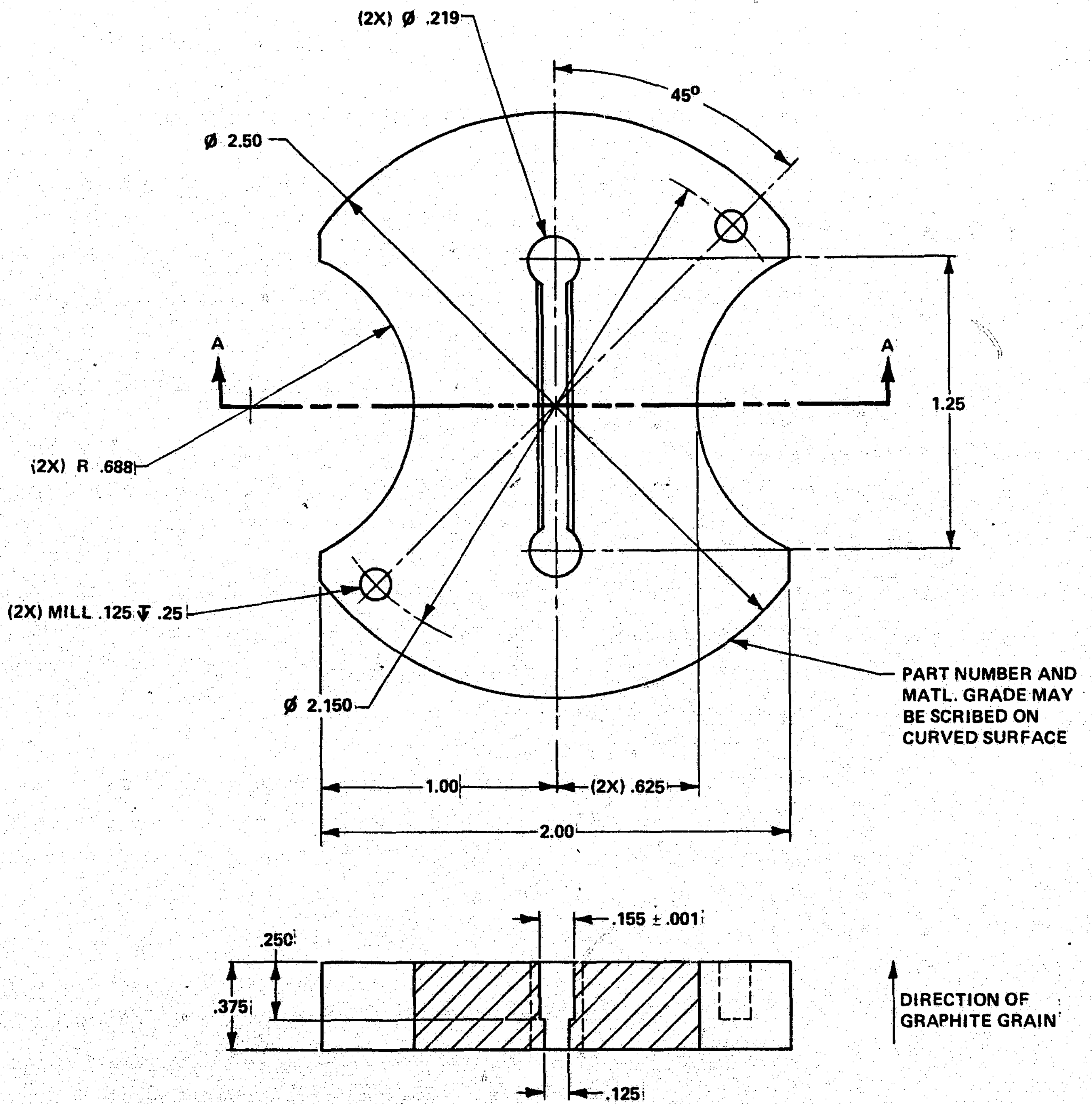

Fig. 3. Die holder, 25L.

MILL .75 ↧ .030

(2X) R .047

Ø 2.150

(2X) Ø .128

45°

PART NUMBER AND
MATL. GRADE MAY BE
SCRIBED HERE

(2X) R 4.00

(2X) R .688

1.00

1.60

Ø 2.50

1.00

(2X) .625

2.00

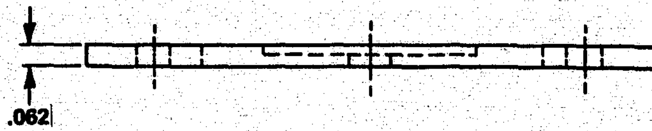

TOLERANCES
2 PLACES ± .01
3 PLACES ± .003

Fig. 4. Lower shield, 25L.

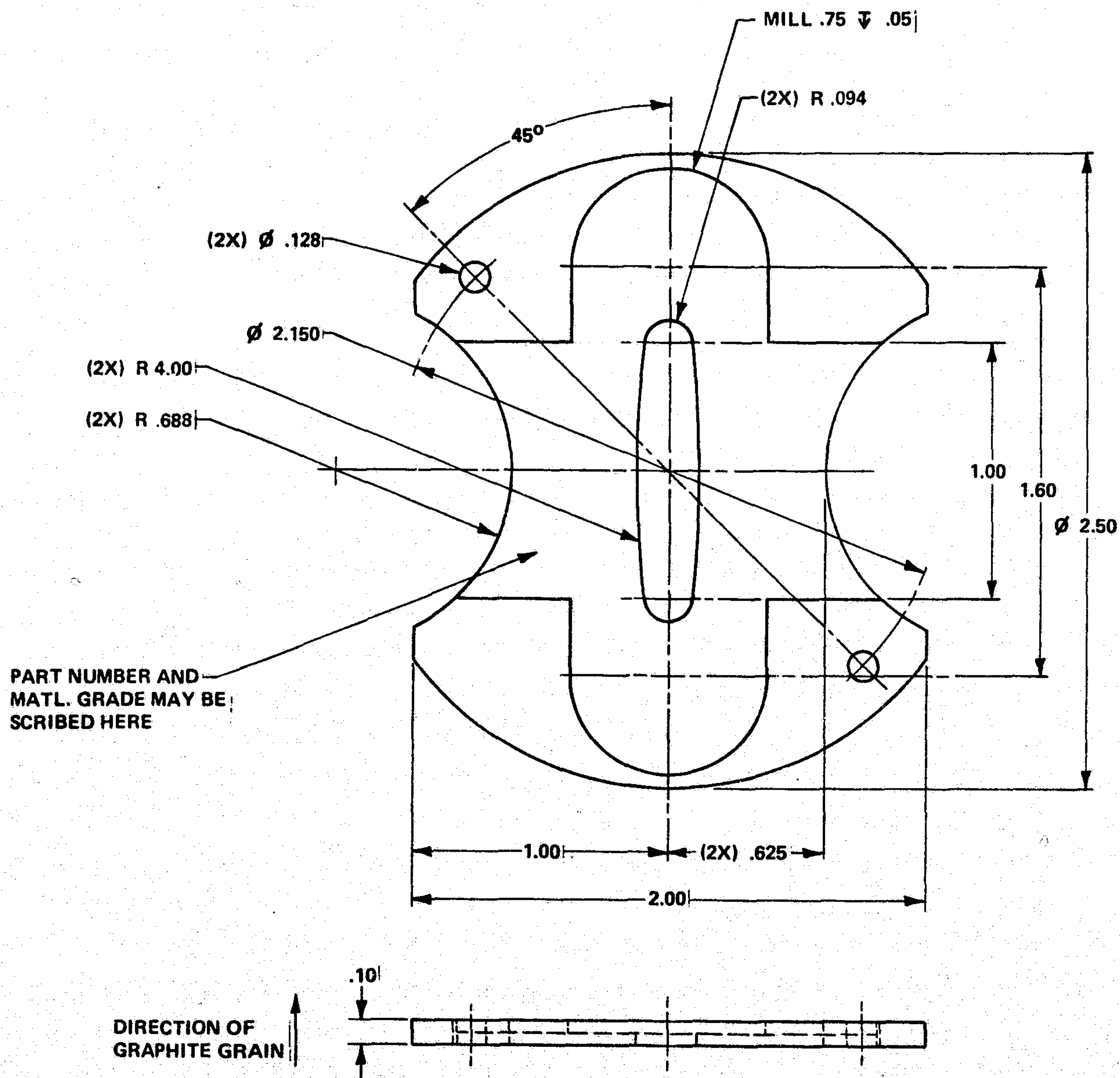

Fig. 5. Upper Shield, 25L.

II STRUCTURAL AND ELECTRICAL CHARACTERIZATION OF CAST SILICON RIBBONS

by

G. H. Schwuttke, K. H. Yang, H. F. Kappert, R. Hezel, and R. G. Dessauer

1.0 INTRODUCTION

CAST crystals display a unique defect structure. Effort was expanded to study, analyze and improve crystal defect structure in such ribbons. The influence of crystal defects in CAST ribbons on solar cell performance was also studied.

The characterization problems encountered in CAST crystals during the contract period were numerous. In the beginning of the program ribbon growth was plagued by the formation of silicon carbide crystallites and epitaxially deposited silicon carbide films. The "high-melt meniscus" technique together with "thermal balancing" using inert-gas streams (described in section Crystal Growth of this report) reduced this problem considerably.

Controlled seeding and control of surface orientation of CAST ribbons remains a problem and needs further

attention. A complete surface orientation analysis of ribbons grown under steady state condition was made using electron channeling patterns in the SEM. Transmission electron microscopy was used to analyze the crystallographic nature of crystal defects. The electrical activity of crystal defects was determined using the SEM-EBIC technique. Lifetime degrading properties of crystal defects were measured using the MOS C-t technique. A correlation of crystal defect density and solar cell performance of ribbons was obtained.

A detailed description of the key efforts is presented in the following sections.

2.0 SILICON CARBIDE FORMATION

The use of carbon as die material causes formation of silicon carbide during ribbon growth. Silicon carbide crystals may form as small crystallites on the die sides or in the die orifice. They may also grow epitaxially on ribbon surfaces. The high melt meniscus technique combined with thermal jet control during ribbon growth reduced such problems considerably.

2.1 SiC Crystallite

During silicon ribbon growth, particularly without thermal

jet control, small SiC crystallites form in the orifice of the die. Such crystallites are also found floating in the meniscus at the top of the die. More or less frequently such a particle becomes attached to the silicon ribbon thus destroying the perfection of the ribbon[1,2].

Similar observations are made on the outside of a carbon die in contact with the molten silicon. An accumulation of crystallites in the orifice of a carbon die is shown in Fig. II-1(a) and on the outside of a die in Fig. II-1(b). Scanning electron micrographs of such small crystals scraped from the orifice and from the side of the die are shown in Fig. II-2(a,b). These crystals appear equi-axed and expose mainly (111) and (100) surfaces. The morphology of the SiC crystals is in agreement with the growth from a liquid phase by precipitation. Some of these crystals are found in clusters bonded to each other with a very limited area where their orientations are identical. It is obvious that beautiful small SiC crystals can be grown by this technique as an unwanted "side-product" of Si ribbon pulling.

2.2 Silicon Carbide Film

SiC films form on the ribbon surface via vapor transport deposition. Vapor-phase deposition of SiC is particularly active during the seeding phase and during the initial

ORIGINAL PAGE IS
OF POOR QUALITY

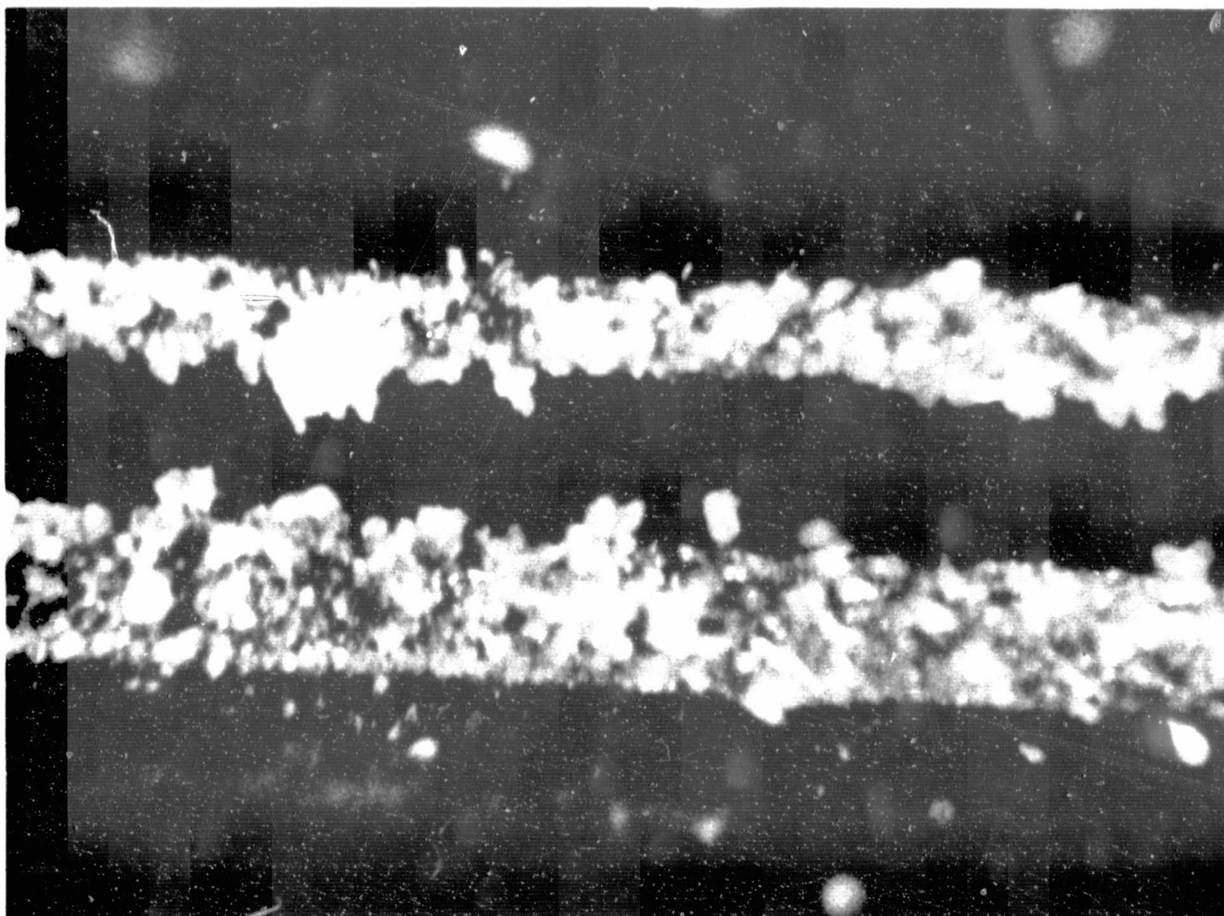

Fig. II-1(a). Precipitates in carbon die orifice after silicon-ribbon growth.

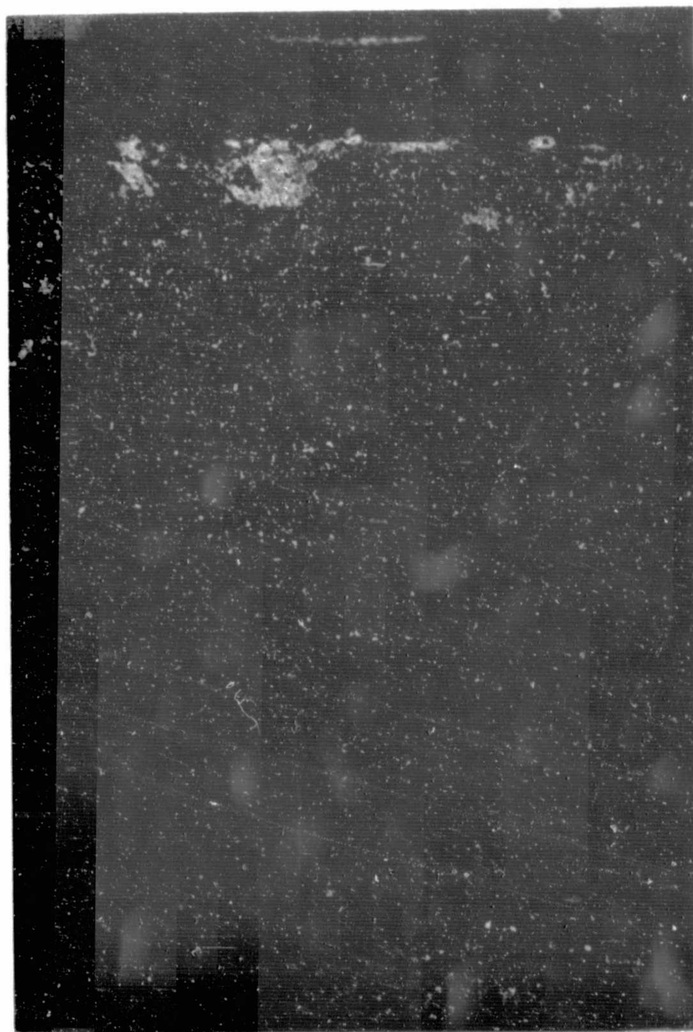

Fig. II-1(b). Precipitates on side of carbon die after silicon-ribbon growth.

ORIGINAL PAGE IS
OF POOR QUALITY

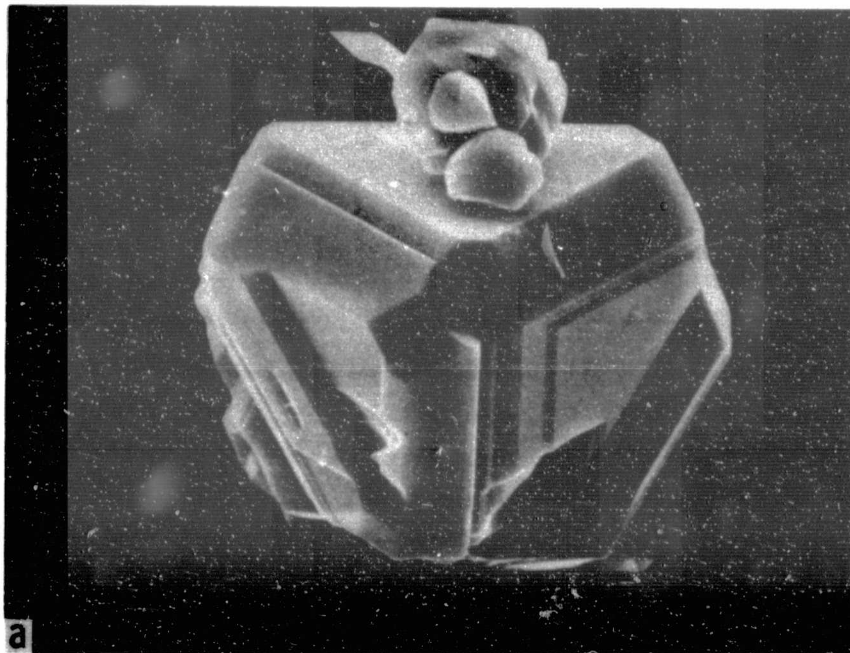

2a

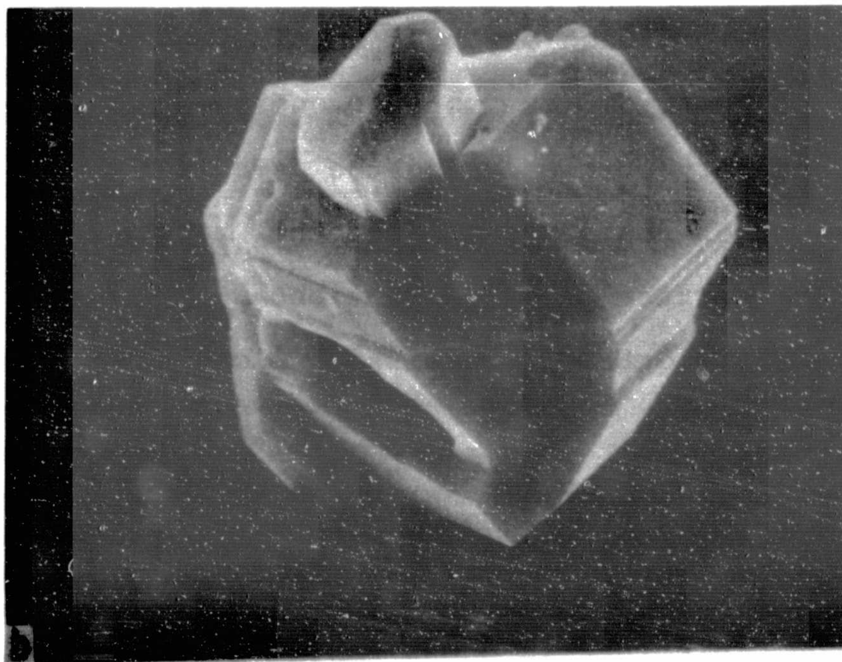

2b

Fig. II-2. Scanning electron micrographs of SiC crystals scraped from the orifice of carbon die.

growth period, leading to a more or less dense SiC film on the ribbon surface. Such SiC films influence destructively the efficiency of ribbon solar cells[17]. To minimize film formation it is important to understand the crystallographic nature of the film as well as the mechanism of growth. This study relates to these problems and presents a complete analysis of such films.

2.2.1 Analysis of Surface Films

Visual inspection of seed-ribbon crystals as grown reveals that the seed is covered with a dull bluish film while the surface of the ribbon close to the initial seed interface looks dull and dark. The surface dullness decreases rapidly with the distance from that interface, and a shiny ribbon surface is normally obtained after 10 cm of ribbon growth. The surface film formation is more pronounced for lower growth speeds and very strong during the seeding operation because of the longer residence time of the seed. In the following, such surface films on ribbons are analyzed through optical and electron transmission microscopy.

2.2.2 Optical Microscopy

The variation of surface-film morphology with distances from the seed-ribbon interface is shown in the photomicrographs of Figs. II-3(a) to II-3(f). Figures II-3(a) and II-3(b)

show the film structure on the seed and on the ribbon, above and below the interface. No particular features are resolved optically. The film covers the silicon surface completely. With increasing distance from the interface, the ribbon surface is covered less completely and the optical microscope reveals well-developed dendritic crystal structures covering the ribbon surface. The number of dendrites on the ribbon surface decreases rapidly with increasing distances from the interface. Note the preferential nucleation of dendrites in grain boundaries, shown in Figs. II-3(d) and II-3(e). Twin boundaries do not act as preferential nucleation sites, shown in Fig. II-3(f). Single isolated dendrites may form during successive ribbon growth, particularly if a change in growth speed occurs.

2.2.3 Transmission Electron Microscopy

Optical microscopy cannot identify the crystallographic nature of the films. Therefore, a transmission electron microscopy analysis was made. For this purpose, 3-mm-diameter specimens were cut ultrasonically out of seed and ribbon crystals at different locations. The specimens were jet-etched, using a mixture of HNO_3/HF. Before etching, the specimens were thinned by mechanical lapping (on one side only), mainly for film removal. Subsequently, the jet etch was applied to the lapped side until the

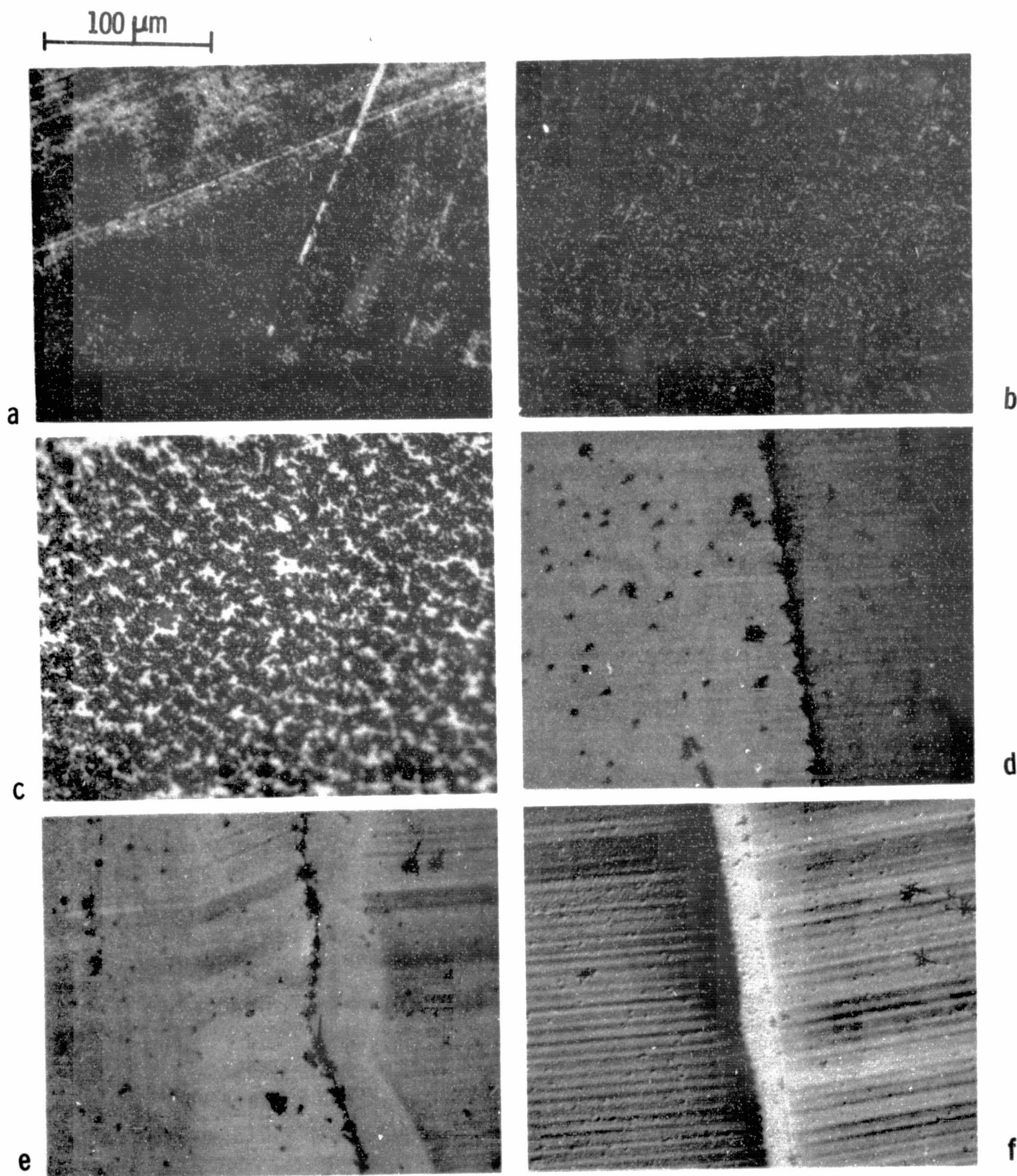

Fig. II-3. Optical micrographs showing (a) β-SiC film on seed surface; (b) unresolvable morphology of dull surface at s ~ 2 mm, well-defined dendrites; (c) at s ~ 1 cm; (d) at s ~ 7 cm; (e) at s ~ 10 cm; and (f) at s ~ 20 cm. Note that the density of dendrites decreases with increasing s.

ORIGINAL PAGE IS
OF POOR QUALITY

ORIGINAL PAGE IS
OF POOR QUALITY

specimen was thin enough for electron beam penetration. It was noted that the surface film was very resistant to the etch. Consequently, it was easy to etch holes into the silicon and thus isolate the film for transmission electron microscopy work. Figure II-4 shows some typical results for the films covering the seed section. Figure II-4(a) is a transmission electron micrograph of a seed specimen. Note the square structure of the silicon holes typical for the (100) orientation of the seed face. Figure II-4(b) is the corresponding electron diffraction pattern, and Fig. II-4(c) gives the aperture-limited dark-field picture obtained at position A indicated in Fig. II-4(b). The diffraction pattern Fig. II-4(b) is analyzed as β-SiC. The results are summarized in Table I-1. The dark-field analysis, Fig. II-4(c), indicates that the film consists of randomly oriented crystallites. The size of these crystallites ranges approximately from 700 to 1500Å.

Similar transmission electron micrographs of specimens taken from the ribbon at positions close to the interface indicate that the surface film on the ribbon also consists of SiC crystals. However, the crystallite size is approximately 1 μm. Examples of such crystallites are given in Figs. II-5(a-c). Figure II-5(a) is a standard bright-field micrograph, while Fig. II-5(b) is the corresponding dark-field picture obtained by placing the "limited"

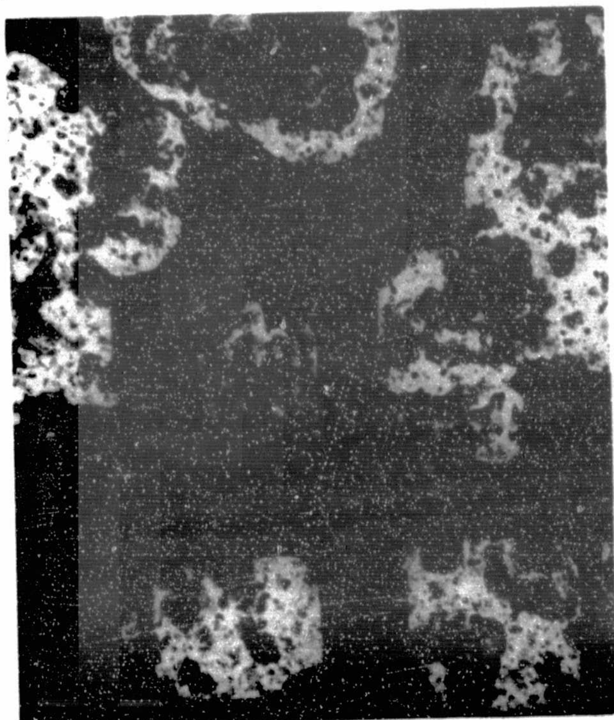

a

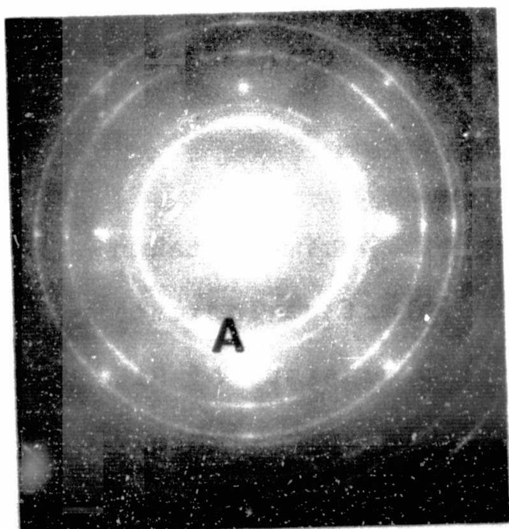

b

c

Fig. II-4. TEM micrographs showing (a) β-SiC film on (001) seed surface; (b) electron diffraction pattern of (a); and (c) dark-field image taken from A in (b).

ORIGINAL PAGE IS
OF POOR QUALITY

TABLE II-1. Identification of Surface Film on Crystal Seed

Surface Film d, Å	Reflection HKL	ASTM #1-119, β-SiC d, Å
2.510	111	2.51
2.173	200	2.17
1.541	220	1.54
1.298	311	1.31
1.258	222	1.26
1.089	400	1.09
0.999	331	1.00
0.972	420	0.97
0.888	422	0.89
0.837	333, 511	0.84
0.767	440	0.77
0.733	531	0.74

aperture at a section of the (111) SiC ring Fig. II-5(c). This result identifies the grains marked α, β, and γ in Fig. II-5(a) as β-SiC, γ not visible in II-5(a). the aperture around the (111) SiC ring to different positions causes crystallites of different orientation to show up successively in the corresponding micrographs. From such observations it follows that the film consists of randomly oriented β-SiC crystals.

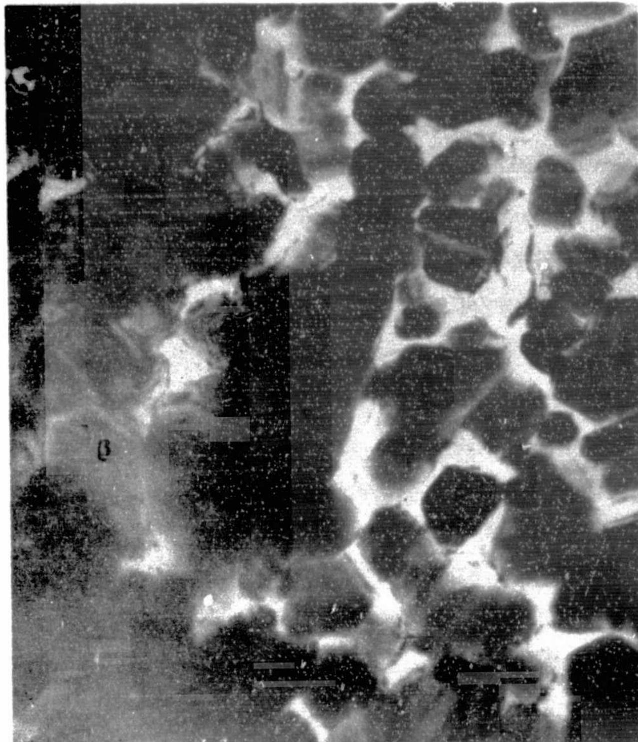

1μm

a

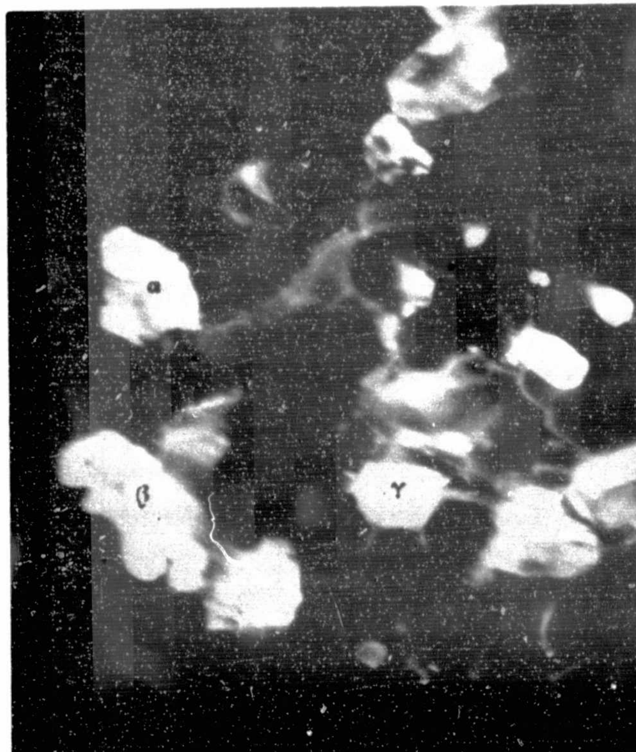

b

ORIGINAL PAGE IS
OF POOR QUALITY

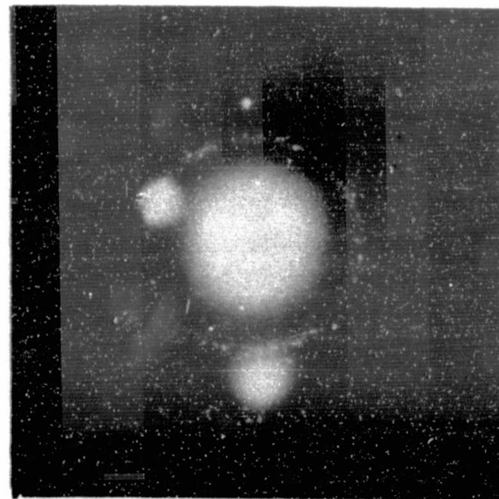

c

Fig. II-5. TEM micrographs showing (a) the bright-field image of β-SiC particles on ribbon surface close to seed-ribbon interface; (c) corresponding electron diffraction pattern.

Dendritic SiC structures on ribbon surfaces have been found for growth rates of 12 mm/min to 30 mm/min. The dendrites occur randomly over the ribbon surface or preferentially along grain boundaries, and are of submicron size for faster growth rates. Such small particles are difficult to see in the optical microscope. The dendrites have been found to influence generation lifetime of the silicon ribbon surfaces.

Results of lifetime measurements made on ribbons as grown and on ribbons slightly etched before processing are summarized in Table II-2. It can be seen that due to the presence of β-SiC dendrites, the occurrence of leaky MOS dots can be very high on ribbon sections cut as far as 40 cm from the interface. Etching before processing eliminates this problem.

The transmission electron micrographs of a dendrite cluster in bright and dark fields are shown in Figs. II-6(a) and (b). The corresponding transmission electron diffraction pattern is presented in Fig. II-7(a). The diffraction pattern is reproduced schematically in Fig. II-7(b). The diffraction pattern of Fig. II-7(a) contains the basic [001] silicon diffraction pattern, but, in addition, every silicon reflex is surrounded by characteristic satellite reflexes.

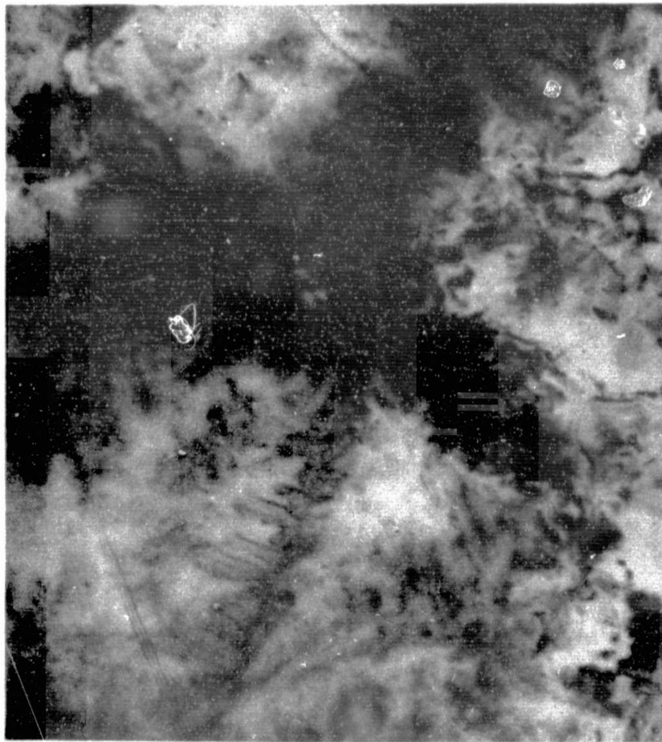

a

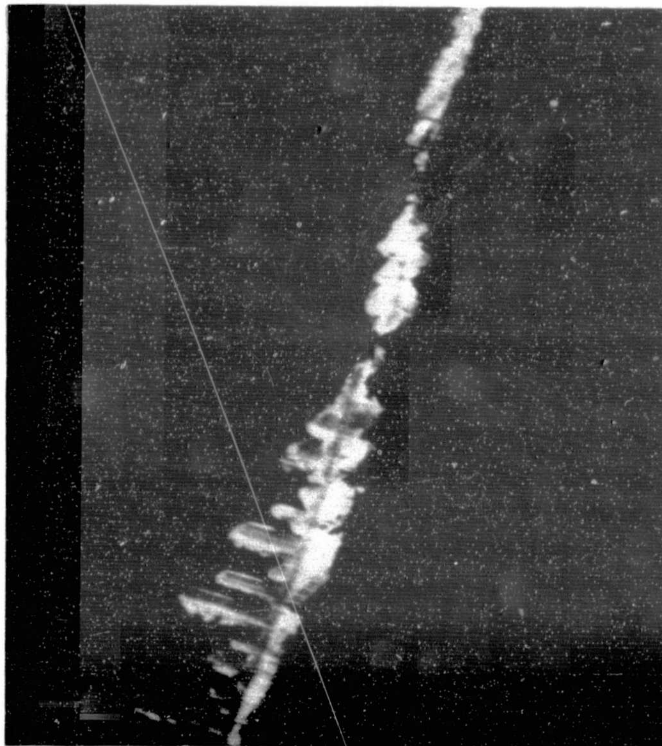

b

ORIGINAL PAGE IS
OF POOR QUALITY

Fig. II-6. TEM micrographs showing (a) bright-field image; and (b) dark-field image of a dendrite cluster.

TABLE II-2. Influence of β-SiC Dendrites on Lifetime of Silicon Ribbons

Ribbon Number	Distance from Seed (cm)	MOS dot size (mm)	Range of Lifetime (μsec)	Average Lifetime (μsec)	Relative Area Containing SiC (%)
60337 (as grown)	6-12	0.5	0.011-10.5	2.26	68
60337 (as grown)	18-24	0.5	0.001-1.64	0.20	52
60337 (as grown)	30-36	0.5	0.005-6.48	1.07	31
		1.5	0.081-1.13	0.34	58
60337 (as grown)	42-48	0.5	0.020-52.7	2.50	12
		1.5	0.028-2.42	0.44	21
60305 (as grown)	Unknown	0.5	0.0003-0.096	0.034	77
60305 (etched)	Unknown	0.5	0.039-44.3	6.54	0
60305 (etched)	Unknown	1.5	0.011-29.0	5.93	0

For analysis of the result contained in Fig. II-7(a) the diffraction pattern of Fig. II-7(b) was reconstructed with the following assumptions:

1. The dendrites consist of β-SiC and grow epitaxially with [001] orientation on the [001] oriented silicon.

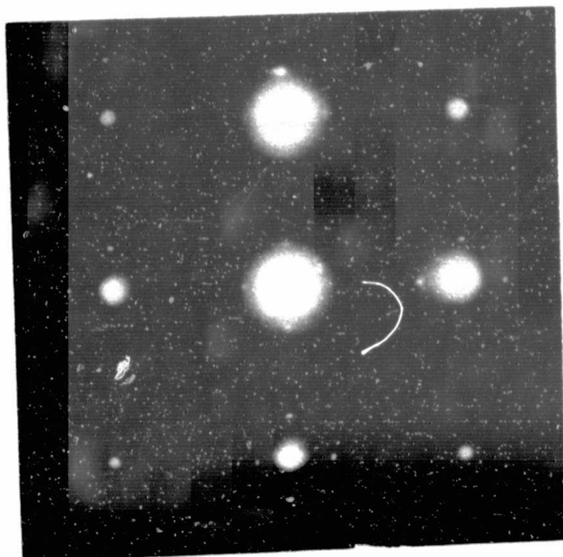

a

ORIGINAL PAGE IS
OF POOR QUALITY

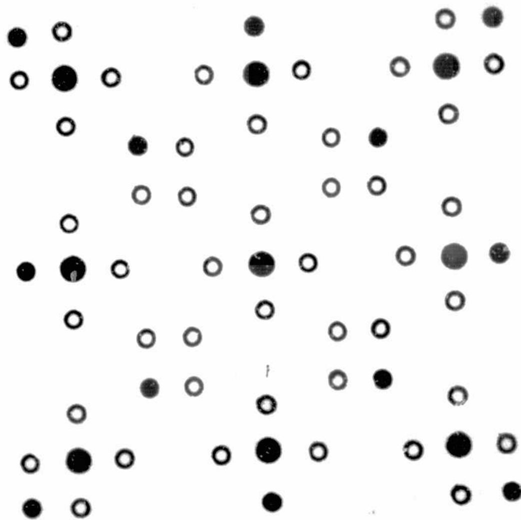

b

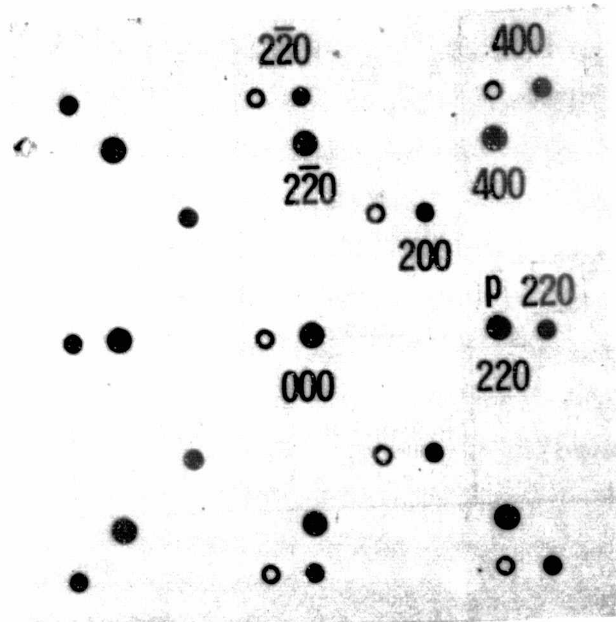

c

Fig. II-7. (a) selected-area electron diffraction pattern of β-SiC and Si (001) diffraction patterns with Si (220) reflex p acting asd a secondary source for double diffraction. Largc and small solid dots represent Si and βSiC reflections, respectively. The small solid dots represent the double-diffraction spots due to p.

The epitaxial relationship between SiC and silicon is perfect for the (110) β-SiC planes parallel to the (110) silicon planes. Under such conditions, extra diffraction spots due to SiC appear in the silicon pattern. The distance between the silicon main reflex and any (h, k, l) diffraction spot due to β-SiC is obtained as follows. The ratio of lattice constants between β-SiC (a = 4.538Å) and silicon (a = 5.403Å) is 0.803. In reciprocal space, this corresponds to a distance of 1:0.803 = 1.245. Consequently, any (h, k, l) SiC reflection is located at the distance 1.245 h, k, l from the main beam.

2. Additional satellite reflexes around the silicon dots are produced by the epitaxial β-SiC phase due to double reflection. Double diffraction occurs if a diffracted beam form the silicon passes into the epitaxial SiC, or vice versa. In both cases the double-diffracted beam is determined by adding together the reciprocal lattice vectors corresponding to the two component diffractions. Extra reciprocal lattice points displaced from the silicon matrix result.

Taking these two mechanisms into consideration and the additional fact that double diffraction from SiC (400) planes is found to be very weak, the diffraction pattern of Fig. II-7(c) was constructed. The large solid spots in this

pattern are due to silicon of <001> orientation. The small solid dots represent the double-diffraction spots for the silicon reflex (220), p, acting as a secondary source. If this pattern is reproduced for the four (220) and four (400) silicon reflexes acting as secondary sources and the results are superimposed into a single schematic pattern, the superposition yields the pattern given in Fig. II-7(b), which describes exactly the diffraction pattern of Fig. II-7(a).

Additional information on the epitaxial relationship between β-SiC and Si is obtained through tilting experiments in the electron microscope. Analysis of electron diffraction patterns of [114], [112], and $[\bar{1}14]$ orientation yields the orientation relationships summarized in Table II-3.

TABLE II-3. Epitaxial Relationship Between β-SiC and Si

	Orientation Relationship	
Orientation	β-SiC parallel	Si
114	$[31\bar{1}]$	$[31\bar{1}]$
	$[13\bar{1}]$	$[13\bar{1}]$
112	$[3\bar{1}\bar{1}]$	$[3\bar{1}\bar{1}]$
	$[11\bar{1}]$	$[11\bar{1}]$
$\bar{1}14$	$[3\bar{1}1]$	$[3\bar{1}1]$
	$[1\bar{3}1]$	$[1\bar{3}1]$

Further insight into the SiC growth on silicon is obtained from the following results. Figure II-8(a) shows the bright-field micrograph of a dendrite on a <112> ribbon surface. This particular surface plane is perpendicular to (111) crystal planes. This surface orientation is the result of twinning. The dendrite grows again preferentially in <1$\bar{1}$0> directions. This is similar to dendrites growing on <001> ribbon surfaces. Interesting is the dark-field image of this dendrite recorded through use of the (2$\bar{2}$0) β-SiC reflection, as indicated in Fig. II-8(c). The dark-field image is given in Fig. II-8(b) and shows a group of parallel layers spaced at approximately 500Å in the [1$\bar{1}$0] direction. This result indicates that the dendrites consist of a succession of silicon and SiC layers which are stacked along (111) planes.

The electron diffraction pattern of Fig. II-8(c) indicates that the epitaxial relationship between β-SiC and silicon is (112) β-SiC parallel to (112) Si, with (2$\bar{2}$0) β-SiC parallel to (2$\bar{2}$0), and (11$\bar{1}$) β-SiC parallel to (11$\bar{1}$) Si. Fig. II-8(c) is essentially identical with the diffraction pattern taken by tilting a [001]-oriented specimen into the [112] orientation.

The simple epitaxial relationship observed in this study is in good agreement with the results reported previously[3-5].

a

1μm

ORIGINAL PAGE IS
OF POOR QUALITY

ORIGINAL PAGE IS
OF POOR

b

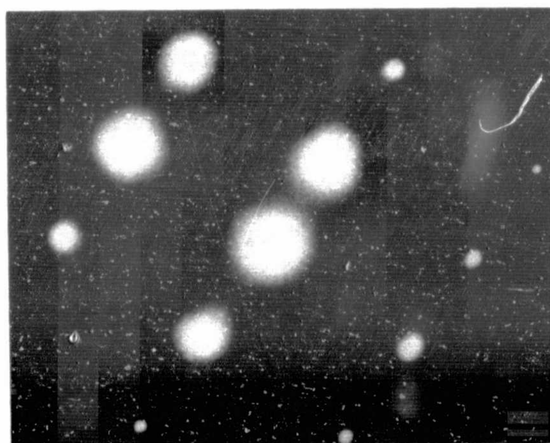

c

Fig. II-8. TEM micrographs showing (a) bright-field image of a dendrite on a <112> ribbon surface; and (c) electron diffraction of (a) and (b).

Brown and Watts[3] and Jacobson[4] reported that the growth of β-SiC on (001) silicon substrates, by use of chemical vapor deposition, results in the orientation relationship of (001) β-SiC parallel to (001) Si with (220) β-SiC parallel to (220) Si, and $(2\bar{2}0)$ β-SiC parallel to $(2\bar{2}0)$ Si. On (110) and (111) silicon substrates, similar epitaxial relationships are established between β-SiC and the silicon substrate[3,5].

2.3 Summary

Surface films on silicon ribbons grown by the Capillary Action Shaping Technique by use of carbon dies are analyzed through optical and transmission electron microscopy. The films are formed through vapor deposition and consist of β-SiC. The SiC shows significant structural differences, depending on deposition location - seed or ribbon - and on ribbon growth speed. On the seed surface the SiC deposits as randomly oriented crystallites ranging in size from 700 to 1500Å. Close to the seed-ribbon interface the crystallite size increases to 1 μm. The small crystals are of well-defined crystallographic shape. With the increasing speed of silicon ribbon growth, epitaxial formation of SiC dendrites on the silicon ribbon surface becomes the dominant SiC growth mechanism. The epitaxial growth of β-SiC occurs through preferential incorporation of (111) SiC planes

parallel to (111) silicon planes according to the epitaxial relationship (001) β-SiC parallel to (001) Si with (110) β-SiC parallel to (110) Si, and $(1\bar{1}0)$ β-SiC parallel to $(1\bar{1}0)$ Si. The silicon dendrites degrade minority carrier lifetime in ribbons.

3.0 RIBBON QUALITY

It has been our experience that crystallographic perfection of capillary action grown silicon ribbons rapidly deteriorates as ribbon length increases - particularly in the case of wide ribbons. This is due in part to the effects of carbon on silicon. Mechanical and thermal perturbations may, because of the very thin melt boundary between the die and the growth interface, also contribute to the degradation. However, it is difficult to isolate their contribution in the presence of the carbon effects.

3.1 Seeding and Surface Problems

Major problems exist during the seeding operation. Single crystal growth is difficult to achieve during this initial phase. Presently, it is not possible to control the "seeding operation" sufficiently to influence the surface orientation and perfection of the ribbon grown during

"steady state". Because of silicon carbide formation during seeding, the original seed/crystal relation is rapidly lost and the final ribbon quality is mostly dominated by twin lines in the <112> direction. An x-ray topograph of a typical crystal-seed interface is given in Fig. II-9 and shows the catastrophic collapse of seed orientation due to heavy twinning. All twins inclined towards the growth direction grow out relatively fast. If the inclusion of silicon carbide particles in the ribbon surface can be avoided, steady-state growth is dominated by surface orientations close to a <110> direction.

To define the surface orientation of ribbons grown under steady-state conditions, we introduce the convention summarized in Fig. II-10. Accordingly, the angle between the growth direction and the twin boundaries is called α. The resultant tilt angle, θ_r, gives the actual surface orientation of the ribbon. This surface orientation is measured as a misorientation against the [011] direction and has the two components θ_g and θ_a, where θ_g is the tilt along the growth direction and θ_a is the tilt around the growth direction perpendicular to it.

Figure II-11 summarizes typical surface orientations obtained for different seed orientations. On the basis of these and

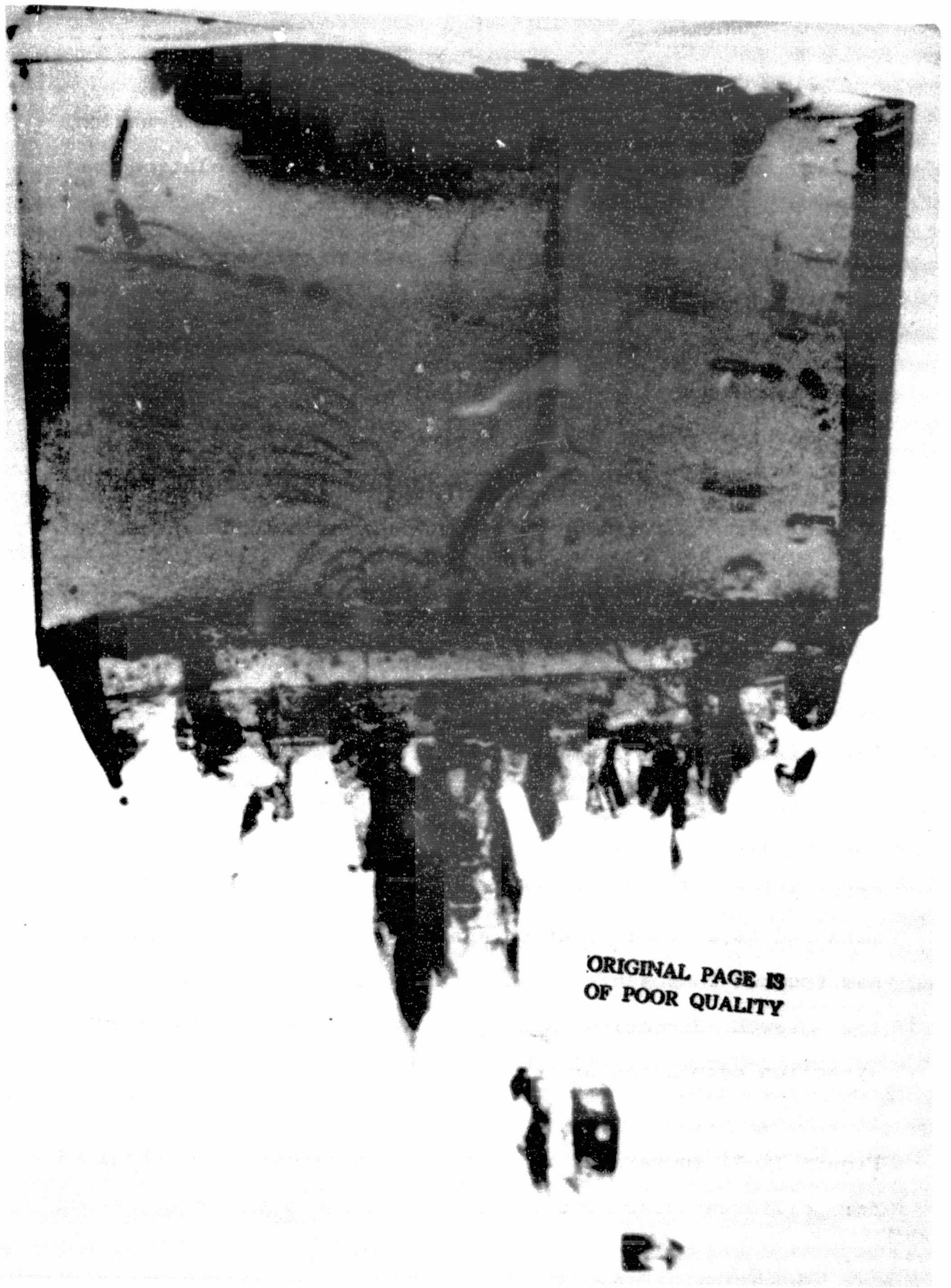

ORIGINAL PAGE IS
OF POOR QUALITY

Fig. II-9. An x-ray topography of a typical crystal-seed interface showing the catastrophic collapse of seed orientation due to heavy twinning.

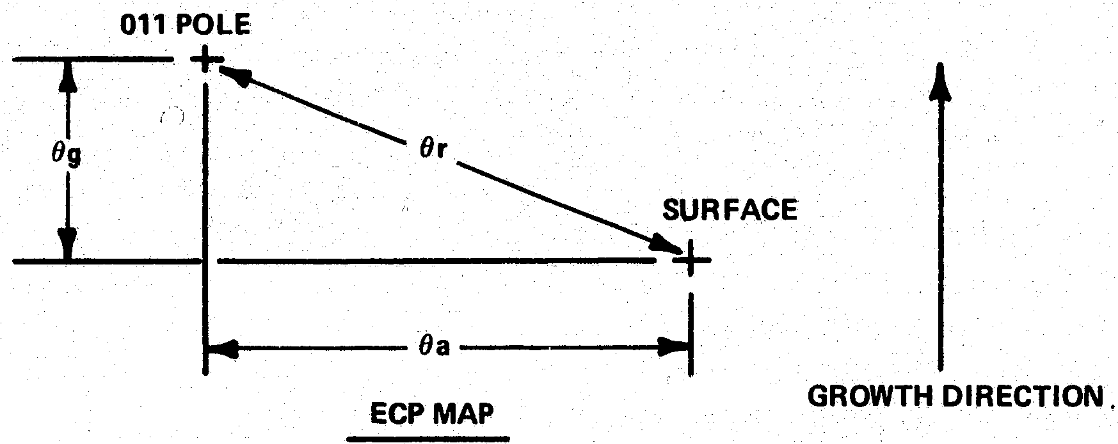

ORIGINAL PAGE IS
OF POOR QUALITY

SURFACE
011
θa
θg
θr
GROWTH DIRECTION
α
TWIN BOUNDARIES
(111) TWIN PLANES
RIBBON CRYSTAL

Fig. II-10. A schematic drawing of a ribbon crystal with misorientation θ_r against the {011} direction.

Ribbon Number	Seed Orientation: Face	Seed Orientation: Growth Direction	Sample Distance from Seed (cm)	Sample Orientation: Face Nearest Pole	Sample Orientation: Face Deviation (degrees)	Sample Orientation: Growth Direction	Twin Axis a/b	Remarks
40404	(111)	$\langle \bar{1}\bar{1}2 \rangle$	>50	011	$\theta_R = 11.3$ $\theta_a = 3.5$ $\theta_g = 10.7$	$2\bar{1}\bar{1}$	$11\bar{1} \leftrightarrow \bar{1}\bar{1}1$	Twin boundaries in growth direction
40812	$(1\bar{1}0)$	$\langle 111 \rangle$	50	011	$\theta_R = 9.7$ $\theta_a = 5$ $\theta_g = 8.3$	$21\bar{1}$	$1\bar{1}1 \leftrightarrow \bar{1}1\bar{1}$	Twin boundaries not in growth direction (10° off)
40820	$(1\bar{1}0)$	$\langle 111 \rangle$	50	011	$\theta_R=\theta_a=8.4$ $\theta_g = 0$	$21\bar{1}$	$1\bar{1}1 \leftrightarrow \bar{1}1\bar{1}$	Twin boundaries in growth direction
50520	(100)	$\langle 110 \rangle$	120	011	$\theta_R = 18$ $\theta_a = 14$ $\theta_g = 11$	$21\bar{1}$	$1\bar{1}1 \leftrightarrow \bar{1}1\bar{1}$	Twin boundaries in growth

Fig. II-11. Steady-state Growth of Ribbon.

other results, we conclude that control of surface orientation of ribbons grown under steady-state conditions does not, at present, exist. It can be noted that surface misalignment covers a range between 5 and 15° against the [011] surface. Ribbons with twin planes inclined almost perpendicular to the surface and a surface tilt of $\theta_r = \theta_a = 8^{o}$ (with $\theta_g = 0$) have been grown. For such ribbons the twin boundaries are parallel to the [211] growth direction.

Examples of ribbon surfaces are shown in Figs. II-12. Figure II-12(a) shows a ribbon surface with parallel twinning, Fig. II-12(b) is a ribbon surface containing non-parallel twinning and grain boundaries.

A higher complexity of surface disorder is seen in Fig. II-12(c). This ribbon section contains different grains, silicon carbide inclusions and different types of twinning. All these defencts are normally encountered during ribbon growth and once analyzed by transmission electron and scanning electron microscopy, are readily interpreted through optical microscopy.

3.2 Analysis of Surface Orientation

Surface orientations and the nature of boundaries encountered in Fig. II-12(c) were analyzed through the electron channeling technique (ECP) in the SEM. The photomicrograph of Fig. II-12(c) shows a ribbon section selected for its complexity of different surface features and is not representative of the IBM state-of-art of ribbon crystal growing. The sample of Fig. II-12(c) is useful for demonstration of the channeling technique to analyze surface orientations of small crystallites. The sample contains different grains, silicon carbide inclusions, and different types of twinning. All these defects can be encountered during ribbon crystal growing using carbon dies and, once analyzed, are readily interpreted through optical microscopy. For this reason, a thorough analysis is presented in the following section.

3.2.1 <112> Twinning

Orientation analysis of crystal areas bounded by parallel lines in the <112> direction is summarized in Figs. II-13(a) and II-13(b). Each figure shows a sequence of ECPs for each crystallite. One ECP covers only an angle of $\sim 6^{\circ}$. Thus it is difficult to recognize the orientation pattern of crystal surfaces if they are not close to a low-index

ORIGINAL PAGE IS
OF POOR QUALITY

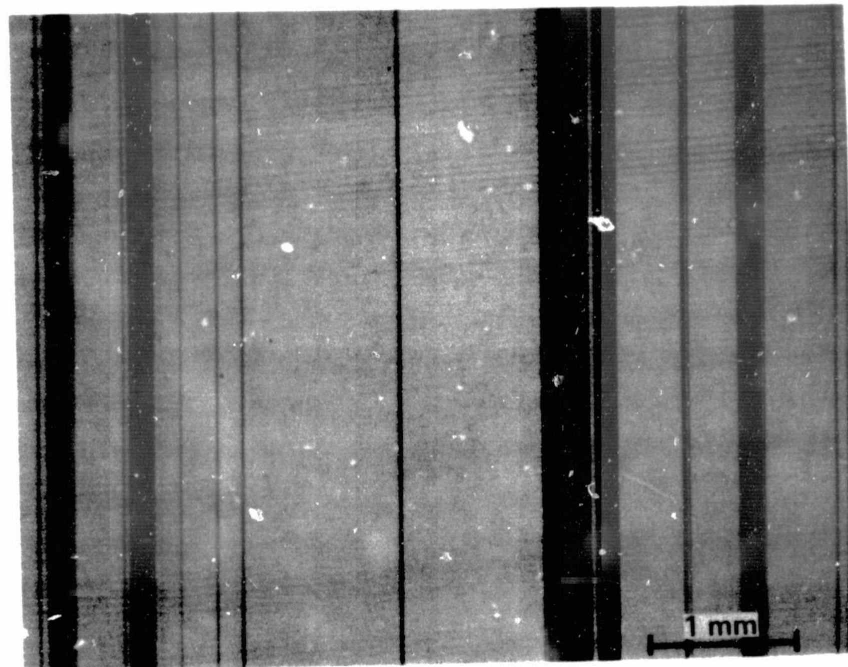

a

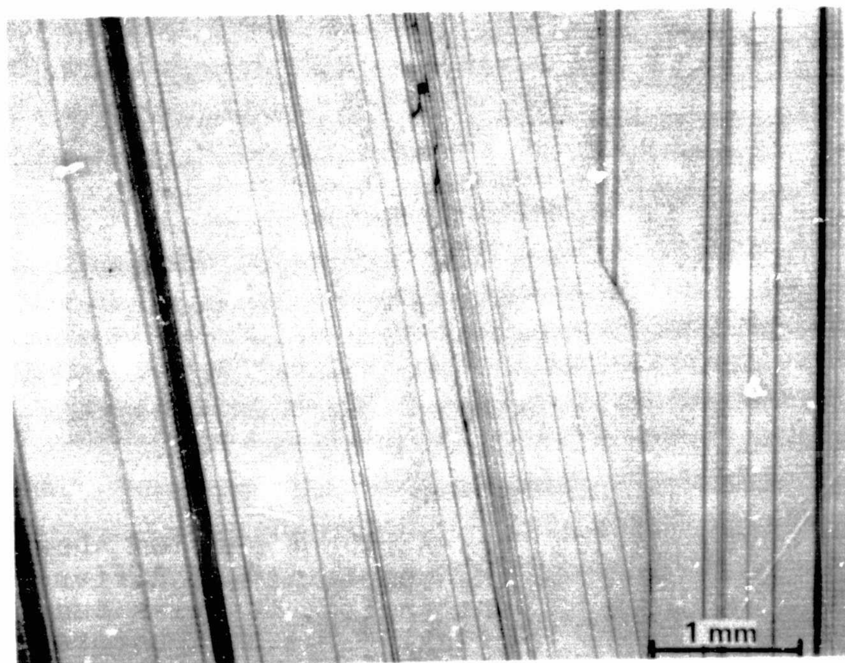

b

Fig. II-12. Ribbon sections of various perfection; (a) Steady-state grown, parallel twinning only; (b) parallel twinning and grain boundary.

Fig. II-12. (c) A ribbon section showing complexity of different surface features and twinning. a,b,c--refers to crystallite; A, B--refers to surface orientation.

ORIGINAL PAGE IS
OF POOR QUALITY

surface. This difficulty is overcome by tilting the sample in steps of 6° until the ECP on the screen can be matched with the computer-generated ECP. A sequence not larger than three ECPs is found sufficient to recognize the orientation of the sample in all cases.

The exact surface orientation of the sample is given by the center of the ECP obtained for zero sample tilt. Thus the orientation of the crystallite marked "a" in Fig. II-12(c) and determined by the ECP sequence of Fig. II-13(a) is in the neighborhood of the $[01\bar{1}]$ pole but tilted 10° away from this pole. The ECP sequence of Fig. II-13(a) indicates that this tilt is approximately along the (022) lines. From the pole map given in Fig. II-14 it follows that this position is near the lower periphery of the circle around the $[01\bar{1}]$ pole. A comparison of the ECP map Fig. II-13(a) and of the pole map Fig. II-14 shows that (022) lines displayed in the ECP Fig. II-13(a) go exactly parallel to the great circle through $[01\bar{1}]$, $[13\bar{3}]$. etc. Therefore, the true surface orientation of crystallite "a" is tilted approximately 10° away from the $[01\bar{1}]$ direction towards the $[11\bar{1}]$ pole.

Next we discuss the channeling pattern of the crystallite "b" shown in Fig. II-12(c). Inspection of the ECP in Fig. II-13(b) indicates that the surface orientation of this

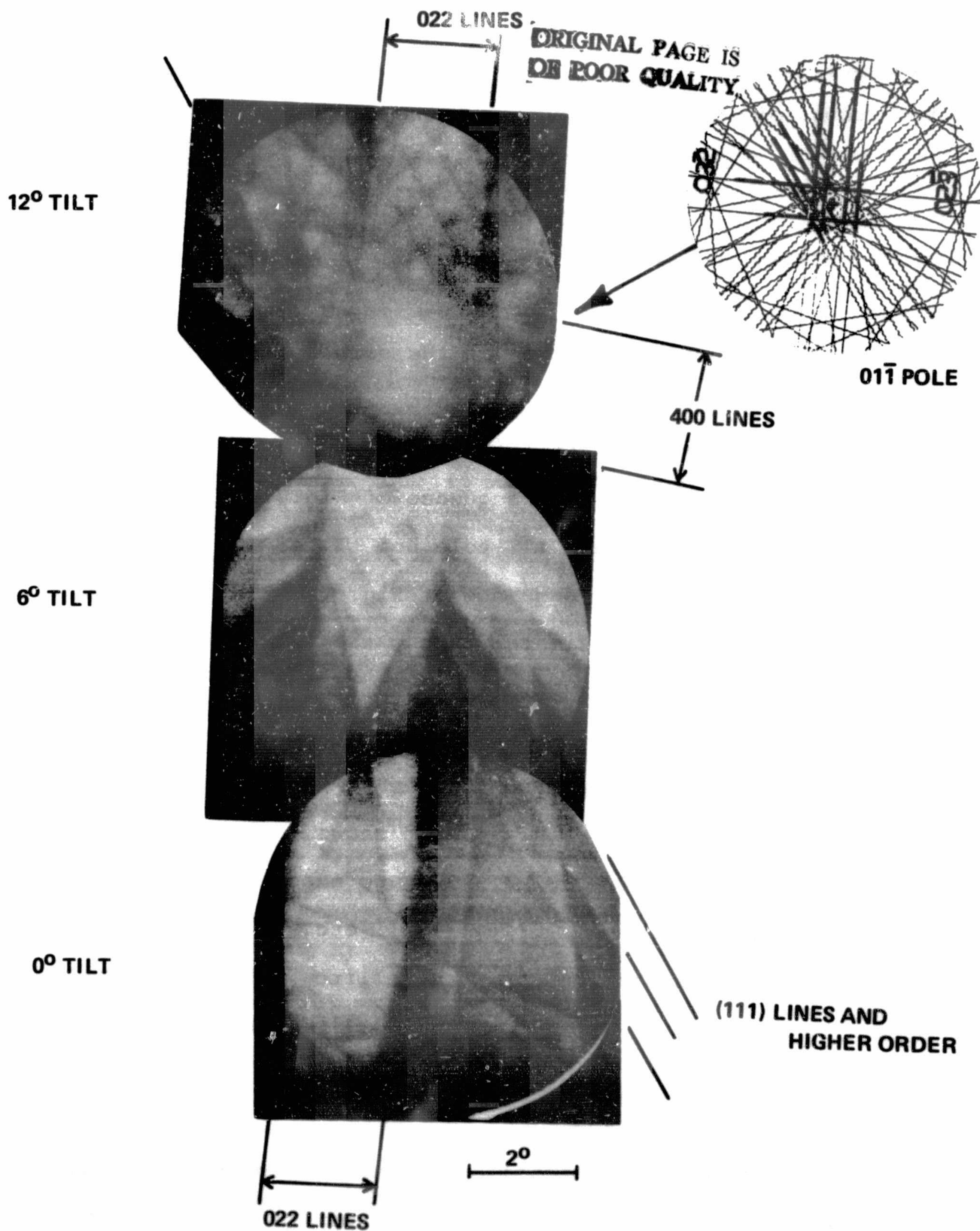

Fig. II-13(a). ECP sequence of crystallite "a" in Fig. 12(c).

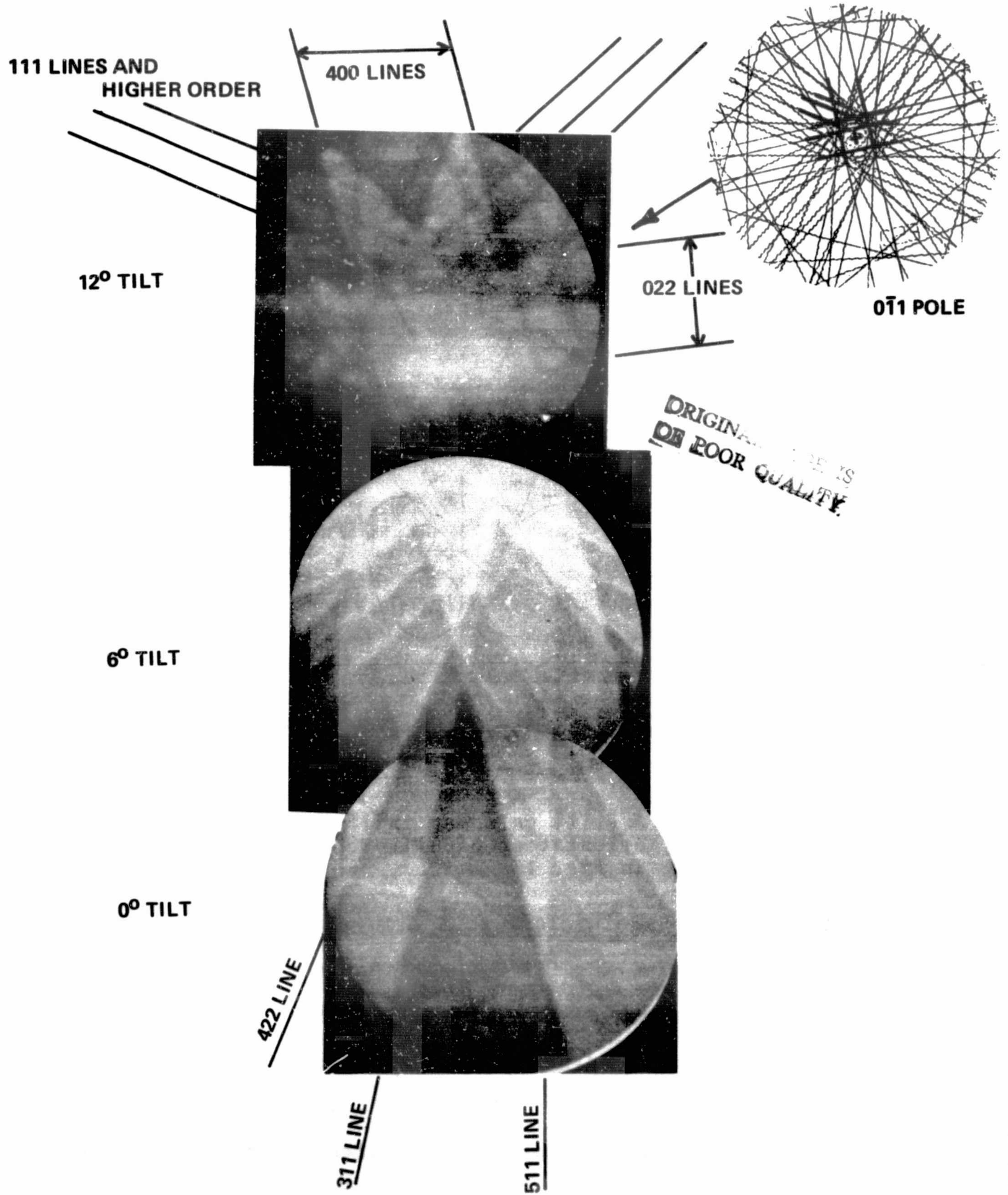

ORIGINAL PAGE IS
OF POOR QUALITY

Fig. II-13(b). ECP sequence of crystallite "b" in Fig. 12.

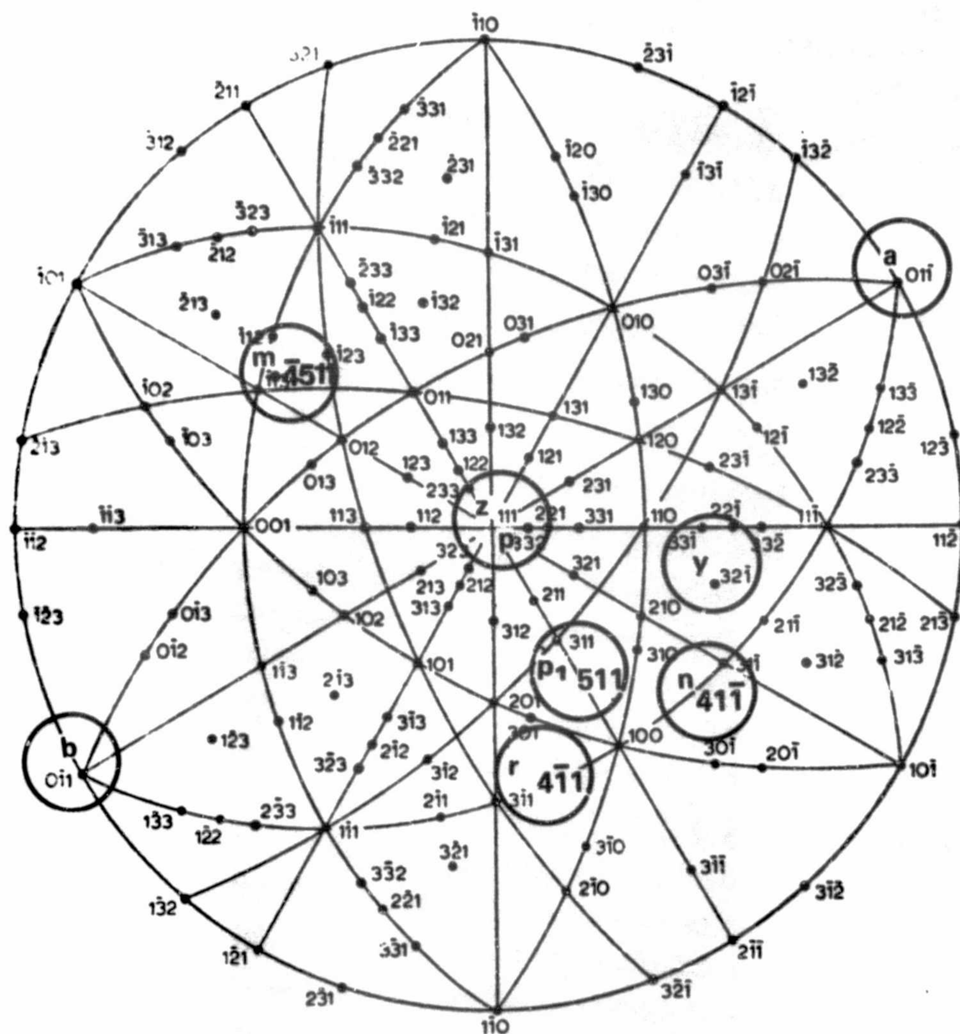

Fig. II-14. A [111] pole map indicating the surface orientation of different crystallites in Fig. 13.

crystallite is again close to a <110> direction. However, note that this time the ECP reveals that the (022) lines are 70° rotated relative to the (022) lines in the ECP of crystallite "a" in Fig. II-13(a). It follows, from the ECP sequence given in Fig. II-13(b), that the true surface orientation of crystallite "b" is tilted approximately 10° toward a direction located between the [511] and [311] lines Fig. II-13(b). The exact direction is determined as follows.

First we anticipate that the crystallites "a" and "b" are in a twin relationship and that twinning occurred on the (111) plane. Under such conditions, the surface orientation of b must be close to the $[0\bar{1}1]$ direction. Comparing the ECP in Fig. II-13(b) and the pole map of Fig. II-14, it follows that the great circle discussed in the analysis of crystallite "a" intersects the $[0\bar{1}1]$ pole in a direction which is 70° rotated relative to the direction of the same circle through the $[01\bar{1}]$ pole. A great circle through the poles $[\bar{1}31]$, $[\bar{1}22]$, and $[\bar{1}13]$ would therefore indicate an identical direction through the $[01\bar{1}]$ pole. In addition, this circle would go parallel to the (411) channeling lines. As determined by the silicon "Structure Factor", however, these lines are forbidden reflections. Consequently, only the (511) and (311) lines are seen in the ECP of Fig. II-13(b). The true surface orientation of crystallite "b" is tilted 10° towards the [411] direction between the [511] and [311] directions.

The orientation of the parallel strips labelled a to j in Fig. II-12(c) alternates between the "A" and "B" surface orientation. The complete sequence of parallel twinning in the <112> direction is summarized as follows:

Surface	Twin Plane	Surface
$[01\bar{1}]$A	(111)	$[0\bar{1}1]$B
$[0\bar{1}1]$B	(111)	$[01\bar{1}]$A

Note that the twin lines are in the [112] direction and the (111) twin plane is perpendicular to the <011> ribbon surface.

3.2.2 Non-Parallel Twinning

The crystallites labelled n and m in Fig. II-12(c) are bounded by lines of different directions. The ECP of crystallite n, given in Fig. II-15(a), indicates that the surface of n is close to a $[41\bar{1}]$ pole. Consulting the pole map given in Fig. II-14, it follows that the surface of n is tilted approximately 10° away from the $[41\bar{1}]$ pole. The ECP of crystallite j indicates a $[01\bar{1}]$ surface orientation. Thus the surface orientation of crystallite n is the result of (111) twinning of crystallite j. This reaction is summarized as follows:

Surface	Twin Plane	Surface
$[01\bar{1}]$J	$(11\bar{1})$	$[41\bar{1}]$N

The ECP of crystallite m is shown in Fig. II-15(b). The surface orientation of m is close to the $[\bar{1}12]$ and [113] pole. With the help of the pole map (Fig. II-14) the twin reaction is analyzed as summarized below:

Surface	Twin Plane	Surface
$[41\bar{1}]$N	(111)	$[\bar{4}\ 5\ 11]$M

The high-order orientation of m is calculated and fits the

ECP orientation exactly, (Fig. II-15(b)). The boundary line between crystallites m and j (Fig. II-16) corresponds to a change in orientation from $[\bar{4}\ 5\ 11]$ to $[01\bar{1}]$ and cannot be explained by twinning. Consequently, this line is a grain boundary.

3.3 Analysis of Twin Lamellae

Another interesting subject for ECP analysis is the lamallae of closely spaced lines at position p in Fig. II-12(c). These lamallae are generated by double twinning as follows:

Surface	Twin Plane	Surface	Twin Plane	Surface
(111)P	$(\bar{1}11)$	(511)P_1	$(\bar{1}11)$	(111)P

The twinning occurs on the $(\bar{1}11)$ plane, which is not perpendicular to the ribbon surface. The ECPs identifying this reaction are given in Figs. II-16(a,b and c).

A complete orientation list of all crystallites labelled in Fig. II-12(c) and analyzed through ECPs is given in Table II-4.

The non-parallel twinning leading to grain-boundary formation is the result of inclusions embedded during ribbon growth into the ribbon surface. Such inclusions were identified as SiC particles. The SEM micrograph of the inclusion shown in Fig. II-12(c), position I is given in Fig. II-17.

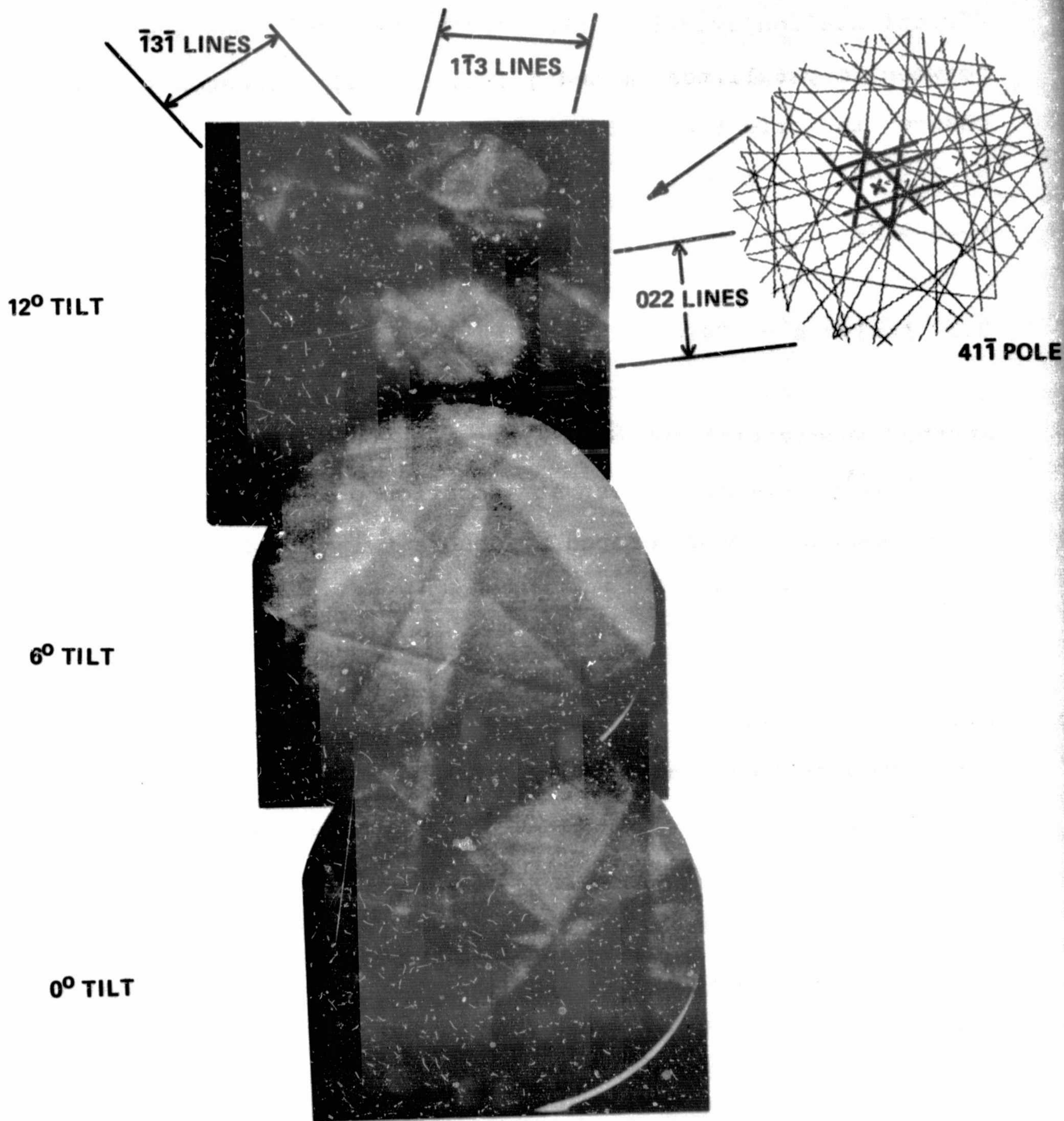

Fig. II-15(a). ECP sequence of crystallite "n" in Fig. 12(c).

ORIGINAL PAGE IS
OF POOR QUALITY

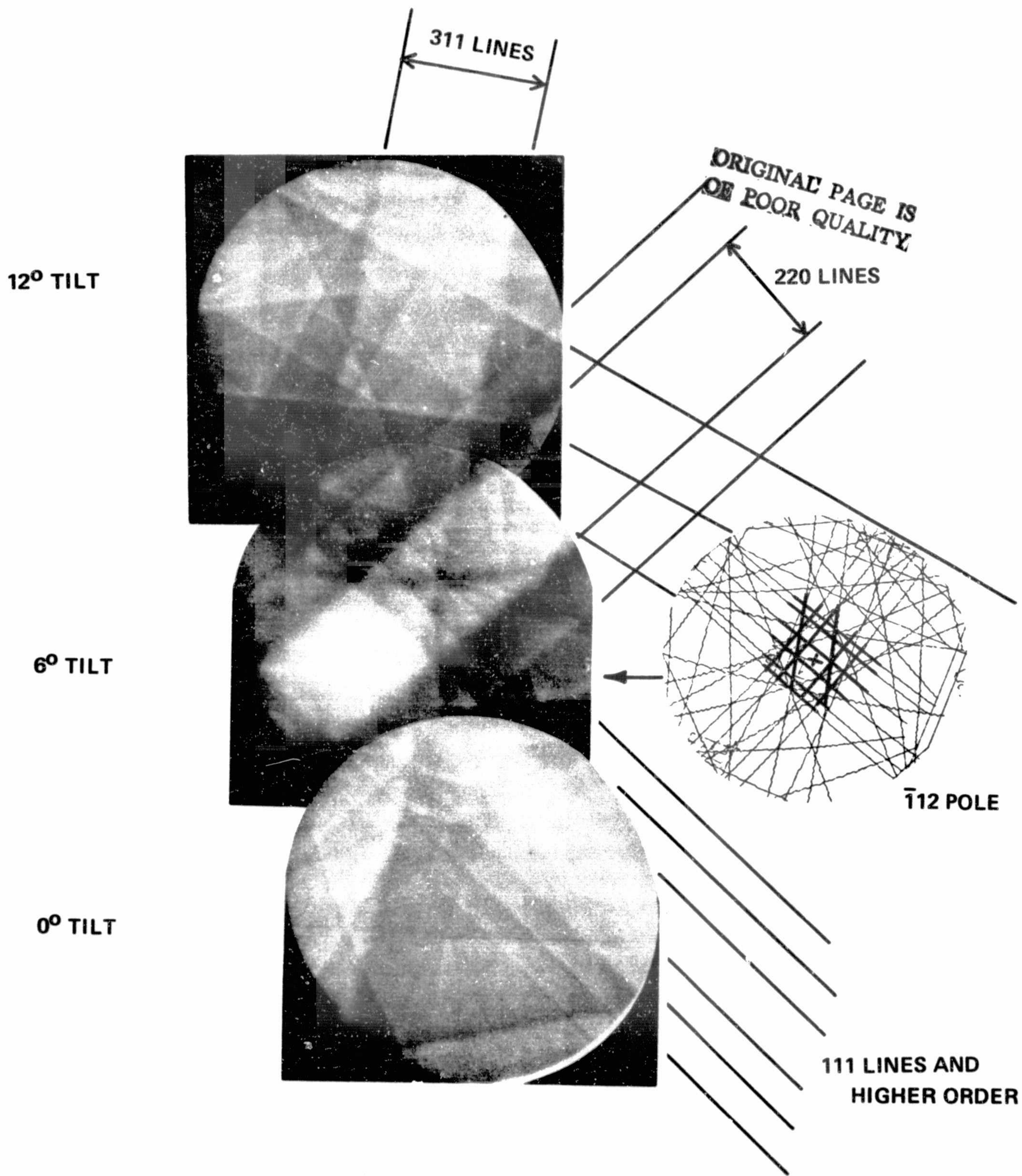

Fig. II-15(b). ECP sequence of crystallite "m" in Fig. 12(c).

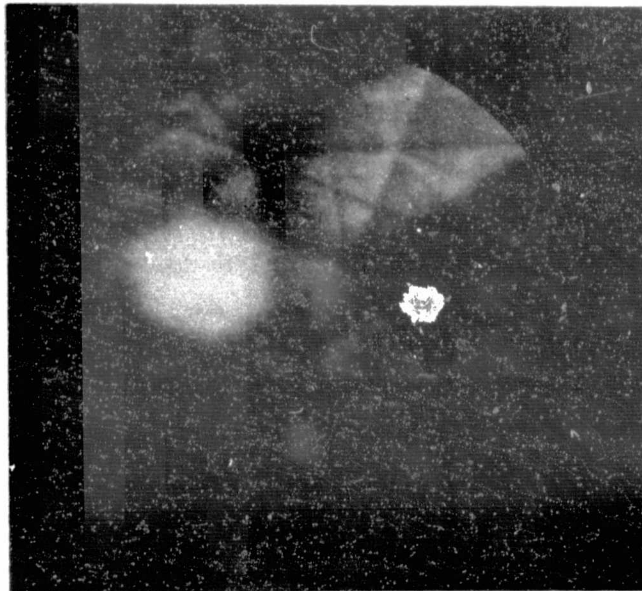

Fig. 16a ECP sequence of crystallite "z" in Fig. 12c

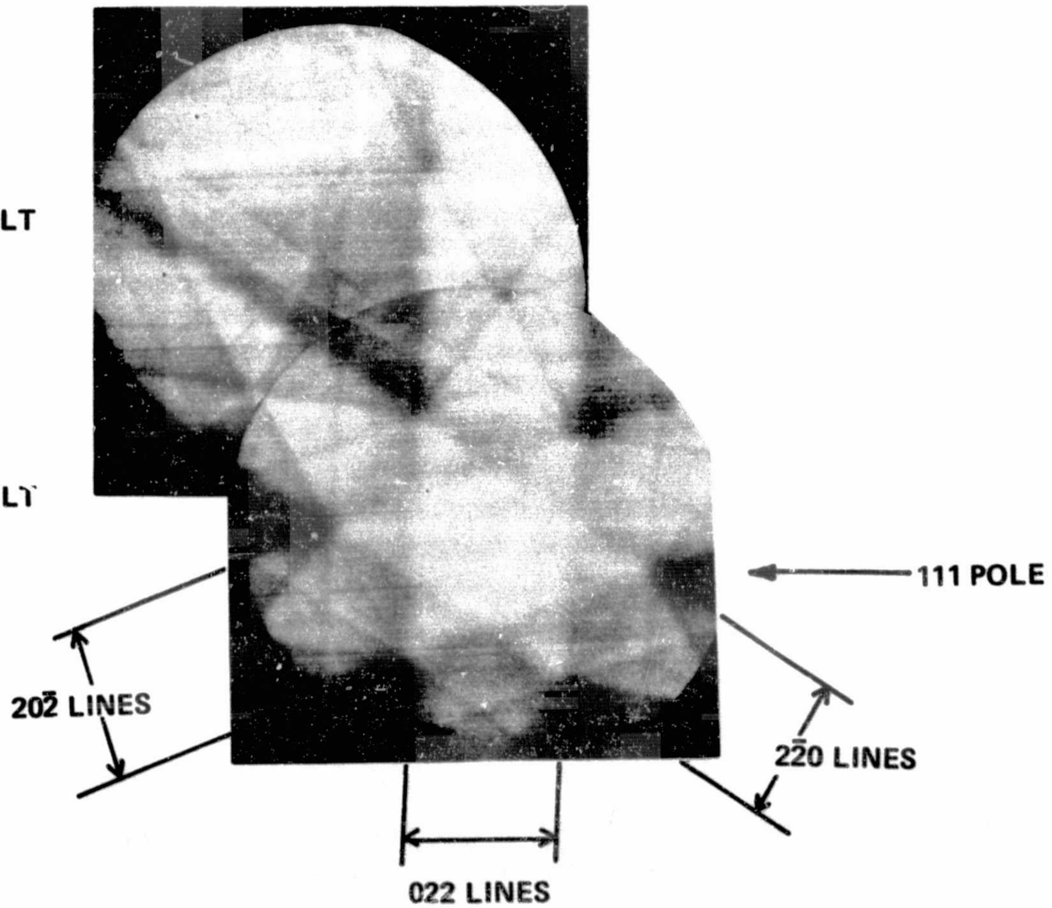

Fig. II-16(b). ECP sequence of crystallite "p" in Fig. 12(c).

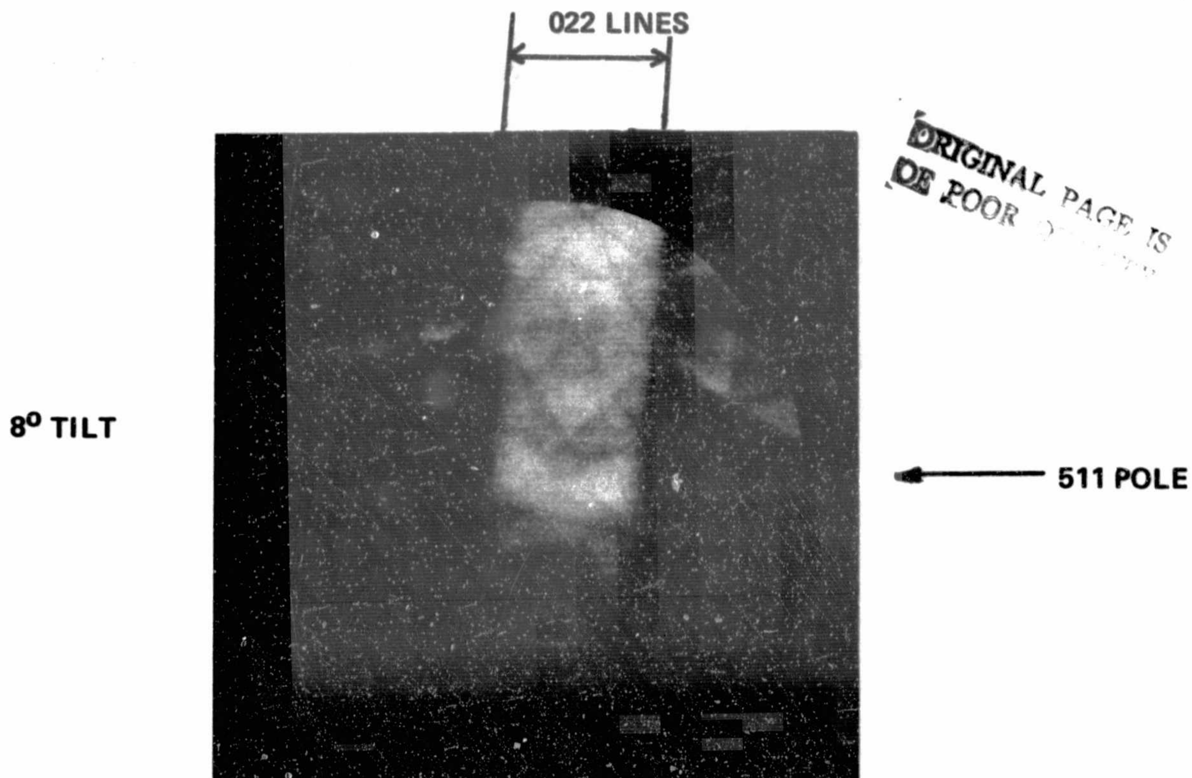

ORIGINAL PAGE IS
OF POOR

Fig. II-16(c). ECP sequence of crystallite "p_1" in Fig. 12.

TABLE II-4. Surface Orientation and Nature of Boundaries in Fig. II-13

Type of Boundary	Surface Orientation	Twin Plane*	Nature of Boundary
A/B	$(01\bar{1})/(0\bar{1}1)$	$(111)_p$	Twin
A/N	$(01\bar{1})/(41\bar{1})$	$(11\bar{1})_i$	Twin
N/M	$(41\bar{1})/(\bar{4}\ 5\ 11)$	$(111)_i$	Twin
M/A	$(\bar{4}\ 5\ 11)/(01\bar{1})$		Grain boundary
Z/A	$(111)/(01\bar{1})$		Grain boundary
p/p_1	$(111)/(511)$	$(\bar{1}11)_i$	Twin
B/R	$(0\bar{1}1)/(4\bar{1}1)$	$(1\bar{1}1)_i$	Twin

*Subscripts p and i refer to twin plane perpendicular to and inclined to ribbon surface, respectively.

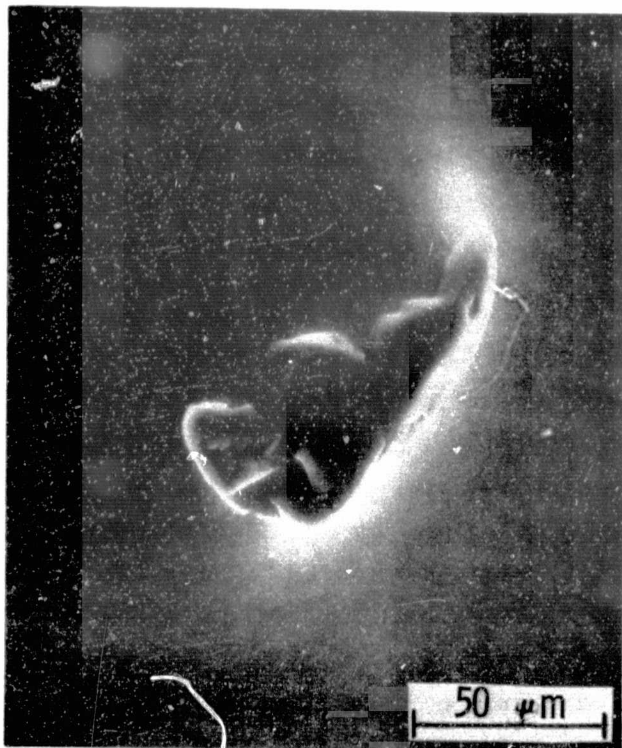

a

b

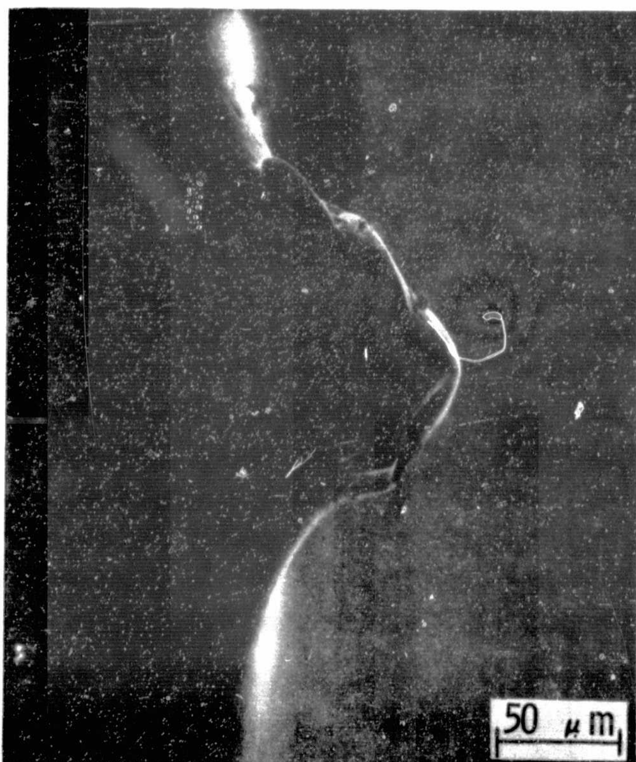

c

d

Fig. II-17. SEM micrographs of a SiC particle; (a) before etching; (b) after 10-sec Sirtl etch; (c) closeup view of etched area in and around particle; (d) view of etched area showing surrounding unetched walls of SiC.

ORIGINAL PAGE IS
OF POOR QUALITY

4.0 ELECTRICAL CHARACTERIZATION OF SILICON RIBBONS

This section of the report provides additional information about the electrical properties of CAST ribbons. The influence of crystal defects, such as surface inclusions, dislocations, twins, and grain boundaries, on generation lifetime of minority carriers is investigated through MOS C-t measurements. Lifetime distribution data of different samples 25 x 60 mm in size are thus obtained and compared with the efficiency of solar cells made from such samples.

4.1 Experimental

CAST Silicon ribbons doped with boron to a resistivity of 2 Ω-cm were used for this investigation. Lifetime measurements are made using the approach described by Fahrner and Schneider[6]. Their technique allows relatively fast large-scale measurements of generation lifetime in the range < 1 msec to > 0.1 nsec. For the measurements a metal oxide semiconductor (MOS) capacitor is biased into strong inversion and subsequently switched into deep depletion. An appropriate experimental setup prints out or displays a typical MOS recovery time, which is introduced into a computer fed by a theoretical generation-lifetime model and the pertinent wafer data. Thus minority-carrier generation-

lifetime values of the silicon under the MOS capacitor (depletion zone) are obtained. The error limit of this technique, compared with a Zerbst plot[7], is less than 20% for lifetime values $t \leq 10$ μsec. For $t > 1$ msec the error can increase to 100%. Best lifetime values encountered in ribbons are approximately 500 μsec compared with Czochralski silicon wafers, where lifetimes of over 1000 μsec are encountered.

4.2 Fabrication of MOS Capacitors and Solar Cells

Ribbon sections of full width (50 mm) doped to approximately 2 Ω-cm, p-type, and 60 mm in length are processed to contain two groups of circular MOS capacitors. Each group consists of 36 capacitors of different dot size. One group uses 1.5-mm-diameter dots, and the other 0.5-mm dots. Before oxidation, ribbon sections are first etched for 30 seconds in a mixture of 3 parts nitric, 2 parts acetic, and 1 part hydrofluoric acid. Subsequently, the ribbon sections are MOS-processed using standard techniques. They are cleaned in NH_4-H_2O_2, HCl-H_2O_2, and HF solutions. Subsequently, a 5000 Å-thick oxide is grown at 1000°C using a dry-wet-dry oxidation cycle. Aluminum metallurgy is used.

After metallization the wafers are annealed for 15 minutes at 400°C in forming gas. For comparison, 57-mm-diameter

Czochralski wafers of zero dislocation density, p-type, and 2 Ω-cm are also MOS-processed.

For solar-cell processing, lifetime evaluated ribbon sections and Czochralski standards are stripped of all MOS capacitors and subsequently solar cell processed using a standard procedure. The starting wafers are boron doped, dislocation free, Czochralski grown silicon wafers or ribbon sections. Resistivity of the wafers or ribbons is 1-2 Ω-cm. The wafers are $POCl_3$ diffused for 30 minutes at 900°C to a junction depth of 4000Å. Aluminum and silver is used to deposit the contact pattern. The process produces a solar cell of better than 10% efficiency on a standard wafer.

4.3 Measurements

Ribbon crystals grown by the capillary action shaping technique display a unique defect structure. Under steady state growth conditions the defect structure is dominated by linear boundaries parallel to the ribbon edges[1,2]. Best ribbons obtained have a surface orientation close to (011) and boundaries in the [211] growth direction[1,2]. Seed orientation has no influence on the steady state growth perfection of the ribbon[1,2]. The electrical effects associated with the equilibrium defect structure are of

interest because they influence solar cell efficiency[1,2]. In this section the electrical activity of the defects is investigated qualitatively through use of the electron beam induced current (EBIC) signal in the scanning electron microscope while the influence of defects on minority carriers is measured quantitatively through MOS C-t measurements.

4.3.1 EBIC Measurements

The EBIC technique is useful for non-destructive imaging of electrically active defects in silicon. EBIC investigations of ribbons as grown are done with Schottky contacts. Solar cells are investigated in the EBIC mode through use of diffused p-n junctions[8].

The electrically-active defect density in a ribbon crystal can be considerably lower than its total defect density. The total defect density is found by Sirtl etching and optical microscopy of the ribbon surface.

Figure II-18(a) shows an optical micrograph of a ribbon solar-cell section. The two fingers of the Al-Ag metal grid are visible and can be used for area identification. The parallel lines perpendicular to the fingers are the linear

ORIGINAL PAGE IS
OF POOR QUALITY

ORIGINAL PAGE IS
OF POOR QUALITY

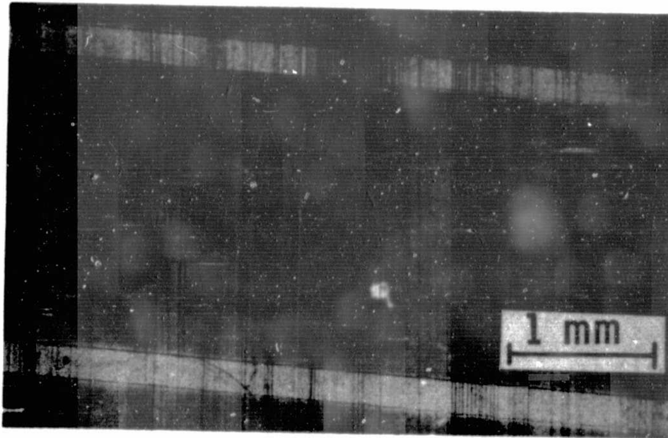

a. Optical micrograph of solar-cell surface

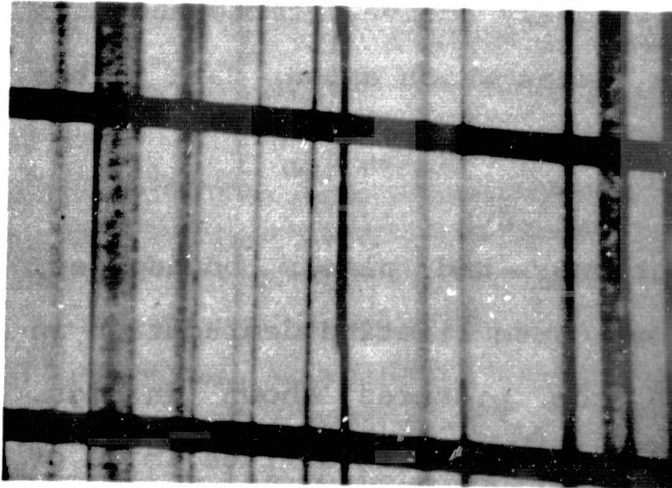

b. Corresponding EBIC picture

Fig. II-18. Electrical activity of defects in solar cells.

boundaries typical for ribbons grown under steady-state conditions. Note the high density of the lines. Figure II-18(b) is the corresponding EBIC picture. The dark horizontal lines are the Al-Ag fingers. The dark vertical lines and bands in the EBIC picture indicate a local reduction in the beam-induced current when the beam scans over these areas. This is caused by crystal defects which act as preferred recombination centers. The dark bands correlate well with the crystal sections that show etch pits (dislocations) after Sirtl etching, while the sharp boundary lines correspond to electrically-active twin or grain boundaries. The areas which appear white in the EBIC picture are free of electrically active defects and have better lifetimes than the areas which appear dark in the EBIC picture.

In addition to dislocations and planar boundaries, silicon-carbide dendrites also cause lifetime degradation in ribbons. This is seen in the pictures shown in Figs. II-19(a,b). Figure II-19(a) is the SEM surface image of dendrites covering the ribbon surface. The corresponding EBIC image, using p-n junction contrast, is given in Fig. II-19(b). Such dendrites are very strong recombination centers. The efficiency of solar cells is reduced to the 1 to 3% range if such dendrites are present.

4.3.2 Lifetime Measurements

The EBIC measurements are in good qualitative agreement with MOS C-t lifetime data obtained from such crystals. Lifetime values of typical defect areas are obtained by placing MOS capacitors into these areas. Thus the lifetime degrading property of a particular defect pattern can be measured directly. A comparison of the EBIC picture and lifetime data is also possible because the same MOS capacitor can be used for EBIC display and lifetime measurements. Examples of lifetime variation and its dependency on ribbon perfection are shown in Figs. II-20. Figure II-20(a) is a ribbon section of highest perfection. The crystal section between the twin boundaries is very perfect. A less perfect twin section is shown in Fig. II-20(b). Note the etch pits - indicating dislocations - in the left and right crystal section. The middle section between the twin boundaries is free of etch pits. Other defect configurations found in steady-state grown ribbon sections are given in Figs. II-20(c,d). A small-angle grain boundary is shown in Fig. II-20(c). Note the dislocation pits right and left from the boundary. A silicon carbide surface inclusion is shown in Fig. II-20(d). The measured lifetimes are noted in each figure for each defect pattern and represent typical data.

Fig. II-19(a)
SEM surface image of silicon carbide dendrites on ribbon surface.

Fig. II-19(b) EBIC image (junction contrast) of ribbon surface similar to the one shown in Fig. 19(a).

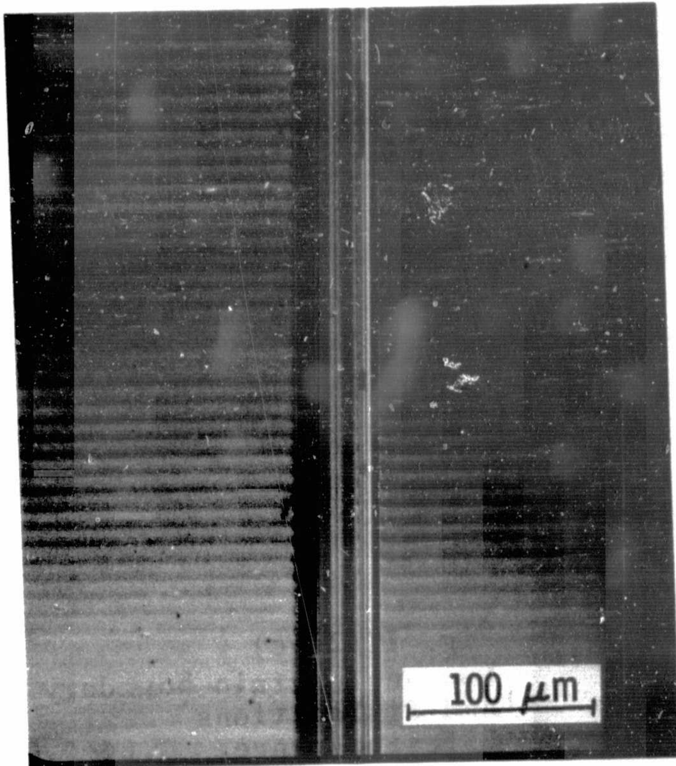

ORIGINAL PAGE IS
OF POOR QUALITY

Fig. II-20(a)
Twinning in perfect crystal
Lifetime range: 73~17.0μsec

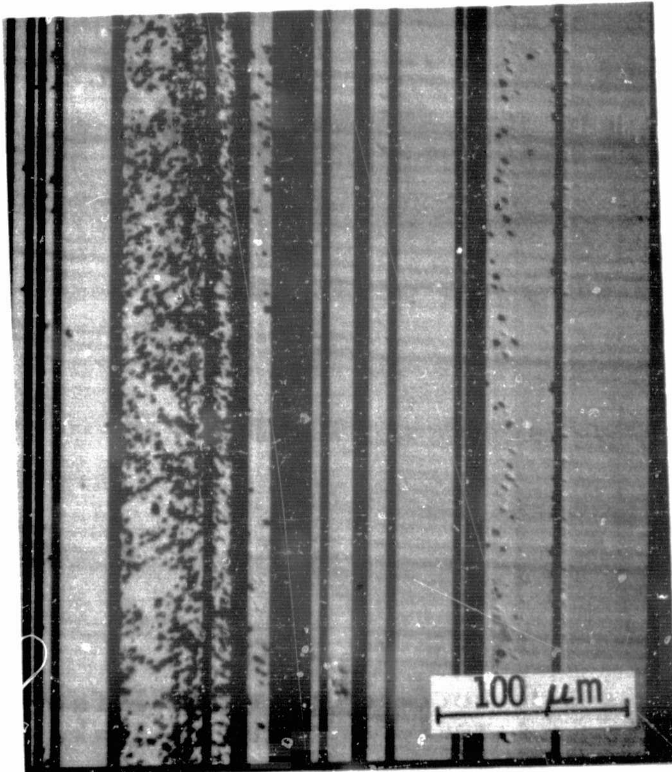

Fig. II-20(b)
Twinning and dislocations
Lifetime range: 0.67~1.4μsec

Fig. II-20. Defect patterns in ribbon surfaces.

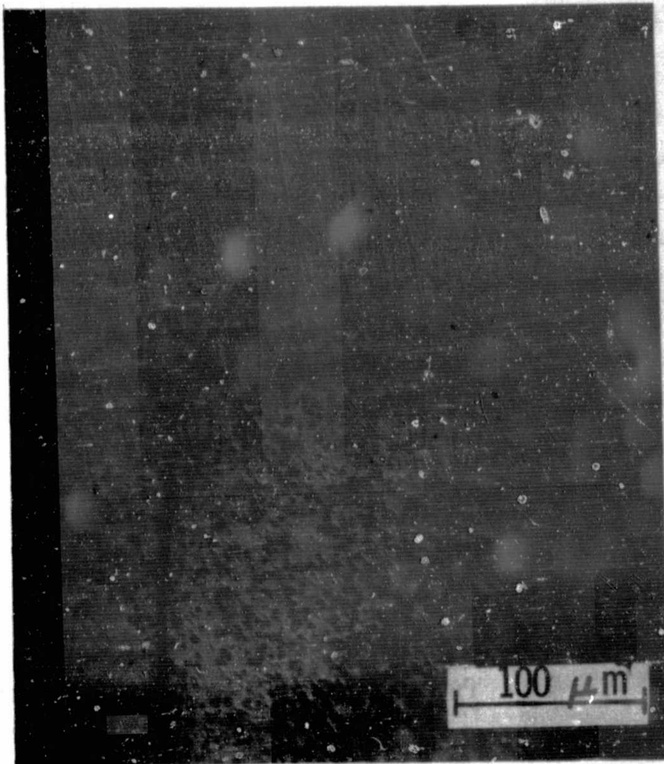

Fig. II-20(c)
Low-angle grain boundary
and dislocations
Lifetime range: 0.01~0.03μsec

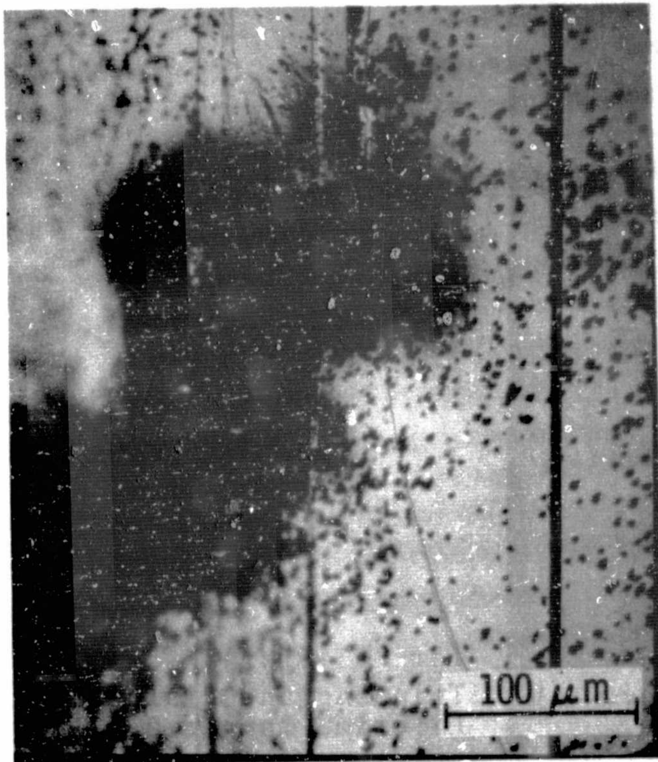

ORIGINAL PAGE IS
OF POOR QUALITY

Fig. II-20(d)
Surface inclusion lifetime: not
measurable due to leaky oxide

Lifetime of minority carriers in ribbon varies with the position of the MOS dots relative to the edges of the ribbon. Longer lifetimes are found for dots located in the center of the ribbon. This is illustrated in Fig. II-21. This figure summarizes lifetime measurements made for three different crystals. In Fig. II-21 the generation lifetime is plotted, in microseconds, as the ordinate and the position of the MOS dot relative to the ribbon edge as the abscissa. The dots A and G are close to the left and to the right edges of the ribbon. The solid line in the figure connects lifetime values obtained by averaging the single-lifetime values per column and plotting this averaged column value against the distance from the edges for the different ribbon sections. The ratio of average lifetime for dots located in the middle of the ribbon and for those located close to the edge can be as large as 200. Perfection studies made on these ribbon sections indicate that the degradation of lifetime correlates with crystal perfection, which improves towards the center.

Lifetime values larger than 500 μsec have been measured in defect-free sections of CAST ribbons. This indicates that ribbons grown from carbon dies have potential for high-efficiency solar cells.

As indicated by the EBIC measurements the presence of β-SiC dendrites cause a serious lifetime and solar cell problem. Such dendrites have been found to deposit epitaxially on ribbon surfaces during ribbon growth. (See Section 2.0 of this report). The density of such dendrites is highest near the seed-ribbon interface and decreases rapidly with increasing distance from the interface. The dendrites cause leaky MOS devices and low efficiency solar cells. This problem is eliminated by removing a thin layer (< 10 μm) of the as-grown surface through etching in a mixture of 3 HNO_3-2 HAC-1 HF acid. It is found that etching the ribbons before processing also relieves the problem of breakage, which is more pronounced for as-grown ribbons.

Results of lifetime measurements made on ribbons as grown and on ribbons slightly etched before processing are summarized in Table II-2, section 2.0 of this report. It can be seen that due to the presence of β-SiC dendrites, the occurrence of leaky MOS dots can be very high on ribbon sections cut as far as 40 cm from the interface. Etching before processing eliminates this problem.

4.5 Discussion

The conversion efficiency of silicon solar cells depends on a variety of factors and their complex interactions. Most important in this context is the presence or absence of

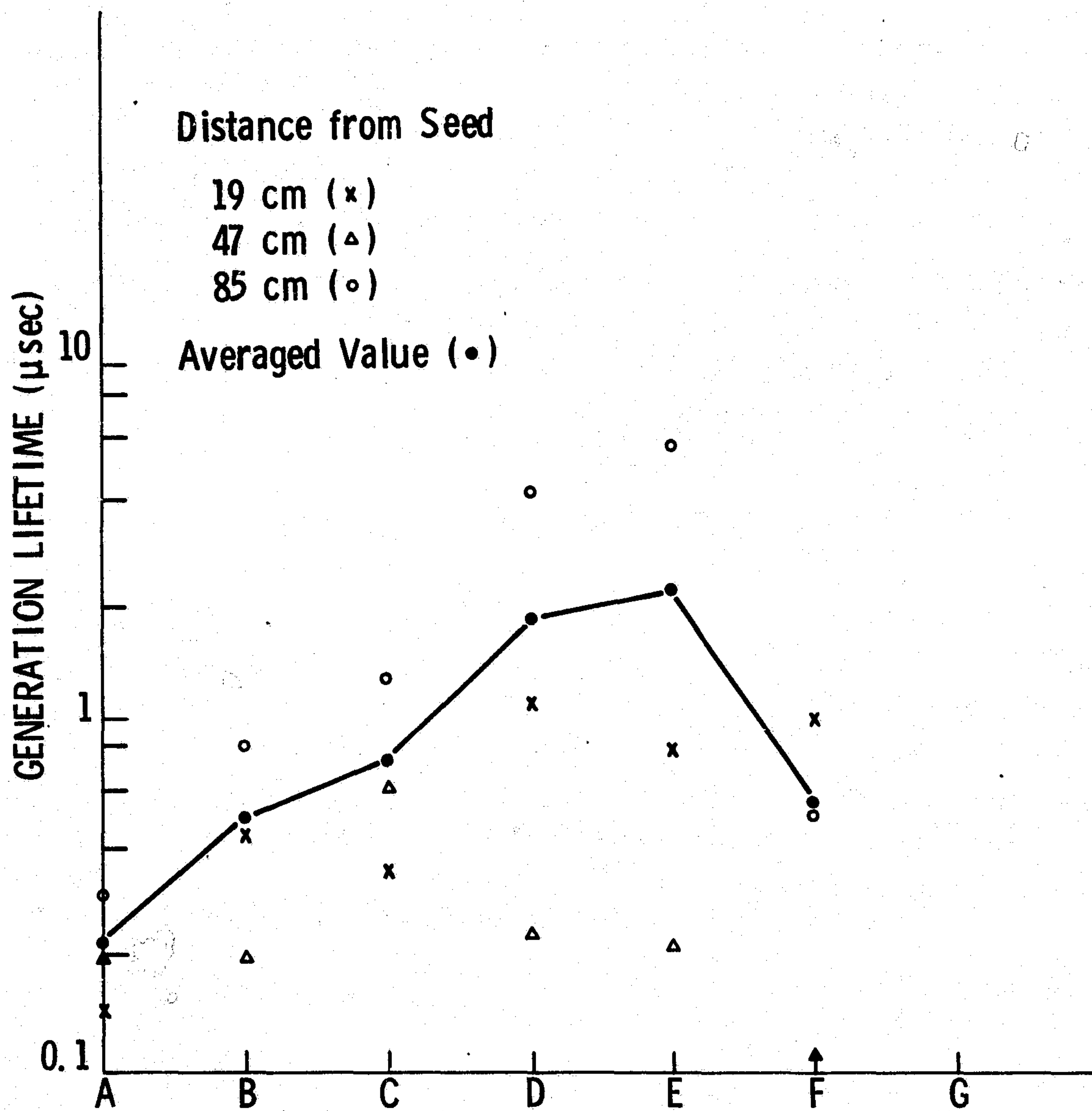

Fig. II-21. Position dependency of lifetime values in ribbon surfaces: ribbon 213.

non-radiative recombination centers. Also of great influence on solar cell efficiency is the presence of transition metals in silicon. There is evidence that crystallographic defects in silicon can influence solar-cell efficiency[2]. Only few exact data are available correlating the influence of crystal defects, lifetime, and solar-cell efficiency. Therefore, we have measured the influence of dislocations and other defects in ribbons on generation lifetime and solar cell efficiency.

Dislocations in ribbons are randomly distributed throughout the grains or they are aligned in the slip directions. Transmission electron microscopy investigations of ribbons with (011) surface orientation show that these dislocations have Burgers vectors a/2 [110] parallel or inclined to the (011) ribbon surface. For such dislocations one finds that the product of lifetime (τ) and dislocation density (N_D) is approximately $\tau \times N_D \approx 0.5$ sec$\cdot$cm^{-2}. This is a factor of 30 lower than reported for grown-in dislocations in float zone silicon of 1000 Ω-cm resistivity[9]. Assuming that the lifetime measuring techniques used in reference 9 (photovoltaic decay technique) and the MOS C-t technique[6] give comparable results for the bulk lifetime this would indicate that the electrical activity of 60° dislocations in ribbons is higher than the electrical activity of grown-in dislocations in float zone crystals. This conclusion appears reasonable. (See also page 248 of this report.)

Transmission electron microscopy investigations of electrically active and non-active boundaries were also made and are presented in the next section. These investigations indicate that all non-active boundaries are either first order (coherent) twin boundaries or are composed of multiple stacking faults. The electrically active boundaries are found to contain various amounts of dislocations. The electrical-activity of such boundaries depends on the number of dislocations present in the boundaries.

Based on such electrical measurements and detailed structural investigations, ribbon quality is classified as shown in Table II-5. One arrives at four different categories of crystal perfection which are related to lifetime ranges and corresponding solar cell efficiency ranges.

The classification presented in Table II-5 is a phenomenological correlation of lifetime data and solar cell efficiencies. This classification is based on a large amount of experimental data and presents a good guide-line to ribbon quality and its influence on solar cell efficiency. Interesting in Table II-5 is the correlation given in columns three and four. Every lifetime range corresponds to a specific solar-cell efficiency range. Note that the standard Czochralski wafer, a defect-free wafer, has the best lifetime and also the best solar-cell efficiency.

TABLE II-5 Classification of Ribbon Quality

Class	Lifetime Range [μsec]	Solar Cell Eff.* [%]	Dominant Defects
I	1 to 10	5 to 8	Coherent twins, stacking faults, dislocations below $10^4/cm^2$.
II	0.01 to 1	3 to 5	Non-coherent twins, multiple stacking faults, low angle grain boundaries, dislocations above $10^4/cm^2$.
III	< 0.01	1 to 3	Grain boundaries, dislocations above $10^6/cm^2$.
IV	Not measurable	----	Silicon carbide dendrites on surface.
Standard CZ	10 to 500	8 to 12	None

*Measured at AM1, no anti-reflective coating.

In this context we tend to believe that "high-efficiency" solar cells may require a well controlled defect state in the silicon material.

4.6 Summary

Using MOS C-t measurements, lifetime degrading defects in silicon ribbons are classified into four groups according to

the severity of their impact on lifetime: silicon carbide dendrites, grain boundaries, dislocations, and partial dislocations. First order twins do not influence lifetime.

The impact of these defects on solar-cell efficiency is established, and solar-cell efficiency ranges are given for the four different perfection states encountered in ribbons.

Lifetime-degrading properties of different defects are qualitatively discussed and displayed through SEM EBIC contrast using Schottky contacts and solar-cell p-n junctions.

5.0 STRUCTURAL CHARACTERIZATION OF SILICON RIBBONS

This section of the report describes the analysis of crystal defects in CAST ribbons. First, the electrically-active defects are identified through EBIC contrast in the scanning electron microscope as decribed in the preceding section. Subsequently, the crystallographic structure of a specific defect is analyzed through transmission electron microscopy. Finally, its influence on minority carrier lifetime is determined through MOS C-t measurements.

5.1 Measurements

Based on electrical measurements and preliminary structural

investigations, ribbon quality can be classified into four categories. This classification was shown in Table II-2 in the preceding section entitled: Electrical Characterization.

Accordingly, the different ribbon quality groups are related to certain lifetime and solar cell efficiency ranges. This classification presents a good guide-line to solar cell efficiency obtainable from ribbon sections of certain perfection. The following investigations have produced results in support of this original classification.

5.2 Experimental

Examples of ribbon sections representing the different quality groups listed in Table II-5, section 4.5 are shown in Fig. II-22. MOS capacitors were fabricated on such ribbon sections, 24 mm x 60 mm, or 50 mm x 60 mm in size. Normally, 36 capacitors of 1.5 mm diameter were placed on a section. In some cases, high density masks with 400 capacitors were used. The two masks are shown in Fig. II-23. Subsequently, generation lifetime of each capacitor was measured using the MOS C-t technique. After the lifetime measurements, the EBIC image of the MOS capacitor was obtained in the SEM, as described in reference 8. Thus, the subsurface defect structure in the silicon was displayed and qualitative information about the electrical activity of

ORIGINAL PAGE IS
OF POOR QUALITY

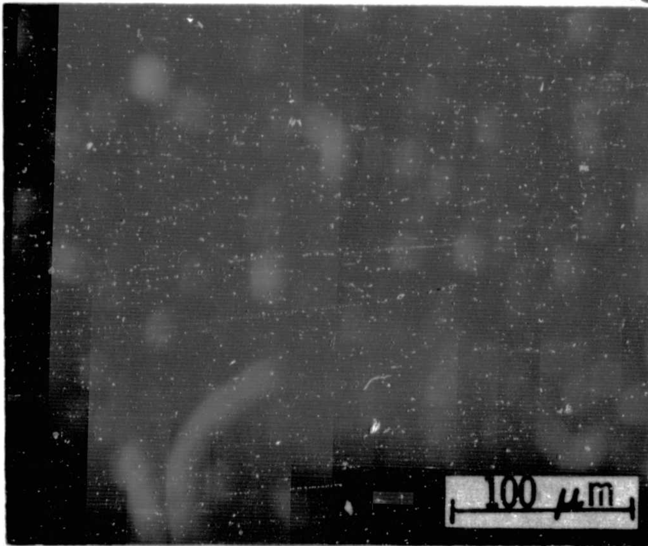

a. Perfect crystal
Lifetime: 825 μsec

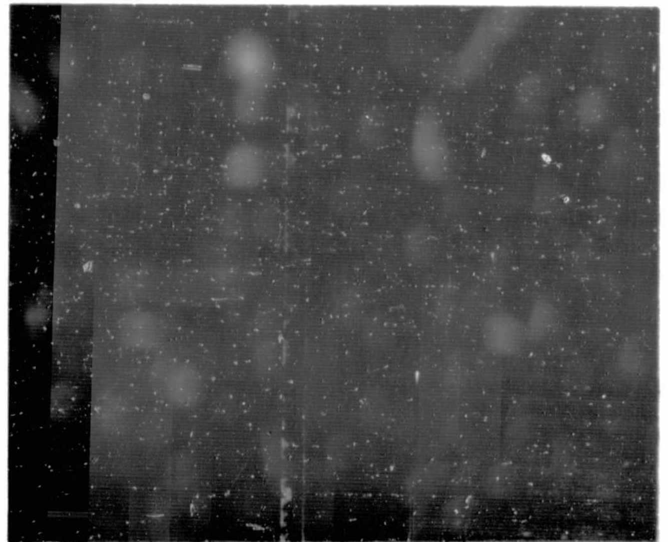

b. Dislocations in boundary and in left crystal section
Lifetime: 1.5 μsec

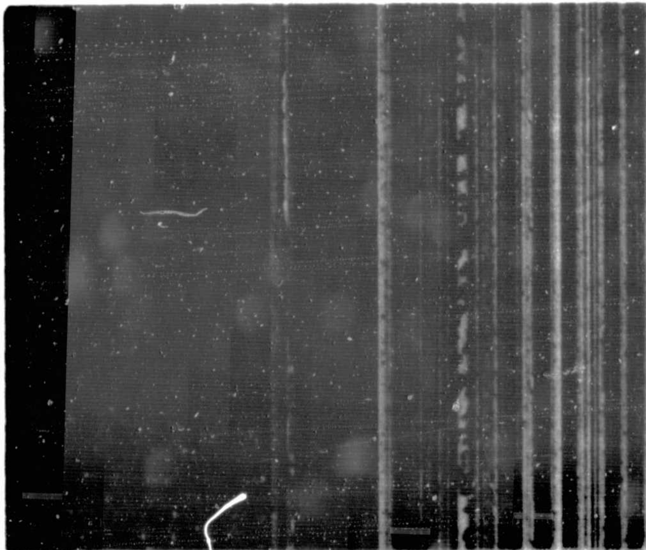

c. Dislocations and active boundaries
Lifetime: 0.145 μsec

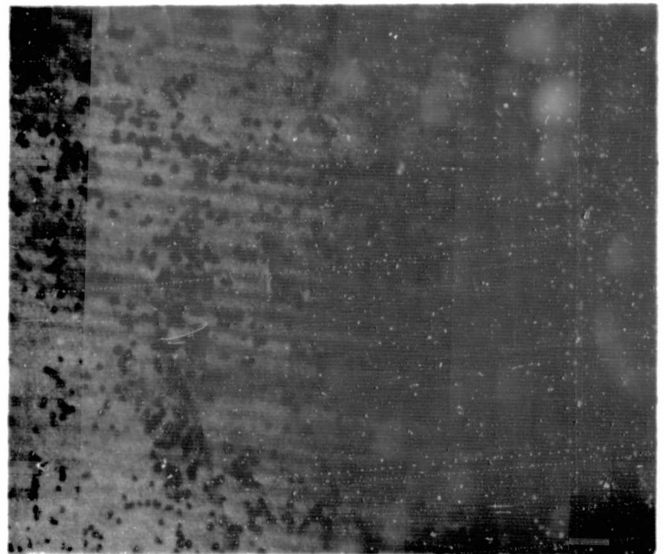

d. Dislocations and low-angle boundary
Lifetime: 0.02 μsec

Fig. II-22. Defect pattern and lifetime distributions.

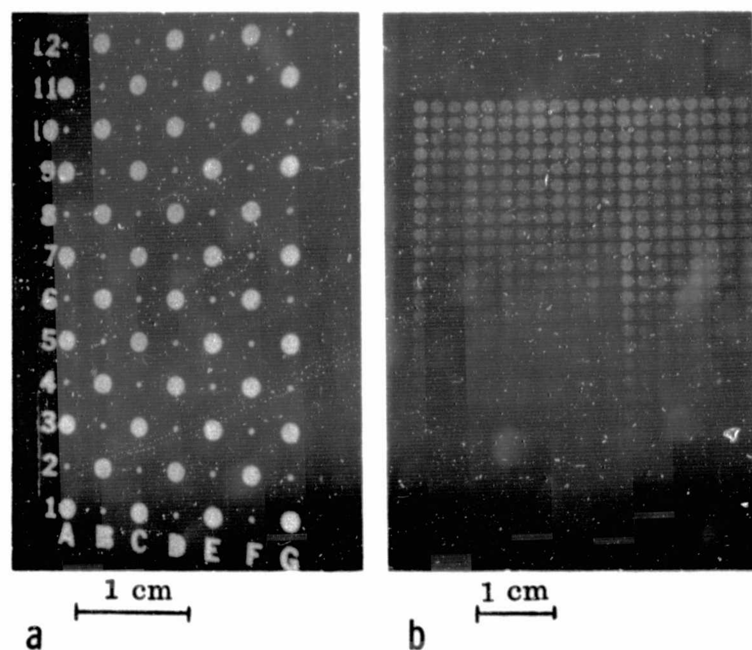

Fig. II-23. (a) low density and (b) high density MOS capacitor mask as used for the evaluation of lifetime for silicon ribbons. Dot size for both (a) and (b) is 1.5 mm.

the crystal defects under the MOS dot was obtained. After the SEM investigation, the Al MOS dots and the SiO_2 were stripped of the ribbon surface and some MOS areas were Sirtl etched to reveal the crystal defects under the MOS dot in the optical microscope. A comparison of EBIC picture and optical picture allowed one to differentiate between the electrically active and the non-active defects. However, most of the MOS capacitors were punched out after stripping Al and SiO_2 as 2 mm disks (not Sirtl etched) and processed for TEM investigations. Before TEM investigations, the corresponding EBIC image of the MOS capacitor was studied. Details were obtained about the defect state in the silicon under the MOS dot as well as information was obtained about the electrical activity of the defects in the silicon under the MOS dot. Subsequently, the defects were analyzed in the TEM. A good correlation between defect state, type of defect, its influence on generation lifetime, and its electrical activity was thus possible.

5.3 Results

5.3.1 Defects in Class I Ribbons

The most obvious defects encountered under steady state growth conditions are linear boundaries which are visible in the ribbon surface even prior to etching. These boundaries

tend to grow parallel to the ribbon edges. While the majority of these boundaries are twins or stacking faults, some of them are multiple stacking faults or low angle grain boundaries. The electrical activity of these boundaries depends on their crystallographic nature and can vary significantly. This is illustrated in Figs. II-24. The EBIC picture of Fig. II-24(a) shows that most of the linear, parallel boundaries displayed in the optical micrograph of Fig. II-24(b) are electrically non-active except those at positions indicated by F and L. The activity is moderate for boundaries at F but is strong for boundaries at position L.

Figure II-24(c) is an optical micrograph of area A indicated in Fig. II-24(b) at higher magnification and shows that the non-active boundaries are free of dislocation etch pits. TEM micrographs of this type of boundary are shown in Figs. II-25(a and b) for ribbons of [011] and [211] surface orientation, respectively. These two surface orientations, especially the [011] are preferred orientations under steady state growth conditions. Twinning occurs in the (111) plane perpendicular to the [011] surface but inclined to the [211] surface. Using TEM image characteristics associated with twin boundaries and stacking faults, the boundaries in Figs. II-25(a and b) are analyzed as first order (coherent) twin

ORIGINAL PAGE IS
OF POOR QUALITY

a

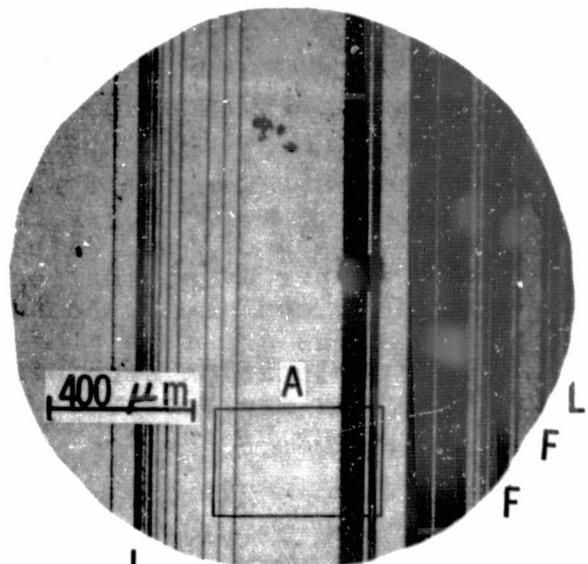

b

Fig. II-24. (a) EBIC micrograph showing that most of the linear, parallel boundaries displaced in the optical micrograph of (b) are electrically non-active except for those at the position indicated by F and L.

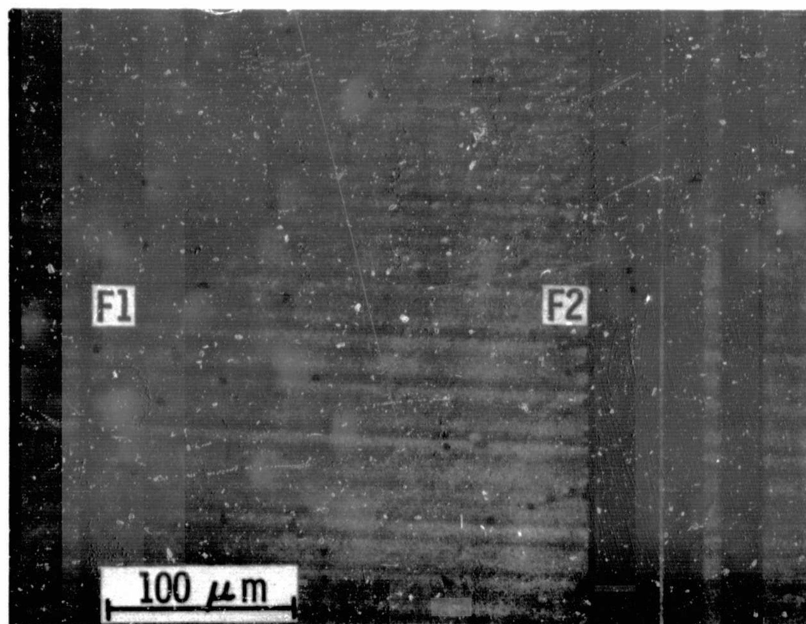

C

Fig. II-24(c). Area A of Fig. 24(b) at higher magnification. The non-active boundaries are free of dislocation etch pits. Pits are observed along F1 and F2.

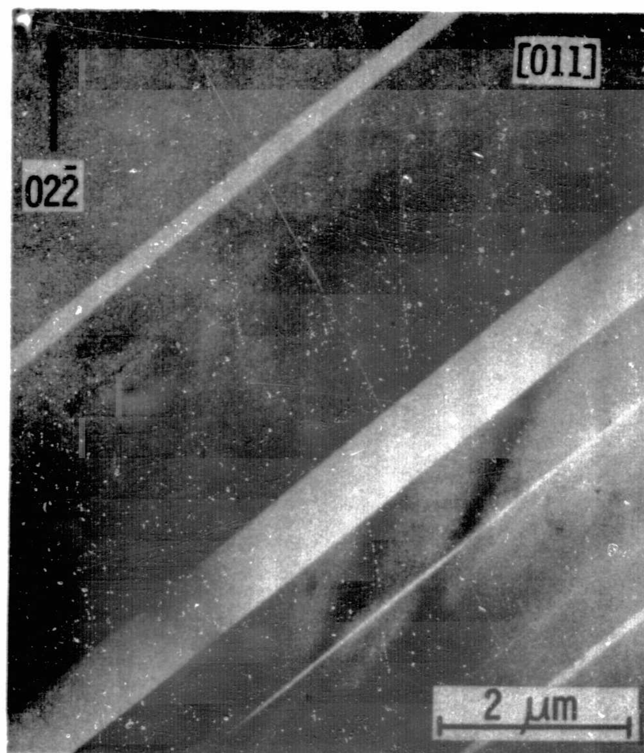

a

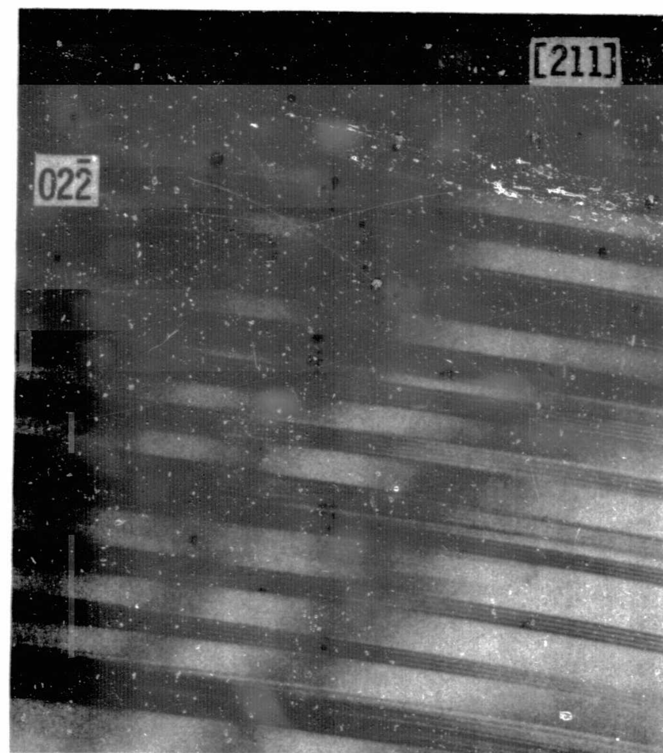

b

Fig. II-25. TEM micrographs showing that the non-active boundaries are either coherent twin boundaries or stacking faults. (a) (011); and (b) (211) surface orientation.

ORIGINAL PAGE IS OF POOR QUALITY

boundaries and stacking faults[10]. Dislocations in or between these non-active boundaries, if any, are of very low density. There is only very weak electrical activity connected with such crystal areas.

Electrical activity of dislocations depends on type, distribution, and density. It can vary from weak to strong. First, we discuss homogeneously distributed dislocations. An example is seen in the EBIC image shown in Fig. II-26(a). The corresponding optical micrograph obtained after Sirtl etching is given in Fig. II-26(b). A small area out of Fig. II-26(b) is shown magnified in Fig. II-26(c).

The electrical activity of dislocations can be described by the product of minority carrier lifetime (τ) and dislocation density (N_D). For the 60° dislocations in ribbons, we find experimentally that $N_D \times \tau \simeq 0.5 \text{ sec} \cdot \text{cm}^{-2}$.

This would indicate that a dislocation density of $5 \times 10^5/\text{cm}^2$ results in a lifetime of 1 μsec. Thus dislocation densities of up to $10^5/\text{cm}^2$ are of relatively low electrical activity and acceptable in ribbon section.

The crystallographic nature of such dislocations was investigated. TEM studies show that for ribbons of [011]

ORIGINAL PAGE IS
OF POOR QUALITY

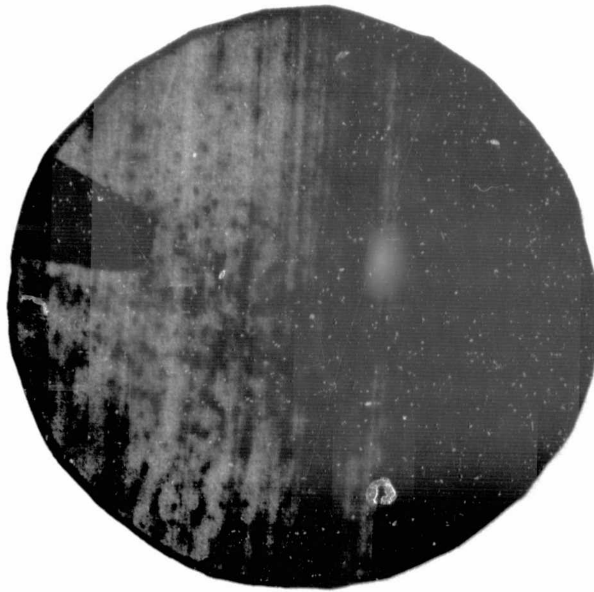

a

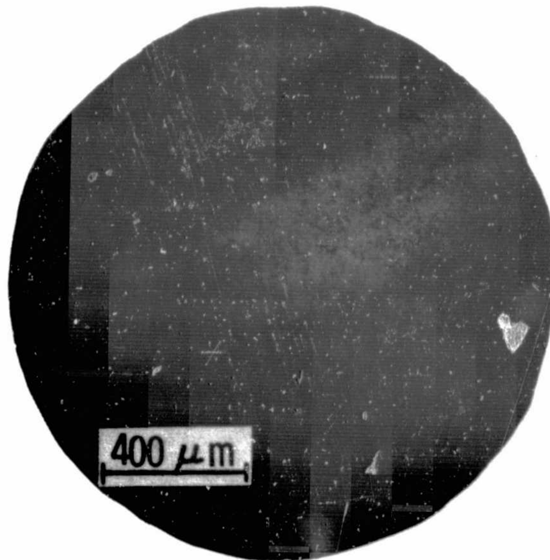

b

Fig. II-26. (a) EBIC micrograph showing the electrical activity of dislocations; (b) the corresponding optical micrograph obtained after Sirtl etching.

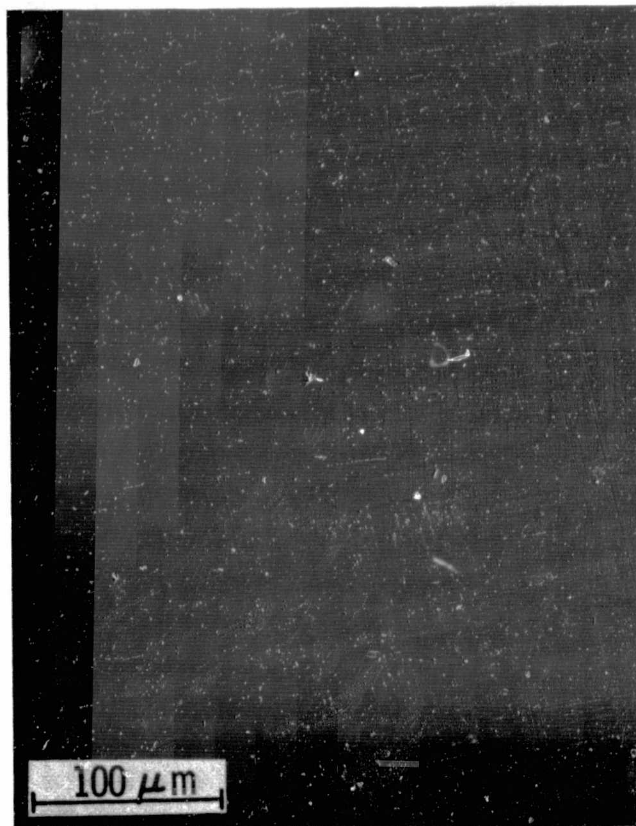

C

Fig. II-26. (c) a small area of 26(b) at higher magnification showing dislocation etch pits. The dislocation density, N_D, is about 1×10^5 per cm^2.

ORIGINAL PAGE IS
OF POOR QUALITY

surface orientation, the dislocations are of the 60° type with Burgers vector either parallel or inclined to the ribbon surface.

The dislocations are generated by stresses produced through the relatively large thermal gradients associated with the CAST growth technique. The density of dislocations (N_D) resulting from thermal stress effects can be estimated according to: $N_D = (\alpha/a) \cdot \delta\Delta T$ where $\alpha = 5 \times 10^{-6}/^oC$, is the expansion coefficient of Si, $a = 5.42 \times 10^{-8}$ cm, is the lattice constant of Si, and $\delta \Delta T$ is the deviation from the average thermal gradient ΔT at the interface. The deviation from the average thermal gradient at the growth front is estimated to be approximately 100^oC. This yields a dislocation density of approximately $10^4/cm^2$, in good agreement with the density observed in the ribbons.

Quite frequently a second type of dislocation arrangement occurs in CAST ribbons. Typical for this arrangement are dislocations piled up against twin boundaries in the slip directions. Such dislocation pile-ups lead to interesting interactions between twin boundaries and dislocations. As a result of this interaction, twin boundaries deteriorate and become electrically active. A TEM micrograph of such a boundary section is shown in Fig. 27 for a ribbon of [211]

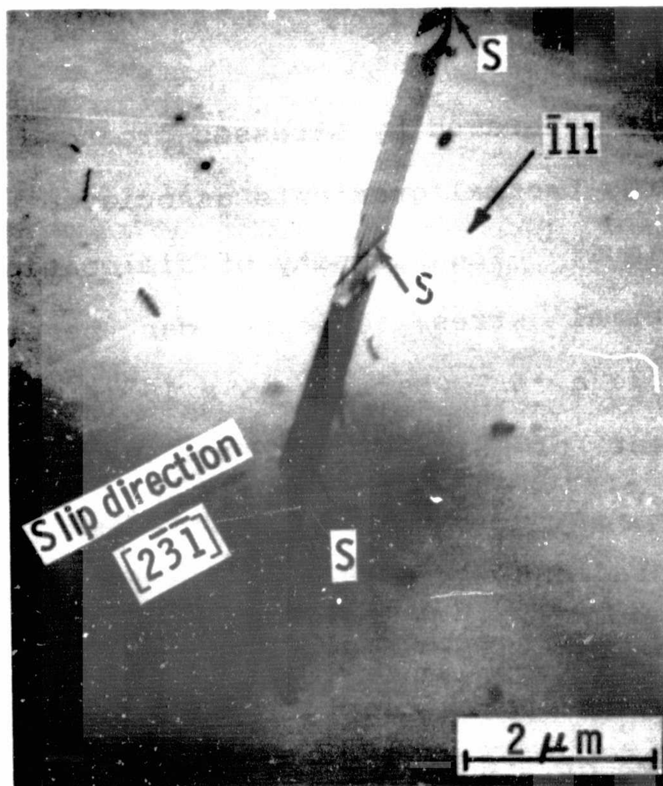

Fig. II-27. TEM micrographs showing dislocation piling-up against a twin boundary in the slip direction.

ORIGINAL PAGE IS
OF POOR QUALITY

surface orientation. Figure II-27 shows that the slip dislocations pile-up against the linear boundary. In this area, the boundary degenerates into multiple overlapping faults. The structure of this boundary is remarkably different from the structure of non-active twins and faults shown in Figs. II-24(a), II-25(a and b). The degeneration of this boundary is at least partially due to the interaction with the slip dislocations. A mechansim for a possible reaction has been proposed by Friedel[11]:

$$a/2[110] + a/b[112] \rightarrow a/3[111] \rightarrow a/b[211] + a/6[011]$$

This mechanism suggests that a slip dislocation with Burgers vector a/2[110] in the (111) slip plane reacts with a twin dislocation b = a/6[112] in the [111] twin plane to form a Frank dislocation a/3[111]. The Frank dislocation disassociates into a Shockley and a stair-rod dislocation. In Fig. II-27, the straight dislocations (marked S) in the [011] direction is most likely a stair-rod dislocation. It should be noted that the slip dislocations located approximately in the [011] or [101] directions are 60° dislocations, such dislocations are electrically active due to their dangling bond structure. Quite often different types of linear boundaries of moderate activity are also observed. An example is shown in Figs. II-28. Upon Sirtl etching, such boundaries show a high density of dislocation

etch pits. This can be seen in Fig. II-28(a). Note that the dislocation density between such boundaries in a grain is very low. A TEM micrograph showing these boundaries is given in Fig. II-28(b) for a ribbon of [211] surface orientation. Fig. II-28(b) indicates that the boundaries consist of segments of stacking faults bounded by partial dislocations. The bounding partials arrange in a <110> direction. It is evident that the etch pits observed after Sirtl etching result from the emergence of these partials at the ribbon surface.

It also can be seen that the fringe contrast associated with these faults changes in two neighboring segments. The change in fault contrast is due to the change in fault nature. It changes from intrinsic to extrinsic or vice versa. An example is given in the bright-field and in the dark-field images of Figs. II-28(c and d), respectively. According to established constrast criteria(10), the fault nature is intrinsic for segment I and extrinsic for segment II. These types of stacking faults have been observed in deformed nickel by Murr(12). He considers a single intrinsic stacking fault as a one-layer twin with the twin boundaries characterized by intermixed regions of h.c.p. structure. An extrinsic stacking fault, (two overlapping instrinsic faults) is therefore a two-layer twin with contacting h.c.p. regions. In effect, N-stacking faults on every (111) plane form an N-layer twin. Therefore, the

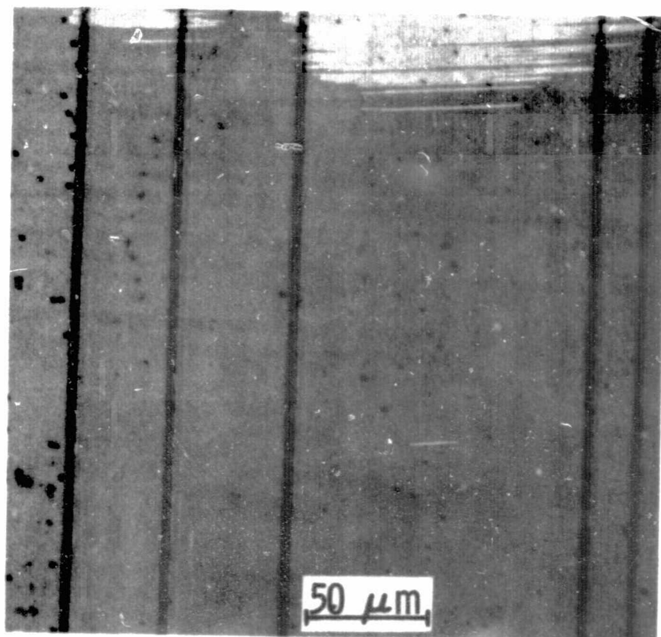

a

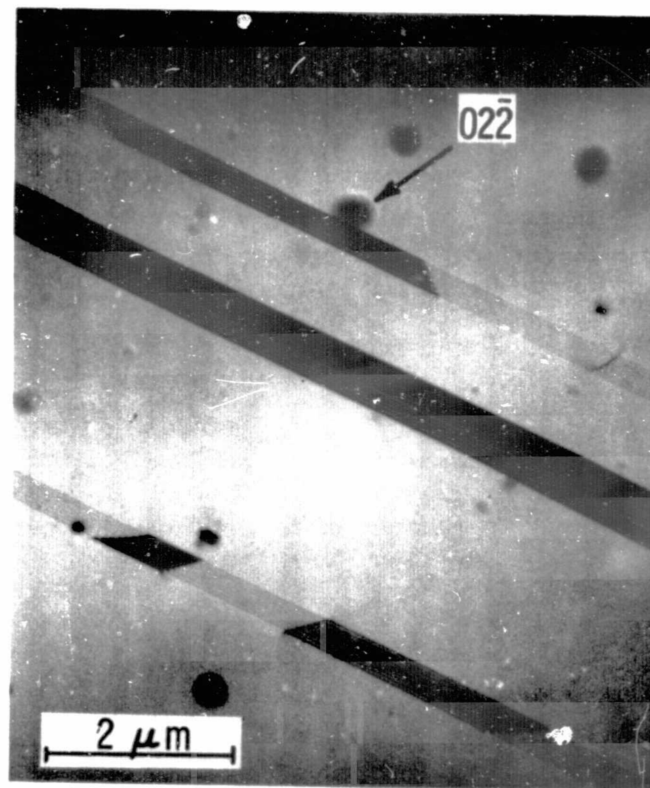

b

Fig. II-28. (a) optical micrograph showing that after Sirtl etching, linear boundaries of moderate activity reveal a high density of etch pits; (b) TEM micrograph showing that the boundaries in (a) consist of segments of stacking faults bounded by partial dislocations.

ORIGINAL PAGE IS
OF POOR QUALITY

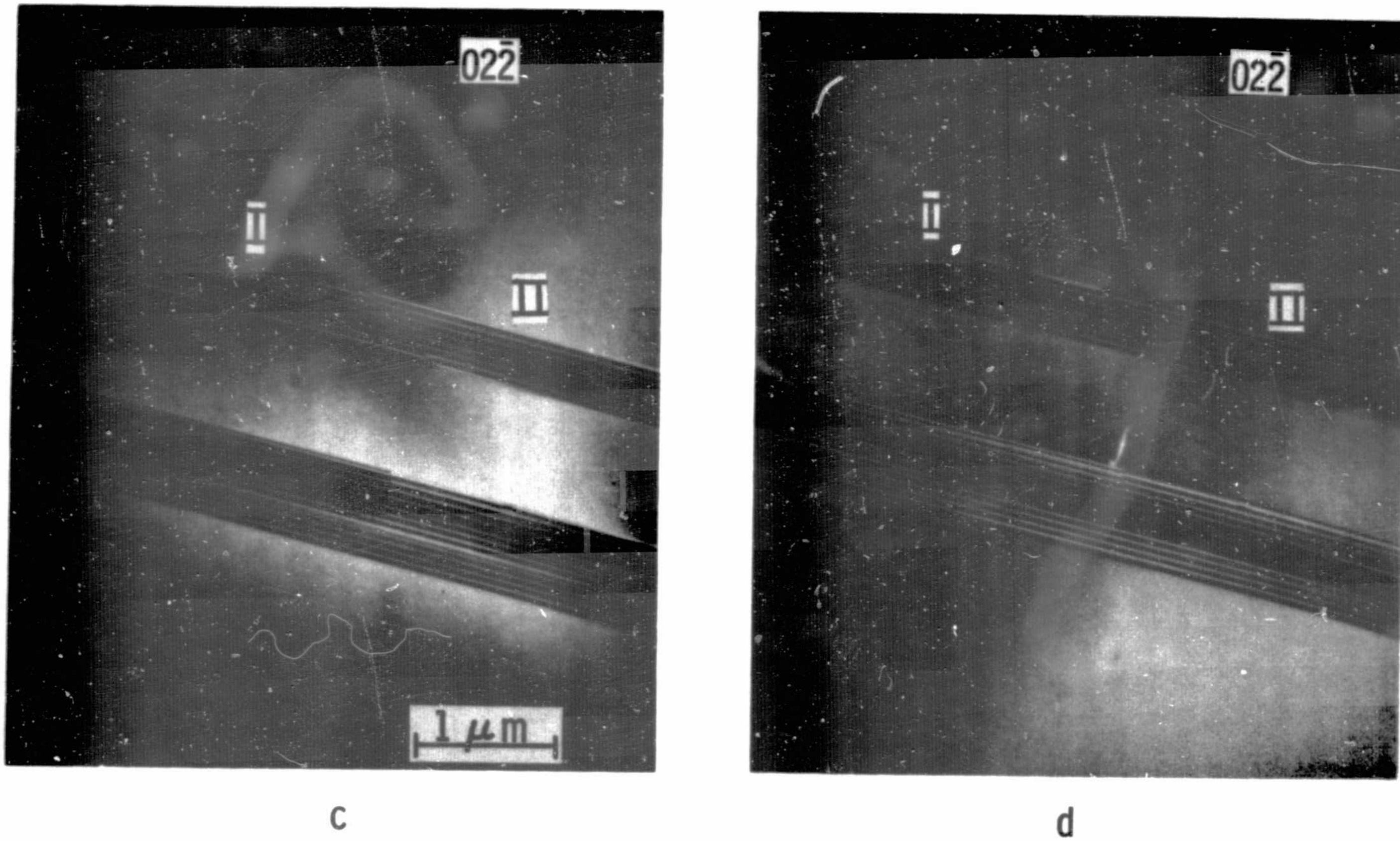

Fig. II-28. (c) the bright-field and (d) the dark-field images showing that two neighboring segments of a fault are different in nature. Segment I is extrinsic and segment II intrinsic.

faults shown in Fig. II-28(b) can be considered as multiple layers of overlapping twins. The intrinsic segments are one-layer twins, and the extrinsic segments are two-layer twins. The fringe contrast arising from a three-layer twin is relatively weak.

5.3.2 Defects in Class II Ribbons

As ribbon quality degrades, dislocation bands and degenerated linear boundaries are the dominant defects in silicon ribbons. Such defects are strongly electrically active and are shown in Figs. II-29(a and b). It can be seen that boundaries at position L are much more active than the boundaries at position F. Fig. II-29(c) is a high magnification of area A indicated in Fig. II-29(a), and shows differences in the etching characteristics of boundaries at positions L and F. While boundary F is revealed as a sharp line, conical etch pits are seen along the boundary L. Linear boundaries of such etching behavior are low-angle grain boundaries. This is supported by the following observation: Conical pits are also observed along such boundaries whenever they are etched from the backside as it is done for TEM specimen preparation. The etch pits are similar to the one observed along low-angle tilt boundaries in germanium[13].

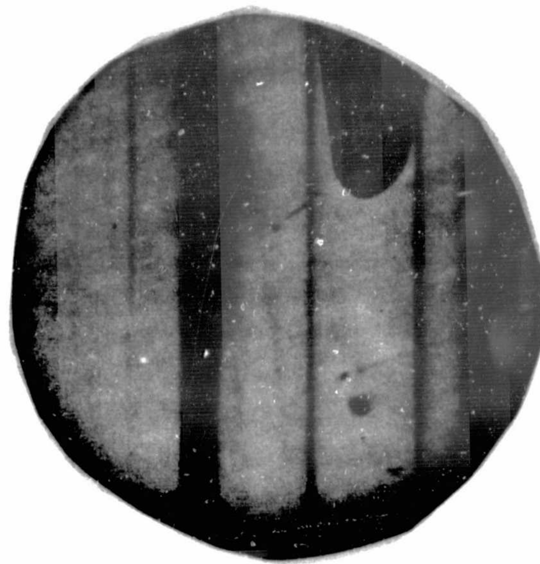

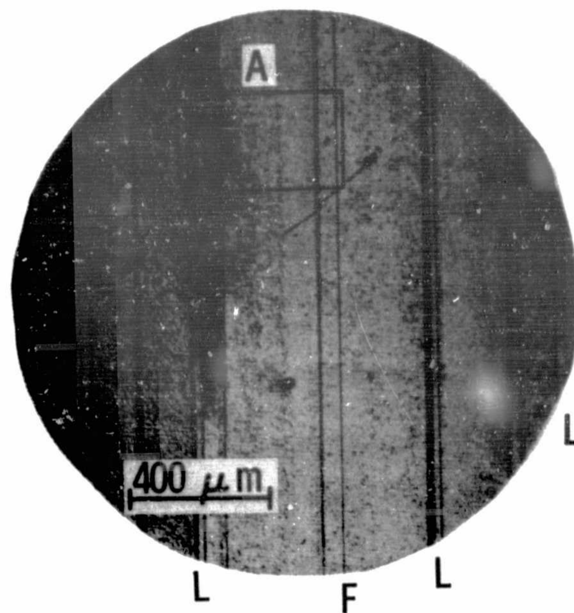

Fig. II-29. (a) EBIC micrograph showing that dislocation bands and degenerated linear boundaries are strongly electrically active; (b) the corresponding optical micrograph of (a).

ORIGINAL PAGE IS
OF POOR QUALITY

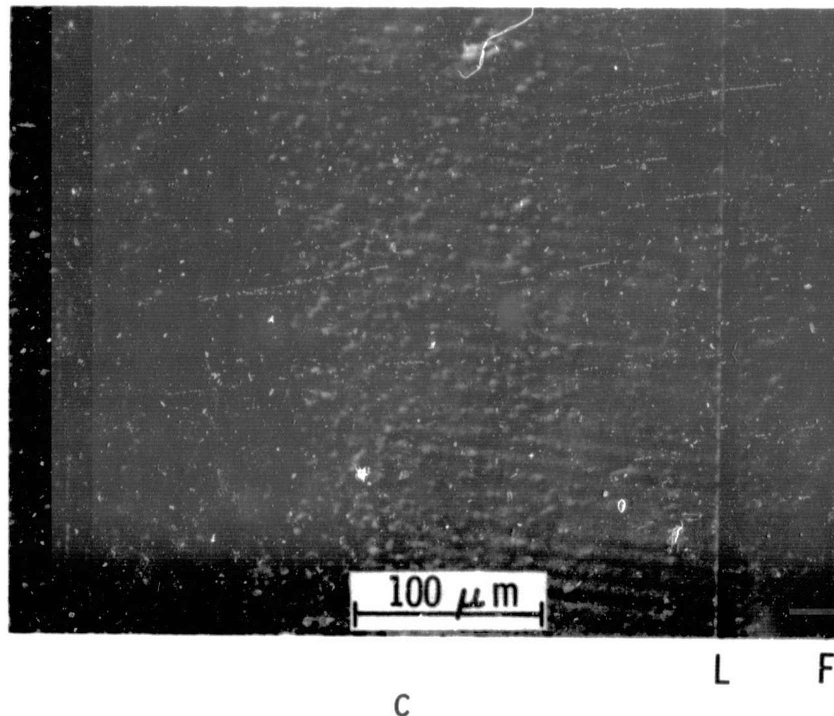

Fig. II-29. (c) area A of Fig. 29(b) at highest magnification. Note differences in the etching characteristics of boundaries L and F.

The TEM micrograph of a low-angle grain boundary L for a ribbon of [011] surface orientation is shown in Fig. II-30. The boundary L as well as the twin planes T are in the $(1\bar{1}1)$ plane perpendicular to ribbon surface. The specimen was tilted into the $\{\bar{1}21\}$ zone to display the dislocation structure in the boundary. Figure II-30 shows that the boundary consists of parallel dislocation arrays in the <110> directions. The spacing between these dislocations ranges from 0.1 to 0.4 μm with an average spacing of 0.2 μm. Most of the dislocations are out of contrast for the $[11\bar{1}]$ reflection in the $\{\bar{1}21\}$ zone and also for the $[13\bar{1}]$ reflection in the {013} zone. Thus the Burgers vector, b, of these dislocations is a/2[101].

The misorientation Θ between the grains A and B associated with the boundary can be measured directly from the diffraction pattern of a selected area (SAD). This is done in the microscope by adjusting the surface normal of grain B, the [011] axis, almost parallel to the main beam as shown in Fig. II-30. The misorientation between grains A and B is measured as the shift of the [011] axis with respect to the main beam. The SAD of grain A shows that the shift is approximately two [111] spacings in the $[1\bar{1}1]$ direction. From the Bragg equation, one [111] spacing corresponds to 0.46° for 200 keV electrons. The misorientation is therefore approximately 0.92°. Thus, the boundary is a low

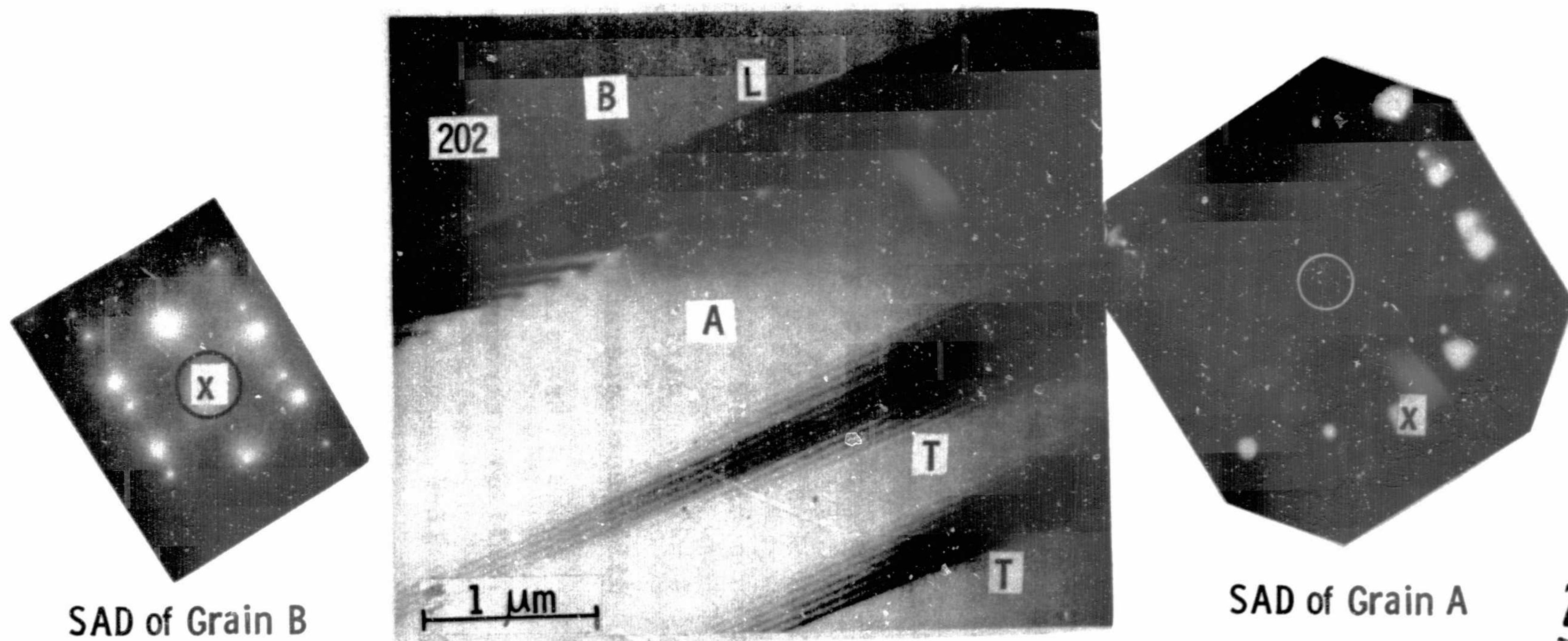

Fig. II-30. TEM micrograph showing dislocations associated with a low-angle grain boundary. The misorientation between grain A and B as measured from the shift of the [011] axis (O) with respect to the main beam (X) is about 0.92°.

ORIGINAL PAGE IS OF POOR QUALITY

angle tilt boundary with the rotation axis in the $[21\bar{1}]$ direction. This direction is the growth direction. The misorientation, is only 0.22° if calculated from the dislocation spacing D (taken as 0.2 μm). However, it should be noted that in some cases, the shift of the surface normal is in the $[0\bar{1}1]$ direction rather than in the $[1\bar{1}1]$ direction. Thus, the boundary is not of the pure tilt type but is a mixture of a tilt and a twist boundary.

Although areas of low dislocation densities have a negligible influence on the minority carrier lifetime high dislocation densities as present in dislocation clusters or bands Fig. II-29(c) represent areas of strong electrical activity. Again, a Burgers vector analysis of the dislocations in such clusters was made. For the sample area shown in Fig. II-29(c), different TEM micrographs were recorded using different operating reflections (g) in the <011> and <112> zones. Examples of these micrographs are given in Fig. II-31(a) through 31(e). The results are summarized in Table II-6.

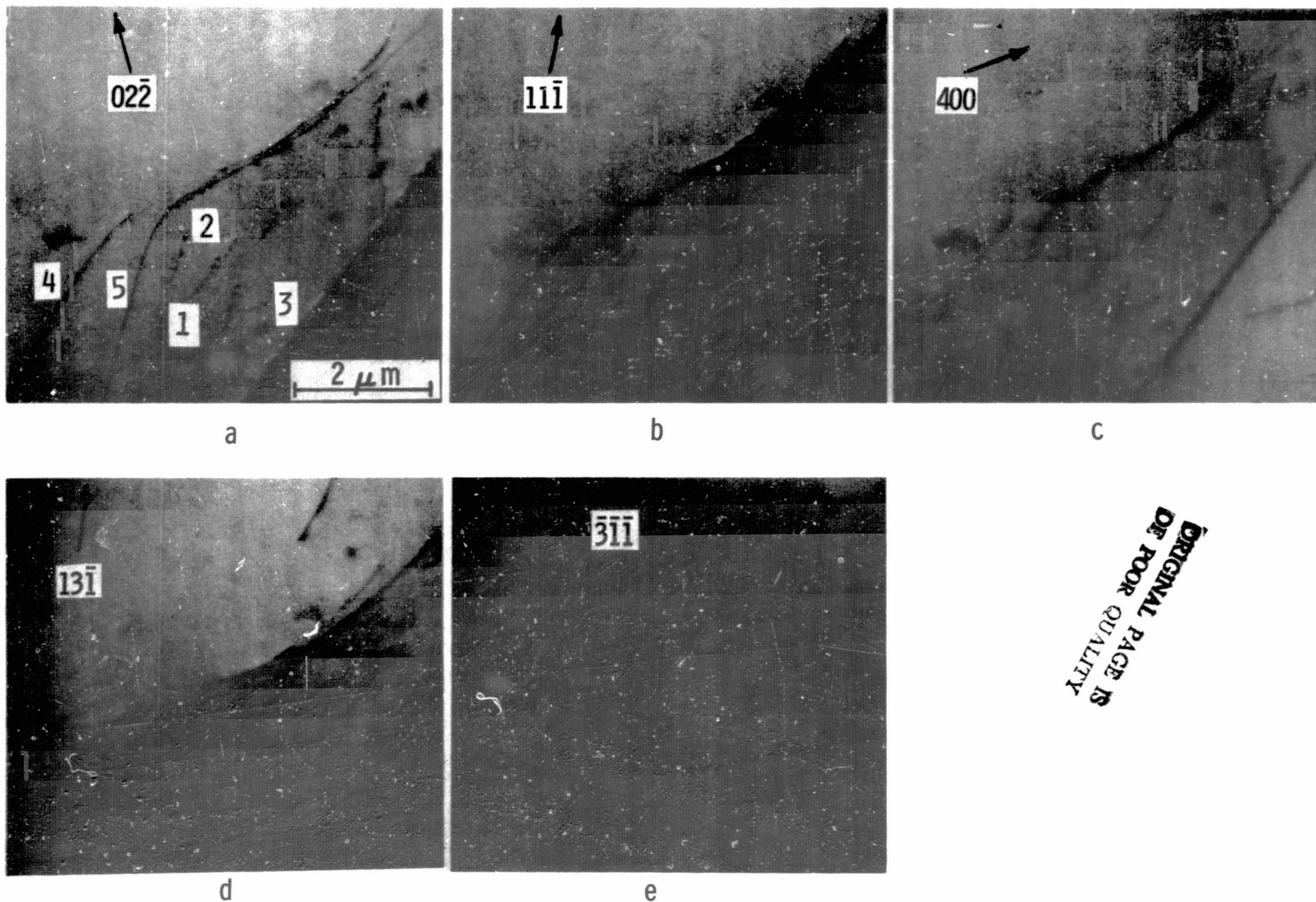

ORIGINAL PAGE IS
OF POOR QUALITY

Fig. II-31. TEM micrographs for the determination of Burgers vectors of band dislocations. (a) 022; (b) 111; (c) 400; (d) 131 and (e) 311 reflection.

TABLE II-6. Burgers Vector Analysis of Dislocation Bands

Disloca-tion No.	g for Dislocation Invisibility	Burgers Vector b	Dislocation Direction
1	111, 131	a/2 [101]	[110]
2	400, 311	a/2 [011]	[110]
3	111, 131	a/2 [101]	
4	400, 311	a/2 [011]	
5	400, 311	a/2 [011]	

Accordingly, the dislocations have Burgers vectors of the a/2 <110> type, either parallel or inclined to the (011) ribbon surface.

There are two groups of dislocations distinctly different in their line directions. One group, dislocations #1, 2 and 3, in Table II-6 is inclined to the surface and the other, dislocation #5 in Table II-6 is nearly parallel to the surface in the [211] growth direction. Both groups have similar Burgers vectors. Stereomicrographs reveal that the inclined dislocations tend to stay in a <110> direction whenever they are in the neighborhood of a linear boundary. Their orientation becomes ill-defined when they move away from the boundary. An example of such inclined dislocations present in a relatively small grain of several microns in

size and bounded by two linear boundaries is shown in Fig. II-32.

The long dislocations with line directions directed into the growth direction are observed at a relatively large distance from a linear boundary. Fig. II-33(a) shows such long dislocations. The Burgers vectors of these dislocations, is either a/2[011] or a/2[101], and is the same as found for the inclined dislocations Fig. II-32. The formation of these dislocations is observed independent of surface orientation. Another example of long dislocations for the [211] surface orientation, is shown in Fig. II-33(b). This type of long dislocation directed along the growth direction has also been observed in silicon web-dendrite crystals[14]. In dendrites, their occurrence is stress-induced and is the result of liquid entrapment in the dendrite-filled region. The similarity of such dislocations in web-dendrite and in CAST ribbons is shown in the x-ray topographs of Figs. II-34(a,b). Both have the same Burgers vector.

In most cases, the dislocations assume an intermediate structure between these two groups of dislocations. A stable configuration is formed through interaction of dislocations with different Burgers vectors. Such configurations are shown in Fig. II-35(a and b). Quite often, triple nodes are observed which form according to the

C-4

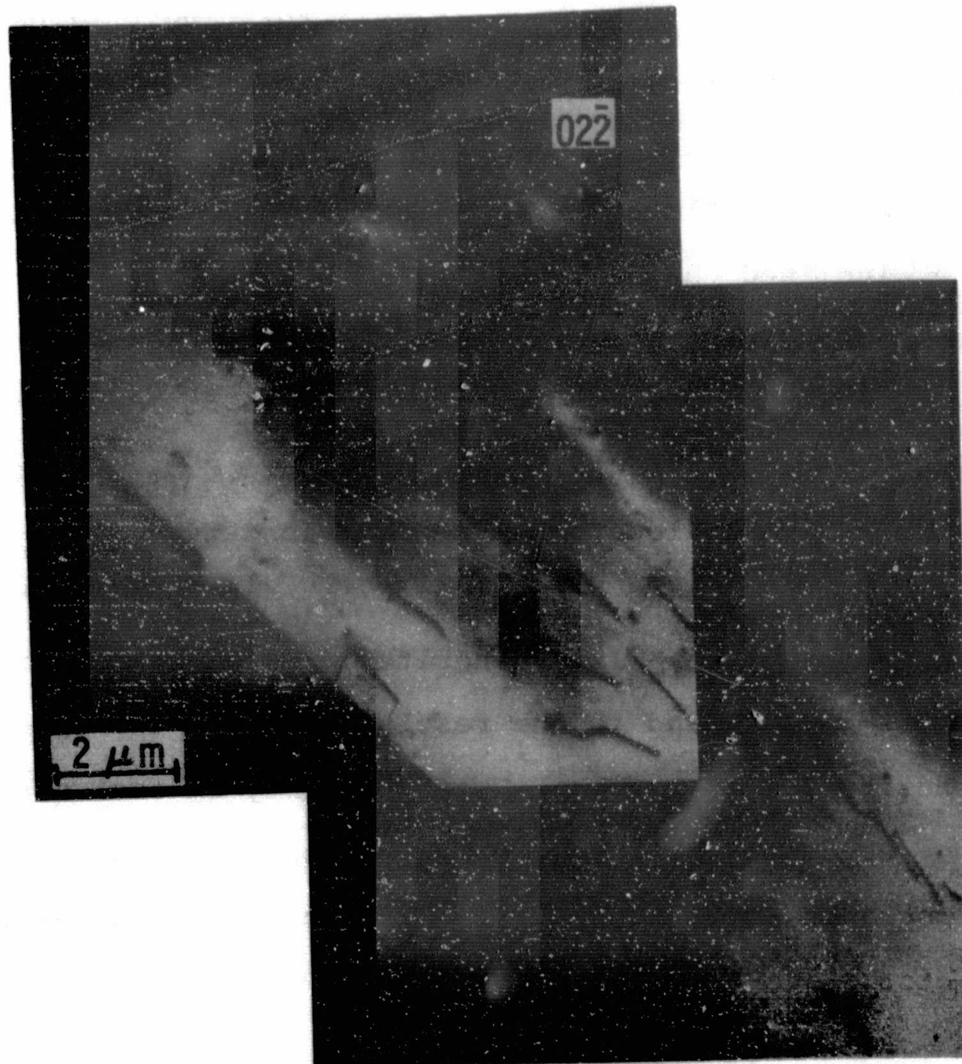

Fig. II-32. TEM micrographs showing arrays of inclined dislocations in a grain bounded by two linear boundaries.

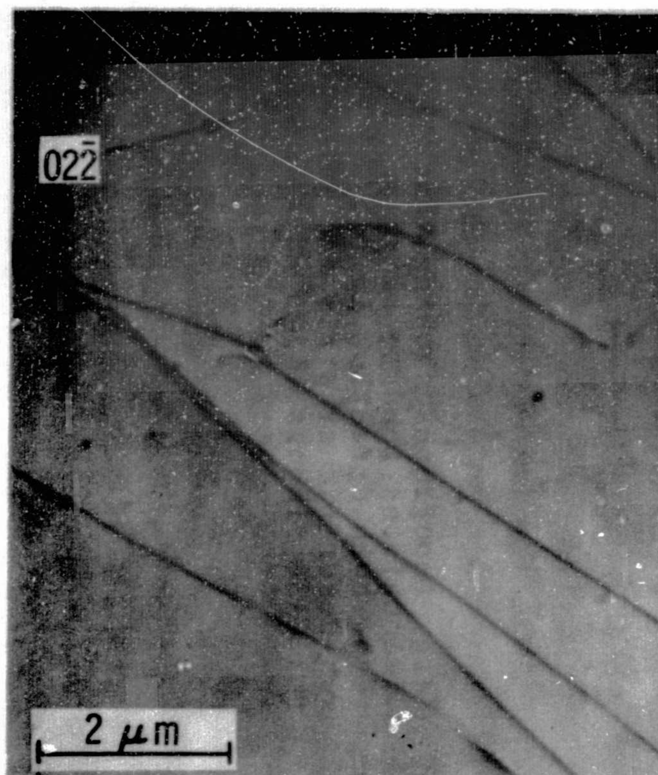

a

b

ORIGINAL PAGE IS
OF POOR QUALITY

Fig. II-33. TEM micrographs showing dislocations lying nearly parallel to the ribbon surface and running in the ribbon growth direction in ribbons of (a) (011) and (b) (211) surface orientation.

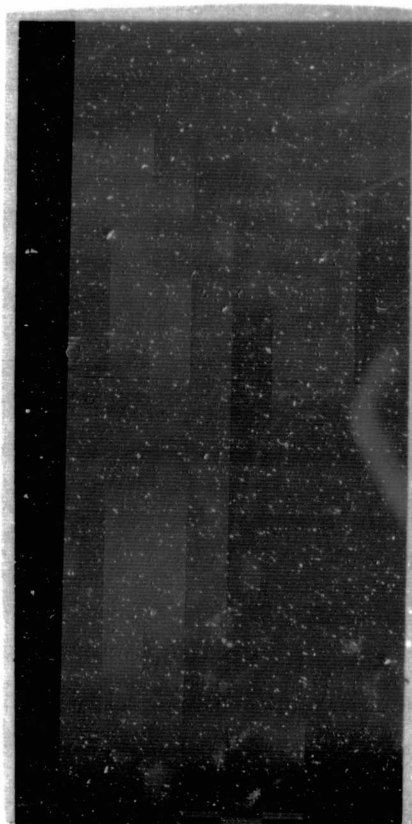

Fig. II-34. X-ray topographs showing that dislocations tend to align in the growth direction in (a) web-dendritic crystals and in (b) CAST ribbons.

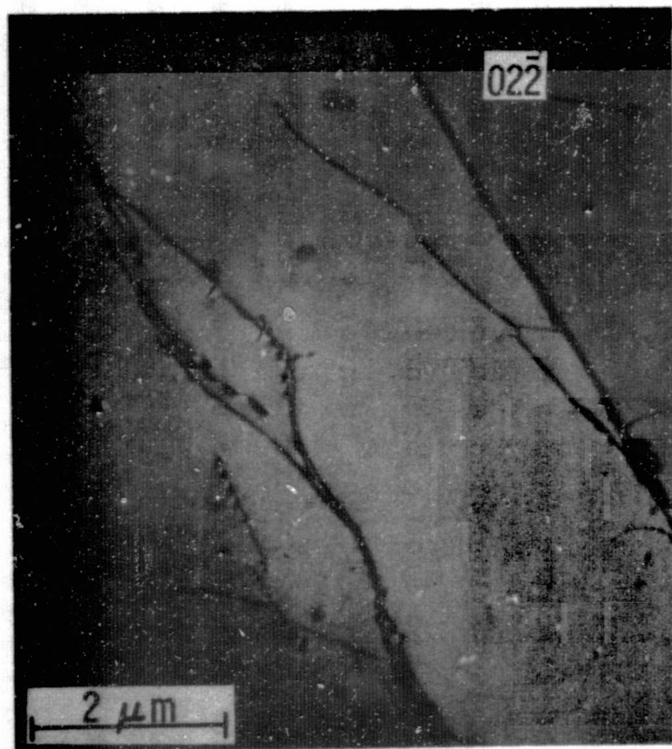

a

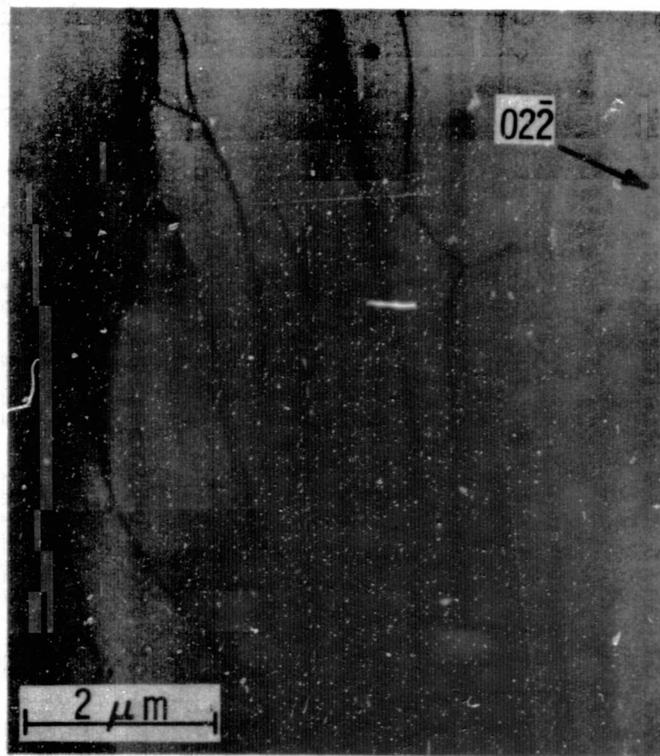

b

ORIGINAL PAGE IS
OF POOR QUALITY

Fig. II-35.. TEM micrographs showing two examples; (a) and (b), of stable dislocation configurations formed through interaction of dislocations with different Burgers vectors.

reaction: a/2[011] + a/2[101] → a/2[110]. This reaction results in a reduction of half the dislocation energy. The resultant segments, with Burgers vector b = a/2[110], are in the [$\bar{1}$10] direction. Thus, they are 90° dislocations with the unfavorable (001) slip plane. The movement of dislocations of type #5 in Table II-6 is retarded through this reaction.

The misorientation of the grains across the boundaries and the detailed structure of such boundaries as shown in Figs. II-29 through 32 were also investigated. The misorientation ranges in general from 0.5 to 1° off the [1$\bar{1}$1] direction. A typical structure of such a boundary as viewed from a [211] projection is shown in Figs. II-36(a) and 36(b). These boundaries consist of multiple overlapping layers of stacking faults or twins. Note that quite often they act as dislocation sources. While one end of a dislocation is emitted from a boundary, Fig. II-36(a), the other end is still pinned at the boundary. This suggest that the emission of a dislocation may result from the defaulting or from the detwinning of such a boundary. The formation of dislocation loops and dislocation lines as a result of such defaulting processes can also be clearly seen in Fig. II-36(b). Figure II-36(c) shows that one dislocation loop and two dislocation segments are about to be emitted from a linear boundary.

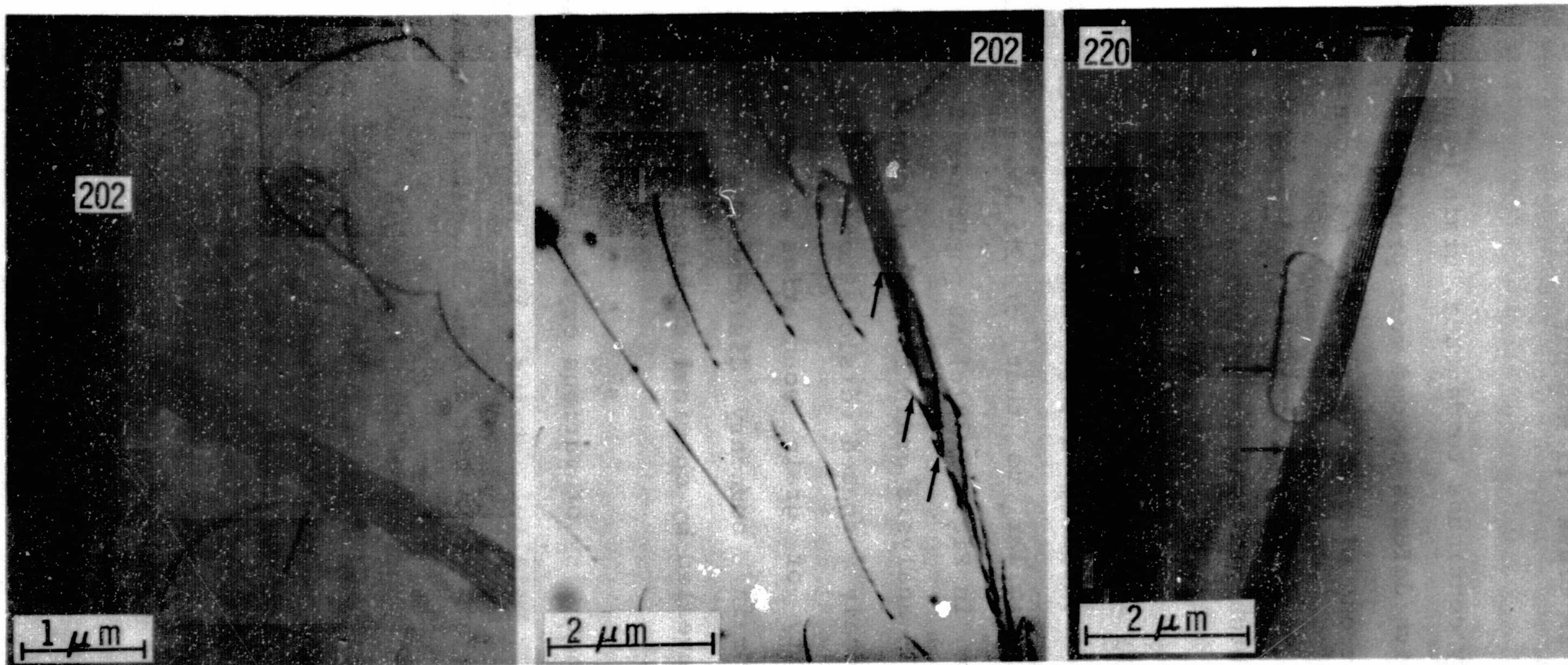

Fig. II-36. TEM micrographs showing that (a) a dislocation segment; (b) dislocation segments and loops and (c) one loop and two segments as indicated by arrows are about to be emitted from a linear boundary.

ORIGINAL PAGE IS OF POOR QUALITY

5.3.3 Defects in Class III Ribbons

As ribbon quality continues to degrade, grain boundaries as well as other active defects become more predominant. Grain boundaries show strong electrical activity as shown in Figs. II-37(a,b) and II-38(a,b). Figs. II-37(c) and II-38(c) show also that a high etch-pit density is typical for dislocation bands. However, close to the grain boundaries the dislocation density is relatively low. The structure of the grain boundaries obtained after chemical etching Fig. II-37(c) appears similar to that of the low-angle grain boundaries, shown in Fig. II-29(c) at positions L. As shown later, by TEM analysis grain boundaries contain a high density of closely spaced dislocations. The strong electrical activity of grain boundaries arises from such dislocations. Grain boundary dislocations in silicon ribbons are not revealed by chemical etching.

The electrical activity of various crystal defects ranging from non-active parallel twins to strongly active dislocation bands and grain boundaries is again illustrated in Figs. II-38(a,b).

Grain boundaries are the result of non-accommodation of two crystal lattices at the intersection of two crystal grains.

ORIGINAL PAGE IS
OF POOR QUALITY

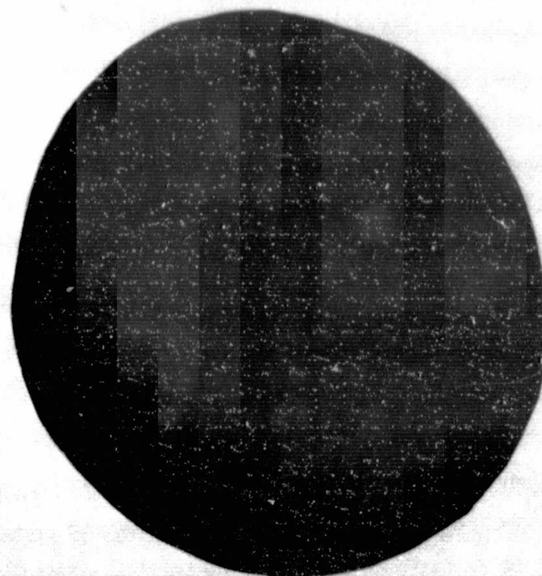

a

b

Fig. II-37. (a) EBIC micrograph showing that grain boundaries and dislocation bands are strongly electrically active; (b) the corresponding optical micrograph of (a).

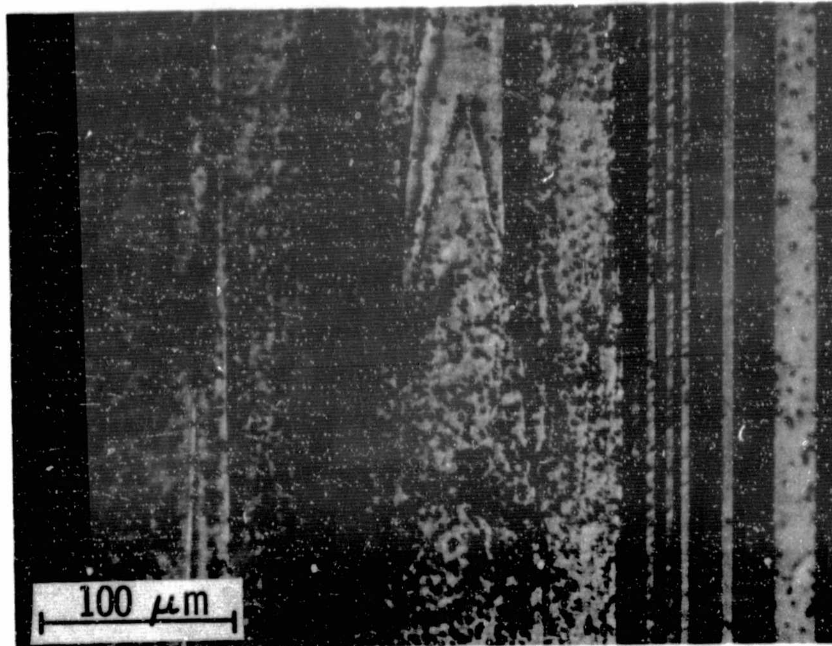

c

Fig. II-37. (c) area A marked, in Fig. II-37(b) at higher magnification. Note a high density of dislocation etch pits.

ORIGINAL PAGE IS
OF POOR QUALITY

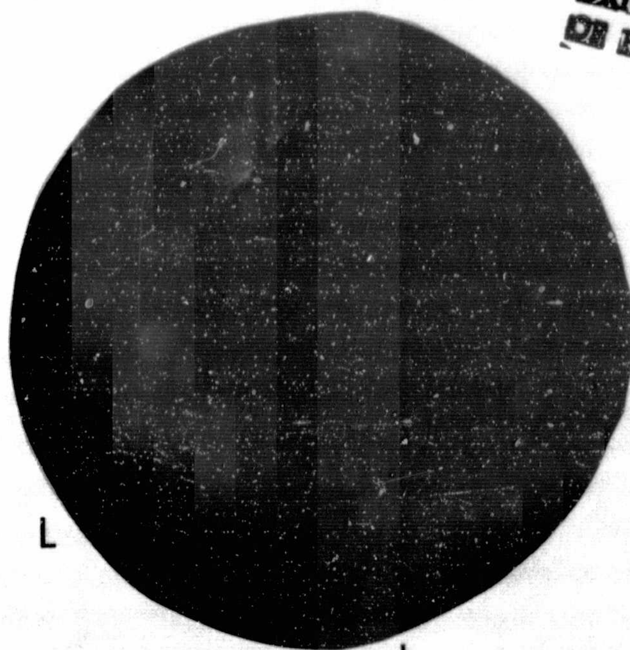

Fig. II-38. (a) EBIC micrograph showing electrical activity of grain boundaries at position "L"; (b) optical micrograph corresponding to (a).

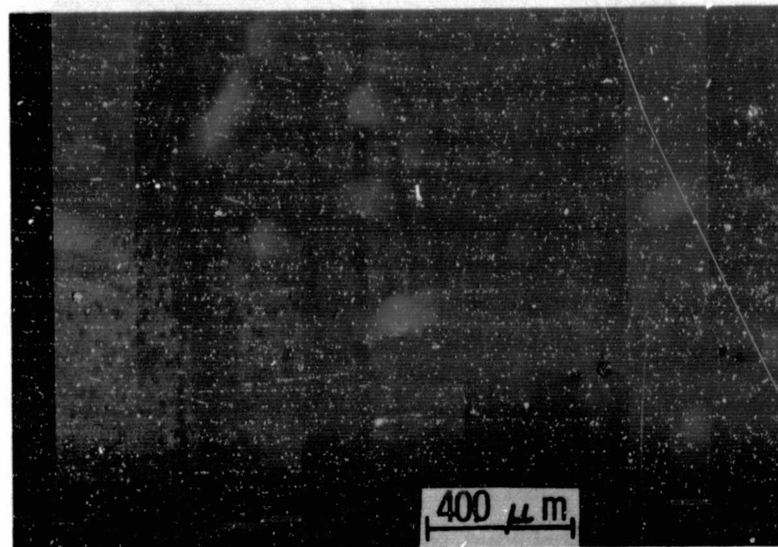

L L

C

Fig. II-38. (c) area A in Fig. II-38(b) at higher magnification shows high etch-pit density in dislocation bands. Note relatively low density close to grain boundaries. Note etch pits in boundaries at positions L.

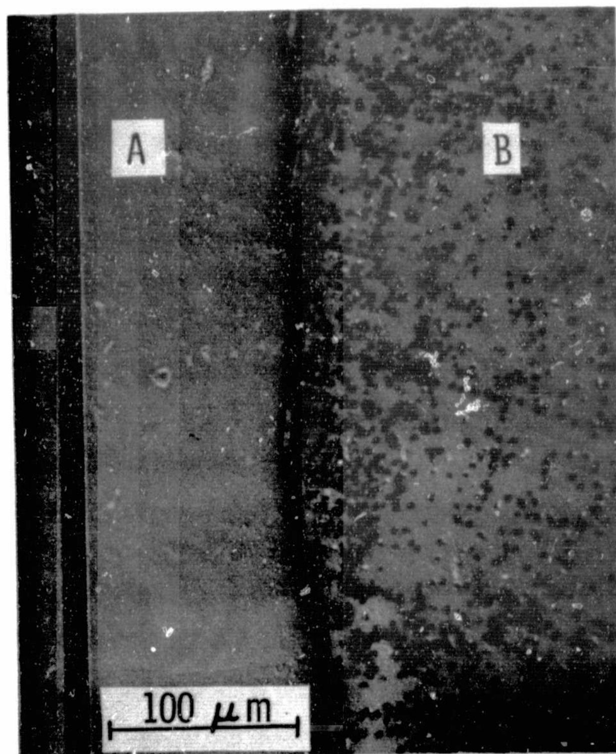

a

Fig. II-39. (a) optical micrograph showing a zigzag boundary with a high density of dislocations piled up against the boundary. Dislocations left of boundary not revealed by etching.

PRECEDING PAGE BLANK NOT FILMED

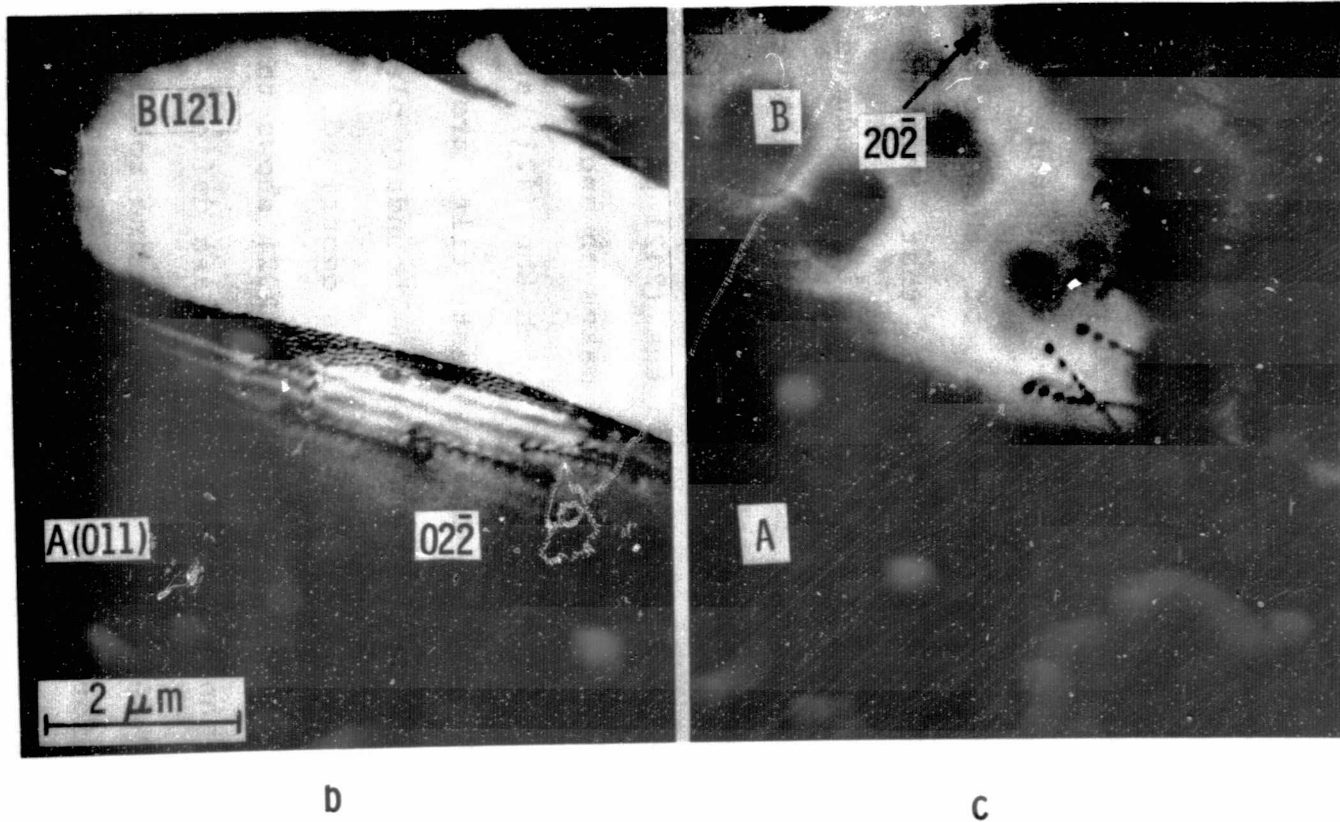

Fig. II-39. (b) and (c) are TEM micrographs showing dislocation pile-up on both sides of a grain boundary. Due to a change in thickness across the boundary, (b) and (c) were taken with different exposure times.

ORIGINAL PAGE IS OF POOR QUALITY

grain is higher than it is in the $[\bar{1}21]$ grain. The linear faults in the $[011]$ grain are in the $(1\bar{1}1)$ plane perpendicular to the surface and run in the $[\bar{2}\bar{1}1]$ direction (Figs. II-40(a,b)). The faults in the $[\bar{1}21]$ grain are in the inclined (111) plane and are in the $[\bar{1}\bar{2}3]$ direction. The grain boundary is in the $[\bar{3}\bar{2}2]$ direction of the $[011]$ grain or in the $[\bar{3}45]$ direction of the $(\bar{1}21)$ grain. Thus the boundary direction makes an angle of 10.7^{o} or 8.05^{o} with the fault direction of the two grains, respectively. Figure II-40(a) shows that this angle is about 9° in both grains. From such data, it is deduced that the grain boundary is in the $(2\bar{1}2)$ plane of the $[121]$ grain. This indicates that both grains have a common (122) boundary plane with a misorientation between the $(2\bar{1}2)$ plane and the $(\bar{2}\bar{1}2)$ plane. This boundary plane makes an angle of 76.3^{o} with the (011) surface or 74.2^{o} with the $(\bar{1}21)$ surface. This indicates that both grains must tilt around the boundary direction by 2.1^{o}, such that the boundary plane can satisfy the crystallographic conditions described. Figure II-40(b) recorded with the g-vector $[202]$ shows that the boundary contains many "ledges". Ledges are defined at the end of the next paragraph. It is interesting to note that the faults typical for each grain do not intersect the grain boundary. Apparently, there is a repulsive force active preventing such an interaction.

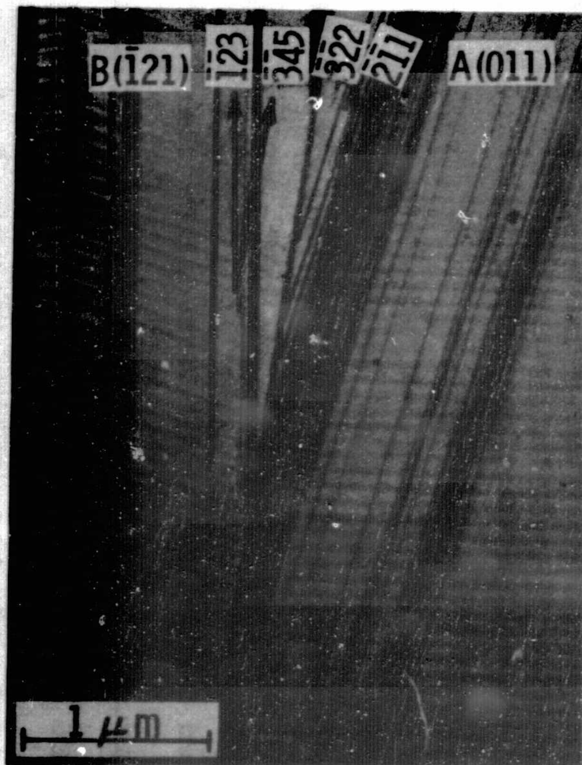

a

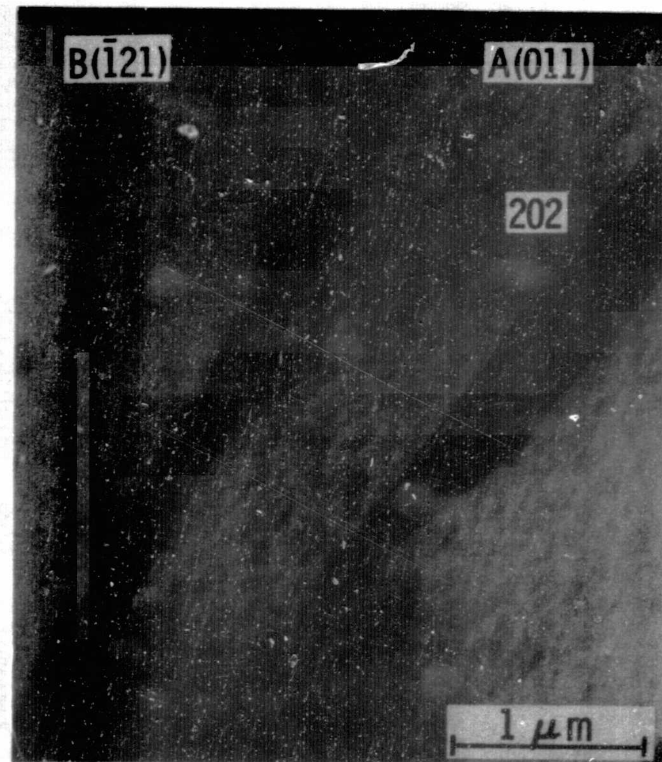

b

Fig. II-40. (a) optical micrograph showing a grain boundary formed at the intersection of the [011] and the [1̄21] grains; (b) TEM micrograph showing that the boundary contains many ledges. The ledges in the boundary and the fault were revealed by tilting the {022} grain to the {1̄21} zone.

ORIGINAL PAGE IS OF POOR QUALITY

A "ledge" structure is observed in nearly all straight portions of a grain boundary independent of the crystallographic plane it occupies. Figures II-41(a,b) show that the ledge contrast arises from the $(11\bar{1})$ grain boundary of a (211) grain. The micrographs in Figs. II-41(a,b) were taken with g-vectors $[\bar{1}11]$ and $[2\bar{2}0]$. With the $[2\bar{2}0]$ reflection, obtained by tilting the specimen towards the [111] zone axis, the ledge contrast disappears and dislocation contrast can be recognized. It is evident that not all "ledges" are dislocations. A similar ledge structure has been observed in grain boundaries of stainless steel[15]. Murr, et al,[15] interpreted such grain boundary ledges as a result of adjustment or of shuffling of the crystal planes forming the boundary. Shuffling of crystal planes is necessary to give rise to coincident lattice sites or boundary positions resulting into a lower energy configuration.

Grain boundaries formed by two grains--one of low index orientation and the other of high-index orientation are also frequently observed. Such grain boundaries contain many dislocations. Figure II-42 shows such a boundary formed by grains A, B, and C. As determined from Kikuchi patterns, the surface orientations of the grains marked A, B, C, are [011], [237], and [273], respectively. The dislocation

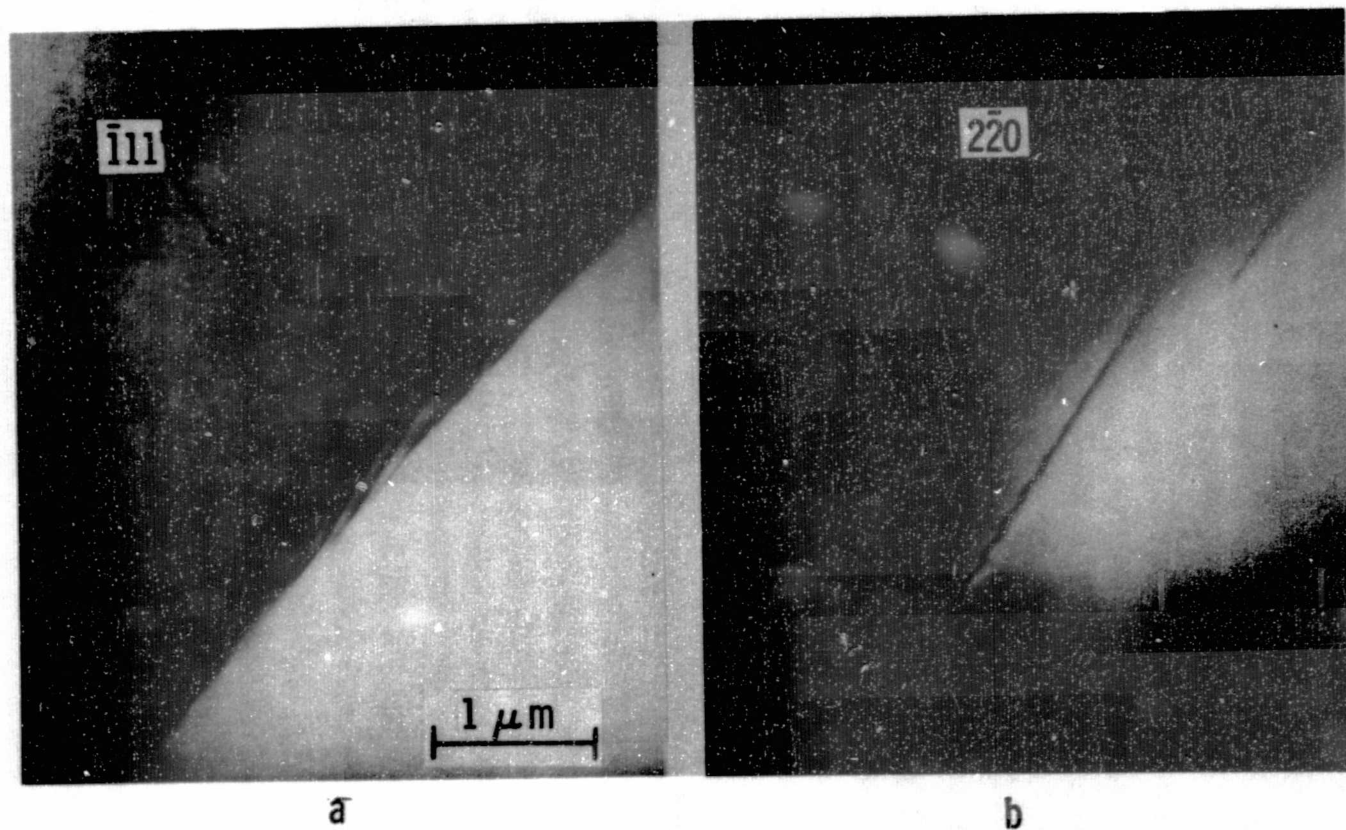

Fig. II-41. TEM micrograph showing that the ledges lying in the (111) plane of a (211) grain are (a) in contrast with $g = 11\bar{1}$, and (b) out of contrast with $g = 2\bar{2}0$ by tilting the grain toward the (111) zone.

ORIGINAL PAGE IS
OF POOR QUALITY

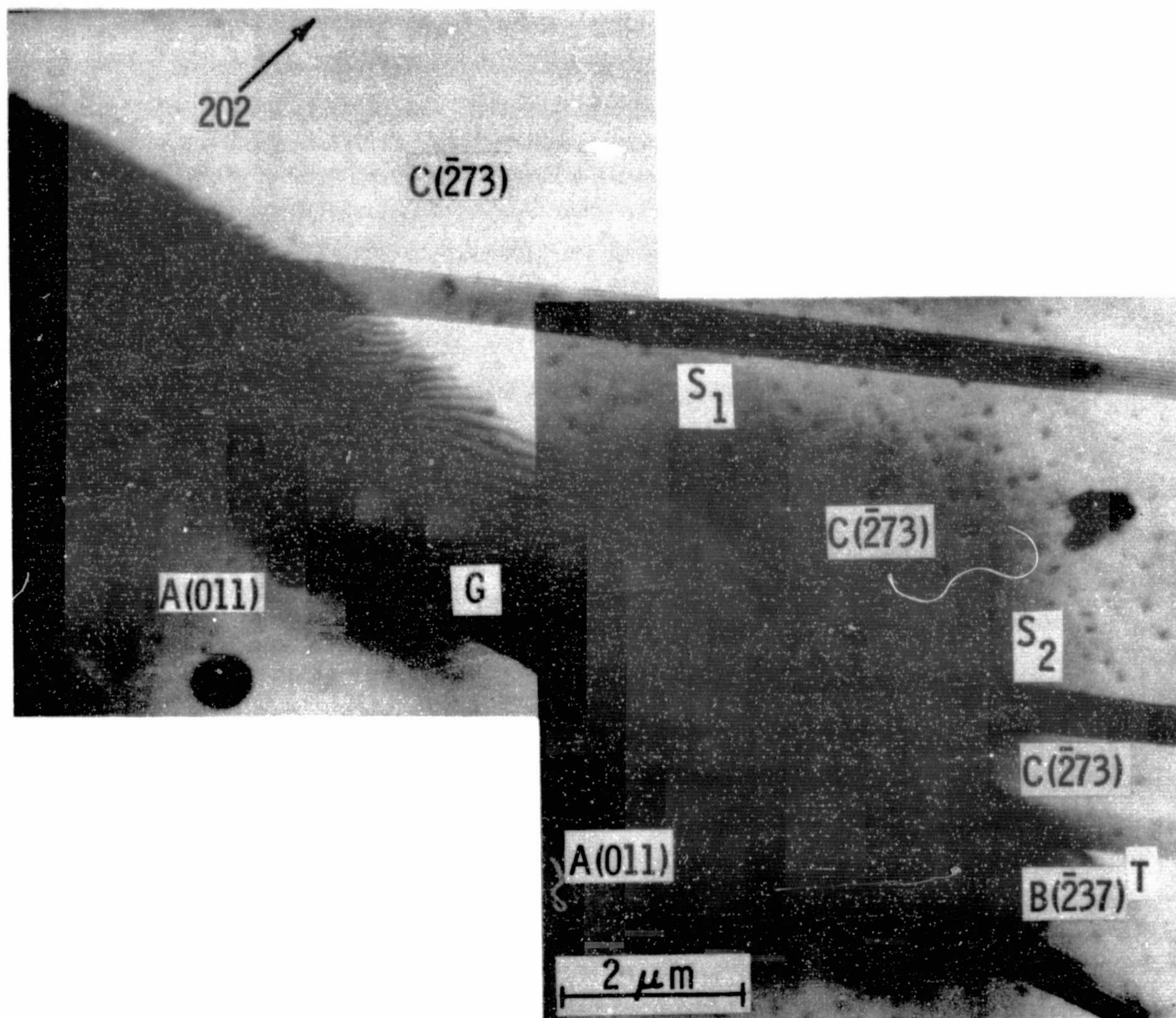

Fig. II-42. TEM micrograph showing a grain boundary (g) formed by the (011) grain (A) and the ($\bar{2}73$) grain (c). The boundary contains a high density of dislocations. S_1 and S_2 are stacking faults. T is twin boundary.

spacing in the boundary varies from 0.1 to 0.2 μm. As the spacing decreases, the dislocations progress from curved lines to straight, parallel lines. These straight dislocations finally pile up at the intersections formed by the grain boundary G and boundaries S_2', and T. This indicates that such intersections act as a barrier for the movement of these dislocations. The parallel boundaries, S_1 and S_2, are stacking faults, boundary T is a twin boundary as determined from the contrast of the outer fringes. It should be noted that the dislocation contrast appears to be dark when grain C is the strongly diffracting grain (Fig. II-42). The contrast reverses for opposite g vector. This contrast reversal is not observed when grain A acts as the strongly diffracting grain. According to McDonald and Ardell[16], such a contrast reversal occurs only in the grain boundary which lies in the lower surface of the strongly diffracting grain. Therefore, the boundary G lies in the lower surface of grain C or the upper surface of grain A.

The strong activity of grain boundaries is tied to the low density of coincidence lattice sites available in such boundaries. In order to lower the boundary energy, lattice bonds at the boundaries must rearrange themselves. This leads to bond distortion and, as a result gives rise to a high density of dislocations or ledges. These dislocations

and/or ledges act as strong recombination centers and cause the strong electrical activity of the fault.

5.3.4 Defects in Class IV Ribbons

Silicon Carbide Dendrites and Inclusions

Silicon carbide inclusions lead to the formation of various kinds of grain boundaries. These boundaries can be twin boundaries, low-angle and/or high-angle grain boundaries.

An example of a SiC inclusion and its result on ribbon perfection is shown in Fig. II-43(a). In these figures, the inclusion is indicated at position I. As determined from the Kikuchi patterns shown in Figs. II-43(b and c), the surface orientation for grain A, is [211]. For grain B it is [255]. The boundary, B_{AB}, in the $[01\bar{1}]$ direction, is a twin boundary with the (111) twin plane inclined 19.5^{o} to the surface of both grains. The surface orientation of grains C and D is about 1° off the [211] orientation of grain A. Thus, the boundaries, B_{AC} and B_{CD} represents a low-angle grain boundary. The boundaries, B_{BC} and B_{BD} are high-angle grain boundaries. Such boundaries are not in fixed position relative to the lattice but tend to rotate during the growth of the ribbon. The rotation is accomplished by the generation of ledges and dislocations in the boundary plane.

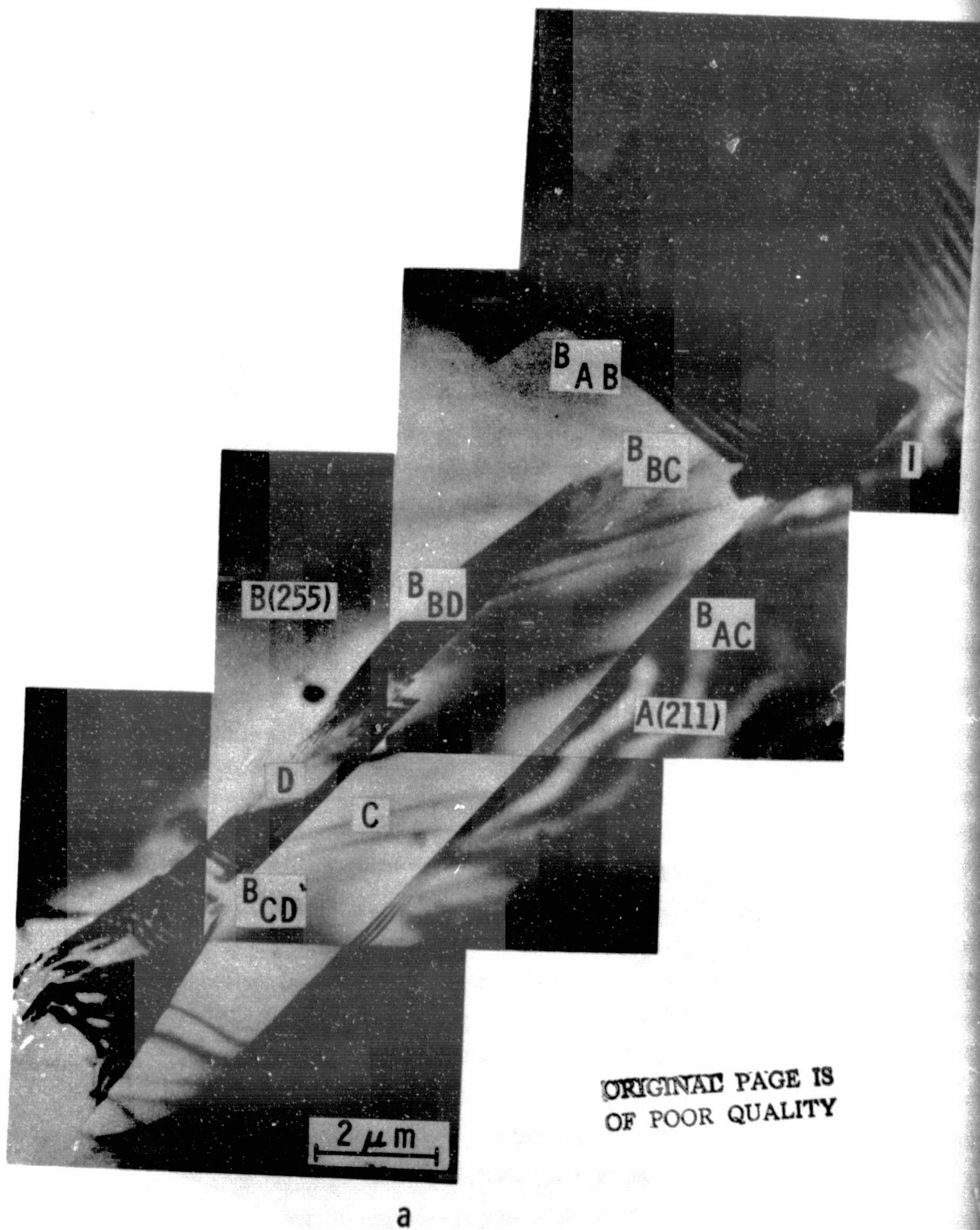

ORIGINAL PAGE IS
OF POOR QUALITY

a

Fig. II-43. (a) TEM micrographs showing that the inclusion of a SiC particle leads to the formation of various kinds of grain boundaries.

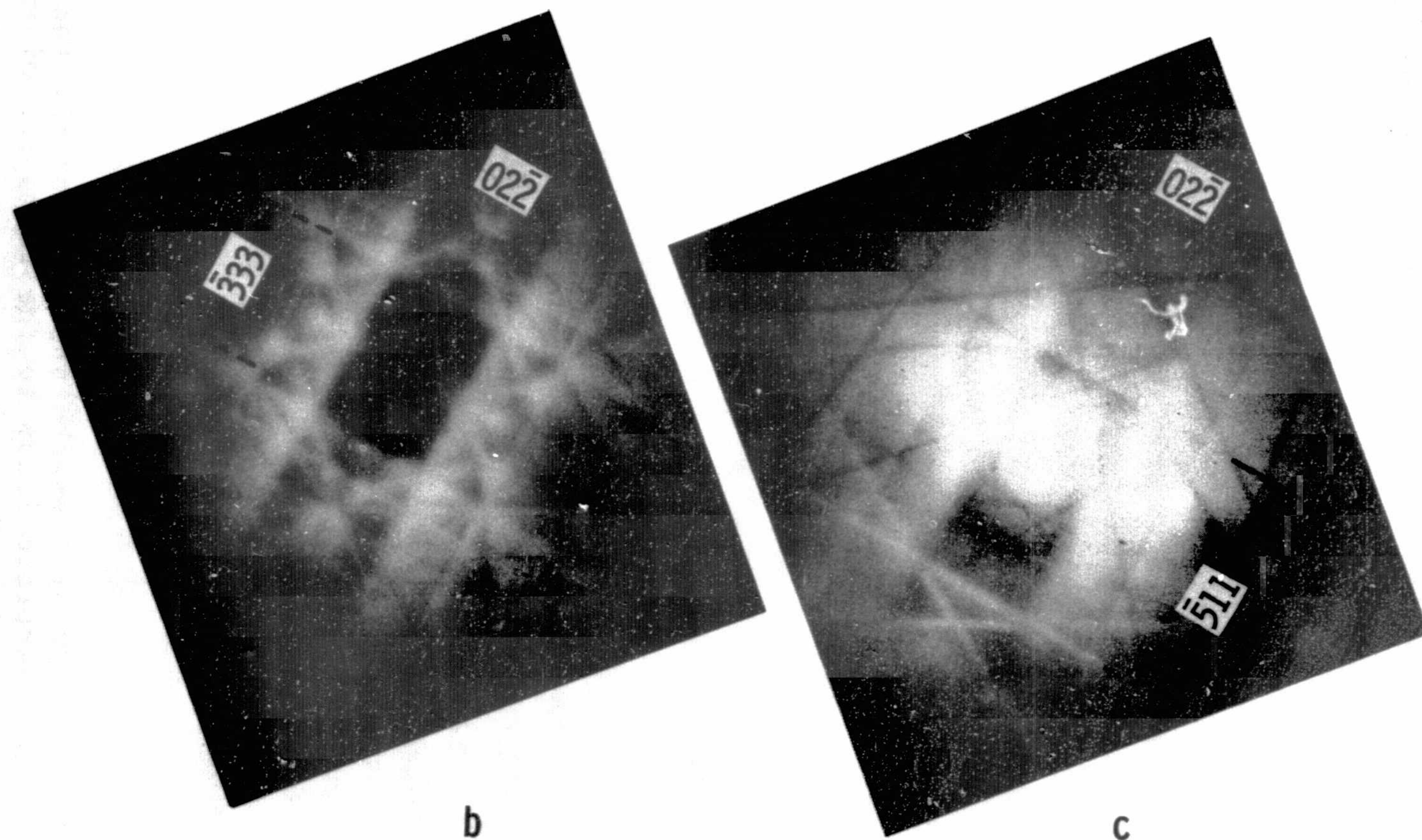

Fig. II-43. (b) electron diffraction pattern of grain A and (c) of grain B.

ORIGINAL PAGE IS OF POOR QUALITY

Considerable progress in ribbon perfection could be made through achieving control of seeding and thus control of surface orientation. So far, surface orientation of ribbons, even if obtained under steady-state growth conditions, is at best fortuitous.

To obtain ribbon of controlled surface orientation must be a major goal of all future work in ribbon growth. Otherwise, there is little hope to eliminate grain boundaries and dislocation clusters during ribbon growth.

The reduction or total elimination of SiC particles is also an important goal of future ribbon growth development. Here we have made considerable progress. In this context clever die design leading to the high melt meniscus technique and the use of silicon carbide coated dies are helpful factors. In conclusion, we feel that ribbon growth through capillary action shaping remains a redoubtable task if it has to compete with the perfection level of Czochralski, Float Zone, or even web-dendrite crystals. Nevertheless, the technique has an excellent potential to out perform CZ or FZ techniques. One future breakthrough--most likely in the die material--could tip the balance in favor of CAST or similar techniques.

6.0 FUTURE QUALITY IMPROVEMENTS

Compared to Czochralski (CZ) or Float Zone (FZ) techniques ribbon growth is a fairly young crystal growing technology. Therefore, it is anticipated that future improvements of the growth technique will give better control of ribbon perfection. Ribbon quality should be such that better than 12% solar cell efficiency can be obtained. Such high efficiencies are possible through a reduction of electrically active defects. Table II-7 summarizes these defects in CAST ribbons.

TABLE II-7. Electrical Activity of Crystal Defects in Ribbons

Group I Strongly Active	Group II Moderately Active	Group III Non-active
Silicon carbide dendrites and inclusions	Multiple over-lapping stacking faults	First order (coherent) twins
Grain boundaries	Grown-in dislocations	Stacking faults
Degenerated twins, low-angle boundaries		
Dislocation bands		

We have evidence that elimination of group I defects as listed in Table II-7 could result in a better than 12% solar cell efficiency. This is supported by measurements presented in Fig. II-44 which gives the I-V characteristics of a 1 cm^2 CAST solar cell processed and tested by the JPL laboratory. The ribbon section comprising the cell contains one low-angle boundary but nevertheless the efficiency of the cell is 11.9%. Without the boundary the efficiency of this cell would compare favorably with the efficiency of a solar cell made from material of high perfection.

7.0 ACKNOWLEDGMENTS

Technical assistance during the contract period was obtained in all areas of characterization. Specifically we would like to thank Mr. H. Ilker for TEM work, Mr. C. Hoogendoorn for x-ray work, Mr. C. P. Schneider for electrical measurements, Ms. S. Focht for computational support, Mr. H. Stellefson and Mr. S. Scilla for process support.

JET PROPULSION LABORATORY

PHOTOVOLTAIC MFG & TEST PROJECT GROUP

I-V CHARACTERISTIC CURVE
BY ______ DATE ______
☒ CELL ☐ SUBMODULE ☐ PANEL
SERIAL No. 201-2 TYPE ______
TEST AM 1.5 (83.2 mw/cm²)
TEST TEMP ☒ 28°C ☐ ______°C
INTENSITY ______ MW/CM² ☐ SUNLIGHT
SIMULATOR: ☒ X25L ☐ X25MK2
☐ TUNGSTEN OTHER ______
Isc 94.2 MA Imp 88 MA
Voc 544 MV Vmp 450 MV
I ______ mv ______ MA Pmax 39.6 MW

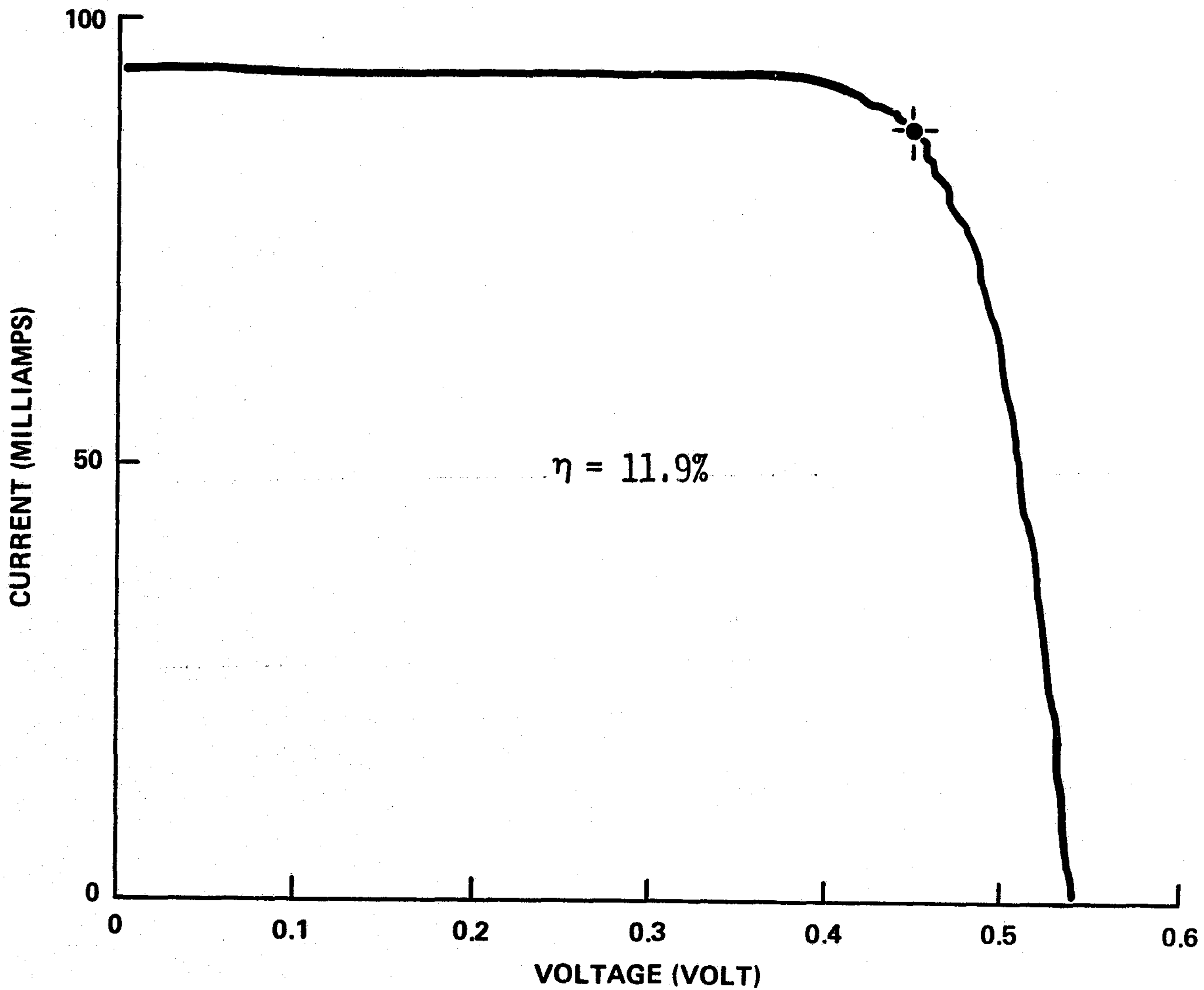

Fig. II-44. I-V characteristic of 1 cm^2 large CAST solar cell processed by JPL. Efficiency 11.9%.

8.0 REFERENCES

1. T. F. Ciszek and G. H. Schwuttke, phys. stat. sol. (a) 27, 231, 1975.

2. G. H. Schwuttke, phys. stat. sol. (a) 43, 43, 1977.

3. A. S. Brown and B. E. Watts, J. Appl. Crystallogr. 3, 1972 (1970).

4. K. A. Jacobson, J. Electrochem. Soc., 118, 1001 (1971).

5. I. H. Khan, Mater. Res. Bull. 4, S285, Pergamon Press, Inc. (1969).

6. W. Fahrner and C. P. Schneider, J. Electrochem. Soc. 120, 100, (1976).

7. M. Zerbst, Z. Angew. Phys. 22, 1, 30, (1966).

8. J. J. Lander, H. Schreiber, Jr., and T. M. Buck, Appl. Phys. Letter, 3, 206, (1963).

9. H. Lemke, phys. stat. sol. 12, 125 (1965).

10. R. Gevers, A. Art and S. Amelinckx, phys. status solidi, 31, 363 (1963).

11. J. Friedel, "Dislocations," pp. 181, Addison-Wesley Publishing Co., Reading, Mass. (1964).

12. L. E. Murr, Thin Solid Films, 4, 389 (1969).

13. F. L. Vogel, Jr., Acta Met., 3, 245 (1955).

14. S. O'Hara and G. H. Schwuttke, J. Appl. Phys., 36, 2475 (1965).

15. L. E. Murr, R. J. Horylev and W. N. Lin, Phil. Mag., 22, 515 (1970).

16. R. C. McDonald and A. J. Ardell, phys. stat. sol. (a), 18, 407 (1973).

17. G. H. Schwuttke, K. Yang and T. F. Ciszek, J. of Crystal Growth 43, 329 (1978).

III SILICON RIBBON TECHNOLOGY ASSESSMENT: 1978-1986

by

A. Kran

1.0 INTRODUCTION

This chapter of the final report presents our current economic outlook for silicon ribbon technology from 1978 to 1986. The outlook is presented within the framework of two sets of scenarios, which develop strategy for approaching the 1986 national energy capacity cost objective of \$0.50/WE peak. This objective translates to ~ $\$25/m^2$ at the level of silicon sheet material. Scenario set 1 leads to $\$50/m^2$ and scenario set 2 to ~ $\$25/m^2$ silicon sheet material. (All costs are in 1975 dollars.)

Scenario set 1 defines what we today consider practical ribbon technology. (Technical feasibility already demonstrated). Using PECAN*, our decision analysis and support

*Photovoltaic Energy Conversion Analysis

system, we develop a 1986 sheet material price ($\$50/m^2$), which we believe can be attained without further scientific breakthrough. A sensitivity analysis, which further examines key technology parameters (ribbon width, growth rate, conversion efficiency, poly cost) is also presented.

Scenario set 2 also analyzes 1986 ribbon technology, but from the premise that technical feasibility has yet to be demonstrated. Silicon ribbon technology is still young, and the possibility of major advances must not be underestimated. Here "show-stoppers" are envisioned that might occur if ribbon technology development continues.

2.0 PECAN DECISION ANALYSIS SYSTEM DESCRIPTION

PECAN is a decision analysis and support system for the evaluation of production units (or manufacturing sectors) required during photovoltaic product fabrication[1]. For the analysis of ribbon material, PECAN is used in its simplest form, since only one production unit (ribbon growth) is involved.

Following is a general description of PECAN, as it is utilized for evaluating the technology/economic tradeoffs of fabricating solar cells. Broadly speaking, PECAN is a

deterministic simulator coded in APL[2], which is a high level, interpretive programming language. Fully documented, the software system consists of about 40 functions (subroutines) and requires approximately 80,000 bytes of storage. It was designed for evaluating the potential of terrestrial photovoltaic solar energy conversion in a highly interactive manner.

PECAN has been implemented in a time-shared manner on large host systems supporting APL.SV or VSAPL. It is primarily designed for use on cathode-ray tube type terminals and high speed (1200 baud) telephone lines.

PECAN was structured such that when analyzing technology, the decision maker and simulation model interact as a team. This is represented in Fig. III-1, showing where (display symbol) the decision maker interacts with the model.

As can be seen, the simulation model handles production units sequentially, starting with the first manufacturing operation.

3.0 INTERACTIVE SIMULATION AND THE PRODUCTION UNIT CONCEPT

The PECAN simulation concept has become a valuable aid for making tactical decisions concerning near-in development

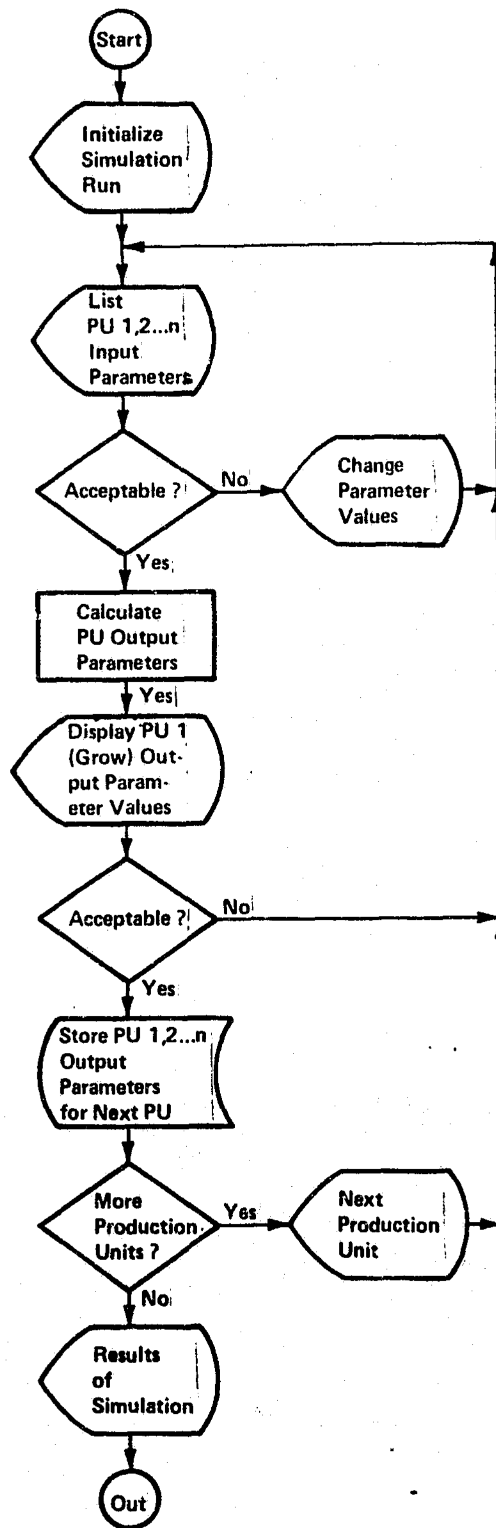

Fig. III-1. Interactive Approach to Evaluating Production Units.

milestones. Because the technologist is aware that economics, not technology, will limit the early utilization of solar power, he must be able to measure the quantitative impact on solar cell cost of pursuing one technological goal as compared to another. (For instance, should he work on increasing ribbon width or growth rate?)

In general, the purpose of the PECAN simulation system is to mimic the factory in a carefully defined manner, following a narrow path between oversimplification and overcomplication. To do this, solar cell fabrication is divided into its major functional operations, or production units. Each production unit is described to the simulation system in terms of about 70 parameters contained within three categories: processing technology, resources (capital equipment, manpower, etc.) and raw materials.

Category 1 consist of processing-related parameters, such as crystal growth rate, crystal diameter, and percent yield of material for solar-cell fabrication.

Category 2 comprises direct cost items, such as crystal growth system cost. Also included here are direct personnel required to assure efficient operation of the factory.

Category 3 contains polysilicon cost, services and supplies, and completes the list of specifically named items. The remainder--overhead, general and administrative expenses, and profit--are defined as percentages relating to other direct-cost-items.

Output consists of the major factors contributing to sheet material and energy capacity cost. They include the following direct cost elements, calculated in dollars per square meter: labor, equipment capital recovery, materials, and services and supplies. Also calculated in dollars per square meter are overhead cost, G&A expense, and profit.

4.0 ECONOMIC OUTLOOK FOR $50/m^2 SILICON RIBBON (Scenario Set 1)

4.1 Business Strategy of Hypothetical Firm

After a decision has been made to produce ribbon material in quantity, the following question must be answered: at what point should technology development be frozen in order to set up a production capacity? It is generally understood that at least a four-year lead time is required to progress from technology readiness to a full-scale production capability.

For this hypothetical firm, let's assume a three-stage business implementation strategy. The strategy consists of entering the market place with new product at three points in time: 1982, 1984 and 1986. To accomplish this, technology must be frozen in 1978, 1980 and 1982 respectively. Such strategy represents one approach to the dilemma of entering the market early with a high-cost product, as compared to delaying market entry until a low-cost product is ready, but then facing established competition.

Table III-1 summarizes the strategy timetable. Scenario 1 (of set 1) proposes to freeze ribbon technology in 1978 and phase it into large scale production by 1982. This implies that between 1978 and 1982, no technological advances can be incorporated, and that the difference between 1978 and 1982 ribbon price is solely attributable to (hopefully) lower poly cost. The same conditions apply to the other two scenarios, except that there will be opportunity to continue technology development for two and four more years, respectively.

TABLE III-1. Ribbon Technology Scenario Set 1

SCENARIO NUMBER	FREEZE TECHNOLOGY	FULL-SCALE PRODUCTION	TECHNOLOGY OUTLOOK
1	1978	1982	1986
2	1980	1984	1986
3	1982	1986	1986

4.2 Silicon Ribbon Technology Requirements

The Table III-2 conservative outlook for ribbon technology is based on the assumption that no further scientific breakthroughs will occur between now and 1982. In addition, practical considerations are given preference over technological availability. For instance (see Table III-2), ribbon geometry objectives (10 cm width, 0.3 mm thickness) for solar cell applications have already been met. Even though wider and/or thinner ribbon may be possible from a crystal growth standpoint, no change is reflected in this conservative analysis, because 10 cm wide, 0.3 mm thick ribbon is attractive from the standpoint of subsequent solar cell processing.

As stated before, the following procedure is used in defining parameter values, which result in the 1986 sheet material prices: once technology is frozen for the three

TABLE III-2. Conservative Outlook for Ribbon Technology

TECHNOLOGY STATUS:	1978	1980	1982
WIDTH (cm)	10	10	10
GROWTH RATE (% of Max)	35	50	75
(m/hr)	1.8	2.5	3.8
THICKNESS (mm)	0.3	0.3	0.3
YIELD (QUALITY) (%)	80	85	90
(TO RIBBON) (%)	80	85	90
EFFICIENCY (%)	11	12	13
RIBBON PULLER (k$)	50	50	50
AVAILABILITY (%)	80	85	90
INTEREST RATE (%)	10	10	10
POLY COST ($/kg)	60	45	25
CRUCIBLE/DIE/PARTS ($/DAY)	58	62	45
POWER ($/kWH)	0.05	0.05	0.05
ENERGY (kW)	16	16	12
LABOR (PER SHIFT PER MACH)			
SUPV./SUPT.	0.05	0.05	0.05
ENGRG	0.10	0.10	0.10
TECHNICIAN	0.10	0.10	0.10
LABOR RATES (K$/YEAR)			
SUPV./SUPT.	25	25	25
ENGRG	20	20	20
TECHNICAN	10	10	10
PLANT OPERATION			
HOURS PER WEEK	168	168	168
WEEKS PER YEAR	50	50	50
OVERHEAD RATE			
AS % OF PERSONNEL COST	100	100	100
AS % OF RAW MAT'L COST	25	25	25
G & A			
AS % OF DIRECT COST Plus OVERHEAD	25	25	25
PROFIT (%)	15	15	15

cases shown in Table III-2, no further technology advances may be introduced through 1986. However, moderate improvements, brought on by effective manufacturing engineering, are possible. (For example: better labor efficiency, lower parts costs).

Review of Table III-2 shows that many parameter values are identical for the three years. This is to be expected for the non-processing related ones, since parameters, such as direct labor or labor rates, are unlikely to change as a function of improving technology performance.

Processing technology parameter values, however, are expected to improve. Here, our previous work[3] has shown that ribbon width, poly silicon cost, conversion efficiency, and growth rate are most sensitive to achieving lower sheet material cost. Since ribbon width is already fixed at 10 cm, and poly silicon is a bought raw-material item, the direction of our subsequent work is clear: strive for improved quality ribbon, grown at twice the current growth rate (3.8 m/hr). Ribbon quality must be "good" in order to yield 13% conversion efficient cells.

4.3 Discussion of Business Implementation Alternatives*

4.3.1 Approach to Scenario Development

Table III-2 presented our conservative outlook for silicon ribbon. It is based on the assumption that technology development is to be continued until the three years (1978, 1980, 1982) shown, and frozen thereafter. These three years are subsequently used as the base for developing the three scenarios for the target year 1986.

Figure III-2 repeats the information previously shown in Table III-2, but is using the PECAN input data format. As can be seen, the anticipated benefit of continuing ribbon development beyond 1978 up to 1982, is that growth rate is expected to double (from 1.8 to 3.8 m/hr), yields to improve from 80% to 90%, conversion efficiency to increase from 11% to 13%, and equipment availability (better machines) to advance from 80% to 90%.

*All costs are in 1975 dollars.

308

ORIGINAL PAGE IS
OF POOR QUALITY

```
LIST OF RIBBON PARAMETERS AND THEIR ASSIGNED VALUES

RIBBON DATA FROM SIMULATIONS 70 71 72 FILE OPENED 11/04/75

YEARS ARE:    1978    1980    1982

1  RIBBONS GROWN SIMULTANEOUSLY -     1    1    1
2  RIBBON WIDTH, CM -   10.0 10.0 10.0
3  RIBBON GROWTH RATE,M/HR -    1.78   2.54   3.81 ..OR AS PCT   35   50   75
4  RIBBON THICKNESS, MM -_ 0.30 0.30 0.30
5  YIELD OF "CELL QUALITY" RIBBON, PCT -    80   85   90

  DIRECT COST
6  RIBBON FURNACE, DOLLARS -    50000  50000  50000
7      EQUIPMENT LIFE, YEARS -    7.0   7.0   7.0
8      INTEREST RATE, PERCENT -   10.0 10.0 10.0
9      EQUIPMENT AVAILABILITY, PERCENT -     80    85    90
   PERSONNEL PER SHIFT PER MACHINE
10 11 NO. OF SUPVS -   0.05 0.05 0.05 AT $ -   25000 25000 25000
12 13 NO. OF ENGRS -   0.10 0.10 0.10 AT $ -   20000 20000 20000
14 15 NO. OF TECHN -   0.10 0.10 0.10 AT $ -   10000 10000 10000
16 POLY SILICON COST, DOLS/KG -    60   45   25
17 POLY YIELD TO RIBBON,PERCENT -    80   85   90
   SERVICES AND SUPPLIES
18     CRUCIBLE/DIE/PARTS COST PER DAY -    58   62   45 DOLLARS
19     POWER COST AT -   0.05 0.05 0.05 DOLLARS PER KWH
20     ENERGY TO OPERATE EQUIPMENT -    16   16   12 KW

21 22  O/H -   100 100 100 PCT OF PERS+    25   25   25 PCT OF RAW MATL COST
23  G_AND_A -    25   25   25 PERCENT OF DIRECT COST+OVERHEAD

24  PROFIT BEFORE TAX, PERCENT - 15 15 15 OF DC+O/H+G+A

  MISCELLANEOUS
25 WORKWEEK, HOURS -   168 168 168
26 CONVERSION EFFICIENCY, PERCENT -  11.00 12.00 13.00
27 ENERGY DENSITY AT AM1,KW/SQ M PEAK -     1    1    1

                                        08:50:36  APR 20,1978
```

Fig. III-2. Conservative Outlook For Ribbon Technology. PECAN Input Format.

The result from running the model with the input parameter values of Fig. III-2 is shown in Table III-3. The prices reduction from $\$209/m^2$ to $\$72/m^2$, or about a factor of three, includes the anticipated lower cost of polycrystalline silicon in 1982 (\$25/kg rather than \$60/kg). Without the lower cost poly, the reduction in price would have been from $\$209/m^2$ to $\$124/m^2$, or about 41%. The three scenarios will be discussed next.

ORIGINAL PAGE IS
OF POOR QUALITY

ECONOMICS OF SILICON RIBBON - ONE RIBBON PULLER

SIMULATION NO:	70	71	72
YEARS:	1978	1980	1982
RIBBONS GROWN SIMULTANEOUSLY	1.00	1.00	1.00
RIBBON WIDTH, CM	10.00	10.00	10.00
AVG YIELDED GROWTH RTE,SQ M/HR	0.11	0.18	0.31
COMBINED YIELD FACTOR	0.64	0.72	0.81
DIRECT COST IN DOLS/SQ METER			
EQUIPMENT CAPITAL RECOVERY	10.75	6.67	3.97
PERSONNEL	18.69	11.59	6.89
POLY SILICON COST	65.53	43.54	21.57
SERVICES/SUPPLIES	20.81	13.77	6.09
SUBTOTAL:	115.79	75.57	38.53
OVERHEAD COST IN DOLS/SQ METER	29.18	19.45	11.26
G&A EXPENSES IN DOLS/SQ METER	36.24	23.76	12.45
PROFIT IN DOLLARS/SQ METER	27.18	17.82	9.33
TOTAL COST IN DOLS/SQ METER	208.39	136.59	71.57
DOLLARS PER KW	1894.42	1138.26	550.52

TABLE III-3. Conservative Outlook For Ribbon Technology. Output From PECAN.

4.3.2 Three Technology Implementation Scenarios

Scenario 1 postulates that technology be frozen in 1978 and manufacturing readiness is achieved four years later, in 1982. Subsequently, ribbon is produced through 1986, the target year for this analysis. The years of interest then are 1982, 1984, and 1986, and are the respective input parameter values to PECAN, as shown in Fig. III-3. There is no difference between 1978 (Fig. III-2 and 1982 (Fig. III-3) except for the lower poly cost.

```
         LIST OF RIBBON PARAMETERS AND THEIR ASSIGNED VALUES
RIBBON DATA FROM SIMULATIONS 73 74 75 FILE OPENED 11/04/75
YEARS ARE:    1982   1984   1986

1  RIBBONS GROWN SIMULTANEOUSLY -     1    1    1
2  RIBBON WIDTH, CM -  10.0 10.0 10.0
3  RIBBON GROWTH RATE,M/HR -    1.78  1.78   1.78 ..OR AS PCT   35   35   35
4  RIBBON THICKNESS, MM -  0.30 0.30 0.30
5  YIELD OF  CELL QUALITY  RIBBON, PCT -    80   82   85

  DIRECT COST
6  RIBBON FURNACE, DOLLARS -    50000  45000  45000
7     EQUIPMENT LIFE, YEARS -    7.0   7.0   7.0
8     INTEREST RATE, PERCENT -   10.0 10.0 10.0
9     EQUIPMENT AVAILABILITY, PERCENT -    80    82    85
   PERSONNEL PER SHIFT PER MACHINE
10 11 NO. OF SUPVS -   0.05 0.05 0.05 AT $ -   25000 25000 25000
12 13 NO. OF ENGRS -   0.10 0.07 0.07 AT $ -   20000 20000 20000
14 15 NO. OF TECHN -   0.10 0.10 0.10 AT $ -   10000 10000 10000
16 POLY SILICON COST, DOLS/KG -    25   15   10
17 POLY YIELD TO RIBBON,PERCENT -    80   82   85
   SERVICES AND SUPPLIES
18    CRUCIBLE/DIE/PARTS COST PER DAY -    58   55   50 DOLLARS
19    POWER COST AT -   0.05 0.05 0.05 DOLLARS PER KWH
20    ENERGY TO OPERATE EQUIPMENTM-    16   16   16 KW

21 22  O/H -   100 100 100 PCT OF PERS+    25   25   25 PCT OF RAW MATL COST
23   G AND A -    25   25   25 PERCENT OF DIRECT COST+OVERHEAD

24  PROFIT BEFORE TAX, PERCENT - 15 15 15 OF DC+O/H+G+A

  MISCELLANEOUS
25 WORKWEEK, HOURS -   168 168 168
26 CONVERSION EFFICIENCY, PERCENT -  11.00 11.00 11.00
27 ENERGY DENSITY AT AM1,KW/SQ M PEAK -     1    1    1
```

Fig. III-3. Scenario 1 (Set 1). Technology Frozen: 1978; Full Production: 1982.

Inspection of Fig. III-3 reveals that between 1982 and 1986, there are some relatively minor improvements, such as in yields and equipment availability, attributable to manufacturing engineering effort. The output from the model (Table III-4) reflects this as a reduction in price from $\$145/m^2$ to $\$94/m^2$, or abot 45%.

ECONOMICS OF SILICON RIBBON - ONE RIBBON PULLER

SIMULATION NO:	73	74	75
YEARS:	1982	1984	1986
RIBBONS GROWN SIMULTANEOUSLY	1.00	1.00	1.00
RIBBON WIDTH, CM	10.00	10.00	10.00
AVG YIELDED GROWTH RTE,SQ M/HR	0.11	0.12	0.13
COMBINED YIELD FACTOR	0.64	0.67	0.72
DIRECT COST IN DOLS/SQ METER			
EQUIPMENT CAPITAL RECOVERY	10.75	9.21	8.57
PERSONNEL	18.69	15.28	14.22
POLY SILICON COST	27.30	15.59	9.67
SERVICES/SUPPLIES	20.81	19.20	16.89
SUBTOTAL:	77.56	59.28	49.36
OVERHEAD COST IN DOLS/SQ METER	23.06	17.90	15.97
G+A EXPENSES IN DOLS/SQ METER	25.16	19.30	16.33
PROFIT IN DOLLARS/SQ METER	18.87	14.47	12.25
TOTAL COST IN DOLS/SQ METER	144.64	110.95	93.91
DOLLARS PER KW	1314.94	1008.60	853.70

ORIGINAL PAGE IS
OF POOR QUALITY

TABLE III-4. Scenario 1 (Set 1). Price Reduction Between 1982 and 1986 Due To Manufacturing Engineering and Lower Poly Costs.

Scenario 2, representing technology development until 1980, and manufacturing between 1984 and 1986, is defined in Fig. III-4. Since only two years remain between 1984 and 1986,

LIST OF RIBBON PARAMETERS AND THEIR ASSIGNED VALUES

```
RIBBON DATA FROM SIMULATIONS 76 77 78 FILE OPENED 11/04/75

YEARS ARE:   1980   1984   1986

1  RIBBONS GROWN SIMULTANEOUSLY -    1   1   1
2  RIBBON WIDTH, CM -  10.0 10.0 10.0
3  RIBBON GROWTH RATE,M/HR -   2.54  2.54  2.54 ..OR AS PCT  50  50  50
4  RIBBON THICKNESS, MM -  0.30 0.30 0.30
5  YIELD OF  CELL QUALITY  RIBBON, PCT -   85  85  90

  DIRECT COST
6  RIBBON FURNACE, DOLLARS -   50000  50000  45000
7     EQUIPMENT LIFE, YEARS -   7.0  7.0  7.0
8     INTEREST RATE, PERCENT -  10.0 10.0 10.0
9     EQUIPMENT AVAILABILITY, PERCENT -   85   85   90
   PERSONNEL PER SHIFT PER MACHINE
10 11 NO. OF SUPVS -  0.05 0.05 0.05 AT $ -  25000 25000 25000
12 13 NO. OF ENGRS -  0.10 0.10 0.07 AT $ -  20000 20000 20000
14 15 NO. OF TECHN -  0.10 0.10 0.10 AT $ -  10000 10000 10000
16 POLY SILICON COST, DOLS/KG -    45  15  10
17 POLY YIELD TO RIBBON,PERCENT -    85  85  90
   SERVICES AND SUPPLIES
18    CRUCIBLE/DIE/PARTS COST PER DAY -   62  62  55 DOLLARS
19    POWER COST AT -  0.05 0.05 0.05 DOLLARS PER KWH
20    ENERGY TO OPERATE EQUIPMENT -   16  16  16 KW

21 22  O/H -  100 100 100 PCT OF PERS+   25  25  25 PCT OF RAW MATL COST
23  G_AND_A -   25  25  25 PERCENT OF DIRECT COST+OVERHEAD

24  PROFIT BEFORE TAX, PERCENT - 15 15 15 OF DC+O/H+G+A

  MISCELLANEOUS
25 WORKWEEK, HOURS -  168 168 168
26 CONVERSION EFFICIENCY, PERCENT -  12.00 12.00 12.00
27 ENERGY DENSITY AT AM1.KW/SQ M PEAK -    1   1   1
```

Fig. III-4. Scenario 2 (Set 1). Technology Frozen: 1980; Full Production: 1984.

ECONOMICS OF SILICON RIBBON - ONE RIBBON PULLER

SIMULATION NO:	76	77	78
YEARS:	1980	1984	1986
RIBBONS GROWN SIMULTANEOUSLY	1.00	1.00	1.00
RIBBON WIDTH, CM	10.00	10.00	10.00
AVG YIELDED GROWTH RTE,SQ M/HR	0.18	0.18	0.21
COMBINED YIELD FACTOR	0.72	0.72	0.81
DIRECT COST IN DOLS/SQ METER			
EQUIPMENT CAPITAL RECOVERY	6.67	6.67	5.35
PERSONNEL	11.59	11.59	8.88
POLY SILICON COST	43.54	14.51	8.63
SERVICES/SUPPLIES	13.77	13.77	11.47
SUBTOTAL:	75.57	46.54	34.33
OVERHEAD COST IN DOLS/SQ METER	19.45	14.21	10.63
G+A EXPENSES IN DOLS/SQ METER	23.76	15.19	11.24
PROFIT IN DOLLARS/SQ METER	17.82	11.39	8.43
TOTAL COST IN DOLS/SQ METER	136.59	87.33	64.62
DOLLARS PER KW	1138.26	727.77	538.49

TABLE III-5. Scenario 2 (Set 1). Price Reduction Between 1984 and 1986 Due to Manufacturing Engineering and Lower Poly Cost.

the potential for improvement is obviously smaller than in scenario 1, as inspection of Fig. III-4 for those two years reveals. Consequently, the price reduction (Table III-5) only amounts to about 25%, from $87/m^2$ to $65/m^2$.

Finally, in scenario 3, manufacturing technology is just completed in 1986, the target year. Thus no further opportunity exists to reduce price. The input values to PECAN are listed in Fig. III-5 and the corresponding output in Table III-6. The 31% price decrease (from $72/m^2$ to $49/m^2$) is solely due to the anticipated reduction in poly cost from $25/kg to $10/kg.

```
LIST OF RIBBON PARAMETERS AND THEIR ASSIGNED VALUES

RIBBON DATA FROM SIMULATIONS   FILE OPENED 11/04/75

YEARS ARE:    1982    1986

1  RIBBONS GROWN SIMULTANEOUSLY -     1   1
2  RIBBON WIDTH, CM -  10.0 10.0
3  RIBBON GROWTH RATE,M/HR -   3.81  3.81          ..OR AS PCT  75  75
4  RIBBON THICKNESS, MM -  0.30 0.30
5  YIELD OF  CELL QUALITY  RIBBON, PCT -   90  90

 DIRECT COST
6  RIBBON FURNACE, DOLLARS -   50000  50000
7      EQUIPMENT LIFE, YEARS -   7.0  7.0
8      INTEREST RATE, PERCENT -  10.0 10.0
9      EQUIPMENT AVAILABILITY, PERCENT -    90   90
   PERSONNEL PER SHIFT PER MACHINE
10 11 NO. OF SUPVS -  0.05 0.05       AT $ -  25000 25000
12 13 NO. OF ENGRS -  0.10 0.10       AT $ -  20000 20000
14 15 NO. OF TECHN -  0.10 0.10       AT $ -  10000 10000
16 POLY SILICON COST, DOLS/KG -   25  10
17 POLY YIELD TO RIBBON,PERCENT -   90  90
   SERVICES AND SUPPLIES
18     CRUCIBLE/DIE/PARTS COST PER DAY -   45  45    DOLLARS
19     POWER COST AT -  0.05 0.05      DOLLARS PER KWH
20     ENERGY TO OPERATE EQUIPMENT -   12  12     KW

21 22  O/H -  100 100     PCT OF PERS,   25  25    PCT OF RAW MATL COST
23  G_AND_A -    25  25    PERCENT OF DIRECT COST+OVERHEAD
B
24  PROFIT BEFORE TAX, PERCENT - 15 15    OF DC+O/H+G+A

 MISCELLANEOUS
25 WORKWEEK, HOURS -  168 168
26 CONVERSION EFFICIENCY, PERCENT -  13.00 13.00
27 ENERGY DENSITY AT AM1,KW/SQ M PEAK -    1   1
```

ORIGINAL PAGE IS
OF POOR QUALITY

Fig. III-5. Scenario 3 (Set 1). Technology Frozen: 1982; Full Production: 1986.

ECONOMICS OF SILICON RIBBON - ONE RIBBON PULLER

	1982	1986
RIBBONS GROWN SIMULTANEOUSLY	1.00	1.00
RIBBON WIDTH, CM	10.00	10.00
AVG YIELDED GROWTH RTE,SQ M/HR	0.31	0.31
COMBINED YIELD FACTOR	0.81	0.81
DIRECT COST IN DOLS/SQ METER		
EQUIPMENT CAPITAL RECOVERY	3.97	3.97
PERSONNEL	6.89	6.89
POLY SILICON COST	21.57	8.63
SERVICES/SUPPLIES	6.09	6.09
SUBTOTAL:	38.53	25.58
OVERHEAD COST IN DOLS/SQ METER	11.26	8.64
G*A EXPENSES IN DOLS/SQ METER	12.45	8.56
PROFIT IN DOLLARS/SQ METER	9.33	6.42
TOTAL COST IN DOLS/SQ METER	71.57	49.19
DOLLARS PER KW	550.52	378.40

TABLE III-6 Scenario 3 (Set 1). 1986 Cost Projection.

For ready comparison, the information for target year 1986 is summarized in Fig. III-6 and Tables III-7 and III-8. Fig. III-7 presents the same information in graphical form, and Fig. III-8 the information in \$/kWE instead of \$/m^2. All prices are at the level of silicon sheet material.

LIST OF RIBBON PARAMETERS AND THEIR ASSIGNED VALUES

```
RIBBON DATA FROM SIMULATIONS 75 78 81 FILE OPENED 11/04/75

YEARS ARE:    1986    1986    1986

1  RIBBONS GROWN SIMULTANEOUSLY -    1   1   1
2  RIBBON WIDTH, CM -  10.0 10.0 10.0
3  RIBBON GROWTH RATE,M/HR -   1.78  2.54  3.81 ..OR AS PCT  35  50  75
4  RIBBON THICKNESS, MM -  0.30 0.30 0.30
5  YIELD OF  CELL QUALITY  RIBBON, PCT -   85  90  90

  DIRECT COST
6  RIBBON FURNACE, DOLLARS -   45000  45000  50000
7      EQUIPMENT LIFE, YEARS -   7.0  7.0  7.0
8      INTEREST RATE, PERCENT -  10.0 10.0 10.0
9      EQUIPMENT AVAILABILITY, PERCENT -   85   90   90
   PERSONNEL PER SHIFT PER MACHINE
10 11 NO. OF SUPVS -  0.05 0.05 0.05 AT $ -  25000 25000 25000
12 13 NO. OF ENGRS -  0.07 0.07 0.10 AT $ -  20000 20000 20000
14 15 NO. OF TECHN -  0.10 0.10 0.10 AT $ -  10000 10000 10000
16 POLY SILICON COST, DOLS/KG -   10  10  10
17 POLY YIELD TO RIBBON,PERCENT -   85  90  90
   SERVICES AND SUPPLIES
18     CRUCIBLE/DIE/PARTS COST PER DAY -   50  55  45 DOLLARS
19     POWER COST AT -  0.05 0.05 0.05 DOLLARS PER KWH
20     ENERGY TO OPERATE EQUIPMENT -   16  16  12 KW

21 22  O/H -  100 100 100 PCT OF PERS+   25  25  25 PCT OF RAW MATL COST
23  G_AND_A -   25  25  25 PERCENT OF DIRECT COST+OVERHEAD

24  PROFIT BEFORE TAX, PERCENT - 15 15 15 OF DC+O/H+G+A

  MISCELLANEOUS
25 WORKWEEK, HOURS -  168 168 168
26 CONVERSION EFFICIENCY, PERCENT -  11.00 12.00 13.00
27 ENERGY DENSITY AT AM1,KW/SQ M PEAK -    1   1   1
```

ORIGINAL PAGE IS OF POOR QUALITY

Fig. III-6. Summary of three scenarios (set 1) Input Parameter Values to PECAN (1986 Technology)

ECONOMICS OF SILICON RIBBON - ONE RIBBON PULLER

SIMUL FILE OPENED 11/04/75

SIMULATION NO:	75	78	81
YEARS:	1986	1986	1986
RIBBONS GROWN SIMULTANEOUSLY	1.00	1.00	1.00
RIBBON WIDTH, CM	10.00	10.00	10.00
AVG YIELDED GROWTH RTE,SQ M/HR	0.13	0.21	0.31
COMBINED YIELD FACTOR	0.72	0.81	0.81
DIRECT COST IN DOLS/SQ METER			
EQUIPMENT CAPITAL RECOVERY	8.57	5.35	3.97
PERSONNEL	14.22	8.88	6.89
POLY SILICON COST	9.67	8.63	8.63
SERVICES/SUPPLIES	16.89	11.47	6.09
SUBTOTAL:	49.36	34.33	25.58
OVERHEAD COST IN DOLS/SQ METER	15.97	10.63	8.64
G+A EXPENSES IN DOLS/SQ METER	16.33	11.24	8.56
PROFIT IN DOLLARS/SQ METER	12.25	8.43	6.42
TOTAL COST IN DOLS/SQ METER	93.91	64.62	49.19
DOLLARS PER KW	853.70	538.49	378.40

TABLE III-7. 1986 Economic Outlook for Silicon Ribbon (Three Scenarios).

ECONOMICS OF SILICON RIBBON - ONE RIBBON PULLER

SIMUL FILE OPENED 11/04/75

SIMULATION NO:	75	78	81
YEARS:	1986	1986	1986
RIBBONS GROWN SIMULTANEOUSLY	1.00	1.00	1.00
RIBBON WIDTH, CM	10.00	10.00	10.00
AVG YIELDED GROWTH RTE, SQ M/HR	0.13	0.21	0.31
COMBINED YIELD FACTOR	0.72	0.81	0.81
DIRECT COST IN DOLS/SQ METER			
EQUIPMENT CAPITAL RECOVERY	9.13	8.28	8.06
PERSONNEL	15.14	13.74	14.01
POLY SILICON COST	10.30	13.35	17.54
SERVICES/SUPPLIES	17.99	17.74	12.39
SUBTOTAL:	52.56	53.12	52.00
OVERHEAD COST IN DOLS/SQ METER	17.00	16.44	17.56
G&A EXPENSES IN DOLS/SQ METER	17.39	17.39	17.39
PROFIT IN DOLLARS/SQ METER	13.04	13.04	13.04
TOTAL COST IN DOLS/SQ METER	100.00	100.00	100.00
DOLLARS PER KW	853.70	538.49	378.40

TABLE III-8. 1986 Economic Outlook - Percentage Analysis.

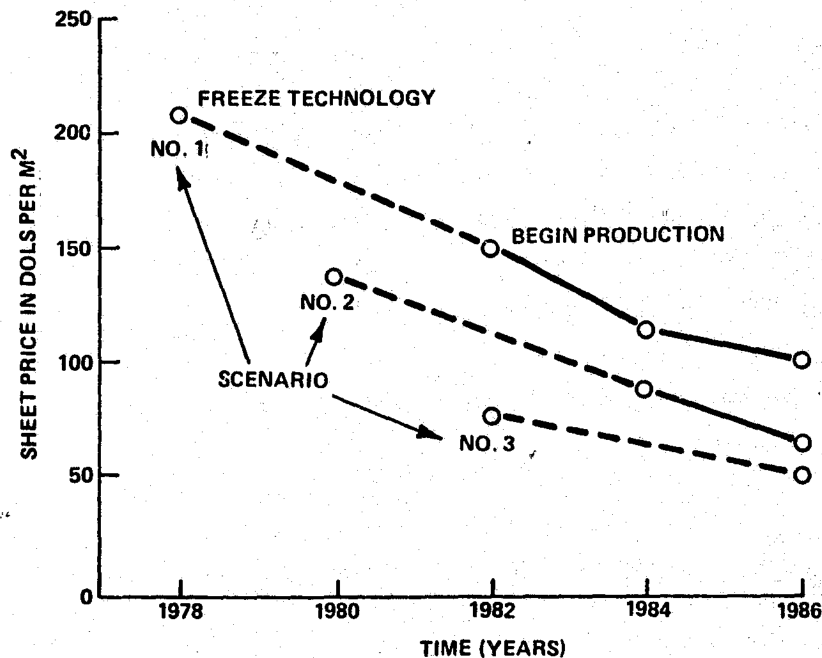

Fig. III-7. Sheet Material Price vs Time. Three Implementation Scenarios.

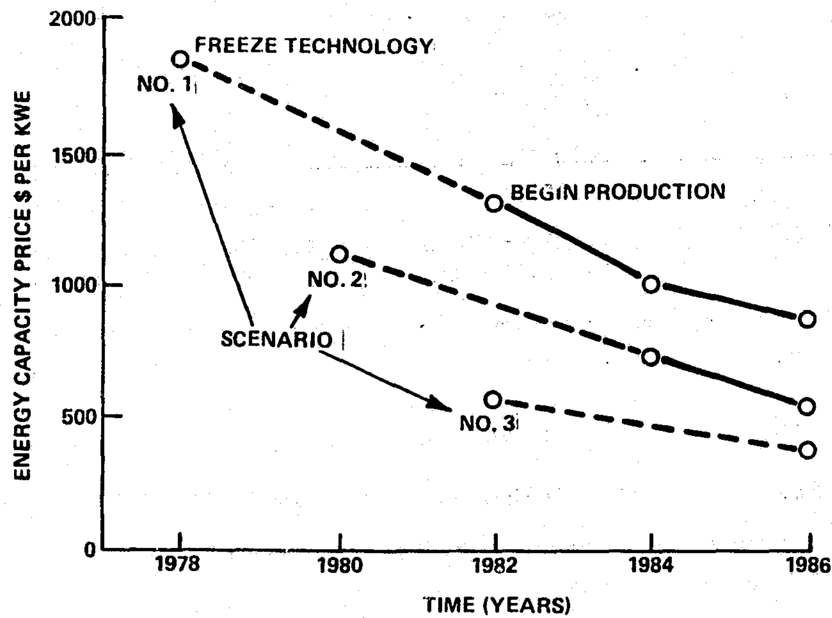

Fig. III-8. Energy Capacity Price ($/kWE) vs Time. Three Implementation on Scenarios.

ORIGINAL PAGE IS
OF POOR QUALITY

4.4 Sensitivity Analysis

Our conservative 1986 outlook for silicon sheet technology is summarized in Tables III-9 and III-10. Our previous work[3] has established that technology parameters, such as ribbon width, growth rate, and conversion efficiency in addition to poly silicon price have the greatest influence

TABLE III-9. 1986 Technology Outlook Based Upon Scenario Set 1

($\$/m^2$)

FREEZE TECHNOLOGY	FULL-SCALE PRODUCTION	1986 PRICE ($\$/m^2$)	PERCENT
1978	1982	94	100%
1980	1984	65	69%
1982	1986	49	52%

TABLE III-10. 1986 Technology Outlook Based Upon Scenario Set 1

($/kWE)

FREEZE TECHNOLOGY	FULL-SCALE PRODUCTION	1986 PRICE ($/kWE)	PERCENT
1978	1982	854	100%
1980	1984	538	63%
1982	1986	378	44%

on ribbon cost. Consequently, these were the items selected for study in the sensitivity analysis.

The method developed for sensitivity analysis is simple, yet effective. It allows the analyst to test the sensitivity of two technology parameters (e.g., poly cost and ribbon width), while holding all other model parameters constant.

For instance, assume that we want to test the 1986 sheet cost of $\$50/m^2$ for possible reduction to $\$20/m^2$ by varying projected poly cost and ribbon width. This is accomplished in the computer program by establishing a range of plausible parameter values. (Poly cost: \$4-25/kg; Ribbon Width: 5-25 cm).

Specific parameter values required for each computer calculation are obtained by stochastically sampling between these limits first, and then calculating the resultant energy-capacity cost at the level of silicon sheet material. Only those parameter values that result in the specified sheet material cost (e.g., \$50.00, $\pm$ 0.5%) are accepted as valid data points. All others are rejected.

The model is iterated until the relationship (if one exists) between the input parameter and the specified output (dollars/m^2) is determined.

Curve 1 of Fig. III-9 is a plot of conversion efficiency versus ribbon width for our conservative technology outlook (feasibility demonstrated). Each point on the

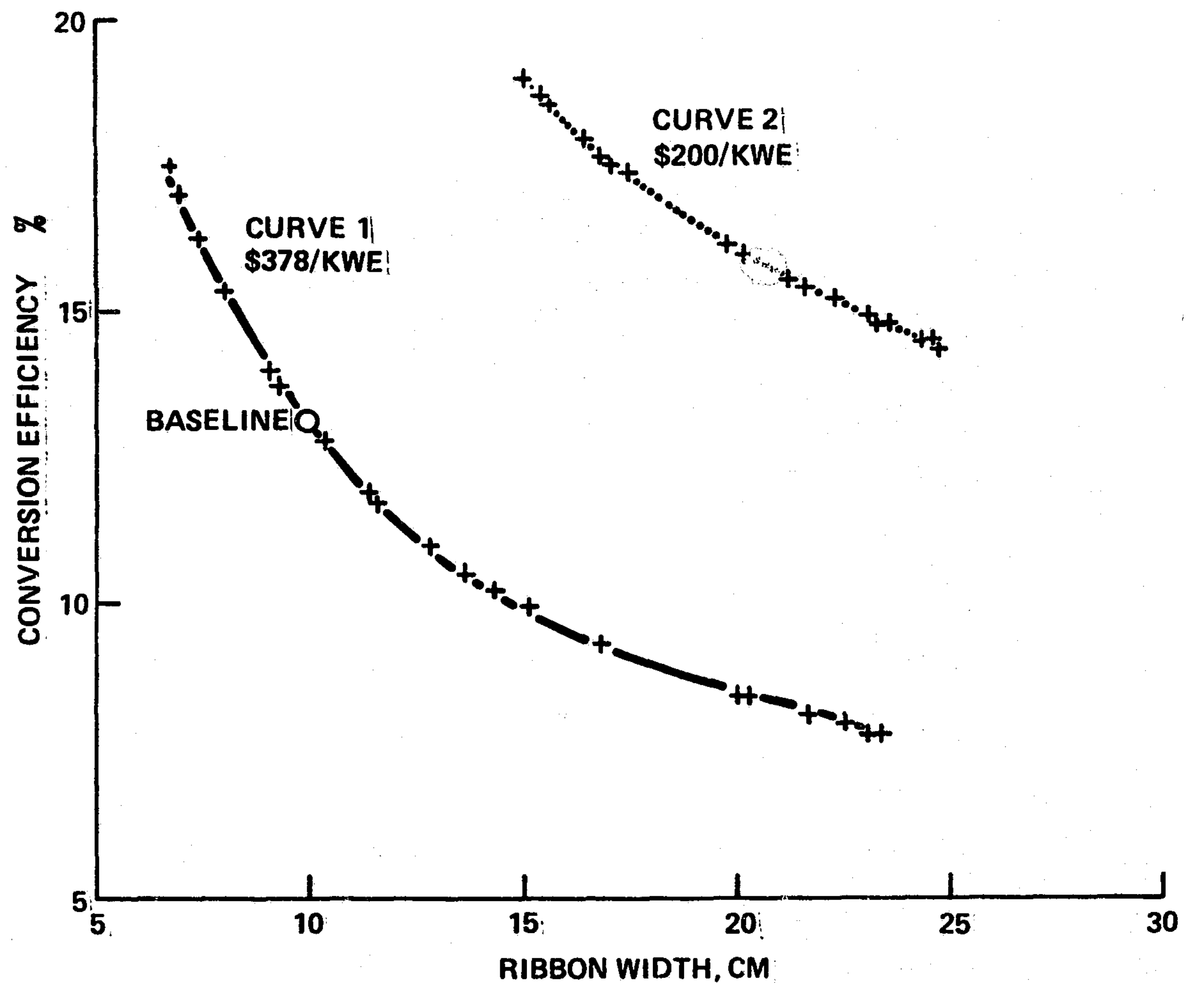

Fig. III-9. 1986 Outlook - Conversion Efficiency vs Ribbon Width - $378/kWE--$200/kWE Technology - Poly Cost $10/kg.

curve (e.g., 13% conversion efficiency, 10 cm wide ribbon), in conjunction with the other technology parameter values of Fig. III-6, (scenario 3, set 1) results, after calculation, in an energy capacity cost of $378/kWE. Curve 2 is a similar plot for conversion efficiency vs ribbon width resulting in $200/kWE at the level of sheet material. As can be inferred from inspecting Fig. III-9, $100/kWE is not yet practical with technology as defined here. In figures III-10 and III-11, poly silicon cost and growth rate,

respectively, are varied and plotted versus ribbon width. In this case, the model only accepts as valid those output values which result in a sheet material cost of $\$50/m^2$ and $\$30/m^2$. In each case, $\$50/m^2$ is a sound value, and $\$30/m^2$ is difficult to approach.

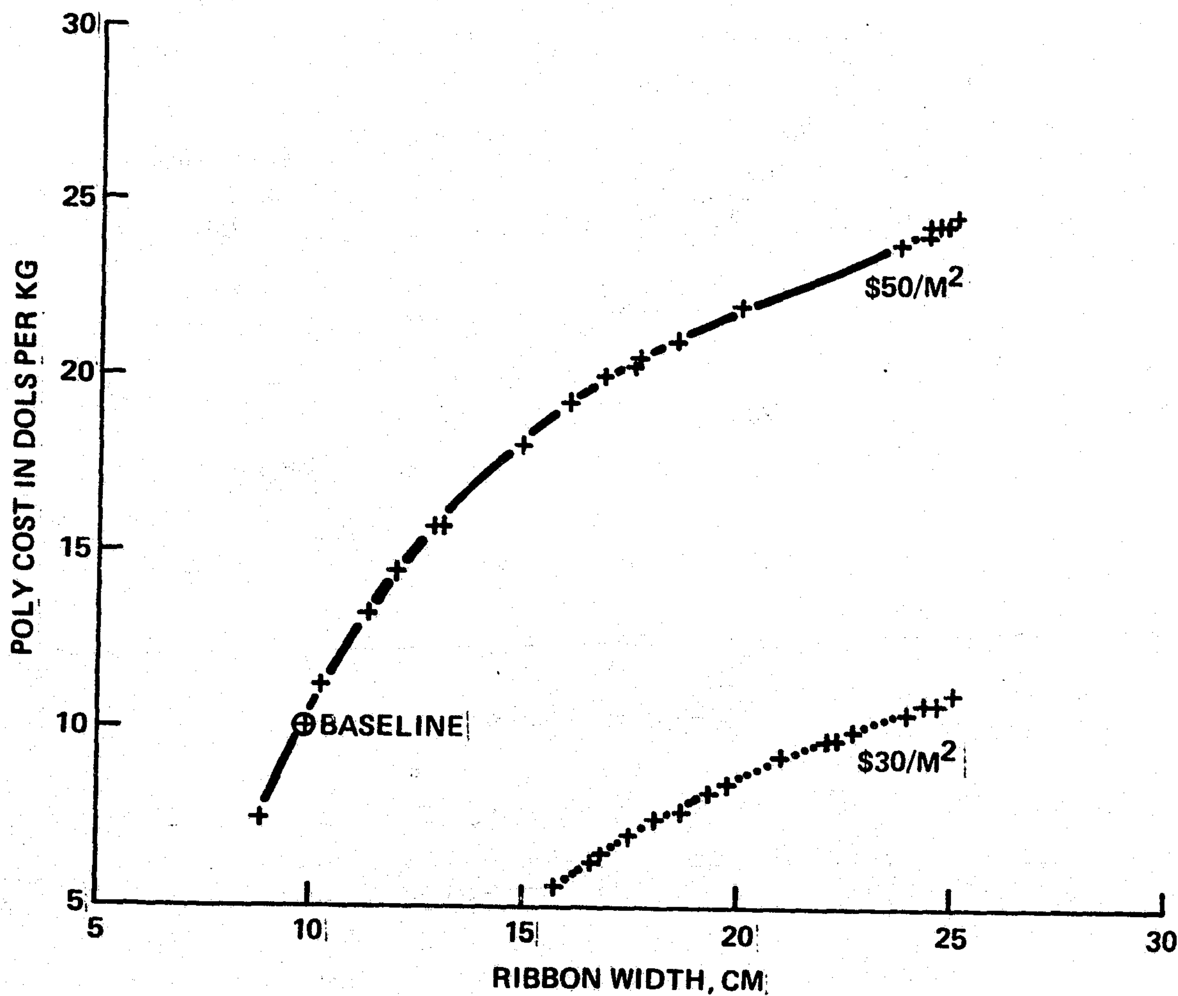

Fig. III-10. 1986 Outlook - Poly Silicon Cost vs Ribbon Width - $\$50/m^2$-$\$30/m^2$ Technology, Growth Rate: 3.8 m/hr.

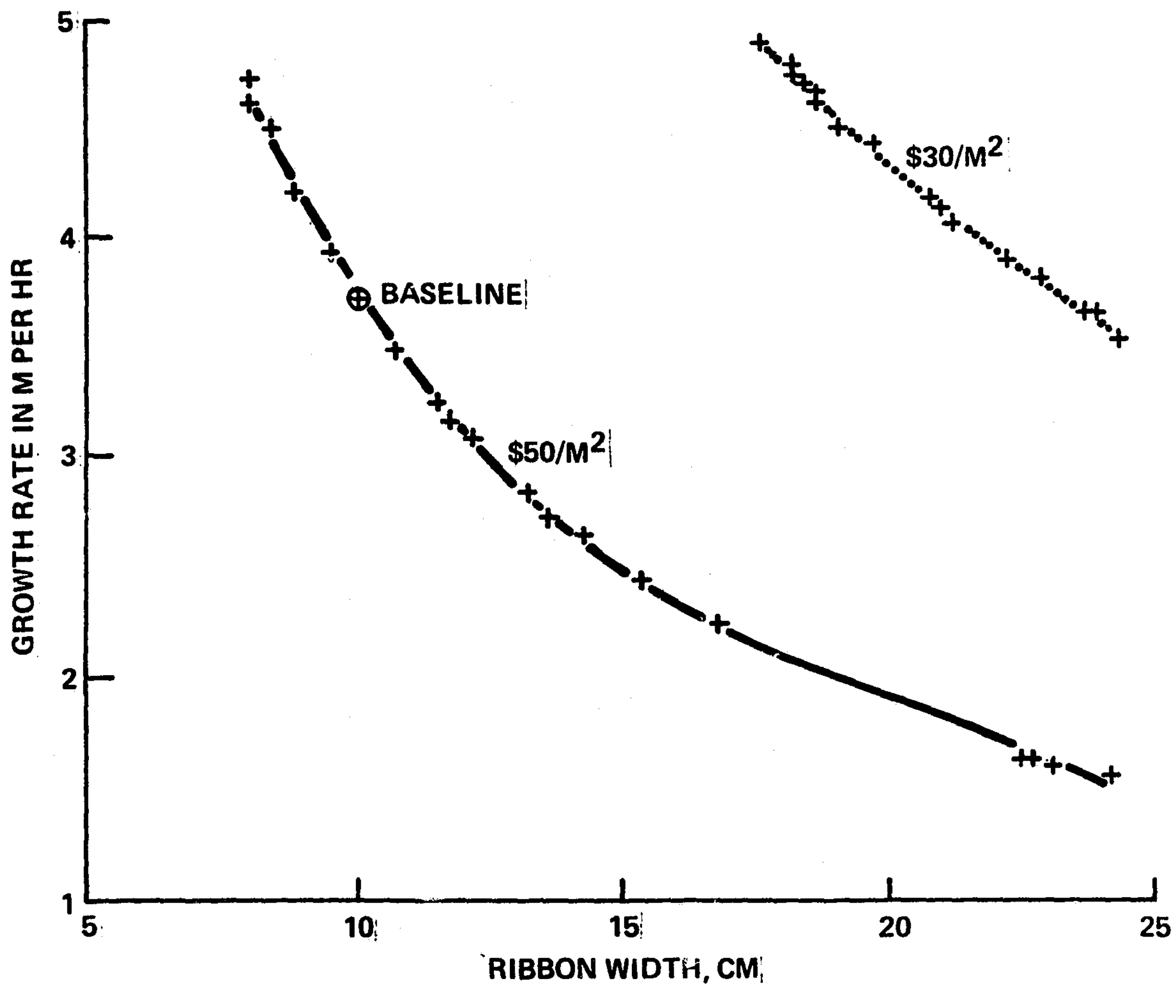

Fig. III-11. 1986 Outlook - Growth Rate vs Ribbon Width - \$50/m² and \$30/m² Technology - Poly Cost \$10/kg.

Finally, Fig. III-12 shows energy capacity cost at the level of silicon sheet material versus ribbon width for three poly silicon price levels: $10/kg, $20/kg, and $30/kg. Figure III-12 confirms our contention that semiconductor grade poly silicon at $10/kg is a prerequisite for low-cost photovoltaic products.

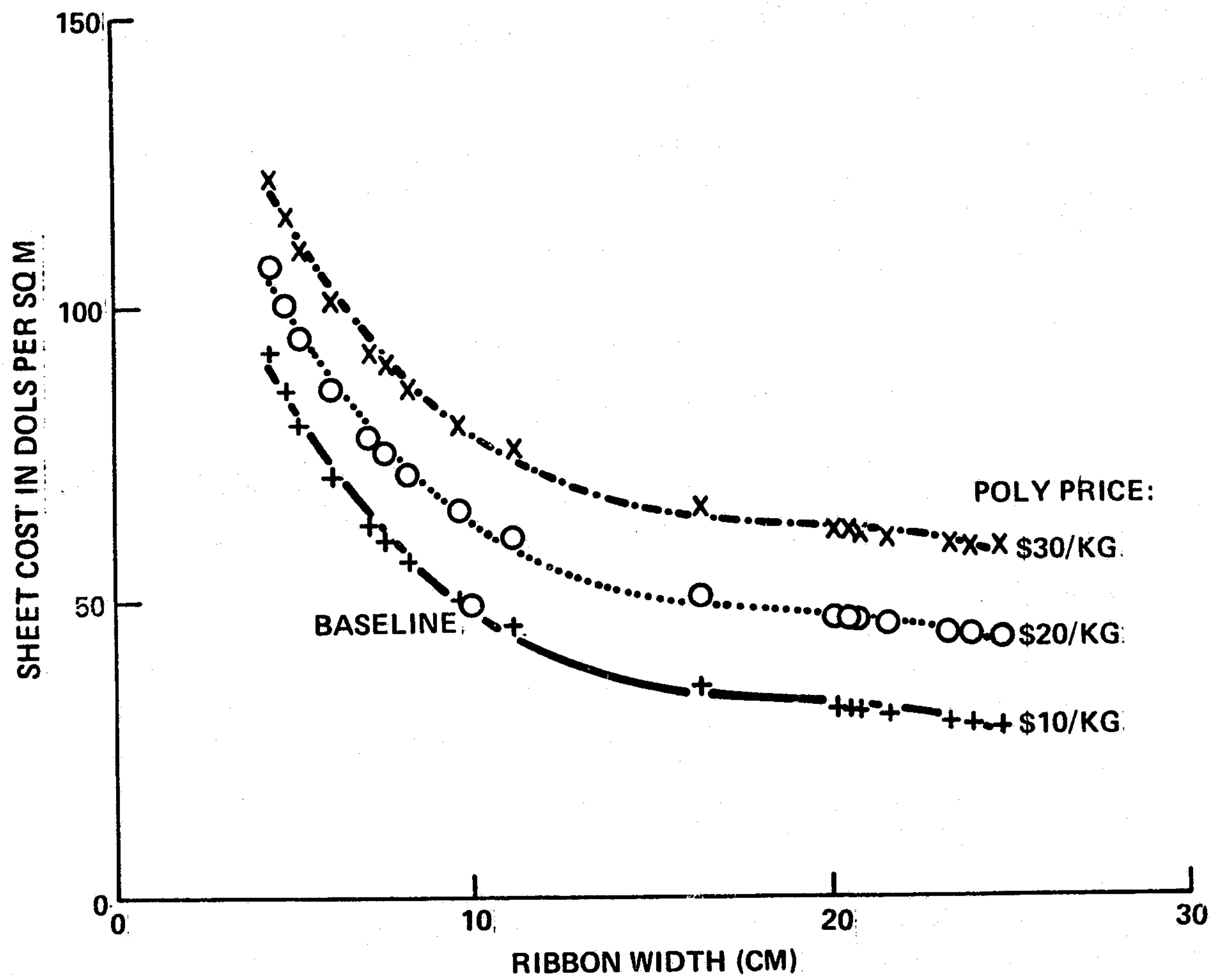

Fig. III-12. 1986 Outlook - Sheet Cost vs Ribbon Width For $30/kg, $20/kg, $10/kg Poly Prices.

5.0 ECONOMIC OUTLOOK FOR $25/m^2 SILICON RIBBON (Scenario Set 2)

The previous section of this chapter presented a business strategy plus an assessment of silicon ribbon technology based upon what we know today, and are already confident can be achieved by 1986: $50/m^2. However, ribbon technology is still young, and the probability is good that further significant advances will occur, reducing prices even below that value. A range of possibilities is discussed within the framework of the second set of scenarios.

Figure III-13 is a listing of three sets of input parameter values to PECAN, which envisions the following advances in ribbon technology beyond those presented in Fig. III-6 (scenario 3, set 1) (simulation 81), and resulted in a sheet material price of $49.19/m^2 (Table III-7):

```
LIST OF RIBBON PARAMETERS AND THEIR ASSIGNED VALUES
RIBBON DATA FROM SIMULATIONS 82 83 84 FILE OPENED 11/04/75
YEARS ARE:    1986   1986   1986

1  RIBBONS GROWN SIMULTANEOUSLY -     1   1   2
2  RIBBON WIDTH, CM -  10.0 10.0 10.0
3  RIBBON GROWTH RATE,M/HR -    4.66  6.59  6.59 ..OR AS PCT  75  75  75
4  RIBBON THICKNESS, MM -  0.20 0.10 0.10
5  YIELD OF  CELL QUALITY RIBBON, PCT -   95  95  95

  DIRECT COST
6  RIBBON FURNACE, DOLLARS -    50000  50000  50000
7      EQUIPMENT LIFE, YEARS -   7.0  7.0  7.0
8      INTEREST RATE, PERCENT -  10.0 10.0 10.0
9      EQUIPMENT AVAILABILITY, PERCENT -    90   90   90
   PERSONNEL PER SHIFT PER MACHINE
10 11 NO. OF SUPVS -  0.05 0.05 0.05 AT $ -  25000 25000 25000
12 13 NO. OF ENGRS -  0.10 0.10 0.10 AT $ -  20000 20000 20000
14 15 NO. OF TECHN -  0.10 0.10 0.20 AT $ -  10000 10000 10000
16 POLY SILICON COST, DOLS/KG -   10  10  10
17 POLY YIELD TO RIBBON,PERCENT -   95  95  95
   SERVICES AND SUPPLIES
18     CRUCIBLE/DIE/PARTS COST PER DAY -   45  45  45 DOLLARS
19     POWER COST AT -  0.05 0.05 0.05 DOLLARS PER KWH
20     ENERGY TO OPERATE EQUIPMENT -   12  12  12 KW

21 22  O/H -   50  50  50 PCT OF PERS,   15  15  15 PCT OF RAW MATL COST
23  G_AND_A -   25  25  25 PERCENT OF DIRECT COST+OVERHEAD

24  PROFIT BEFORE TAX, PERCENT - 10 10 10 OF DC+O/H+G+A

  MISCELLANEOUS
25 WORKWEEK, HOURS -  168 168 168
26 CONVERSION EFFICIENCY, PERCENT -  13.00 13.00 13.00
27 ENERGY DENSITY AT AM1,KW/SQ M PEAK -    1   1   1
```

Fig. III-13. Input Parameter Values to PECAN - Optimistic Outlook (1986 Technology).

Situation	Simulation No.		
	82	83	84
1. The growth of 2 ribbons from 1 crucible becomes possible (third case)...	1	1	2
2. ...requiring one operator to run (no. of machines)	10	10	5
3. Thinner ribbons are becomming practical...(mm)	0.2	0.1	0.1
4. ....resulting in faster actual growth...(m/hr.)	4.66	6.59	6.59
5. Combined yield of "cell quality" and poly yield to ribbon improves to...(%)	90	90	90
6. Assume a "leaner" type of business firm, capable of operation with an overhead of (%)	50	50	50
of personnel cost and (%) of raw material cost.	15	15	15

The result of executing PECAN is listed in Table III-11. It demonstrates that with additional advances in technology, 1986 ribbon prices ranging from $30/m^2$ to $13/m^2$ can be foreseen. Thus our confidence in $25/m^2$ ribbon prevails.

ECONOMICS OF SILICON RIBBON - ONE RIBBON PULLER

SIMUL FILE OPENED 11/04/75

SIMULATION NO:	82	83	84
YEARS:	1986	1986	1986
RIBBONS GROWN SIMULTANEOUSLY	1.00	1.00	2.00
RIBBON WIDTH, CM	10.00	10.00	10.00
AVG YIELDED GROWTH RTE.SQ M/HR	0.40	0.56	1.13
COMBINED YIELD FACTOR	0.90	0.90	0.90
DIRECT COST IN DOLS/SQ METER			
EQUIPMENT CAPITAL RECOVERY	3.07	2.17	1.08
PERSONNEL	5.33	3.77	2.33
POLY SILICON COST	5.16	2.58	2.58
SERVICES/SUPPLIES	4.71	3.33	1.67
SUBTOTAL:	18.28	11.85	7.66
OVERHEAD COST IN DOLS/SQ METER	3.36	2.23	1.51
G&A EXPENSES IN DOLS/SQ METER	5.41	3.52	2.29
PROFIT IN DOLLARS/SQ METER	2.71	1.76	1.15
TOTAL COST IN DOLS/SQ METER	29.76	19.37	12.62
DOLLARS PER KW	228.89	149.01	97.04

ORIGINAL PAGE IS OF POOR QUALITY

TABLE III-11. 1986 Economic Outlook With Unscheduled Major Technology Advances.

6.0 CONCLUSIONS

- Based upon recent significant achievements (e.g., 10 cm wide ribbon; > 11% efficient cell), we believe that $\$50/m^2$ silicon sheet can be obtained with CAST technology by 1986 without further scientific breakthrough.

- $\$25/m^2$ silicon ribbon by 1986 still requires significant technology advances. A set of technology requirements has been defined, which results in ribbon prices ranging from $\$13/m^2$ to $\$30/m^2$.

- Since our ribbon geometry objectives (10 cm wide, 0.3 mm thick) have been achieved, short-range technology development will focus on improving material quality (long-range objective: 13% cell efficiency) and increasing growth rate (objective: 3.8 m/hr.)

- Semiconductor grade poly silicon must by 1986 be available at $10/kg for low-cost photovoltaics to become reality.